

UNIVERSIDAD
NACIONAL
DE COLOMBIA

Photostability enhancement in oligo (phenylene vinylene) systems and their application as heterogeneous photocatalysts

Edgar Mauricio de Jesús Acelas Mantilla

Universidad Nacional de Colombia

Facultad de Ciencias

Departamento de Química

Bogotá, Colombia

2022

Photostability enhancement in oligo (phenylene vinylene) systems and their application as heterogeneous photocatalysts

Edgar Mauricio de Jesús Acelas Mantilla

Thesis presented as partial fulfillment of the requirements for the degree of:
Ph.D. in Sciences - Chemistry

Ph.D. Advisor:
César Augusto Sierra Ávila, Ph.D.

Macromolecules Research Group

Universidad Nacional de Colombia
Facultad de Ciencias
Departamento de Química
Bogotá, Colombia
2022

*“Look around you. That’s how chemistry began – in the
limitless curiosity of human beings about their surroundings”.*

Therold Moeller

Chemistry, Chapter 1 (p. 1)

Academic Press. New York, New York, USA. 1978

Acknowledgements

I gratefully acknowledge the Teaching Assistant Scholarship Program of Universidad Nacional de Colombia for providing such valuable teaching experience and which financial support was essential during the first two years of the PhD program. I would also want to thank the Ministry of Science, Technology, and Innovation (MINCIENCIAS), for the financial support granted through the Bicentenary Scholarship program.

I would also like to extend my deepest gratitude to Prof. César Sierra for all his advice, patience, guidance, and unconditional friendship. His permanent and unwavering efforts to motivate me through this graduate formation process, make him deserve special recognition and endless admiration, not only as an outstanding scientist but as a marvelous human being. I thank him for showing me that innovative chemistry is the foundation to build a better world.

I very much appreciate being part of Makro. I thank all my fellow lab mates the stimulating discussions, especially on Friday's afternoons. In particular, I'm grateful to Diana for her permanent spirit of service and lifesaving advice.

I also wish to acknowledge the support received by Prof. León Pérez (UNAL), Prof. Nelson Castellanos (UNAL), Prof. Gina Hincapié (UNAL), Prof. Crispin Celis (U. Javeriana) and the Mass Spectrometry laboratory at Universidad Industrial de Santander.

Resumen

Mejora de la fotoestabilidad en sistemas oligo (fenilen vinileno) y su aplicación como fotocatalizadores heterogéneos

El primer capítulo revisa los aspectos más relevantes del uso de sistemas conjugados tipo fenilen vinileno (FV) en diferentes aplicaciones fotocatalíticas. A pesar de que la actividad fotoquímica de estos sistemas se ha descrito en campos que van desde la terapia fotodinámica en sistemas biológicos, la degradación de contaminantes, la síntesis química y la producción de hidrógeno, es evidente que se requieren mejoras sustanciales en términos de fotoestabilidad que permitan promover futuras investigaciones en este campo, considerando que el fragmento vinílico es el principal responsable de la degradación de estos materiales limitando su exploración como fotocatalizadores. No obstante, existe suficiente evidencia experimental que permite proponer estrategias como el ensamble de estructuras más rígidas, el uso de sustituyentes electroattractores y el uso de soportes inorgánicos para atenuar la fragmentación del sistema FV y, de este modo, mejorar sustancialmente su desempeño en las aplicaciones mencionadas anteriormente.

El segundo capítulo describe la síntesis y caracterización química y optoelectrónica de cuatro compuestos oligo (fenilen vinileno) *target*, preparados a partir de la reacción de Mizoroki-Heck bajo condiciones solvotérmicas como estrategia sintética para el ensamble de la estructura conjugada en configuración *E-E* con rendimientos de moderados a altos. Se encontró que estos materiales exhiben características de absorción desde la región visible del espectro electromagnético, lo cual sugiere que su actividad fotoquímica puede darse incluso empleando fuentes de irradiación con longitudes de onda >400 nm. Además, sus propiedades optoelectrónicas, tanto en solución como en estado sólido, confirman su potencial como fotocatalizadores orgánicos. Adicionalmente, se exploró la preparación de compuestos amino oligo (fenilen vinileno) a partir de diferentes rutas, encontrándose que

la reducción de nitro oligo (fenilen vinilenos) empleando el sistema Na_2S /piridina constituye una ruta simple que permite superar los inconvenientes relacionados con la solubilidad de estos materiales.

El tercer capítulo muestra el comportamiento fotocatalítico de los cuatro sistemas fenilen vinileno adsorbidos sobre SiO_2 frente a la degradación del colorante índigo carmín (IC), empleando como fuente de luz un panel LED de 350-450 nm. Se logró comprobar mediante diferentes técnicas espectroscópicas, así como espectrometría de masas, que los sustituyentes electroattractores contribuyen a la fotoestabilidad de los sistemas. Adicionalmente, fue posible establecer que el sistema **OPV 1** es el más eficiente y foto-resistente. Llegando también a identificar claramente sus productos de fotodegradación, los cuales están relacionados principalmente con la reacción del sistema conjugado con diferentes ROS. También, fue posible corroborar la ruta a través de la cual transcurre la degradación del colorante. Simultáneamente se realizó la caracterización de los productos de degradación del índigo carmín, descartándose la participación de radicales $\text{OH}\cdot$. No obstante, experimentos de reusabilidad mostraron una baja capacidad de degradación cercana al 20% para el tercer ciclo.

El cuarto capítulo detalla los procesos sintéticos y la caracterización relacionados con el anclaje químico del sistema **OPV 1** sobre SiO_2 y TiO_2 así como su copolimerización con segmentos rígidos y flexibles; estrategias propuestas para la mejora de la estabilidad frente a su uso como fotocatalizadores. Simultáneamente se llevó a cabo su evaluación como fotocatalizadores heterogéneos para la degradación de IC, encontrando que el material **TiO_2 /OPV 1** es capaz de degradar de manera eficiente el IC en tan solo 8 minutos bajo la acción de luz visible. Se determinó que este proceso está facilitado por la transferencia de carga del **OPV 1** hacia el TiO_2 , este último responsable de interactuar con el oxígeno para generar ROS, ocasionando la degradación del colorante. Así mismo, se evidenció reducción directa del IC por el OPV, como ruta de degradación alternativa, exclusiva de este material. Por su parte, cuando se empleó SiO_2 como soporte para el **OPV 1**, la degradación del IC fue baja, inclusive empleando radiación UVA. Por otro lado, los polímeros sintetizados exhibieron una mayor actividad fotocatalítica empleando LEDs de 350-450 nm. En conjunto, la actividad fotocatalítica y la estabilidad mejoraron significativamente, encontrándose que el **TiO_2 /OPV 1** y el polímero con separadores

aromáticos rígidos **Pol-1**, mantienen un elevado porcentaje de degradación del IC hasta el séptimo ciclo de reuso. Lo anterior lleva a que esta tesis se constituya en punto de partida para futuras investigaciones relacionadas con el diseño racional de materiales basados en fenilen vinilenos que puedan presentar mejores propiedades, desempeño y estabilidad para su aplicación como sistemas fotocatalíticos.

Finalmente, el quinto capítulo expone los resultados obtenidos en la fotodegradación de colorantes presentes en una muestra real de agua residual textil y de soluciones de 17β -estradiol, hormona excretada en el proceso productivo avícola, empleando como fotocatalizadores los sistemas **TiO₂/OPV 1** (bajo irradiación con luz visible) y **Pol-1** (bajo irradiación con luz UV). Lo anterior como propuesta de remediación a problemáticas de impacto nacional tanto para la industria textil como la industria avícola. En general, se confirma que los sistemas FV evaluados tienen potencial para abordar de manera preliminar estos desafíos ambientales, proyectándose como una alternativa relevante en el control de contaminantes acuosos.

Palabras clave: oligo (fenilen vinileno), fotocatalisis heterogénea, estabilidad, anclaje químico, fotodegradación.

Abstract

Photostability enhancement in oligo (phenylene vinylene) systems and their application as heterogeneous photocatalysts

The first chapter revises the most relevant aspects of phenylene vinylene (PV) systems applied to photocatalysis. Despite the photochemical applications of these conjugated systems that have been widely described and involve photodynamic therapy, pollutants degradation, chemical synthesis, and hydrogen production, among others, it should be noted that a major photostability improvement is required to promote future research in this field. Evidence has pointed out that the vinyl segment directly contributes to the degradation of the PV materials, thus limiting its exploration as organic photocatalysts. Notwithstanding, the scientific literature provides some clues regarding strategies such as structural rigidification and the use of electron-withdrawing groups and inorganic supports to attenuate the PV system fragmentation and therefore enhance the materials' photocatalytic performance.

The second chapter describes the synthesis and chemical/optoelectronic characterization of four target OPVs, prepared via Mizoroki-Heck reaction under solvothermal conditions as a strategy to assemble the conjugated framework with *E-E* configuration in moderate to high yields. These OPV materials displayed absorption features that included the visible region of the electromagnetic spectrum, suggesting their photochemical activity can be achieved under irradiation with wavelength values >400 nm. Moreover, their optoelectronic properties in both solution and solid-state confirm their potential as organic photocatalysts. Additionally, the preparation of amino OPVs was rationally explored. It was found that the

reduction of nitro OPVs employing Na₂S/pyridine provides a simple and straightforward synthetic tactic to overcome all the solubility issues related to these materials.

The third chapter summarizes the photocatalytic behavior towards the degradation of indigo carmine dye (IC) of the four target OPVs when adsorbed on SiO₂ and irradiated using a 350-450 nm LED panel. Different spectroscopic techniques and mass spectrometry allowed us to corroborate that tethering electron-withdrawing groups around the conjugated backbone contribute to the OPV systems' photostability. **OPV 1** resulted in the most efficient and photo-resistant material; its photodegradation products were clearly identified and found to directly relate to the chemical reaction of the conjugated framework with different ROS. The IC photodegradation route was also established, simultaneously identifying the dye degradation products, where the participation of OH[•] radicals could be disregarded. Nevertheless, reusability experiments confirmed a very low degradation percentage (20%) for the third cycle.

The fourth chapter provides detail of the synthetic process and characterization of the chemical immobilization of **OPV 1** onto SiO₂ and TiO₂ along with its copolymerization with rigid and flexible spacers as strategies to improve the photostability of the PV system during the heterogeneous photocatalytic degradation of IC. The assessment of the materials as photocatalyst was simultaneously carried out, where **TiO₂/OPV 1** displayed outstanding IC degradation performance under visible light. It was found that this process is boosted by the charge transfer process from the OPV moiety towards the TiO₂ support, the latter responsible for directly interacting with oxygen to generate ROS producing the dye degradation. Additionally, a direct reductive IC decoloration pathway was observed for this material. On the other hand, when SiO₂ was employed as support for **OPV 1**, the IC degradation was inferior compared to all other materials, even under UVA irradiation. Also, the prepared polymers exhibited a greater photocatalytic activity when 350-450 nm LEDs were used. In summary, both photocatalytic activity and stability significantly improved as demonstrated by **TiO₂/OPV 1** and the polymer with aromatic rigid spacers **Pol-1**, which preserved a significantly high IC degradation percentage up to the seventh reuse cycle. This thesis comprises the starting point for future research concerning the rational design of PV-based materials with enhanced properties, performance, and stability for their application as photocatalytic systems.

Finally, the fifth chapter discloses the obtained results concerning the treatment of a real textile wastewater sample and 17 β -estradiol solutions, the hormone released in the poultry process, using **TiO₂/OPV 1** (under visible light) and **Pol-1** (under UV light) as photocatalysts. This, as a remediation strategy for national environmental issues of concern. In general, it was confirmed that the evaluated PV systems serve as preliminary approaches to address the above-mentioned environmental challenges, comprising a pertinent alternative towards the control of aqueous pollutants.

Keywords: oligo (phenylene vinylene), heterogeneous photocatalysis, stability, chemical immobilization, photodegradation

Content

Content	Page
1. Phenylene vinylene systems in photochemistry	3
1.1 Phenylene vinylene systems	3
1.1.1 Synthesis	4
1.1.2 Photophysical and photochemical properties	9
1.2 Photochemical applications	12
1.2.1 Strategies for photostability enhancement	12
1.2.2 Photosensitization and photodynamic therapy	20
1.2.3 Hydrogen production	25
1.2.4 Photosynthetic and other miscellaneous applications	28
1.3 Aims and objectives	32
1.4 Originality of the thesis	34
2. Synthesis and optoelectronic characterization of <i>trans-trans</i> oligo (phenylene vinylene) systems	37
2.1 Introduction	37
2.2 Experimental section	38
2.2.1 Materials	38
2.2.2 Characterization	39
2.2.3 Synthesis of starting materials	40
2.3 Results and discussion	45
2.3.1 Synthesis and structural characterization of OPVs	45
2.3.2 Optoelectronic characterization of target OPVs	57
2.4 Conclusions	62
3. Assessment of OPVs photocatalytic activity in the degradation of indigo carmine dye 64	
3.1 Introduction	64
3.2 Experimental section	66
3.2.1 Materials	66
3.2.2 Analytical techniques	66
3.2.3 Photocatalyst preparation	67
3.2.4 Photocatalytic IC degradation	67
3.2.5 Photostability experiments	68
3.2.6 Singlet oxygen quantum yield determination	69

3.3	Results and discussion.....	69
3.3.1	Optoelectronic properties of SiO ₂ adsorbed OPVs.....	69
3.3.2	Photostability of OPV systems.....	71
3.3.3	Photocatalytic performance of OPVs.....	77
3.4	Conclusions.....	86
4.	Photostability enhancement in OPV systems.....	89
4.1	Introduction.....	89
4.2	Experimental section.....	90
4.2.1	Materials.....	90
4.2.2	Analytical techniques.....	90
4.2.3	Chemical modifications of OPV 1	91
4.2.4	Photocatalytic IC degradation.....	95
4.3	Results and discussion.....	96
4.3.1	Synthesis and characterization of OPV grafted SiO ₂ and TiO ₂	96
4.3.2	Synthesis and characterization of OPV 1 copolymers.....	107
4.3.3	Photocatalytic performance of OPV 1 derivatives.....	115
4.4	Conclusions.....	127
5.	Other photocatalytic applications.....	129
5.1	Introduction.....	129
5.2	Experimental section.....	131
5.2.1	Materials.....	131
5.2.2	Analytical techniques.....	131
5.2.3	Preparation of poultry litter extracts.....	132
5.2.4	Photocatalytic experiments.....	132
5.3	Results and discussion.....	133
5.3.1	Discoloration of an actual textile wastewater sample.....	133
5.3.2	Control of aqueous 17- β estradiol.....	136
5.4	Conclusions.....	144
6.	Perspectives.....	145
7.	Appendices.....	147
7.1	Spectroscopic characterization of precursors and target OPVs 1-4	147
7.2	Synthetic procedures for nitro and amino-OPVs employed for Na ₂ S/pyridine reduction scope determination.....	158
7.3	Experimental data for nitro and amino OPVs employed for Na ₂ S/pyridine reduction scope determination.....	170
7.4	Experimental data for polymerization precursors.....	184
7.5	Plots for Φ_{Δ} estimation.....	185
7.6	HPLC calibration curve for 17 β -estradiol.....	187
7.7	Mass spectra set for 17 β -estradiol UPLC traces in poultry litter extracts.....	188
7.8	Publications and conferences.....	189

List of figures

Figure 1-1: Examples of PV systems. (a) PV structural unit, (b) OPV, and (c) PV copolymer.	3
Figure 1-2: Pd-catalysts employed for cross-coupling reactions.	8
Figure 1-3: Jablonski diagram illustrating photoluminescence processes and type I/type II photoreactions.	10
Figure 1-4: Photoinduced electron transfer mechanisms for the sensitizer (Sens) with; (a) an acceptor <i>A</i> , and (b) with a donor <i>D</i>	11
Figure 1-5: Participation of the PV excited triplet state in the overall photodegradation.	14
Figure 1-6: Chemical modifications on the PPV aryl rings leading to exceptional photostability.	17
Figure 1-7: Sp ³ carbon-bridge rigidification of PV systems and proposed reversible alkene scission.	18
Figure 1-8: Two-photon photosensitized production of singlet oxygen by OPVs. S _n : excited singlet states; S _{vir} : virtual excited state.	21
Figure 1-9: Enhanced singlet oxygen production by polymerization.	22
Figure 1-10: Schematic illustration of PPV self-assembly with siRNA and photochemical disruption of the endosomal membrane. Adapted from Ref. 101.	23
Figure 1-11: Schematic illustration of the BRET process with a cationic OPV. Adapted from Ref. 103.	24
Figure 1-12: PPV evaluated for hydrogen production.	26
Figure 1-13: Molecular and 3D-core structure of g-C ₄₀ N ₃ -COF employed for photocatalytic hydrogen evolution.	27
Figure 1-14: Highly porous PV-polymer photocatalyst for visible-light driven oxidative hydroxylation of aryl boronic acids. Adapted from Ref. 112.	28
Figure 1-15: Rhodium-coordinated PV-containing copolymer for NAD ⁺ photocatalyzed reduction.	29
Figure 1-16: Photoinduced cationic polymerization employing PPV-g-PSt. Adapted from Ref. 118.	30
Figure 1-17: OPV light-promoted synthesis of Au nanoparticles. Adapted from Ref. 119.	30
Figure 1-18: PDPB chemical structure and schematic photodegradation of phenol. Adapted from Ref. 120.	32
Figure 1-19: Structure and content overview of the thesis.	34
Figure 1-20: Number of publications by year containing the term “phenylene vinylene”. Source: Scopus.	35

Figure 2-1. Overall synthesis route for OPVs 1-4	45
Figure 2-2. Products observed under the evaluated reaction conditions for nitro-OPVs 3i and 3j	52
Figure 2-3. MALDI-ToF spectrum of purified fraction for 3i reduction product.....	52
Figure 2-4. ¹ H-NMR expanded aromatic region of 3i reduction products.....	53
Figure 2-5. Proposed mechanism of OPV azo-dimerization.	53
Figure 2-6. IR spectrum of compound OPV 3	54
Figure 2-7: MALDI-ToF MS spectrum of compound OPV 3	55
Figure 2-8: ¹ H-NMR spectrum for compound OPV 3 , aromatic region (6.85–7.55 ppm) expansion.	55
Figure 2-9: Normalized absorption and emission spectra for OPVs 1-4 in MeCN.....	58
Figure 2-10: Excitation-Emission Matrices (EEM) for OPVs 1-4 in MeCN.	59
Figure 2-11: (a) Diffuse reflectance spectra of OPVs, (b) Kubelka-Munk function of OPVs, and (c) solid-state emission spectra for OPVs.....	60
Figure 2-12: Cathodic (left) and anodic (right) scans for OPVs 1 (a), 2 (b), 3 (c) and 4 (d).	61
Figure 2-13: Relative HOMO-LUMO levels alignment for OPVs (vs. NHE).....	62
Figure 3-1: Schematic preparation of OPVs photocatalyst by the wet impregnation method.	67
Figure 3-2: Experimental set-up for IC degradation.....	68
Figure 3-3: LED panel emission spectrum.....	68
Figure 3-4: (a) Diffuse reflectance spectra, (b) Kubelka-Munk function, and (c) solid-state emission spectra of OPVs adsorbed in SiO ₂	70
Figure 3-5: Absorption decay profile at λ _{max} for OPVs 1-4 in MeCN solution.	71
Figure 3-6: UV-Vis monitoring of stability for OPVs 1-4 upon irradiation. Initial and final UV-vis spectra are shown for comparative purposes.....	73
Figure 3-7: Spectral changes observed at various times for OPVs 1-4 upon irradiation under open and nitrogen atmosphere. Isosbestic points are highlighted.	74
Figure 3-8: ¹ H-NMR spectrum of (a) OPV 1 , and (b) OPV 2 after irradiation in open (red spectra) and nitrogen atmosphere (blue spectra).	75
Figure 3-9: ESI (-)-IT mass spectrum of OPV 1 after irradiation under open atmosphere and structure of the identified degradation products.....	76
Figure 3-10: ESI (+)-IT mass spectra of OPV 3 before and after irradiation under aerobic and anaerobic conditions.	77
Figure 3-11: (a) SiO ₂ -OPVs induced photodegradation of IC dye and (b) dye degradation profile at λ _{max} employing SiO₂-OPV 1 as photocatalyst.....	77
Figure 3-12: Scavengers effect on IC degradation with SiO₂-OPV 1 after 45 minutes of reaction. Control: SiO₂-OPV 1 without the addition of any scavenger.....	78
Figure 3-13: Color degradation profile of IC in the presence of SiO₂-OPV 1 and oxalic acid (2 mM) as sacrificial electron donor.....	79
Figure 3-14: Reaction of 2-furoic acid with singlet oxygen.....	80
Figure 3-15: Singlet oxygen mediated degradation of furoic acid. Left: With SiO₂-OPV 1 ; Right: Control experiment (no photocatalyst).	80

Figure 3-16: Negative mode ESI-MS spectra of IC and its photo-irradiated solutions in the presence of SiO₂-OPV 1 and structure of most abundant ions observed in MS spectra. 81	81
Figure 3-17: Effect of oxygen in the degradation profile of IC for SiO₂-OPV 1 82	82
Figure 3-18: ESI (-)-IT mass spectrum of IC irradiated under inert atmosphere for SiO₂-OPV 1 and proposed direct oxidative degradation pathway for isatin-5-sulfonic. Marked peaks belong to desorbed OPV 1 (■) and OPV 1 degradation products (▼). 83	83
Figure 3-19: Relative HOMO-LUMO levels alignment for OPVs (vs. NHE) and IC. The LUMO position was estimated by adding the experimental optical ΔE value. 84	84
Figure 3-20: Photocatalytic schematic pathway for IC degradation in the presence of SiO₂-OPV 1 and oxalic acid as sacrificial electron donor. 85	85
Figure 3-21: Reusability of SiO₂-OPV 1 in the degradation of 50 μM IC aqueous solution. 86	86
Figure 4-1: White LED panel emission spectrum. 95	95
Figure 4-2: Experimental set-up for IC degradation employing TiO₂/OPV 1 and polymer catalysts. 96	96
Figure 4-3: FTIR spectra (KBr disc) of OPV 1 , modified SiO ₂ and TiO ₂ (solid lines) and pristine SiO ₂ and TiO ₂ (dashed lines). 97	97
Figure 4-4: Comparative Raman spectra of (a) SiO₂/OPV 1 and (b) TiO₂/OPV 1 98	98
Figure 4-5: Comparative solid-state ¹³ C CP/MAS NMR spectra for OPV 1 and prepared SiO₂/OPV 1 and TiO₂/OPV 1 photocatalysts. 99	99
Figure 4-6: Deconvoluted XPS spectra of (a) Ti2p, (b) O1s, and (c) C1s regions for TiO₂/OPV 1 100	100
Figure 4-7: Deconvoluted XPS spectra of (a) Ti2p, (b) O1s, and (c) C1s regions for SiO₂/OPV 1 101	101
Figure 4-8: Comparative XRD traces for TiO ₂ , TiO ₂ /SiMe ₃ and, TiO₂/OPV 1 102	102
Figure 4-9: TGA curves for (a) silica gel (solid line), trimethylsilylated SiO ₂ (dots) and SiO₂/OPV 1 material (dashed lines), (b) TiO ₂ P25 (solid line), trimethylsilylated TiO ₂ (dots) and TiO₂/OPV 1 material (dashed lines), and (c) OPV 1 103	103
Figure 4-10: Nitrogen adsorption/desorption isotherms for (a) SiO₂/OPV 1 , and (b) TiO₂/OPV 1 materials. 104	104
Figure 4-11: (a) Diffuse reflectance spectra, (b) Kubelka-Munk function and (c) solid-state emission spectra for OPV 1 grafted materials..... 105	105
Figure 4-12: Molecular representation of interfacial electron transfer reactions and relative energy levels for OPV 1 (HOMO and LUMO), TiO ₂ and SiO ₂ (conduction band: CB, and valence band: VB). 106	106
Figure 4-13: FTIR spectra of polymeric materials Pol-1 and Pol-2 108	108
Figure 4-14: ¹ H-NMR (DMSO-d ₆) spectrum for Pol-1 109	109
Figure 4-15: ¹ H-NMR (CDCl ₃) spectrum for Pol-2 109	109
Figure 4-16: GPC traces of (a) Pol-1 , and (b) Pol-2 110	110
Figure 4-17: ESI-MS spectra set for (a) Pol-1 , and (b) Pol-2 110	110
Figure 4-18: (a) TGA (inset: Pol-1 and Pol-2 films obtained after solvent casting) and (b) DSC heating curves obtained for Pol-1 and Pol-2 112	112
Figure 4-19: SEM micrographs of Pol-1 (a,b) and Pol-2 (c,d) particles..... 112	112

Figure 4-20: Normalized absorption (black) and emission (blue) spectra for Pol-1 and Pol-2	113
Figure 4-21: Excitation-Emission Matrices (EEM) for OPV 1 and materials Pol-1 and Pol-2	113
Figure 4-22: (a) Diffuse reflectance spectra, (b) Kubelka-Munk function, and (c) solid-state emission spectra for polymers Pol-1 and Pol-2 . Emission of OPV 1 was included in (c) for comparative purposes.....	115
Figure 4-23: Degradation profile of OPV 1 derivatives employing (a) white LEDs and (b) UVA-Vis LEDs (350-450 nm).	116
Figure 4-24: (a) Effect of scavengers and (b) electrons donors in the IC photodegradation mediated by TiO₂/OPV 1	118
Figure 4-25: Schematic representation of (a) the electron donor (<i>D</i>) effect on the photocatalyst surface, and (b) oxidation potential values of the employed electrons donors.	119
Figure 4-26: Emission spectra of coumarin solutions after irradiation in control and photocatalysis experiments.....	120
Figure 4-27: Degradation of the IC solution (50 μM) employing TiO₂/OPV 1 as photocatalyst under visible light.	121
Figure 4-28: Reversible redox reaction of IC and the λ_{\max} value for each specie.	121
Figure 4-29: Mass spectra set for the degradation of 50 μM IC aqueous solution under different conditions using TiO₂/OPV 1 as photocatalyst. Marked peaks (Δ) correspond to previously identified OPV degradation products.....	122
Figure 4-30: Photocatalytic schematic IC degradation pathway, employing TiO₂/OPV 1 and visible light.	123
Figure 4-31: (a) Effect of scavengers and electrons donors in the IC photodegradation for Pol-1 at 25 min, and (b) Pol-2 at 30 min.	124
Figure 4-32: Degradation of the IC solution (50 μM) employing (a) Pol-1 , and (b) Pol-2 as photocatalysts.....	124
Figure 4-33: Reusability of TiO₂/OPV 1 , Pol-1 and Pol-2 in the degradation of 50 μM IC aqueous solution.....	125
Figure 4-34: (a) Raman spectra set for TiO₂/OPV 1 , and (b) IR spectra set for Pol-1 before photocatalysis and after 5 photocatalytic cycles.....	126
Figure 4-35: Comparative TGA profiles of the TiO₂/OPV 1 photocatalyst before use, and after five photocatalytic cycles.....	127
Figure 5-1: Hormones released by poultry farming activities.	130
Figure 5-2: UV-Vis spectrum of the 1:5 diluted wastewater sample. Inset displays a close-up of the absorption band within the visible region.	133
Figure 5-3: (a) Induced discoloration of wastewater, and (b) discoloration profile at wastewater λ_{\max} employing TiO₂/OPV 1 as photocatalyst under white light irradiation...	134
Figure 5-4: Color degradation profile of the wastewater sample during the photocatalytic process.	134
Figure 5-5: Fluorescence intensity increase of the wastewater sample during the photocatalytic process with TiO₂/OPV 1 under visible light.....	135

Figure 5-6: (a) Induced discoloration of wastewater, and (b) discoloration profile at wastewater λ_{\max} (b) employing Pol-1 as photocatalyst under UV irradiation (350-450 nm).	136
Figure 5-7: UV spectrum of 17- β estradiol.	137
Figure 5-8: (a) HPLC traces of a E2 solution (2500 ng/mL) throughout photodegradation, and (b) degradation profile employing TiO₂/OPV 1 as photocatalyst under white light irradiation.	137
Figure 5-9: Total HPLC chromatograms of an E2 solution (2500 ng/mL) during photocatalysis with TiO₂/OPV 1 under white light irradiation.....	138
Figure 5-10: TIC trace and single ion curves of the ions at m/z 255, 285 and 303 for the E2 solution (2500 ng/mL) after five minutes treatment with TiO₂/OPV 1 under white light illumination.	139
Figure 5-11: (a) HPLC traces of an E2 solution (2500 ng/mL) throughout photodegradation, and (b) degradation profile employing Pol-1 as photocatalyst under UVA light irradiation.	140
Figure 5-12: Total HPLC chromatograms of a 17 β -estradiol solution (2500 ng/mL) during photocatalysis with Pol- 1 under UVA light irradiation.....	141
Figure 5-13: Comparative HPLC traces between 17- β estradiol standard and the obtained poultry litter solutions extracted with water and methanol (mobile phase: formic acid (0.1%)/methanol 30:70 %v/v).	142
Figure 5-14: Comparative HPLC traces between 17- β estradiol standard and the obtained poultry litter solutions extracted with water and methanol (mobile phase: acetonitrile/water 50:50 %v/v).	143
Figure 5-15: Comparative UPLC-MS TIC traces between the 17- β estradiol standard and the obtained poultry litter solutions extracted with water and methanol.....	143

List of schemes

Scheme 1-1: Gilch synthesis of PPV	4
Scheme 1-2: Synthesis of PPV via Wittig reaction.....	5
Scheme 1-3: Synthesis of PV-polymers via Wittig-Horner reaction.....	6
Scheme 1-4: Knoevenagel condensation.	6
Scheme 1-5: Pd-catalyzed reactions for the synthesis of PV materials.....	7
Scheme 1-6: Synthesis of OPVs via Mizoroki-Heck reaction employing triphenyl phosphite as Pd ligand.....	8
Scheme 1-7: Hydroperoxide formation and decomposition in the alkoxy group.	15
Scheme 1-8: Photoinduced transformations of the vinyl fragment.	16
Scheme 1-9: Proposed degradation mechanism of PV systems in the absence of oxygen.	17
Scheme 4-1: Synthesis of precursor 5	93
Scheme 4-2: Synthesis of Pol-1	94
Scheme 4-3: Synthesis of Pol-2	94
Scheme 4-4: Attempts for Pol-3 synthesis.....	95
Scheme 4-5: Synthesis of OPV 1 grafted SiO ₂ and TiO ₂	97
Scheme 4-6: Synthesis of OPV 1 polymeric derivatives.	107
Scheme 4-7: Reaction of coumarin with OH radicals.	120

List of tables

Table 2-1: Preliminary formation of amino and nitro OPV derivatives via direct Mizoroki-Heck coupling reaction.	47
Table 2-2: Reduction conditions evaluated for the synthesis of amino OPVs.	48
Table 2-3: Pd-catalyzed coupling reaction for direct synthesis of nitro OPV precursors.	49
Table 2-4: Sodium sulfide/pyridine reduction of other nitro OPV systems.	51
Table 2-5: ¹ H-NMR signals (ppm) for OPVs.	56
Table 2-6: ¹³ C-NMR signals (ppm) for OPVs (table continues in next page).....	56
Table 2-7: Optoelectronic properties of OPVs 1-4 in MeCN solution and in solid state. .	58
Table 2-8: Electrochemical data obtained for OPVs 1-4	60
Table 3-1: Comparative optoelectronic properties of OPVs 1-4 in solid-state and adsorbed in SiO ₂	70
Table 3-2: Singlet oxygen quantum yields determined for OPVs 1-4 in MeCN solution..	81
Table 4-1: FTIR (KBr disc) carbonyl vibrations for OPV 1 and prepared photocatalysts.	97
Table 4-2: Results of nitrogen sorption and OPV loading for prepared photocatalysts. .	104
Table 4-3: Optoelectronic properties of OPV 1 grafted materials.	106
Table 4-4: GPC data of OPV-1 copolymers.	110
Table 4-5: Estimated chemical structure of polymer adducts.	111
Table 4-6: Optoelectronic properties of OPV 1 polymeric derivatives.	114
Table 4-7: Kinetic parameters determined for IC photodegradation experiments.	117
Table 5-1: Textile wastewater sample chemical analysis results.	134
Table 5-2: Probable structures of products after photocatalytic treatment of aqueous E2 with TiO ₂ /OPV 1.	139

List of commonly used abbreviations.

Ac	Acetyl
CP	Conjugated Polymer
δ	Chemical shift
dba	Dibenzylacetone
DBU	1,8-Diazabicyclo(5.4.0)undec-7-ene
DMF	Dimethylformamide
DMSO	Dimethylsulfoxide
DSC	Differential Scanning Calorimetry
EDG	Electron Donating Group
ESI-IT	ElectroSpray Ionization – Ion Trap
EtOH	Ethanol
eV	Electronvolts
EWG	Electron Withdrawing Group
Φ_{Δ}	Singlet oxygen quantum yield
Φ_f	Fluorescence quantum yield
HMDA	Hexamethyldisilazane
HOMO	Highest Occupied Molecular Orbital
HPLC	High-Performance Liquid Chromatography
hv	light
IC	Indigo Carmine

J	Coupling constant
K_{ap}	Apparent rate constant
λ_{em}	Maximum emission wavelength
λ_{max}	Maximum absorption wavelength
LUMO	Lowest Unoccupied Molecular Orbital
MALDI-ToF	Matrix Assisted Laser Desorption Ionization – Time of Flight
MeCN	Acetonitrile
MeOH	Methanol
NMP	<i>N</i> -Methyl-2-pyrrolidone
NMR	Nuclear Magnetic Resonance
OPV	Oligo (Phenylene Vinylene)
QTOF	Quadrupole Time-of-Flight
ROS	Reactive Oxygen Species
S_{NAr}	Aromatic nucleophilic substitution
T_g	Glass Transition
t_R	Retention time
TIC	Total Ion Current
TGA	Thermogravimetric Analysis
UPLC	Ultra-Performance Liquid Chromatography
XPS	X-Ray Photoelectron Spectroscopy

Introduction

Over the recent years, special efforts have been devoted to responding to the urgent need for more environmentally friendly chemical processes. In this context, several green chemical approaches have been developed, being photochemistry an alternative that has gained exceptional recognition chiefly due to the possibility of employing sunlight as a freely available energy source and reagent. Nevertheless, the global chemical industry has not implemented at a large-scale the use of light-driven processes considering the high costs associated with the energy demand of most common artificial light sources required to fulfill the radiative requirements of most materials.¹ This issue has prompted the development of novel compounds and composites with a broader absorption in the visible region of the spectrum. But their use as photoactive starting materials or photocatalysts can be hampered by poor stability or the presence of heavy and toxic metals.

Still, organic photocatalysts provide noticeably more advantages than just a metal-free approach and include a potent reactivity, an enormous assortment of synthetic routes for their preparation, and outstanding optoelectronic properties that can be tuned by means of chemical diversification.^{2,3} Among them, conjugated systems such as phenylene vinylenes (PV) have been extensively studied since the 1970s, bearing exceptional optical, emissive, and electrical features that led to their insertion in solution-processable organic electronics, flexible circuits, OLEDs, lasers, sensors, and many other photovoltaic applications.⁴ Despite the fact that PV systems have long been acknowledged for their photochemical behavior,⁵ their poor to moderate photostability has prevented a massive use of these materials as photocatalysts and, only a modest but noteworthy number of research dedicated to this field have been described in the literature.^{6,7}

The poor solubility of PV materials is another flaw that has been an extensive subject of research and has prevented the study of critical properties that are often measured in solution and could provide a deeper understanding of PVs photochemical behavior.⁸ To

overcome this issue, the oligomer approach has emerged as a valid alternative to investigate, by extrapolation, the required properties of their high-molecular weight analogs surpassing all solubility and homogeneity limitations.⁹

In this research, four oligo (phenylene vinylene)s (OPVs) are prepared by the Mizoroki-Heck reaction, simultaneously exploring their behavior as heterogeneous photocatalysts in the degradation of indigo carmine dye. The influence of functional groups in their stability, optoelectronic properties, and overall photochemical behavior and performance is investigated, along with the role of oxygen and other reactive species. Moreover, chemical immobilization on solid surfaces and polymerization are examined as promising strategies to enhance not only the photostability but also the photochemical performance of PV materials. Finally, the most promising photovoltaic materials were evaluated as photocatalysts in the remediation of an actual wastewater from a textile company, and also for the degradation of 17 β -estradiol in aqueous solution from a poultry company. All this, as a contribution to addressing some environmental pollution challenges of the Colombian industry.

1. Phenylene vinylene systems in photochemistry

1.1 Phenylene vinylene systems

The phenylene vinylene (PV) moiety (**Figure 1-1**) has served as the basic archetypical candidate structure in the design and development of unnumbered organic and organometallic conjugated compounds (e.g., **1,2** and **3**). Their unique and easily tunable photophysical properties have set the prospect of high-performance emissive and semi-conductive materials suitable for technological applications in organic light-emitting diodes (OLEDs), photovoltaic devices, chemical sensing, and nanoscale molecular wires to enhance charge transfer processes.^{10,11} These organic systems have also been subjected to important structural modifications such as tethering around the PV scaffold fragments with significant molecular complexity that have included, for example, crown ether and organometallic centers, allowing remarkable improvements in terms of thermal stability and photoluminescent quantum yield.^{12,13}

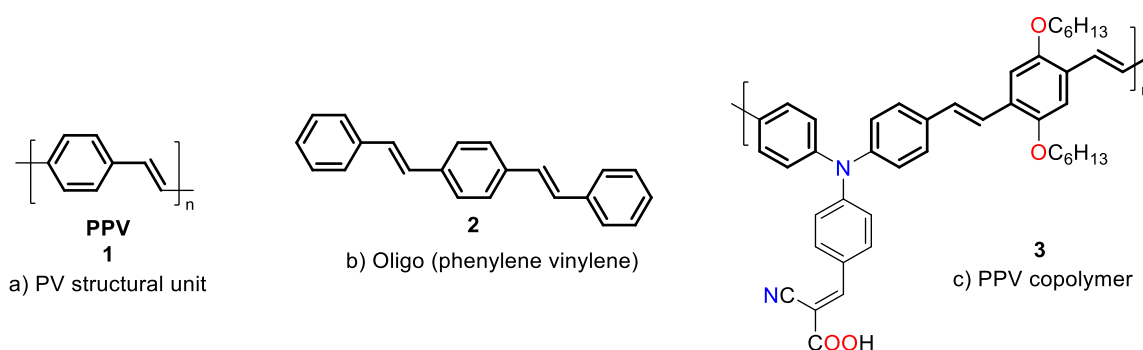


Figure 1-1: Examples of PV systems. (a) PV structural unit, (b) OPV, and (c) PV copolymer.

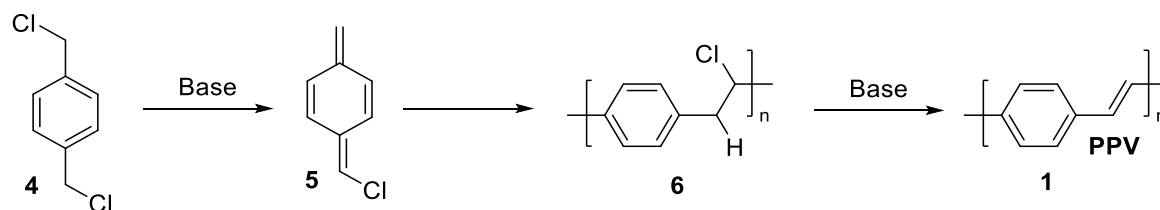
One of the major drawbacks that have prevented a complete study of the properties of PV systems is the poor solubility and processability of these materials. Despite substantial efforts directed to address this problem,^{8,14,15} the oligomer approach, a method to assess the properties of PPVs by extrapolation from low-molecular weight analogs, is presented as a valuable tool to accurately explore a wide range of properties, overcoming structural defects that substantially affect homogeneity in high-molecular weight structures.⁹ In this regard, our research group has markedly contributed to the investigation of oligo (phenylene vinylene)s' (OPVs) chemical and optoelectronic behavior where significant advances have been made in terms of synthetic strategies and the prospect of trending technological applications.¹⁶⁻¹⁹

1.1.1 Synthesis

The vast chemical space covered by PV derivatives is clearly justified by the currently available array of synthetic procedures, classical and new, based exclusively on C-C bond formation as the strategy to incorporate the vinylene moiety into aryl rings. Three main categories of the most commonly used synthetic approaches to assemble the PV backbone can be found and include the reaction of quinodimethane intermediates, nucleophilic condensations, and palladium-catalyzed cross-coupling.⁴

- **Quinodimethane intermediates reactions**

Gilch reaction is considered the most employed route involving a quinodimethane intermediate.²⁰ In this case, the PV synthesis proceeds via reaction of 1,4-bis(chloromethyl)benzene **4** with a strong base, yielding an α -chloro-p-xylylene **5** after HCl 1,6-elimination. This chemical intermediate has a biradical behavior, easily converting into a chlorine-containing polymeric intermediate **6**, which, in the presence of base excess, undergoes E2 elimination to obtain the desired PPV material **1** (**Scheme 1-1**).

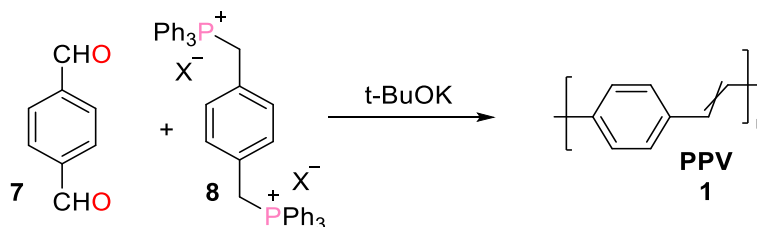


Scheme 1-1: Gilch synthesis of PPV.

Several modifications of this reaction have been explored and involve the substitution of the Cl atoms by sulfonium, sulfinyl, sulfanyl, or xanthate groups to enable greater control of the polymerization process and the geometry of the double bonds.^{21,22}

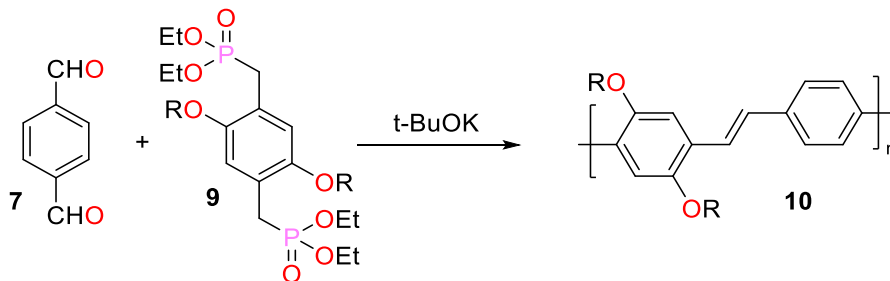
- **Nucleophilic condensations**

Wittig and Wittig-Horner reactions are amongst the most employed synthetic methodologies to assemble the conjugated PV backbone involving a simple, mild, and straightforward protocol as proved by the enormous amount of PV-derivates prepared using this approach.²³⁻²⁵ The Wittig reaction facilitates the formation of the vinyl-bond bridge through the reaction of aromatic aldehydes **7** and the ylide generated from a phosphonium salt **8** (**Scheme 1-2**). However, a major limitation concerning the lack of control in the double bond geometry prevents the design of homogeneous PV materials.



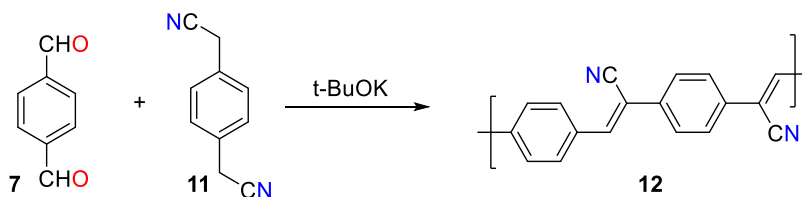
Scheme 1-2: Synthesis of PPV via Wittig reaction.

Interestingly, the Wittig-Horner reaction, which involves the use of phosphonates **9** and aromatic aldehydes **7** to sterically favors the *E*-orientation in the alkene (**Scheme 1-3**), comprises an alternative to provide access to more homogeneous materials **10**.²⁶ More recently, the Wittig-Horner reaction has shown superior high *E*-selectivity, facilitating the synthesis of complex structures and advanced materials such as OPV-hexasubstituted benzenes and OPV-functionalized azafullerenes.^{27,28}



Scheme 1-3: Synthesis of PV-polymers via Wittig-Horner reaction.

Knoevenagel condensation (**Scheme 1-4**) also provides a direct and straightforward methodology for preparing both PPVs and OPVs bearing electron-withdrawing groups directly on the vinyl bridge, taking advantage of the acidic benzylic hydrogens' reactivity. In this transformation, an aromatic aldehyde **7** reacts with a p-xylene derivative **11** in the presence of a base to assemble the desired PV-derivative **12**. Despite the fact that the reaction yields for this synthetic route can be subject to improvement,²⁹ this approach has significantly contributed to expanding the frontiers in top-trending research fields, e.g., throughout the development of PV-materials with exceptional charge transport properties,³⁰ fluorophores for novel AChE activity assays³¹ and, tunable electron transfer UV MALDI-MS matrices for selective ionization of nanoparticles, polymers, porphyrins and fullerenes.³²

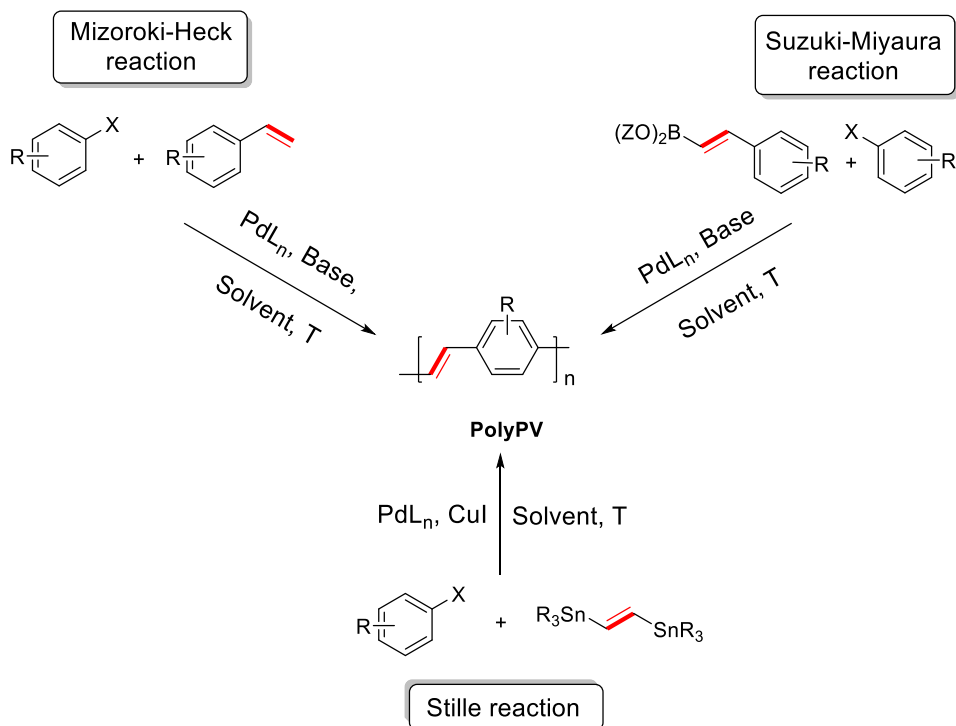


Scheme 1-4: Knoevenagel condensation.

- **Pd-catalyzed cross-coupling**

It is well-known that an exclusive *trans* configuration prompts superior optoelectronic features in virtue of effective orbital alignment and planarity. However, the shortfall of marked stereoselectivity towards *trans* PV-products remains one of the major drawbacks for commonly reported methodologies.³³ To overcome this issue, transition metal complexes - specifically palladium-containing compounds - have emerged as outstanding alternatives, providing unique and powerful synthetic approaches under an exceptional stereoselective regime.

All three different Pd-catalyzed synthetic strategies; Mizoroki-Heck, Stille and Suzuki-Miyaura, have proven to be highly efficient in assembling both oligomeric and polymeric PV materials in a wide range of yields (**Scheme 1-5**).^{34–37} Among them, Mizoroki-Heck has been the most studied reaction being considered the method of choice to assemble PV materials with high *trans* selectivity.



Scheme 1-5: Pd-catalyzed reactions for the synthesis of PV materials.

Three main classes of Pd-complexes have been employed in combination with Mizoroki-Heck conditions to provide efficient access to PV systems and consist in phosphanes **13**, phosphites **14** and *N*-heterocyclic carbenes **15** (**Figure 1-2**).^{18,38,39} Their differences heavily rely on the type of ligand and the distinctive chemical attributes conferred to each class of synthetic process: (1) the substantial modification in reaction conditions; (2) high stereoselectivity; and (3) the diversity of functional groups that can be tolerated.

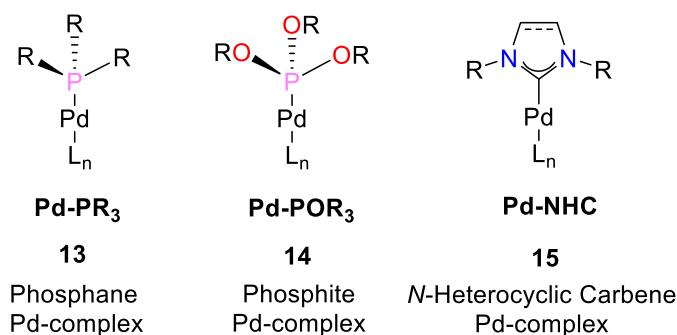
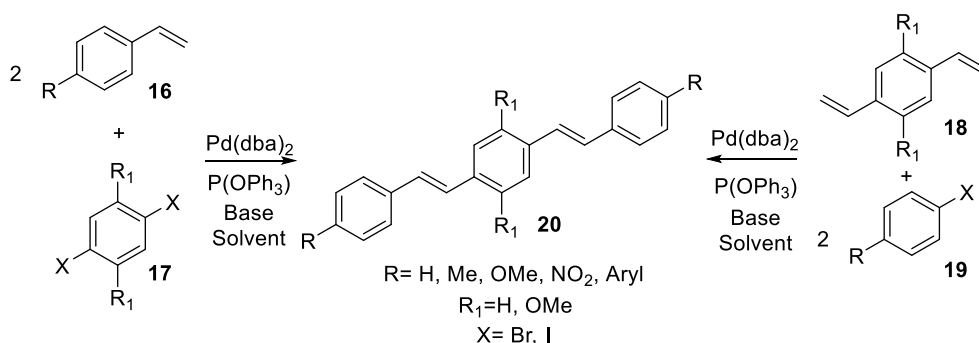


Figure 1-2: Pd-catalysts employed for cross-coupling reactions.

Our research group has robustly demonstrated that the use of phosphite ligands, specifically triphenyl phosphite, stabilizes the Pd (0) species by avoiding the aggregation and precipitation of black palladium. This observed effect is ascribed to a greater π -accepting character as a consequence of the introduction of the oxygen atom, which simultaneously allows a better π -back bonding from the metal, making the Pd-P bond stronger.^{18,40} Moreover, the bulkiness of the ligand exerts a steric effect in the course of the Mizoroki-Heck catalytic reaction pathway boosting the stereospecific formation of *trans* vinyl segments in the OPV.⁴¹ This reaction modification (**Scheme 1-6**) has been widely employed to prepare a plethora of OPV **20** derivatives with unique optoelectronic properties employing two synthetical approaches to promote molecular diversity around the conjugated scaffold. The first one consists of the reaction between styrenes **16** and substituted dihalobenzenes **17**, to directly insert substituents on the central aryl ring of the OPV; and, the second one involves 1,4-divinylbenzene **18** and halobenzenes **19**.⁴²



Scheme 1-6: Synthesis of OPVs via Mizoroki-Heck reaction employing triphenyl phosphite as Pd ligand.

1.1.2 Photophysical and photochemical properties

Phenylene vinylene systems, as π -conjugated materials, exhibit interesting photophysical properties, photoluminescence being the most prominent and relatable of them. The emission of photons of lower energy after light absorption can be explained by means of a Jablonski diagram (**Figure 1-3**). The initial absorption of a photon promotes one electron from the ground state S_0 to any vibrational level within a higher energy state S_n . Once excited, the electron can undergo several relaxation pathways. Typically, the molecule dissipates energy through radiationless vibrational relaxation to reach S_1 . From this energy state, a radiative relaxation, known as fluorescence (timescale 10^{-9} to 10^{-6} s), can occur to return to the ground level S_0 . Additional relaxation pathways involving a photon emission can take place and require a spin inversion process (intersystem crossing, ISC) in the electronic transition from the first singlet state S_1 to the first triplet state T_1 . Once the molecule is in T_1 , the return to S_0 proceeds with the emission of a photon also known as phosphorescence. It should be disclosed that this type of transition comprises a change in multiplicity, and thus, the probability of occurring is low as endorsed by the timescale $>10^{-3}$ s displayed for this process. Moreover, to compensate for the change in spin angular momentum, a shift in orbital angular momentum is required. Thus, the insertion of carbonyl (C=O) or related functional groups that favors $n \rightarrow \pi^*$ transitions, significantly boost the ISC rate, and therefore, the phosphorescence probability. Noteworthy, radiationless relaxation (internal conversion) is simultaneously conceivable in $S_1 \rightarrow S_0$.

Alternative relaxation pathways involve electron or energy transfer. Such excited-state deactivation routes are of the utmost importance to explain the photochemical reactivity of conjugated systems. When employed as photocatalysts for pollutants degradation, phenylene vinylenes can react with molecular oxygen to induce further oxidation of such molecules. These photoreactions are framed as either type I or type II as illustrated in **Figure 1-3**.⁴³ Type I reactions involve the electron transfer from the S_1 or T_1 states to molecular oxygen generating the superoxide radical anion ($O_2^{\cdot-}$). On the other hand, type II reactions consist in the sensitization or energy transfer to molecular oxygen prompting the production of singlet oxygen (1O_2).

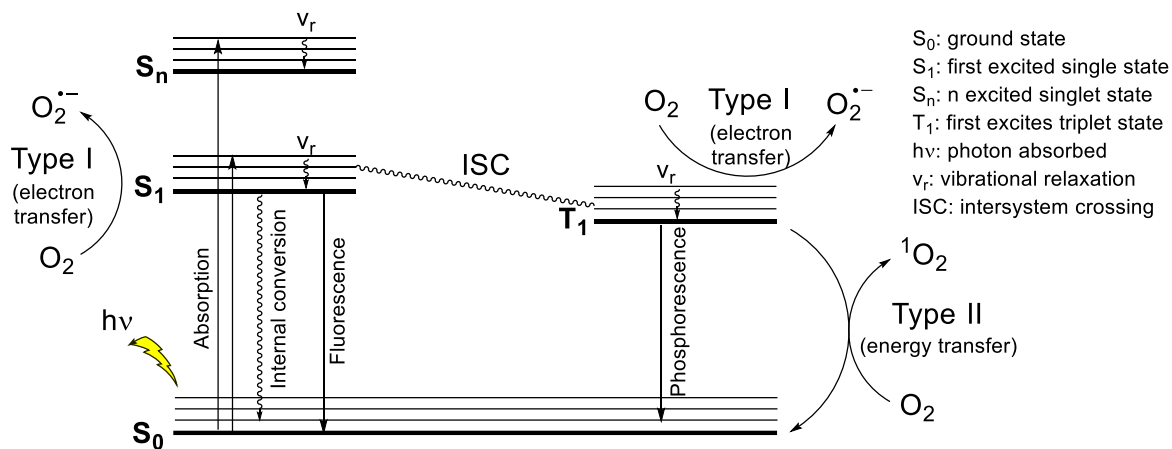


Figure 1-3: Jablonski diagram illustrating photoluminescence processes and type I/type II photoreactions.

Photoinduced electron processes (PET) encompass an additional route for electronic relaxation.⁴⁴ In this mechanism, the electron transfer (ET) entails the excited molecular state of the conjugated PV system or photosensitizer (sens) and a donating (D) or electron-accepting species (A). It should be noted that the excited photosensitizer (sens*) can act as both D or A depending on the matching of the electrochemical and photophysical properties of the reacting molecule, so an exothermic ET is favored (**Figure 1-4**). When an acceptor molecule A interacts with the Sens* ($LUMO_{Sens} > LUMO_A$), the ET process is thermodynamically favored ($\Delta H < 0$), leading to the formation of a photosensitizer radical cation (Sens^{•+}) and a radical acceptor anion (A⁻) (**Figure 1-4a**). Alternatively, when a donating molecule reacts with the Sens* ($HOMO_{Sens} < HOMO_D$), the ET process is also thermodynamically favored ($\Delta H < 0$) and this time the generation of a photosensitizer radical anion (Sens^{•-}) and a donor radical cation (D^{•+}) is achieved (**Figure 1-4b**).⁴⁵ Finally, the regeneration of the photosensitizer to the initial state proceeds throughout the same ET mechanisms.

In this regard, it should be pointed out that within the context of a typical photodegradation, the pollutant can act either as A or D, and its radical species formed can further undergo unimolecular fragmentation processes accounting for an alternative cleavage pathway different than that of the interaction with reactive oxygen species.⁴⁶

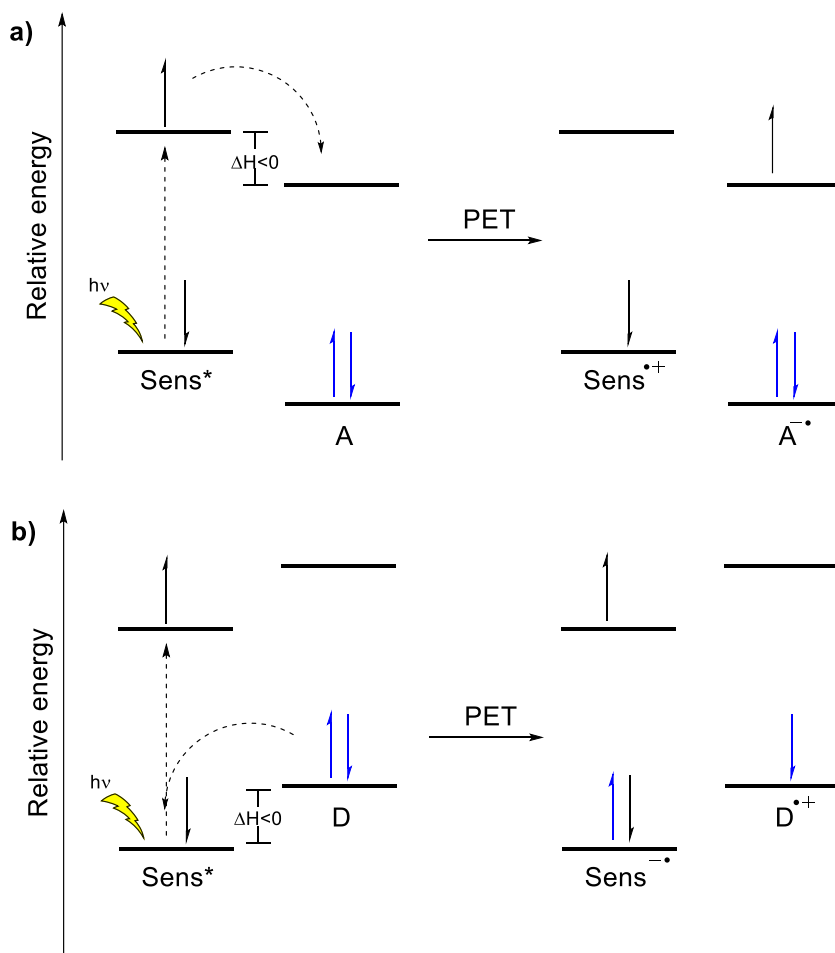


Figure 1-4: Photoinduced electron transfer mechanisms for the sensitizer (Sens) with; (a) an acceptor *A*, and (b) with a donor *D*.

In addition, the organic nature of PV systems as photocatalysts implies a remarkable advantage over inorganic semiconductor materials. The fine-tuning of the HOMO-LUMO levels by means of modification of the conjugated scaffold with EDG or EWG, to match the energy levels of the donor and acceptor, can be employed to promote ET in a wide range of photochemical reactions efficiently.

1.2 Photochemical applications

As previously outlined, the phenylene vinylene (PV) system is widely recognized as a promising model in optoelectronics due to its easily tunable emissive properties. Although other applications involving chemical sensing and tailored design of photovoltaic materials have been described, fewer participation in light-driven chemical processes is found in the literature. Poor solubility and stability issues related to the alkoxy substituents and bridging vinyl fragments are considered debated drawbacks that have limited their broad use as prominent tools in photochemistry. However, more recent investigations have developed strategies for photostability enhancement that can be contemplated to boost PV systems' photochemical performance. In this section, we will discuss the approaches towards their photostability improvement alongside distinct photochemical applications such as photosensitization, photocatalytic hydrogen production, photoredox catalysis, and degradation of pollutants.

1.2.1 Strategies for photostability enhancement

The course of extensive research aimed to identify the degradation routes and products that PVs undergo throughout photoirradiation have pointed out oxygen as the major chemical species responsible for the π -conjugated backbone deterioration. During the initial evaluation of PPV polymer-LED technology, some evidence of important luminescence efficiency decay was observed after the materials were exposed to air. Yan *et al.* first demonstrated that luminescence was totally preserved under nitrogen while in the presence of oxygen, the emissive properties significantly disappeared in time, and directly correlate this to changes in the IR spectra of the PPV, where the appearance of carbonyl groups was simultaneously detected.⁴⁷ Moreover, the dramatic reduction in the emission of PPV was further studied and associated with the decrease in the concentration of bridging vinyl double bonds as a consequence of their cleavage and subsequent formation of terminal aldehyde groups as indicated by Papadimitrakopoulos *et al.*⁴⁸ These authors also discovered that such structural changes could be the result of both photo- and thermal oxidation. However, an intermediate that may lead to a degradation mechanism was not identified at that moment.

Clough and coworkers then employed poly (2,5-bis(5,6-dihydrocholestanoxo)-1,4-phenylene vinylene) (BCHA-PPV), alkoxy-substituted PV polymer with improved solubility compared to the parent compound PPV, to fully explore its photodegradation in solution.⁴⁹ Interestingly, they demonstrated that BCHA-PPV generates singlet oxygen ($^1\text{O}_2$) via energy transfer from the triplet excited state with a singlet oxygen quantum yield (Φ_Δ) value close to 0.025. Even though the Φ_Δ is not very high for this compound, the limited amount of singlet oxygen generated after irradiation causes an extensive scission and shortening of the π -conjugation within the polymer, and simultaneously prompts the formation of carbonyl groups. Furthermore, extensive oxidation of the polymer leads to noticeable IR carbonyl absorption shifts, which may indicate different reactions yielding groups with higher oxidation states such as esters or carboxylic acids. Thus, they proposed the PV-polymer degradation proceeds via a $[2\pi+2\pi]$ cycloaddition where the initial formation of a dioxetane in the bridging double bonds and its consecutive cleavage promote the generation of the observed carbonyl fragments. Simultaneous oxidation of the dihydrocholestanoxo side chain by the dioxetane has also been proposed. The cyclic oxygen species is considered to open and form a biradical that, after hydrogen abstraction, initiates the formation of hydroperoxides that are responsible for additional oxidation. Even though further mechanistic studies are required to validate this pathway.⁵⁰ Unexpectedly, stilbene, the simplest monomeric analog of PV systems, was also brought under the same reaction conditions exhibiting limited reaction with singlet oxygen. This chemical behavior suggests that the extent in conjugation, along with the presence of electron-donating alkoxy groups, significantly promotes the reactivity of the double bonds.

As an attempt to corroborate the hypothesis regarding the extent of conjugation and the electron-donating character of the substituents in the PV moiety, Ogilby and coworkers employed a set of oligomers to evaluate the singlet oxygen reaction rate constants and correlate the obtained results with the above mentioned structural features.⁵¹ The outcomes indicated that the singlet oxygen reaction rate decreases when the oligomer chain length is shortened. This experimental observation was complemented with *ab initio* calculations where the electronic effects of the extended π -conjugation were found to not influence the oligomer reactivity with singlet oxygen in contrast to conformational and steric effects such as deviation of planarity. Additionally, the withdrawal of electron density, achieved by

insertion of -CN substituents, significantly reduced reactivity, especially when the cyano groups are placed directly on the vinyl fragment.

With this information in hand, Zhang *et al.* proposed to deeper investigate the role of the PV triplet state in the overall photodegradation, using seven OPVs as model compounds. The obtained results were of the utmost importance and clearly suggested that the PV triplet state role goes beyond the sensitization of ground-state oxygen ($^3\Sigma_g$) to generate 1O_2 . The research team was able to establish that a superoxide radical anion is also being generated and is directly involved in the PV degradation process. Moreover, under sensitization conditions with biacetyl, a more effective energy transfer process induced the formation of OPVs triplet state in a high yield. Thus, an acceleration of the degradation was observed 1000-fold. Since the results above cannot be explained in terms of singlet oxygen generation ($\Phi_\Delta < 0.1$), the authors suggested a direct and much faster reaction between the PV triplet excited state and ground state oxygen. The proposed participation of the PV excited triplet state in the overall photodegradation process is depicted in **Figure 1-5**.

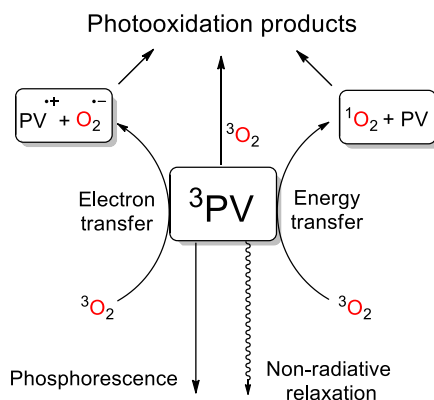
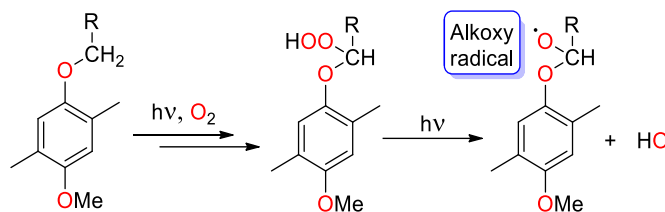


Figure 1-5: Participation of the PV excited triplet state in the overall photodegradation.

A remarkable contribution to the degradation mechanism was made by Chambon *et al.* by thoroughly examining the photoproducts of multiple PV systems.⁵²⁻⁵⁵ Particular emphasis was made on compounds bearing alkoxy groups, such as poly[2-methoxy-5-(3',7'-dimethyloctyloxy)-1,4-phenylenevinylene] (MDMO-PPV), where it was clearly demonstrated that the ether fragment is the most photo-oxidizable region of the molecule, leading to rapid degradation of the molecular structure. The ether group undergoes the formation of a radical in the α -carbon followed by a reaction with molecular oxygen to produce the unstable

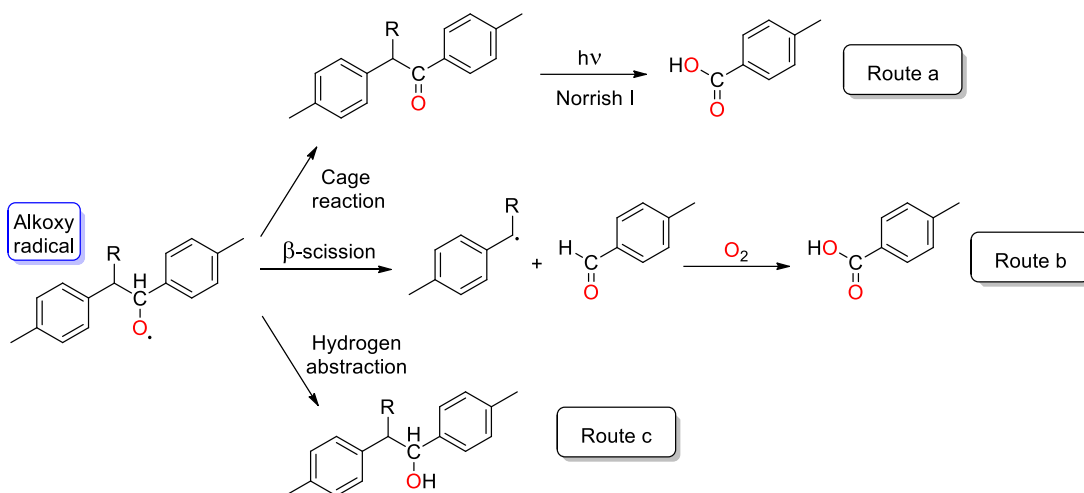
hydroperoxide species. After photochemical decomposition, alkoxy and hydroxide radicals are formed (**Scheme 1-7**).



Scheme 1-7: Hydroperoxide formation and decomposition in the alkoxy group.

Different pathways for the conversion of this alkoxy radical are suggested based on the observed carbonyl products. The first one involves a β -scission where formate derivatives and alkyl radicals are formed. Moreover, the alkyl radicals can further react with oxygen to yield primary hydroperoxides that, after photodecomposition, are converted into carboxylic acids. Also, a cage reaction can occur to yield aromatic esters. Finally, a hydrogen abstraction leads to the formation of a hemiacetal which decomposes into phenol and a carboxylic acid.

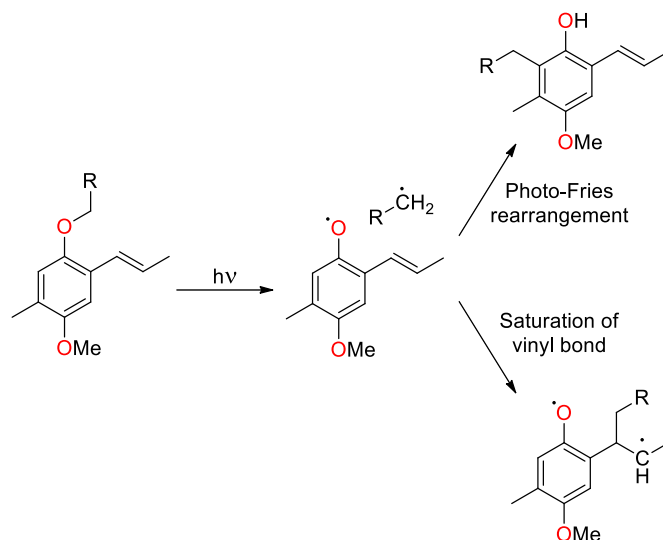
Regarding the reactivity of the vinyl double bonds, the saturation is suggested to proceed via the addition of the alkyl radicals that were formed during the degradation of the ether fragment, followed by the fixation of oxygen to produce a peroxy radical, that is then converted into a hydroperoxide by hydrogen abstraction. The photoinduced dissociation of this group gives an alkoxy and a hydroxy radical. The conversion of the alkoxy radical is proposed to follow three reaction pathways (**Scheme 1-8**). Route *a* involves a cage reaction that produces a ketone, which after continuous irradiation undergoes a Norrish I-type reaction to yield an aromatic carboxylic acid. Route *b* consists of a β -scission that creates a radical and an aldehyde that is susceptible to further oxidation. Finally, route *c* involves a hydrogen abstraction resulting in the formation of the alcohol. Similar degradation pathways have also been reported for analog PV containing systems.⁵⁶



Scheme 1-8: Photoinduced transformations of the vinyl fragment.

This proposed photooxidation mechanism was confirmed by performing the irradiation experiments in a closed chamber under an atmosphere of $^{18}O_2$. The isotope-marked photoproducts were successfully identified and correspond to the previously discussed intermediate structures. Moreover, the use of a heavier oxygen isotope allowed the discrimination of vibrational bands that are attributed to distinct carbonyl compounds and facilitated the monitoring of the PV degradation process by IR spectroscopy.⁵⁷

Most of the research on PV stability has focused on the identification of photoproducts and the elucidation of plausible mechanisms of degradation in the presence of oxygen. However, protecting the PV material against oxygen blocks only one degradation pathway considering that the absorption of radiation itself can induce several photochemical reactions. Thus, to broaden the PV stability outlook, additional efforts were also made by Chambon *et al.* to track structural changes induced by illumination in the absence of oxygen.⁵⁸ Although more time of irradiation was required (~ 1000 h), the photolysis experiments clearly indicated serious modifications in the conjugated structure including the disappearance of the ether groups along with the saturation of the vinyl bonds. The observed chemical changes were attributed to both a photo-Fries rearrangement and the addition of alkyl radicals on the double bond that is generated after the ether function cleavage (**Scheme 1-9**).



Scheme 1-9: Proposed degradation mechanism of PV systems in the absence of oxygen.

The understanding of the photodegradation process has brought into consideration an important number of alternatives to mitigate the effect of oxygen and, at the same time, provide stability to maintain the conjugated backbone undamaged for more extended periods of time. As previously outlined, electron-withdrawing substituents can exert a protective response in terms of degradation, especially when placed directly on the alkene bridging bonds to prevent direct singlet oxygen reactivity. This strategy has proven effective not only for cyano groups^{51,59–61} but also for phenyl rings,^{60,62} nitro groups,⁶³ and fluorine atoms.⁶⁴ Moreover, the modification of the aryl rings in PPVs by insertion of sulfone⁶⁵ (S-EH-PPV) and trifluoromethyl^{66,67} (CF₃-PPV) substituents (**Figure 1-6**) have provided unprecedented photostability that endows these materials with the critical chemical resistance required for demanding photochemical applications.

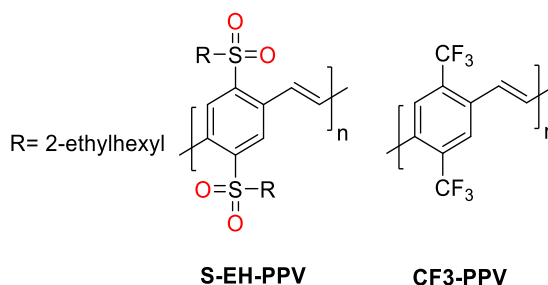


Figure 1-6: Chemical modifications on the PPV aryl rings leading to exceptional photostability.

Another structural modification designed to protect the PV system against photodegradation consists in the rigidification of the polyene structure. The insertion of sp^3 carbon bridges to assemble dihydroindenoindene structures (**Figure 1-7**) ensures both rigidity and planarity providing kinetic and excited-state stabilization ascribed to the absence of nonradiative relaxation processes.^{68,69} Noteworthy, this elegant strategy also offers unique steric protection by preventing the dioxetane scission of the vinylene group introducing a reversible step in the reaction where the conjugated starting material is highly favored.⁷⁰ A similar rigidification approach based on the insertion of boron-fused N=N double bonds units in the PPV chain has also been described and demonstrated high stability towards light irradiation as well.⁷¹

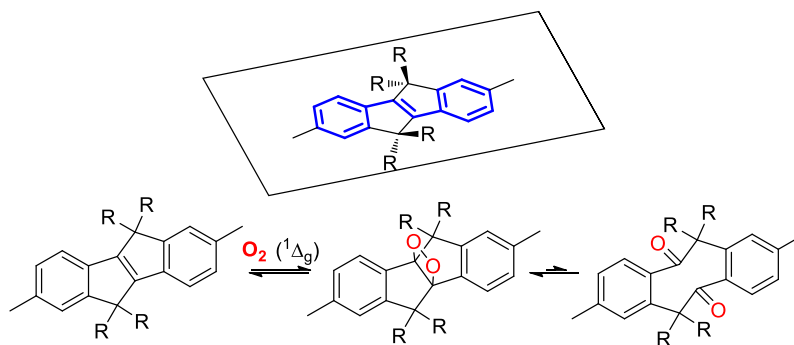


Figure 1-7: Sp^3 carbon-bridge rigidification of PV systems and proposed reversible alkene scission.

As an alternative, the utilization of substances acting as charge acceptors or radical scavengers in combination with PV systems has attracted significant attention in photovoltaic and emissive applications by proving to be an efficient and straightforward methodology to enhance photostability. It should be noted that the pronounced effectiveness of the additives is, in most cases, attributed to a rapid electron transfer from the excited PV to the acceptor. This decreases its reactivity towards oxygen by quenching the triplet state and avoiding the triplet-triplet annihilation responsible for singlet oxygen production. In this regard, blends containing fullerene⁷² and fullerene derivatives⁵⁵ have been employed and exhibited a significant photostability enhancement attributed to both fast charge transfer and radical scavenging mechanisms. Other examples include the dilution of dibenzoterrylene into PPV,⁷³ the use of 2,4,7-trinitrofluorenone,⁷⁴ and pentaerythritol tetrakis (3-(3,5-di-tert-butyl-4-hydroxyphenyl)propionate)⁵⁶ as photodegradation retarders.

Furthermore, protective coatings for PPV derivatives have provided remarkable protection against oxygen diffusion. This approach is oriented to delay or completely prevent the oxidation of the conjugated backbone caused by illumination under direct contact with air. Organic polymeric materials such as corn starch, polyvinyl alcohol (PVA),^{75,76} cellulose acetate, and polyvinylidene chloride (PVDC)⁷⁷ have been evaluated, displaying outstanding performance and preserving the PV stability for up to 28 days. Interestingly, the optoelectronic properties of the PV materials were not significantly affected after the coating layer application. A thin film of aluminum (5 nm) was also used as a protective layer. The aluminum was oxidized after exposure to the atmosphere and enabled the photoluminescence from the PPV without degradation for several hours under blue light.⁷⁸ Alternatively, inorganic materials, including montmorillonite (Na-MMT) and Laponite, have been employed to assemble PPV-layered silicate nanocomposites, also providing consistent protection against oxidative double bonds scission.^{79–81}

An oxygen diffusion barrier scenario can also be generated by simply designing blends of PVs and inorganic materials. For instance, the addition of TiO₂ to PPV using physical methods successfully prevented the oxidation of the alkene chains, as clearly demonstrated by the inhibition in the formation of carbonyl fragments.^{6,82} It should be disclosed that in terms of oxygen diffusion modulation, SiO₂ was found to exert superior performance compared to TiO₂.⁸³ Other materials, including boron-doped freestanding silicon nanocrystals, also prevented photodegradation when combined with MEH-PPV.⁸⁴

Not surprisingly, incorporating inorganic particles such as TiO₂ has additional effects on degradation control than just influencing oxygen diffusion and inducing PPV molecular aggregate states that alter the optical properties.^{85,86} When leaving groups such as tetrahydrothiophene are attached to the PPV scaffold, TiO₂, and SiO₂ nanoparticles also provide their photoprotective activity by strongly interacting with this polar moiety and therefore preventing its photoinduced elimination reaction.⁸⁷ Furthermore, quenching of the PPV excited state by TiO₂ has also been described as a phenomenon responsible for preventing photodegradation.⁸⁸

Despite the herein discussed vast array of strategies for stability enhancement, none of them has been applied to PV systems in specific photochemical applications. We ascertain they may serve as a starting point in the development of high-performance and long-lasting photochemical PV materials. However, the type of protective strategy must be meticulously chosen to guarantee the desired photo transformation.

1.2.2 Photosensitization and photodynamic therapy

Diverse energy transfer processes triggered by molecular excited states are the basis of an innovative type of cancer (and other diseases) therapeutics, known as photodynamic therapy (PDT). In the simplest of cases, the photosensitizer in the tumor site can generate singlet oxygen after light irradiation to cause oxidation of the biomacromolecules prompting a reduction in the viability of the malignant cells. However, its massive application has been hampered by factors such as the penetration depth and delivery efficiency of light and the oxygen concentration within the tumor.

Strategies including two-photon absorption have emerged as an alternative to overcome penetration issues, considering infrared light can reduce this shortcoming. Ogilby and coworkers have dedicated a tremendous effort to investigate the ability of OPV systems towards the non-linear two-photon photosensitized production of singlet oxygen (**Figure 1-8**). A combination of calculations and extensive molecular tuning were performed to establish the contribution of a wide variety of substituents around the conjugated backbone in the singlet oxygen generation.⁸⁹⁻⁹² Moreover, the insertion of polar and ionic groups as a rational approach for evaluating the OPVs performance in water established new horizons in the possible applicability of the oligo (phenylene vinylene) moiety for PDT close to physiological conditions. In this sense, a delicate balance between functional groups aimed to enhance water solubility and promote two-photon absorption must be established to control the influence of rapid charge-transfer-mediated nonradiative deactivation processes in the overall generation of singlet oxygen.^{92,93} Alternatively, organometallic approaches consisting in p-(phenylene vinylene) substituted with platinum acetylides developed by Schanze *et al.* also proved to undergo near-infrared two-photon absorption in solution and solid matrices.^{94,95} However, further studies are required to demonstrate their direct applicability in PDT.

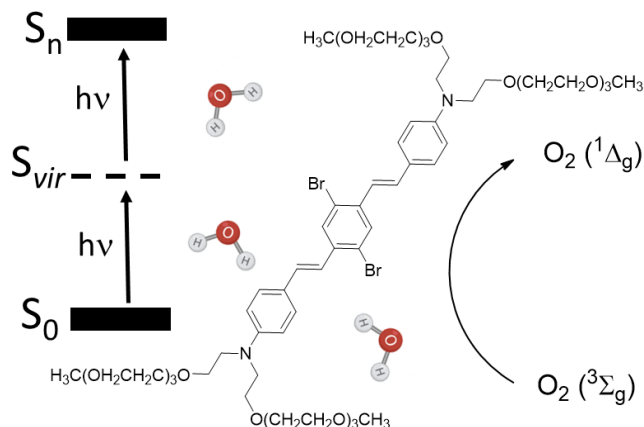


Figure 1-8: Two-photon photosensitized production of singlet oxygen by OPVs. S_n : excited singlet states; S_{vir} : virtual excited state.

Conversion efficiency is considered another critical parameter that defines the performance of a photosensitizer in PDT applications. Wu *et al.* reported that polymeric PV materials show a much higher photosensitization efficiency when compared to their oligomeric counterparts.⁹⁶ The latter is attributed to the gap energy decrease between the excited singlets (S_n) and triplet states (T_n) and those of the lowest excited states (S_1 and T_1) induced by the presence of multiple repeating units in the conjugated polymer. Under these conditions, the ISC is thereby promoted, boosting the efficiency of 1O_2 formation even in aqueous media. PV-containing polymers (**Figure 1-9**, CP1) exhibited up to 5.07-fold singlet oxygen generation efficiency and displayed remarkable photoinduced ablation of 4T1 breast cancer cells under white-light irradiation after dispersion in a DSPE-PEG₂₀₀₀ polymer matrix. Moreover, the *in vivo* evaluation of CP1 demonstrated superior direct tumor growth inhibition ascribed to the generation of singlet oxygen, compared to the reference photosensitizer material Chlorin e6 (Ce6).⁹⁷

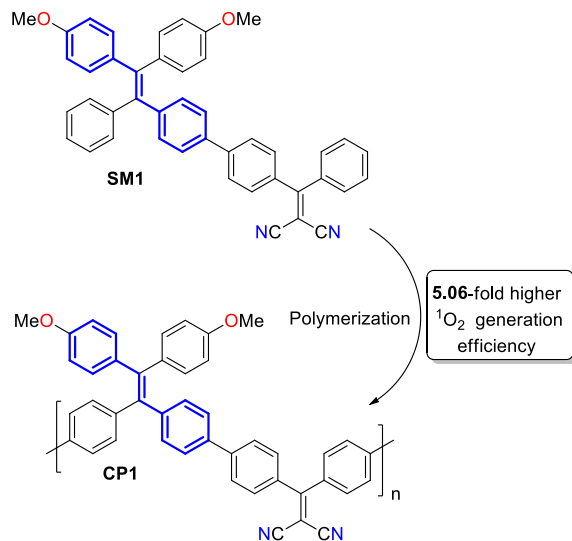


Figure 1-9: Enhanced singlet oxygen production by polymerization.

Light manipulation, another attractive approach to change lipid bilayer permeability, has been successfully carried out with the assist of a cationic OPV photosensitizer upon white light irradiation. After OPV binding to the MCF-7/DOX cells (doxorubicin-resistant), the light-assisted generated ROS caused oxidation of the membrane facilitating the uptake of the anti-cancer drug doxorubicin.⁹⁸ Similar and more recent approaches to assist the delivery of investigational drugs into CMF-7 and iPSC-derived cardiomyocytes cells were performed by Wang *et al.* They have designed amphiphilic liposomes with different formulations containing an OPV-functionalized phospholipid moiety. The liposomes can be inserted in the lipid bilayer, preserving the cell's physiology, while manipulation of the uptake can be controlled by both illumination and lipids composition. Additionally, the OPV-functionalized lipid serves as a fluorescent probe to live-monitor the delivery process.^{99,100}

This same photochemical delivery approach has also unveiled unprecedented perspectives for gene therapy. Li and coworkers have developed a cationic poly(p-phenylene vinylene) for white light-enhanced siRNA administration (**Figure 1-10**).¹⁰¹ After electrostatic self-assembly of the PPV structure with the siRNA, and consecutive endosome uptake, the PPV is able to light-sensitize the oxygen within the cell into ROS, which can disturb the endosomal membrane, thus facilitating the siRNA escape into the cytoplasm. With this information in hand, it can be ascertained that this tailored photochemical delivery strategy

offers an exceptional tool to administrate lipid-insoluble drugs and genetic material into cells, opening new directions in modern therapeutics.

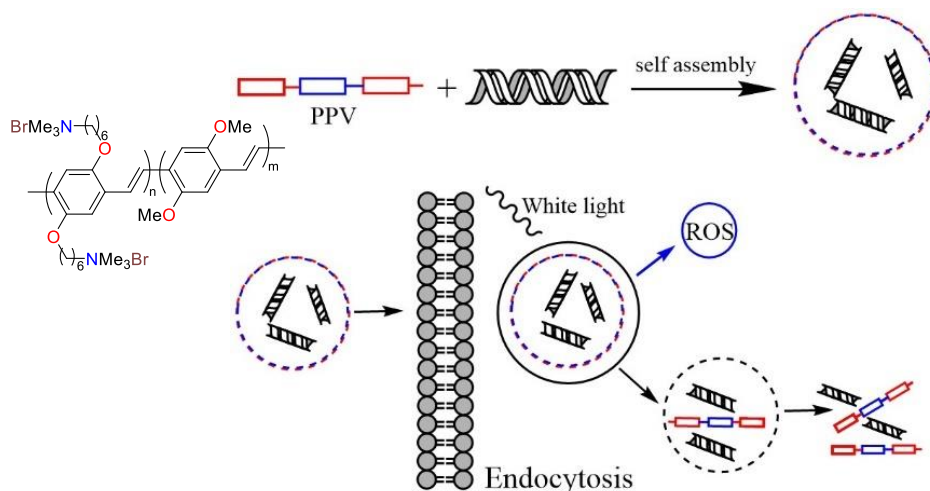


Figure 1-10: Schematic illustration of PPV self-assembly with siRNA and photochemical disruption of the endosomal membrane. Adapted from Ref. 101.

PV-based PDT can also be employed as an alternative, cutting-edge antibacterial treatment given the global concern regarding antibiotics resistance. Wang and coworkers have employed a cationic PPV that selectively binds to the peptidoglycans in the bacteria cell wall. Upon white light irradiation, the biocidal activity arises from the triplet state sensitization of oxygen to generate singlet oxygen and ROS and its direct interaction with biological targets in the cell membrane. This marked selectivity for bacteria over mammalian cells confers this PPV derivative remarkable multifunctionality that combines killing, recognition, and imaging.¹⁰² Interestingly, it was found that for Gram-positive *B. subtilis* the PPV membrane intercalation is enough to induce the desired antibacterial activity even in the absence of illumination.

Finally, bioluminescence resonance energy transfer (BRET) does not require a direct light source, but it takes advantage of the *in situ* bioluminescence of luminol in the presence of H_2O_2 and enzymes like horseradish peroxidase (HRP) instead (**Figure 1-11**). Luminol exhibits a striking emission at 425 nm and acts as a photon donor, which is then absorbed by a photosensitizer acceptor capable of generating singlet oxygen and other ROS. The requirement for this process to occur is an effective spectrum overlapping. This approach has effectively been used to control cancer and microbial infections by direct binding of the

OPV to the membrane of HeLa cells and *Candida albicans*,¹⁰³ and after the assembly of a biomimetic composite hydrogel.¹⁰⁴

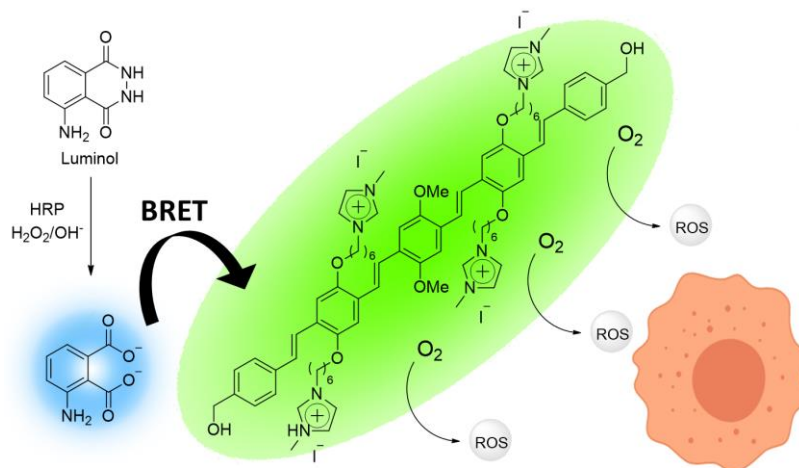


Figure 1-11: Schematic illustration of the BRET process with a cationic OPV. Adapted from Ref. 103.

An alternative pathway to induce luminol luminescence has been explored by Wang and coworkers and consists of electrochemiluminescence (ECL).¹⁰⁵ The oxidation of luminol occurs on the surface of a glassy carbon electrode. The transient luminol product then reacts with superoxide ions that result after the oxidation of H₂O₂, which is used as a co-reactant. The excited state 3-aminophthalate dianion formed, decays to the ground state by emitting light at 425 nm facilitating the energy transfer to the OPV and the subsequent generation of ROS. This ECL system was assessed in antibacterial experiments providing remarkable results against different kinds of pathogens, including *E. coli* (Gram-negative bacteria), *S. aureus* (Gram-positive bacteria), and *C. albicans* (fungi). Interestingly, when a porous polyacrylamide hydrogel replaces the liquid medium, the luminescence was found to last for more than 10 min after only electrifying for five seconds. This unique afterglow characteristic makes this electrochemiluminescent system suitable for persistent PDT antibacterial applications.

To simultaneously address the oxygen availability issues within cancer cells, Wang *et al.* have designed a PDT system that consisted in the functionalization of MEH-PPV/poly(styrene-co-maleic anhydride) (PSMA) nanoparticles with hemoglobin (Hb) and further liposome encapsulation.¹⁰⁶ Hb is responsible for both the luminol–H₂O₂

luminescence catalysis and oxygen supply. Once the Hb-NPs are internalized by HeLa cells, the viability values achieve less than 20%. Moreover, the liposome Hb-NPs system was employed for a simultaneous controlled release of an anticancer prodrug containing a C-B bond as ROS-responsive moiety to increase the efficacy of the cancer treatment. As previously seen, PV systems play an unprecedented role as photosensitizers in PDT applications and have contributed to significant advances in this field.

1.2.3 Hydrogen production

Photocatalytic hydrogen production is considered the best prospective alternative to fossil fuel-based technologies and comprises a high abundance source that meets the increasing global energy demand. Light absorption by a robust and efficient photosensitizer is one of the key steps in solar energy conversion. In this sense, extensive research devoted to developing quantum dots, semiconducting materials, and organometallic compounds has been performed, rendering important limitations in terms of high costs when precious metals are required, toxicity, and the need for a co-catalyst.

Conjugated polymers (CPs) have emerged as easily tunable materials with comparable performance to inorganic photocatalyst by overcoming most of the previously mentioned drawbacks. One of the major advantages of CPs is that the insertion of heteroatoms and different functional groups around the conjugated backbone allows a delicate control of the polymer ionization potential (IP) and electron affinity (EA) to match the thermodynamic requirements of water splitting. Among them, only a few examples of PV systems have been explored, providing a moderately optimistic outlook in terms of hydrogen evolution rate. Zwijnenburg *et al.* performed a comprehensive computational modeling study, calculating the IP and EA adiabatic potentials for several CPs, including raw PPV, where the insertion of nitrogen heteroatoms is proposed as one strategy to shift the IP potentials to more positive values while maintaining negative potentials. This adjustment is required in the pure hydrocarbon backbone to drive hydrogen evolution.¹⁰⁷ Alternatively, Zhang and coworkers evaluated a cationic PPV (**Figure 1-12**, PPV) in combination with EDTA as a sacrificial electron donor and a water-soluble DuBois-type NiP catalyst.¹⁴³ However, upon irradiation ($\lambda > 320$ nm) the PPV system achieved a low H₂ evolution activity of 8 mmolH₂·g⁻¹·h⁻¹. It should be noted that this PPV model itself is unable to promote hydrogen evolution,

making the NiP catalyst an essential part of this photocatalytic system due to its more suitable redox potentials for water reduction.

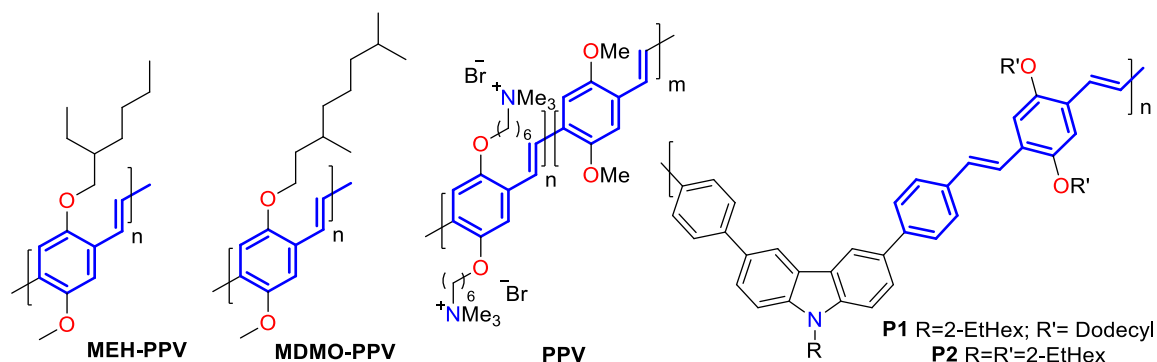


Figure 1-12: PPV evaluated for hydrogen production.

Qurashi *et al.* evaluated an alternative photoelectrochemical approach by coating an FTO glass with PV-containing polymers (**Figure 1-12**, P1 and P2).¹⁰⁸ When assembled into a standard three-electrode photocell system, the overall photocurrent and simultaneous hydrogen evolution were easily tuned by adjusting the electric potential. For P2, a 25% increase in the photocurrent density was achieved at -1.2 V, accompanied by a dramatic rise in the hydrogen evolution rate. Moreover, P2 demonstrated greater stability over P1, boosting its projection as a photocatalysts for water splitting applications. Antognazza and coworkers presented a similar strategy as the fundamentals for the exceptionally easy and inexpensive fabrication of fuel cells.¹⁰⁹ In their work, neat MEH-PPV and MDMO-PPV (**Figure 1-12**) spin-coated onto ITO glass substrate were evaluated as photoelectrodes against a Pt-wire counter electrode. The organic-based system shows hydrogen production capabilities during visible-light illumination, and the NaCl-based electrolyte provides the prospect of a highly desirable and completely clean opportunity of extracting hydrogen directly from seawater.

More recently, and exploiting the top-trending research in 2D-extended polymers or covalent organic frameworks (COFs), Zhang and coworkers developed a PV-like semiconducting material baring a honeycomb-like architecture capable of driving the two half-reactions of water splitting under visible light (>420 nm).¹¹⁰ The sp^2 carbon-jointed-pyridinyl frameworks in the $g\text{-C}_{40}\text{N}_3\text{-COF}$ material resemble those in graphitic carbon nitride ($g\text{-C}_3\text{N}_4$) derivatives and triggered a comparable H_2 evolution rate of $2.9 \mu\text{mol}\cdot\text{h}^{-1}$ employing

TEOA as sacrificial agent (**Figure 1-13**). To improve hydrogen production, the deposition of Pt (3 wt%) was demonstrated to be an excellent tactic allowing the evolution of H₂ in rates up to 129.8 μmol·h⁻¹. Such noteworthy outcomes encouraged a long-term photocatalytic test which, after 28 h of irradiation, achieved approximately 4400 μmol as the total amount of hydrogen evolved. Alternatively, when AgNO₃ was employed as an electron-acceptor, 2.5 μmol·h⁻¹ oxygen evolution rate was observed. It should be disclosed that the apparent quantum efficiency for this material (4.84% at λ=420 nm) is among the highest values reported for COF-type photocatalyst, setting the basis of excellent COF semiconductors for efficient H₂ production.

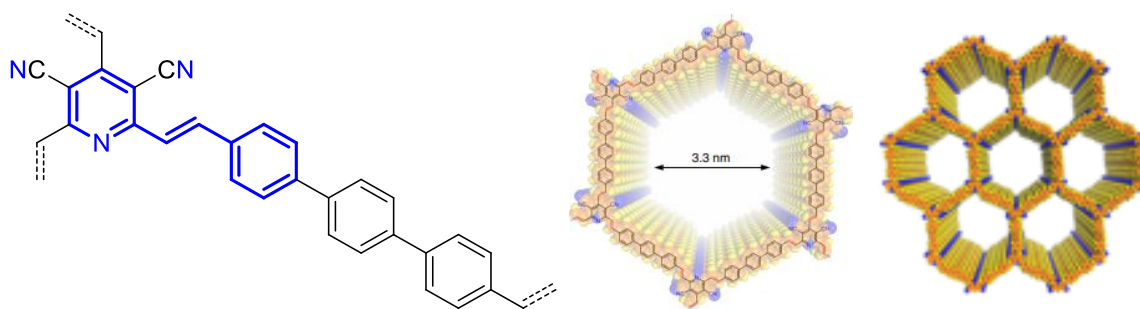


Figure 1-13: Molecular and 3D-core structure of g-C₄₀N₃-COF employed for photocatalytic hydrogen evolution.

Another highly-efficient PV-containing COF material has been reported by Jin *et al.*¹¹¹ Its broad absorption profile ranging from 530 to 800 nm, along with structural features such as a fully 2D π-conjugated lattice, extremely ordered architecture, and an integrated heterojunction have triggered outstanding charge transport, exciton splitting and electron transfer and collection properties, that allow an immediate, continuous, and stable H₂ production from water of up to 2120 μmol·h⁻¹·g⁻¹. Noteworthy, the insertion of CN groups in the vinyl bonds demonstrated to be a robust strategy to improve photostability, preventing any deterioration in H₂ production performance even after 20 hours of irradiation. Additionally, oxygen evolution was also assessed, achieving a maximum rate of 22 μmol·h⁻¹·g⁻¹.

1.2.4 Photosynthetic and other miscellaneous applications

Unnumbered organic chromophores are recognized by their capacity to act as photocatalysts in photoinduced electron transfer (PET) synthetic processes. Although PV systems encompass the requirements to act as effective photoredox catalysts, their reactivity and synthetic potential remain somewhat unexplored, as can be seen by the few reports available in scientific literature. Light-promoted oxidative hydroxylation of aryl boronic acids, for example, was successfully achieved by Zhang and coworkers employing a PV-containing polymer of intrinsic microporosity.¹¹² This porous conjugated polymer (PV-PCP) was prepared by the Knoevenagel condensation and was evaluated as heterogeneous photocatalyst under visible-light illumination using triethylamine as an electron donor to regenerate the vacant valence band of the excited polymer. Spin-trap EPR measurements demonstrated that the generation of superoxide radicals by electron transfer processes is responsible for the aryl boronic acid oxidation (**Figure 1-14**).

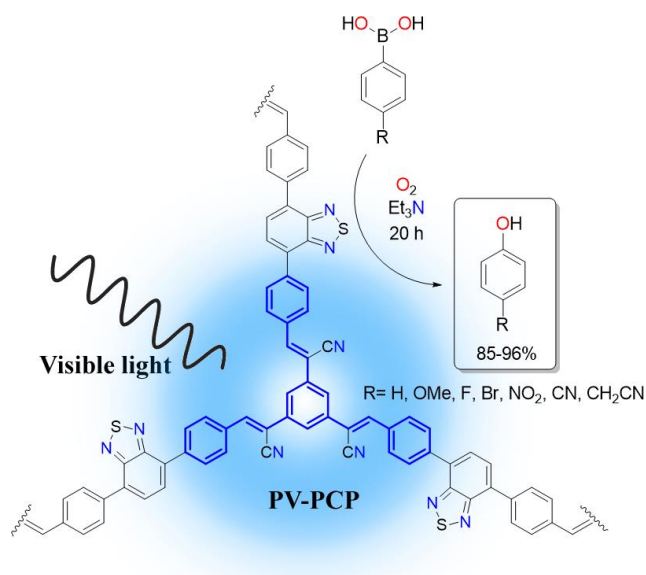


Figure 1-14: Highly porous PV-polymer photocatalyst for visible-light driven oxidative hydroxylation of aryl boronic acids. Adapted from Ref. 112.

Oppelt and coworkers designed a rhodium-coordinated poly(arylene-ethynylene)-alt-poly(arylene-vinylene) copolymer (**Figure 1-15**) for the photocatalytic NAD⁺/NADH reduction under visible light (390–650 nm) as a contribution in the field of artificial photosynthesis.¹¹³ This organometallic approach exhibited relevant performance in the

chemical reduction of NAD^+ to NADH when sodium formate was employed as hydride donor resulting in the formation of CO_2 as a side product but requiring 80 h of illumination. To improve the polymer photocatalytic performance, TEOA was used as an alternative sacrificial agent achieving a 21% conversion towards NADH after 26 h of irradiation. It must be disclosed that the physical immobilization of the polymer in 5 mm glass beads facilitated the photocatalysts reuse in all cases. Moreover, coupling the NAD^+ photochemical reduction with the reduction of α -ketoglutarate by bovine liver glutamate dehydrogenase, demonstrated an effective photo-enzymatic approach that offers attractive alternatives to classical biocatalysis.

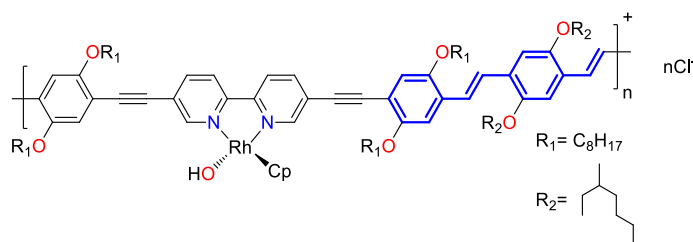


Figure 1-15: Rhodium-coordinated PV-containing copolymer for NAD^+ photocatalyzed reduction.

OPVs also offer an extended scope as efficient organic molecular wires to enhance charge transport during artificial photosynthesis. Different structural models for hybrid-material catalysts containing anchored or embedded OPV units have been proposed by Frei *et al.* consisting of layered SiO_2/CoOx nanostructures.^{114–117} It was demonstrated that the presence of OPV molecular wires boosts the hole transfer from visible-light excited $[\text{Ru}(\text{bpy})_3]^{2+}$ (and derivatives) to the oxide catalyst particle in the ultra-fast time scale (8 ns or faster). This unique approach is projected as a noteworthy enhancement in the catalytic activity towards water oxidation. Another outstanding PET application of PV systems consists of the photoinitiation for the cationic polymerization of oxiranes and vinyl monomers. Yagci *et al.* employed polystyrene and poly(ϵ -caprolactone) grafted-PPVs (PPV-g-PSt and PPV-g-PCL) to enhance the PV backbone processability and to photopolymerize cyclohexene oxide, isobutyl vinyl ether and *N*-vinyl carbazole under visible light irradiation (400-500 nm).¹¹⁸ The experimental outcomes indicate that upon light absorption, the PPV polymers undergo a PET reaction with diphenyliodonium hexafluorophosphate to yield a Brønsted acid (H^+) (**Figure 1-16**), which is responsible for the polymerization reactions as corroborated by the use of 2,6-di-*tert*-butylpyridine as

proton scavenger. The polymers obtained displayed conversions greater than 61% after 1 h of irradiation, achieving Mn values between 8200-10300 g·mol⁻¹ along with moderate dispersity indices. This PPV photoinduced process clearly overcomes typical limitations involving the exclusive UV sensitivity of most common photo-initiators, thus affording lower energetic and radiative requirements.

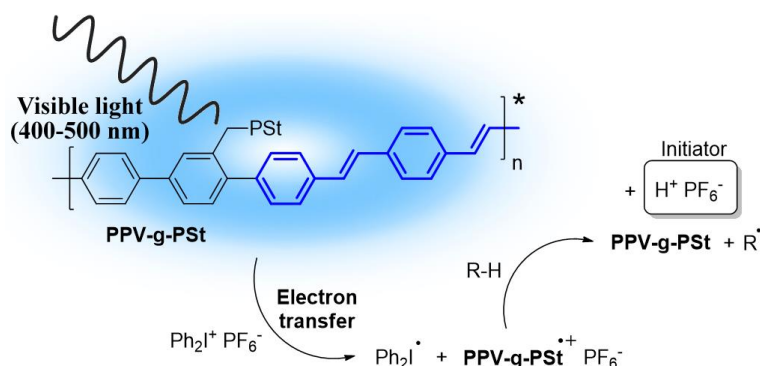


Figure 1-16: Photoinduced cationic polymerization employing PPV-g-PSt. Adapted from Ref. 118.

A photosensitized alternative catalytic pathway for the synthesis of gold nanoparticles and their self-assembly takes advantage of the PV-photodegradation products as demonstrated by Dai *et al.* whose prepared amphiphilic dendrimers containing oligo p-(phenylene vinylene) core branches and oligo(ethylene oxide) terminal chains that act as aqueous photo-reducing agents (**Figure 1-17**).¹¹⁹

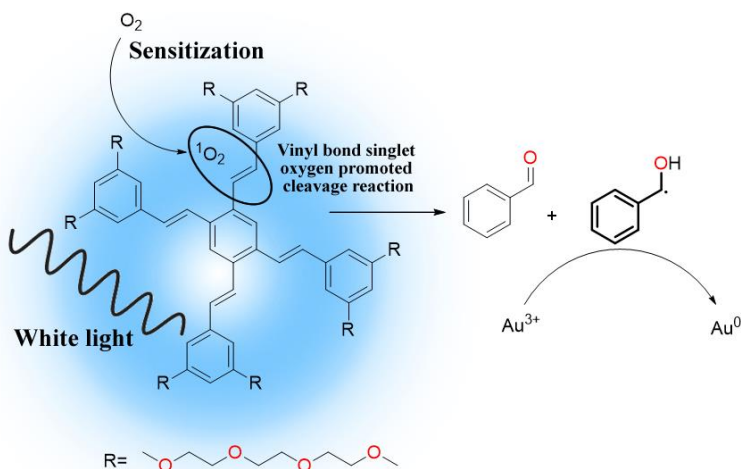


Figure 1-17: OPV light-promoted synthesis of Au nanoparticles. Adapted from Ref. 119.

After excitation and photosensitization of oxygen, the alkene scission yields α -hydroxymethyl radicals responsible for Au^{3+} reduction. Additionally, tuning the OPV concentration allows exquisite control of the size and shape of the Au NPs ranging from polyhedral ultrathin crystals to ribbon-like microfiber clusters.

Wu *et al.* also demonstrated the applicability of CP1 (**Figure 1-9**) as photosensitizer in the oxidation of benzaldehydes under visible-light irradiation (400–700 nm).⁹⁷ This PV-polymer showed superior conversion rates compared to SM1, Rose Bengal, and Ce6 photosensitizers during the transformation of benzaldehyde into benzoic acid within 4 hours of illumination. This synthetic strategy was also evaluated employing EDG and EWG substituents (-OMe, -F), achieving successful conversion in high yields (71-84 %). Such remarkable outcomes arise not only from the continuous oxygen sensitization capacity of CP1 but from the good stability of the polymeric framework.

Another important application of PV systems corresponds to the photocatalytic degradation of aqueous contaminants and dyes. So far, few examples of pure organic materials are described for this purpose due to the photostability issues mentioned before. However, some exceptions related to very stable PV materials have been explored. This is the case of CP1 polymer (**Figure 1-9**), which was employed in the heterogeneous photocatalytic degradation of aqueous Cy7 and rhodamine 6G dyes. This material achieved complete discoloration of Cy7 and rhodamine 6G 1×10^{-4} M solutions in 2 and 120 min, respectively.⁹⁷ In addition, the photocatalyst can be removed by filtration and reutilized in other photocatalytic cycles. MEH-PPV was also employed for the heterogeneous photodegradation of various textile dyes such as Orange G, Alizarin S, Alizarin G, and Remazol brilliant blue. Interestingly, the photocatalytic activity of the conjugated polymer under UVA illumination (365 nm) was superior to that of commercial TiO_2 (Degussa P-25) evaluated under similar conditions.⁵ Furthermore, it was established that the dye-degradation proceeds via the formation of hydroxyl radicals $\text{HO}\cdot$ which may lead to mineralization of organic matter.

A more refined design approach was employed by Remita and coworkers.¹²⁰ The photopolymerization technique allowed the preparation of poly(diphenylbutadiyne) PDPB nanostructures (**Figure 1-18**) capable of degrading methyl orange and phenol under visible

light (>450 nm), exceeding the degradation profile of Ag-TiO₂ catalyst. Radical scavenging experiments indicated that the overall degradation occurs via the generation of superoxide radicals in the valence band (V.B.) and hydroxide radicals in the conduction band (C.B.). Additionally, based on DFT calculations, the polymer holes can directly oxidize the organic matter. It should be noted that the polymer nanofibers can be reused even after five photodegradation cycles, where an appreciable loss of activity was not detected.

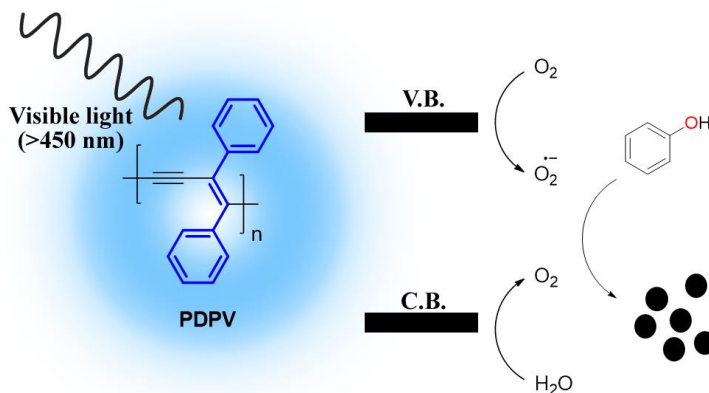


Figure 1-18: PDPB chemical structure and schematic photodegradation of phenol. Adapted from Ref. 120.

1.3 Aims and objectives

The current Ph.D. thesis aims to research the photochemical behavior of oligo (phenylene vinylene)s geared towards developing photostable OPV-based heterogeneous photocatalysts for the degradation of indigo carmine dye, among other pollutants control applications, while simultaneously uncovering their mode of action.

The specific objectives proposed to accomplish this goal are as follows:

- Establish the experimental conditions required to synthesize four target OPVs containing EWG and EDG, using the Mizoroki-Heck Pd-catalyzed cross-coupling reaction as the method of choice to assemble the conjugated backbone.
- Study the influence of the substituents around the OPV structure in their photostability and photocatalytic performance towards the control of aqueous indigo carmine dye, simultaneously assessing their degradation pathway.

- Evaluate the OPV grafting on solid surfaces and polymerization as photostability enhancing techniques applied to the photodegradation of indigo carmine dye.
- Examine the ability of the most promising materials as heterogeneous photocatalysts in the decolorization of a real wastewater sample and the control of 17 β -estradiol as a reference aqueous poultry hormone.

Summarily, chapter 1 reviews general aspects of the synthesis, photostability, and diverse photochemical applications of phenylene vinylene systems. Chapter 2 describes the synthesis and characterization of four target OPVs emphasizing the assessment of reaction conditions necessary to prepare amino OPV-derivatives. Chapter 3 outlines target OPVs' photostability and photocatalytic performance using aqueous indigo carmine as a model pollutant, thoroughly describing the photodegradation pathway. Chapter 4 covers the design of OPV-grafted TiO₂ and SiO₂ and flexible/rigid copolymers as strategies to enhance the photostability and performance of the conjugated backbone in the degradation of aqueous indigo carmine. Finally, chapter 5 explores the use of OPV-grafted TiO₂ and the rigid copolymer as heterogeneous photocatalysts in the control of an actual textile wastewater sample and aqueous 17 β -estradiol (**Figure 1-19**).

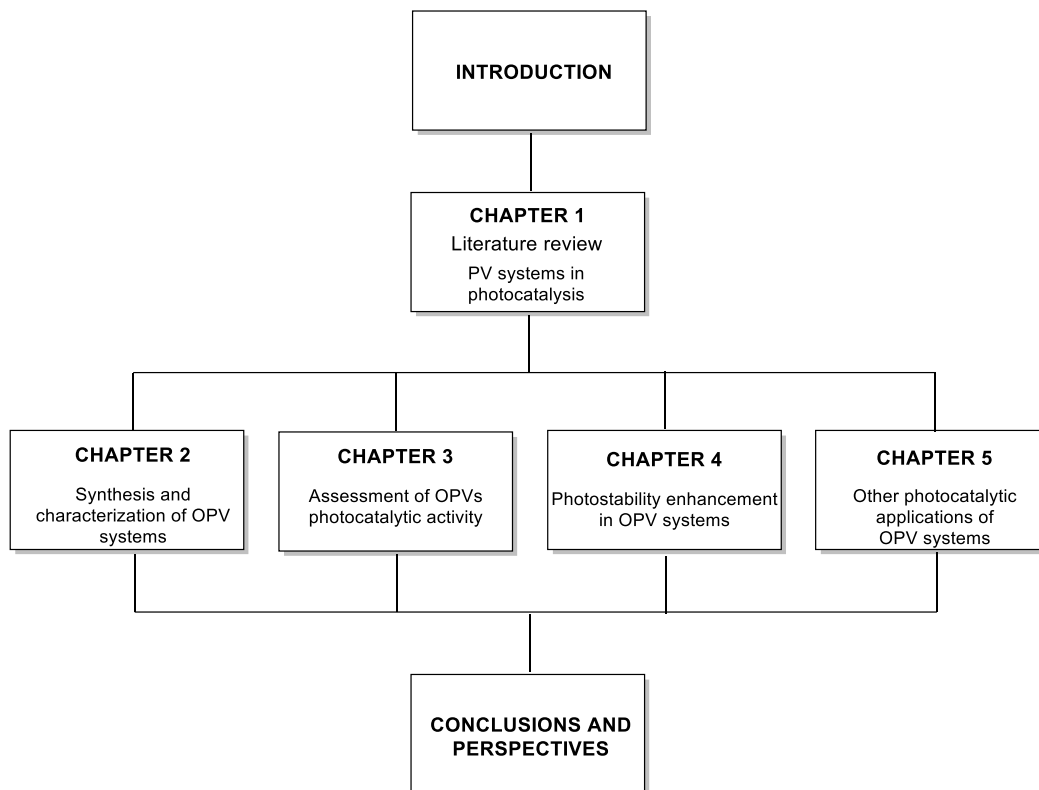


Figure 1-19: Structure and content overview of the thesis.

1.4 Originality of the thesis

A database survey (Scopus) employing the term “phenylene vinylene” provided a total of 4285 results. These materials have been explored since 1983 and have gained special attention from researchers as their properties were progressively unveiled. However, the number of works dedicated to this field has been significantly reduced since 2007 (**Figure 1-20**).

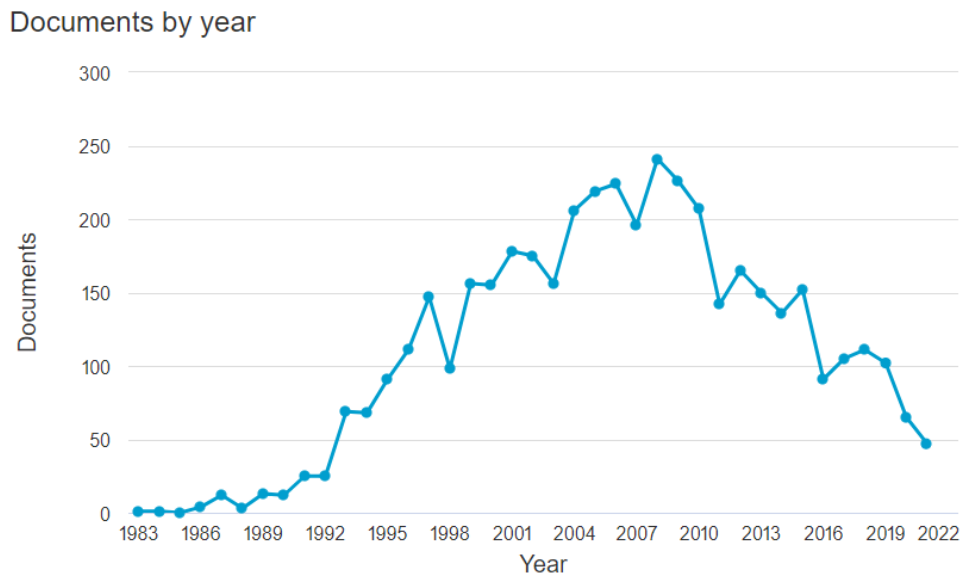


Figure 1-20: Number of publications by year containing the term “phenylene vinylene”. Source: Scopus.

After a search refinement with the terms “phenylene vinylene AND photocatalyst”, and a thorough survey of the scientific literature within the last five years (2016-2021) that included databases such as Scopus, Springer, and Taylor & Francis, only 23 results appeared. It should be disclosed that review articles and book chapters were excluded, and only research articles and patents were considered for this revision. Then, after modification of the search equation to “phenylene vinylene AND photocatalysis”, 95 results appeared. The results are narrowed to 71 when the word “stability” is included in the search equation.

Regarding patents, only five inventions were identified within this same timeframe:

- An antimicrobial photoreactive composition comprising organic and inorganic multijunction composite. 2017. Exion Labs Inc. US10212932B2.
- A kind of conjugated polymer nanoparticle photocatalyst, preparation method, and applications. 2017. Jilin University. CN107790183A.
- Copolymer for photoelectrocatalytic water splitting. 2018. King Fahd University of Petroleum and Minerals. US10882948B2.

- Amphiphilic calixarene-naphthalene derived phenylene vinyl pyridine salt-Nile red light capture system and preparation method and application thereof. 2020. Southeast University. CN111909688A.

Moreover, when the terms “phenylene vinylene AND photostability’ were inserted in the search equation, 89 related documents appeared within the last five years. The low number of publications and patents related to this particular field of the study confirms that PV materials have been poorly employed as photocatalysts. And their potential in light-driven chemical processes remains considerably unexplored due to major photostability drawbacks.

2. Synthesis and optoelectronic characterization of *trans-trans* oligo (phenylene vinylene) systems

Abstract

Four oligo (phenylene vinylene)s (OPVs), containing strategic functional groups for further covalent linkage to solid surfaces, were successfully prepared employing the Mizoroki-Heck cross-coupling reaction as a highly efficient and stereoselective synthetic methodology to assemble the corresponding π -conjugated backbone. As part of the synthesis work, a comprehensive study of different reduction reaction conditions was also performed to determine the most efficient route leading to amino OPV derivatives. The chemical structures of target compounds and intermediates were corroborated by IR, NMR spectroscopy, and MALDI-ToF mass spectrometry techniques. Also, the optoelectronic properties of the target OPVs in MeCN solution and solid-state, were determined and discussed, demonstrating the existence of $\pi\cdots\pi$ stacking interactions and the ability of light absorption, starting in the visible region. Additionally, cyclic voltammetry allowed the establishment of the HOMO-LUMO levels of the compounds. Considering these features, the prepared conjugated systems can serve as promising models not only for the development of photocatalytic applications but as a contribution to the future construction of novel materials in the field of supramolecular electronics and light-harvesting.

2.1 Introduction

The phenylene vinylene (PV) system is considered a promising organic semiconductor material with remarkable optical and electronic properties. Unnumbered applications have been described in light-harvesting,^{121,122} molecular electronics,^{123,124} photocatalysis,⁵ water splitting for hydrogen production,^{107,125} chemosensors,^{126,127} among others.¹²⁸ The oligo (phenylene vinylene) (OPV) moiety, in particular, emerges as a rational model approach offering the possibility to explore by

extrapolation the unique optical, electronic, and thermal properties of their high-molecular weight analogs, overcoming structural defects and other important solubility issues.⁹

Different synthetic approaches, including Gilch,¹²⁹ Knoevenagel,¹³⁰ and Wittig¹³¹ reactions, have been widely used to access the OPV skeleton. Nevertheless, the Mizoroki-Heck reaction, considered the method of choice for arylation of alkenes, also offers a powerful and convenient strategy to provide pure anti-all-*trans* materials under mild conditions as demonstrated by the efforts made by our research group in terms of efficiency and stereoselectivity improvement.^{132,133} Additionally, it is well known that structural and chemical diversity around the conjugated scaffold offers a wide range of controllable properties for light absorption and photocatalytic applications.^{42,134} On the basis of this, numerous functional groups have been tethered on the OPV in both the central and flanking aryl rings; yet, the particular insertion of -NH₂ groups around the OPV remains at some extent challenging. In this regard, the specific preparation of amino OPV derivatives has been exclusively described for soluble starting materials in isolated works, via acid hydrolysis¹³¹ of amide OPV precursors and reduction from NO₂-OPVs employing different reducing agents such as SnCl₂^{135,136} and Na₂S^{137,138}. This points out that a rational evaluation of the most relevant reaction conditions leading to NH₂-OPV has not yet been conducted from poorly soluble starting materials.

In this chapter, the preparation and structural characterization of four target OPV structures containing -COOH, -OH, -NH₂ and -CHO functional groups in their flanking aryl rings, along with their synthesis intermediates and precursors are described. The Mizoroki-Heck reaction between the corresponding iodoarene and styrene precursors comprises the key step in the π -conjugated scaffold formation. Moreover, a rational evaluation of strategies to readily access amino OPV derivatives, including direct assembly of the NH₂-OPV moiety and other reductive approaches, are also presented. Finally, OPVs optoelectronic properties in MeCN solution and solid-state were determined and discussed based on their projected photocatalytic applications.

2.2 Experimental section

2.2.1 Materials

Reagents and solvents were purchased from Sigma-Aldrich Chemical Co. unless otherwise stated. Triethylamine (Merck) was dried and stored in molecular sieves. Anhydrous *N,N*-dimethylformamide (DMF) was purchased from Sigma. 1,4-dioxane was dried under calcium hydride, purified by distillation, and kept under nitrogen prior to its use. All other reagents and solvents were used without further purification. The reaction progress was monitored using thin-layer chromatography on PF254 TLC aluminum sheets from Merck. Column chromatography was performed using Silica gel 60 (Macherey-Nagel GmbH & Co., 0.063-0.200 mm, S_{BET} 480-540 m^2/g).

2.2.2 Characterization

The melting points (uncorrected) were determined using a Stuart SMP10 digital melting point apparatus. IR spectra were recorded on an FTIR Thermo Scientific Nicolet iS10 spectrophotometer coupled to a diamond ATR Smart iTR cell. Mass spectra were collected from m/z 0 – 1000 in reflectron positive ion mode using an UltraFlextreme MALDI-ToF-MS (Bruker) with a solid laser source of Nd:YAG and 1000 Hz acquisition frequency employing the laser desorption ionization (LDI) method at a 25% laser fluency. Elemental analyses were performed on a Thermo Scientific analyzer (Flash 2000) and were within ± 0.4 of theoretical values. NMR spectra (^1H and ^{13}C) were measured on a Bruker Ultrashield-400 spectrometer (400 MHz ^1H NMR and 100 MHz ^{13}C NMR), using CDCl_3 , DMSO-d_6 , methanol- d_4 , pyridine- d_5 , or mixtures as solvents and references. J values are reported in Hz; chemical shifts are reported in ppm (δ) relative to the solvent peak (residual CHCl_3 in CDCl_3 at 7.26 ppm for protons, residual DMSO at 2.50 ppm for protons, and residual pyridine at 8.74 ppm for protons). Signals were designated as follows: s, singlet; d, doublet; dd, doublet of doublets; ddd, doublet of doublets of doublets; t, triplet; td, triplet of doublets; q, quartet; m, multiplet; br., broad. Solid-state ^{13}C CP/MAS NMR spectra were acquired in a Varian UI300 spectrometer at a ^{13}C resonance frequency of 75.47 MHz with a 4-mm probe. The CP technique was applied during the Magic Angle Spinning (MAS) of the rotor at 10 kHz. The contact time was 1 ms and 3500 scans were accumulated using a 2 s delay. The absorption and emission spectra were recorded on 1×10^{-5} M solutions in MeCN using a Thermo Scientific Evolution 300 spectrophotometer and a PTI QuantaMaster™ 40 spectrofluorometer. The EEM was acquired using the Horiba Duetta Fluorescence and Absorbance Spectrometer, and inner-filter effects and Rayleigh scattering were corrected using EzSpec™ software. The absorption λ_{max} and emission λ_{em} maxima were directly obtained from the corresponding spectra set. The optical HOMO-LUMO gap for OPVs in solution was calculated

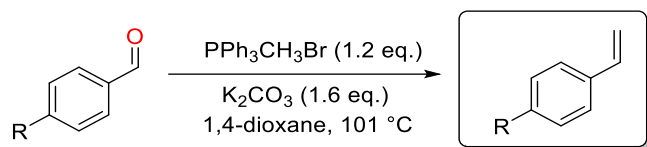
using the onset value of the absorption spectrum in the direction of longer wavelengths.¹³⁹ Finally, the fluorescence quantum yields Φ_f were acquired according to the reference method described in the literature using perylene (in EtOH) as standard.¹⁴⁰ Diffuse reflectance measurements were performed on an Ocean Optics spectrometer adapted to a reflection probe. Cyclic voltammograms were obtained on a Gamry interface 1010E potentiostat. 0.1 M OPVs samples were prepared with 0.05 M tetra-n-butylammonium hexafluorophosphate in anhydrous acetonitrile. Measurements were made employing a glassy carbon working electrode, a platinum wire as a counter electrode, an Ag/Ag⁺ reference electrode, and a scan rate of 50 mV/s. The glassy carbon electrode was polished between each scan.

2.2.3 Synthesis of starting materials

- **Styrene precursors**

4-Vinylbenzoic acid 1a, 4-vinylphenyl acetate 1b, and 4-aminostyrene 1e were commercially available.

Method A: Wittig olefination



The general methodology for the preparation of the styrene precursors via Wittig reaction is as follows: To a 2-necked rounded bottom flask (previously dried) equipped with a magnetic stirrer, a solution of 1.2 mmol of methyl triphenylphosphonium bromide and 1.6 mmol of previously grounded potassium carbonate in 30 mL of 1,4-dioxane was added. The system was purged with nitrogen and stirred at room temperature for 4 hours. Then, 1.0 mmol of the corresponding aldehyde was added dropwise. The reaction was then stirred at 100 °C for 24 hours. After reaction completion, the flask was cooled to room temperature and 50 mL of water was poured. The crude product was extracted with dichloromethane (3 x 20 mL). The combined organic layers were dried over anhydrous MgSO_4 , and the solvent was removed in vacuo. The styrene product was then purified by flash chromatography employing SiO_2 and n-hexane as eluent.

1-Nitro-4-vinylbenzene 1c. Light yellow oil; yield 1.418 g (90%) from of 4-nitrobenzaldehyde (1.600g, 10.58 mmol), methyl triphenylphosphonium bromide (4.536 g, 12.70 mmol), and potassium carbonate (2.339 g, 16.93 mmol). The spectral data of the product agree with those reported in the literature. IR (ATR, cm^{-1}): 3090, 1595, 1512 (νNO_2), 1342 (νNO_2), 1109, 856. $^1\text{H-NMR}$ (400 MHz, CDCl_3) δ (ppm): 5.45 (d, $J=10.9$ Hz, 1H), 5.88 (d, $J=17.6$ Hz, 1H), 6.73 (dd, $J=10.9, 17.6$ Hz, 1H), 7.48 (d, $J=8.8$ Hz, 2H), 8.11 (d, $J=8.8$ Hz, 2H).

4-Vinylbenzaldehyde 1d. Colorless oil; yield 1.205 g (60%) from therephthalaldehyde (2.060 g, 15.36 mmol), methyl triphenylphosphonium bromide (5.625 g, 15.74 mmol) and potassium carbonate (2.760 g, 19.97 mmol). IR (ATR, cm^{-1}): 3010, 2829, 1701, 1685, 1604, 1213, 1166, 920, 839. $^1\text{H-NMR}$ (400 MHz, CDCl_3) δ (ppm): 5.36 (d, $J=10.9$ Hz, 1H), 5.83 (d, $J=17.6$ Hz, 1H), 6.68 (dd, $J=17.6, 10.9$ Hz, 1H), 7.46 (d, $J=8.2$ Hz, 2H), 7.76 (d, $J=8.2$ Hz, 2H), 9.91 (s, 1H).

Method B: Acetylation



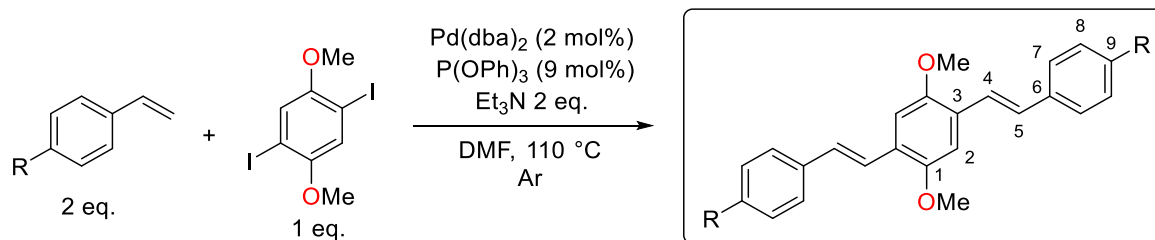
N-(4-Vinylphenyl) acetamide 1f. To a 25 mL round bottom flask equipped with a magnetic stirrer and an addition funnel, a solution containing 4-amino styrene **1e** (0.978 g, 8.2 mmol), triethylamine (0.675 g, 6.67 mmol, 1.1 eq.) and 15 mL of dichloromethane were added, and cooled to 0 °C. Then, acetyl chloride (0.523 g, 6.67 mmol, 1.1 eq.) was slowly added, maintaining the mixture temperature between 0 and 5 °C. The reaction was stirred at room temperature for 4 hours and tracked by TLC. For extraction, 20 mL of a saturated sodium bicarbonate solution were added, and subsequent liquid-liquid extraction was performed employing dichloromethane (3 x 20 mL). The combined organic layers were dried over anhydrous MgSO_4 , and the solvent was removed under vacuum. The styrene product was then purified by flash chromatography employing *n*-hexane as eluent. Yellow solid; yield 0.958 g (72%), m.p. 134-136 °C. (Lit. 133-134 °C).¹⁴¹ The spectral data of the product were in agreement with those reported in the literature. IR (ATR, cm^{-1}): 3287, 3248, 3111, 2998, 2965, 2929, 1659, 1594, 1509, 1320, 1262, 904, 840, 755. $^1\text{H-NMR}$ (400 MHz, CDCl_3) δ (ppm): 2.16 (s, 3H), 5.20 (d, $J=11.0$ Hz, 1H), 5.68 (d, $J=17.6$ Hz, 1H), 6.67 (dd, $J=17.6, 11.0$ Hz, 1H), 7.35 (d, $J=8.5$ Hz, 2H), 7.48 (d, $J=8.5$ Hz 2H), 7.82 (s, 1H).

- **Aryl 1,4-dihalide precursor**

1,4-Diiodo-2,5-dimethoxybenzene 2a. To a 250 mL round bottom flask equipped with a condenser and a magnetic stirrer 1,4-dimethoxybenzene (5.314 g, 38.46 mmol), iodine (11.715 g, 46.16 mmol), potassium iodate (4.116g, 19.23 mmol), acetic acid (120 mL), sulfuric acid (1 mL) and deionized water (10 mL) were added. The reaction mixture was heated to reflux for 24 hours. After reaction completion, the flask was cooled to room temperature and poured over 300 mL of a saturated sodium sulfite solution. The solid formed was filtered and washed with saturated sodium sulfite solution (5 x 20 mL) and cold ethanol (3 x 20 mL). Beige solid; yield 13.444 g (90%), m.p. 172-174 °C (Lit. 174-176 °C).¹⁶ IR (ATR, cm⁻¹): 3068, 2226, 1604, 1506, 1219, 921, 844. ¹H-NMR (400 MHz, CDCl₃) δ(ppm): 3.82 (s, 6H), 7.18 (s, 2H).

- **Synthesis of OPVs**

Assembly of the OPV skeleton via Mizoroki-Heck reaction



To a 10 mL headspace crimp vial equipped with a magnetic stirrer the corresponding styrene **1** (2.0 mmol), aryl 1,4-dihalide precursor **2a** (1.0 mmol), bis(dibenzylidene) acetone palladium (0) (2.0 mol%) and triphenylphosphite (9.0 mol%) were added. The vial was then sealed with a PTFE septum and an aluminum cap followed by purge-saturation with Ar. Dry DMF (3 mL), and triethylamine (2.0 mmol) were subsequently added via syringe. The reaction mixture was stirred at 110°C for 24 hours. After the reaction was complete, the crude was filtered over celite, and precipitation of the product was induced by the addition of cold water (75 mL). Recrystallization from the indicated solvent afforded the desired OPVs (**Appendix 7.1**).

4,4'-((1E,1'E)-(2,5-Dimethoxy-1,4-phenylene)bis(ethene-2,1-diyl))dibenzoic acid OPV 1. Yellow solid. m.p. 232-234 °C (Lit. 233-234 °C)¹⁹; Recrystallized from DMF, yield 0.337 g (79%) from 4-vinylbenzoic acid **1a** (0.250 g, 1.68 mmol), 1,4-diiodo-2,5-dimethoxybenzene **2a** (0.327 g, 0.84 mmol), Pd(dba)₂ (19.3 mg, 0.03 mmol), P(PhO)₃ (46.9 mg, 0.15 mmol) and Et₃N (0.340 g, 3.36 mmol). IR (ATR, cm⁻¹): 3055, 2939, 1678, 1600, 1292, 1207, 1176, 952. ¹H-NMR (400 MHz, DMSO-d₆) δ(ppm): 3.92 (s, 6H o_{Me}), 7.39 (s, 2H H-2), 7.44 (d, J=16.5 Hz, 2H H-5), 7.57 (d, J=16.5

Hz, 2H_{H-4}), 7.69 (d, $J=8.4$ Hz, 4H_{H-7}), 7.95 (d, $J=8.4$ Hz, 4H_{H-8}), 12.89 (bs_{COOH}). ¹³C-NMR (100 MHz, DMSO-d₆) δ (ppm): 56.2_{OMe}, 109.6_{C-2}, 125.0_{C-4}, 125.9_{C-3}, 126.3_{C-7}, 128.3_{C-5}, 129.4_{C-9}, 129.8_{C-8}, 141.8_{C-6}, 151.3_{C-1}, 167.0_{COOH}. MALDI-MS Calc. for C₂₆H₂₂O₆ 430.141; found [M]⁺ 430.57. Anal. Calcd for C₂₆H₂₂O₆: C, 72.55; H, 5.15%. Found: C, 72.26; H, 5.23%.

((1E,1'E)-(2,5-Dimethoxy-1,4-phenylene)bis(ethene-2,1-diyl))bis(4,1-phenylene) diacetate **AcO-OPV**. Light yellow solid, m.p. 221-224 °C (Lit. 220-222 °C)⁴²; Recrystallized from DMF, yield 0.263 g (43%) from 4-vinylphenyl acetate **1b** (0.433 g, 2.67 mmol), 1,4-diiodo-2,5-dimethoxybenzene **2a** (0.526 g, 1.35 mmol), Pd(dba)₂ (30.7 mg, 0.05 mmol), P(PhO)₃ (74.4 mg, 0.24 mmol) and Et₃N (0.270 g, 2.67 mmol). IR (ATR, cm⁻¹): 3053, 2949, 1755, 1504, 1211, 1196, 1041, 966. ¹H-NMR (400 MHz, DMSO-d₆) δ (ppm): 2.28 (s, 6H_{AcO}), 3.90 (s, 6H_{OMe}), 7.14 (d, $J=8.5$ Hz, 4H_{H-8}), 7.35 (d, $J=14.0$ Hz, 4H_{H-4,5}), 7.39 (s, 2H_{H-2}), 7.62 (d, $J=8.5$ Hz, 4H_{H-7}). Due to poor solubility in DMSO-d₆ and pyridine-d₅, ¹³C-NMR data was not obtained. MALDI-MS Calc. for C₂₈H₂₆O₆ 458.173; found [M]⁺ 458.495. Anal. Calcd for C₂₈H₂₆O₆: C, 73.35; H, 5.72. Found: C, 73.66; H, 5.51.

4,4'-((1E,1'E)-(2,5-Dimethoxy-1,4-phenylene)bis(ethene-2,1-diyl))bis(nitrobenzene) **NO₂-OPV**. Red solid, m.p. 275-278 °C (Lit. 272-274 °C)⁴²; Recrystallized from DMF, yield 0.259 g (80%) from 1-nitro-4-vinylbenzene **1c** (0.240 g, 1.61 mmol), 1,4-diiodo-2,5-dimethoxybenzene **2a** (0.314 g, 0.81 mmol), Pd(dba)₂ (18.4 mg, 0.03 mmol), P(PhO)₃ (45.0 mg, 0.145 mmol) and Et₃N (0.163 g, 1.61 mmol). IR (ATR, cm⁻¹): 3043, 2929, 2829, 1629, 1512 (ν NO₂), 1342 (ν NO₂), 1213, 972, 860. ¹H-NMR (400 MHz, Pyridine-d₅) δ (ppm): 3.94 (s, 6H_{OMe}), 7.59 (s, 2H_{H-2}), 7.63 (d, $J=16.5$ Hz, 2H_{H-5}), 7.73 (d, $J=8.8$ Hz, 4H_{H-7}), 7.99 (d, $J=16.5$ Hz, 2H_{H-4}), 8.25 (d, $J=8.8$ Hz, 4H_{H-8}). ¹³C-NMR (100 MHz, Pyridine-d₅) δ (ppm): 56.6_{OMe}, 110.7_{C-2}, 124.8_{C-7}, 127.8_{C-8}, 128.3_{C-4}, 128.6_{C-3}, 130.6_{C-5}, 145.3_{C-6}, 147.4_{C-9}, 152.9_{C-1}. MALDI-MS Calc. for C₂₄H₂₀N₂O₆ 432.132; found [M]⁺ 432.292. Anal. Calcd for C₂₄H₂₀N₂O₆: C, 66.66; H, 4.66; N, 6.48%. Found: C, 66.81; H, 4.57; N, 6.55%.

4,4'-((1E,1'E)-(2,5-Dimethoxy-1,4-phenylene)bis(ethene-2,1-diyl))dibenzaldehyde **OPV 4**. Orange solid. m.p. 212-215 °C (Lit. 230-232 °C).¹⁴² Purified by column chromatography over SiO₂ employing a *n*-hexane:ethyl acetate mixture 1:1, yield 0.427 g (72%) from 4-vinylbenzaldehyde **1d** (0.395 g, 2.99 mmol), 1,4-diiodo-2,5-dimethoxybenzene **2a** (0.583 g, 1.49 mmol), Pd(dba)₂ (34.4 mg, 0.06 mmol), P(PhO)₃ (83.5 mg, 0.27 mmol) and Et₃N (0.302 g, 2.99 mmol). IR (ATR, cm⁻¹): 3032, 2912, 1693, 1595, 1211, 1039, 968. ¹H-NMR (400 MHz, CDCl₃) δ (ppm): 3.96 (s, 6H_{OMe}), 7.16 (s, 2H_{H-2}), 7.19 (d, $J=16.4$ Hz, 2H_{H-5}), 7.65 (d, $J=16.4$ Hz, 2H_{H-4}), 7.70 (d, $J=8.0$ Hz, 4H_{H-7}), 7.88 (d, $J=8.0$ Hz, 4H_{H-8}), 10.00 (s, 2H_{CHO}). ¹³C-NMR (100 MHz, CDCl₃) δ (ppm): 56.4

oMe , 109.5 c-2 , 126.8 c-3 , 126.8 c-4 , 127.2 c-7 , 128.2 c-5 , 130.4 c-8 , 135.4 c-9 , 144.0 c-6 , 152.0 c-1 , 191.7 CHO . MALDI-MS Calc. for $\text{C}_{26}\text{H}_{22}\text{O}_4$ 398.152; found $[\text{M}]^+$ 398.348. Anal. Calcd for $\text{C}_{26}\text{H}_{22}\text{O}_4$: C, 78.37; H, 5.57%. Found: C, 78.56; H, 5.40%.

Synthesis of OPV 2: Hydrolysis of AcO-OPV

4,4'-((1E,1'E)-(2,5-dimethoxy-1,4-phenylene)bis(ethene-2,1-diyl)) diphenol **OPV 2**. On a 50 mL rounded bottom flask equipped with a condenser and a magnetic stirrer the corresponding **AcO-OPV** (0.263 g, 0.57 mmol) was dissolved in 25 mL of a 2:2:1 mixture of methanol, THF and water. Then, KOH (0.322, 5.74 mmol) was added, and the reacting mixture was heated to reflux for 12 hours. After reaction is complete, the crude was poured over 50 mL of cold water. The solid product was filtered and recrystallized from 1,4-dioxane. Light green solid. Yield 0.187 g (87 %), m.p. 292-294 °C (Lit. 294-296 °C)⁴²; IR (ATR, cm^{-1}): 3363 (ν OH), 3043, 2951, 1604, 1514, 1195, 1024, 958. $^1\text{H-NMR}$ (400 MHz, DMSO-d_6) δ (ppm): 3.87 (s, 6H oMe), 6.78 (d, $J=8.1$ Hz, 4H H-8), 7.20 (s, 2H H-2), 7.22 (d, $J=18.7$ Hz, 4H H-4,5), 7.40 (d, $J=8.1$ Hz, 4H H-7), 9.58 (s, 2H OH). $^{13}\text{C-NMR}$ (100 MHz, DMSO-d_6) δ (ppm): 56.1 oMe , 108.8 c-2 , 115.6 c-8 , 119.3 c-4 , 125.6 c-3 , 127.7 c-7 , 128.6 c-6 , 128.6 c-5 , 150.7 c-1 , 157.2 c-9 . MALDI-MS Calc. for $\text{C}_{24}\text{H}_{22}\text{O}_4$ 374.152; found $[\text{M}]^+$ 374.261. Anal. Calcd for $\text{C}_{24}\text{H}_{22}\text{O}_4$: C, 76.99; H, 5.92%. Found: C, 77.21; H, 6.16%.

Synthesis of OPV 3: reduction of NO_2 -OPV

4,4'-((1E,1'E)-(2,5-Dimethoxy-1,4-phenylene)bis(ethene-2,1-diyl)) dianiline **OPV 3**. On a 50 mL round bottom flask equipped with a condenser and a magnetic stirrer, **NO_2 -OPV** (0.327 g, 0.76 mmol) was dissolved in 3.0 mL of pyridine and taken to ebullition. Then, a solution of Na_2S (0.589 g (60%), 4.53 mmol) in 2 mL of water was added while maintaining gentle reflux. At this point, the color of the reaction mixture changes to dark brown. After the addition was complete, the reaction was stirred and heated at 115 °C for 30 additional minutes. Then, the crude was poured over 50 mL of cold water. The solid product was filtered before being washed with water (20 mL) and a water/ethanol (1:1) mixture (20 mL). No further purification procedures were required. Yellow solid. Yield 0.256 g (82 %), m.p. 189-191 °C (Lit. 222 °C)¹³⁸; From **NO_2 -OPV** (0.327 g, 0.76 mmol) and Na_2S (0.589 g (60%), 4.53 mmol). IR (ATR, cm^{-1}): 3446 (ν NH_2), 3369 (ν NH_2), 3213, 3034, 3001, 2954, 1608, 1514, 1207, 1039. $^1\text{H-NMR}$ (400 MHz, CDCl_3) δ (ppm): 3.73 (bs NH), 3.90 (s, 6H oMe), 6.67 (d, $J=8.5$ Hz, 4H H-8), 7.02 (d, $J=16.4$ Hz, 2H H-5), 7.10 (s, 2H H-2), 7.29 (d, $J=16.4$ Hz, 2H H-4), 7.37 (d, 8.5 Hz, 4H H-7). $^{13}\text{C-NMR}$ (100 MHz, CDCl_3) δ (ppm): 56.4 oMe , 108.9 c-2 , 115.2 c-8 , 119.7 c-4 , 126.6 c-3 , 127.8 c-7 , 128.7 c-5 , 128.7 c-6 , 146.0 c-9 , 151.3 c-1 . MALDI-MS Calc. for

$C_{24}H_{24}N_2O_2$ 372.183; found $[M]^+$ 372.314. Anal. Calcd for $C_{24}H_{24}N_2O_2$: C, 77.39; H, 6.49; N, 7.52%. Found: C, 77.04; H, 6.42; N, 7.28%.

2.3 Results and discussion

2.3.1 Synthesis and structural characterization of OPVs

Preparation of OPVs

The Mizoroki-Heck reaction conditions for the preparation of OPVs have been previously optimized by our research group in terms of catalyst, ligand auxiliary, and reaction time. This methodology was employed to provide the desired conjugated skeleton, as shown in **Figure 2-1**. It must be disclosed that most of the styrene precursors are not commercially available due to poor stability and light-induced polymerization susceptibility. Thus, compounds **1c** and **1d** were prepared by the Wittig reaction and used immediately after purification.

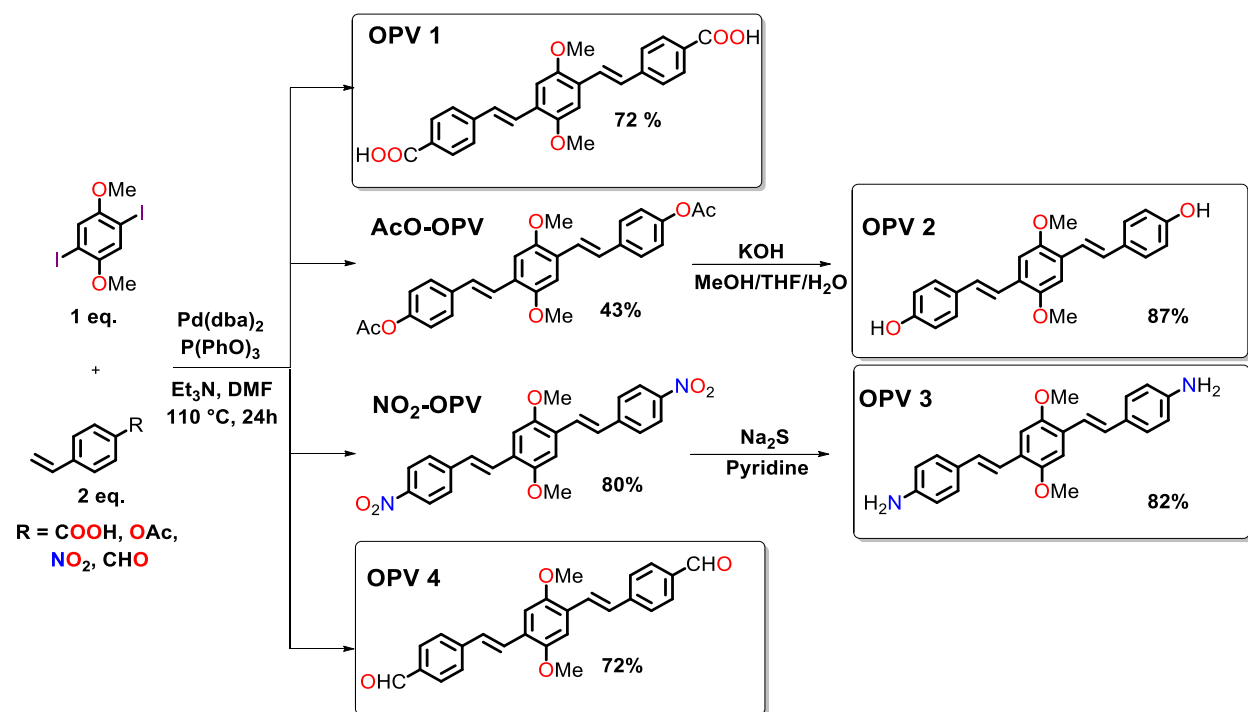


Figure 2-1. Overall synthesis route for **OPVs 1-4**.

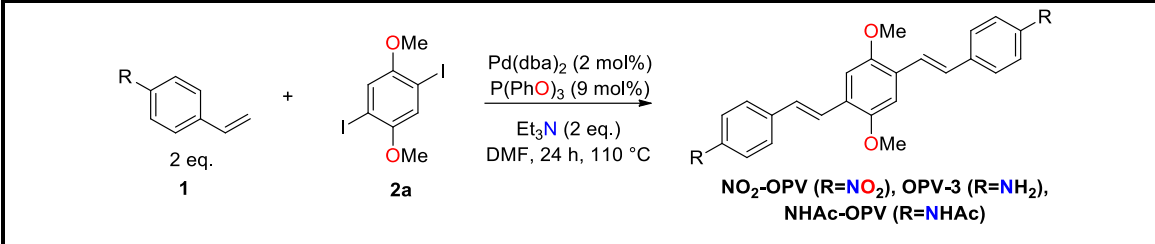
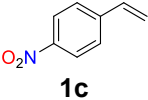
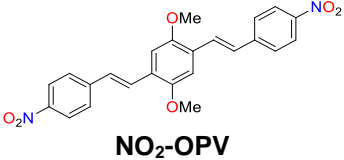
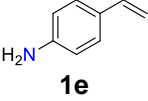
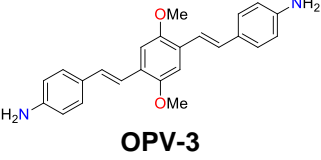
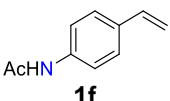
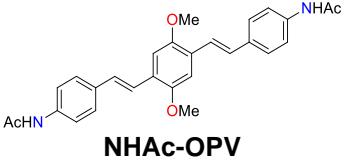
Pd (0)-catalyzed coupling reaction assembly of the OPV moiety was successfully achieved in moderate to good yields (43-80%). It should be noted that construction of **OPV 1** directly from 4-

vinylbenzoic acid via Mizoroki-Heck reaction is first reported. This proposed methodology avoids the use of esters as starting materials, subsequent hydrolysis reactions, and related purification steps. Moreover, it confirms that the carboxylic acid functional group is fully compatible with the employed cross-coupling reaction conditions. Access to **OPV 2** was prompted by alkaline hydrolysis of **AcO-OPV**, in 87% yield. However, the preparation of **OPV 3** required a preliminary evaluation of reaction conditions.

Initial efforts to access the desired amino OPV derivative **OPV-3** involving the direct Mizoroki-Heck coupling reaction of 4-aminostyrene **1e** and 2,5-diiodo-1,4-dimethoxybenzene **2a** (Table 2-1, entry 2) were unpromising. The use of aminostyrene precursor gave multiple products (as observed by TLC) that were not possible to isolate by column chromatography. This observed chemical behavior can be attributed to the low stability exhibited by **1e**, which is reported to involve a spontaneous polymerization caused by the nucleophilic attack of the amino group directly on the activated β -position of the double bond generating a zwitterionic propagating species.¹⁴³ To prevent this phenomenon, amine protection was carried out by treatment with acetyl chloride. The easily formed *N*-(4-vinylphenyl) acetamide **1f** was immediately brought under the same Pd(0)-catalyzed coupling reaction conditions. However, only 5% of the desired *N*-acetyl OPV derivative **NHAc-OPV** (purified by column chromatography) was obtained along with multiple products (Table 2-1, entry 3). These exploratory outcomes confirmed that aminostyrene derivatives are not suitable substrates to get amino OPV compounds under these reaction conditions. Nevertheless, the successful preparation of the **NO₂-OPV** model suggested that a reduction could be a feasible synthetic alternative to **OPV-3**.

Initial nitro reduction experiments were carried out employing a solid mixture of ammonium formate and zinc grounded in a mortar, followed by the addition of the **NO₂-OPV** (Table 2-2, entry 1).¹⁴⁴ After 15 minutes, TLC revealed that no reaction was taking place under these conditions indicating that the use of a grinding auxiliary might be required to enhance the catalytic hydrogen transfer.¹⁴⁵ As an attempt to improve the reactivity through a classical approach, methanol, one of the most commonly used solvents for this transformation, was used, followed by the addition of a few drops of acetic acid (Table 2-2, entry 2). The reaction mixture was then heated to reflux; however, no product formation was observed. These results can be attributed to the poor solubility of the **NO₂-OPV** in methanol, preventing the appropriate interaction between reactants in the solution.

Table 2-1: Preliminary formation of amino and nitro OPV derivatives via direct Mizoroki-Heck coupling reaction.

			
Entry	Styrene	Product	Yield, %
1	 1c	 NO₂-OPV	80
2	 1e	 OPV-3	NR
3	 1f	 NHAc-OPV	5 ^a

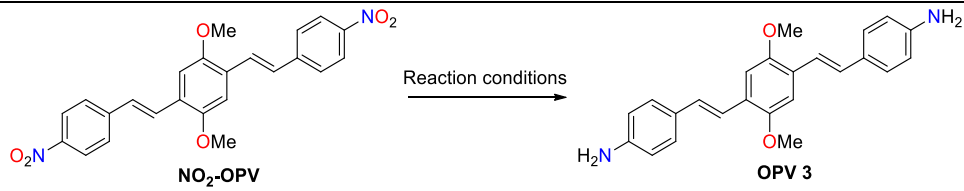
^aMultiple products formation. **NR** No reaction.

Then, to improve the OPV solubility, SnCl₂ in a mixture of EtOH/AcOEt was explored (Table 2-2, entry 3). Although complete solubility of **NO₂-OPV** was reached under reflux conditions, and successful reduction of similar nitro-substituted conjugated systems have been reported,¹³⁵ conversion of **NO₂-OPV** into the corresponding amino derivative was not observed, and multiple products were formed instead. The same chemical behavior was observed when concentrated HCl (37%) was used as a solvent (Table 2-2, entry 4). The use of HCl in combination with Na₂S has been previously reported for selective nitro group reductions.¹³⁷ However, under these conditions, the model compound **NO₂-OPV** was again converted into multiple products (Table 2-2, entry 5).

An analog methodology involving the use of sodium sulfide/pyridine has already been reported, but its application was limited to a single OPV example.¹³⁸ Our exploratory synthetic efforts confirmed that this reduction system serves as a rapid and efficient approach towards amino OPV

derivatives (Table 2-2, entry 6). A greener approach exploring the use of water-miscible, less harmful solvents was unsuccessful. 1,4-dioxane, PEG-600, and a choline chloride/tin (II) chloride deep eutectic solvent (DES)¹⁴⁶ gave the desired product but in low yields (Table 2-2, entries 7, 8, and 9). It should be noted that the purification procedure for these last three systems became tedious, considering that an emulsion was formed after pouring the reaction mixture in water, therefore preventing the formation of the solid **OPV-3** product although TLC indicated the reaction completion. Remarkably, after reaction is complete with the best reaction conditions (Table 2-2, entry 6), the obtained solid product was recovered by filtration followed by washing cycles with water and a 1:1 water/ethanol mixture. No further purification procedures were required. To demonstrate the synthetic scope and applicability of the herein proposed reduction protocol, a total of 10 nitro-OPV derivatives were prepared by the Mizoroki-Heck reaction, as shown in Table 2-3, in moderate to good yields (**Appendix 7.2** and **7.3**).

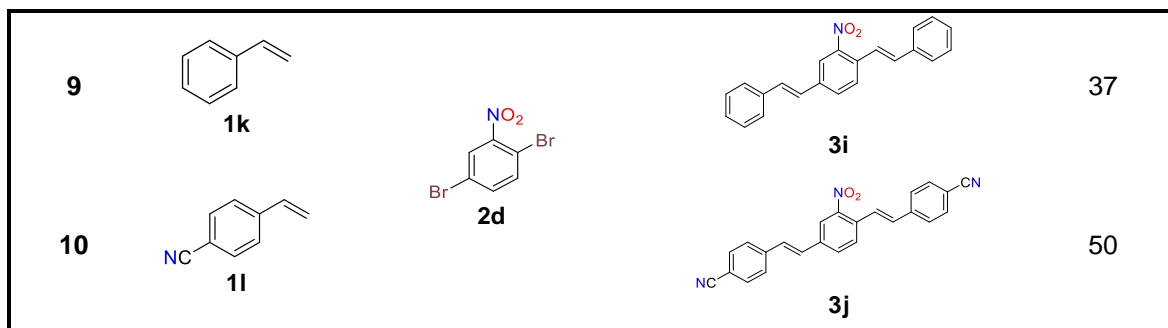
Table 2-2: Reduction conditions evaluated for the synthesis of amino OPVs.

					
Entry	Reducing agent	Solvent	Temperature, °C	Time, h	Yield, %
1	NH ₄ HCO ₂ /Zn	None ^a	r.t.	0.25	NR
2	NH ₄ HCO ₂ /Zn	MeOH/AcOH	118	12	NR
3	SnCl ₂ ·H ₂ O	EtOH/AcOEt (1:1)	78	8	<5 ^b
4	SnCl ₂ ·H ₂ O	HCl (37%)	110	1	<5 ^b
5	Na ₂ S	Pyridine/HCl (37%)	90	2	<5 ^b
6	Na ₂ S	Pyridine	115	0.5	82
7	Na ₂ S	1,4-Dioxane	100	0.5	22
8	Na ₂ S	PEG 600	100	1	18
9	SnCl ₂ ·2H ₂ O	Choline chloride (DES)	120	4	20

^aMechanochemical reaction. ^bMultiple product formation. NR; No reaction

Table 2-3: Pd-catalyzed coupling reaction for direct synthesis of nitro OPV precursors.

Entry	Styrene	Aryl halide	Product	Yield, %
1				80
2				69
3				55
4				62
5				87
6				56
7				70
8				40

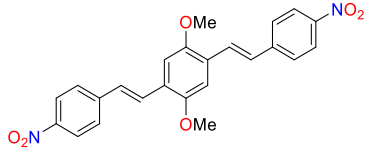
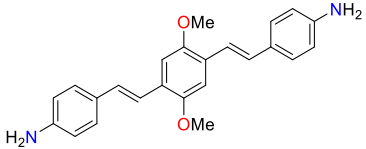
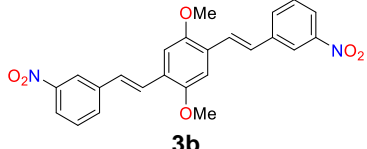
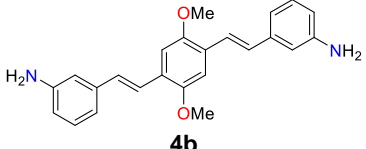
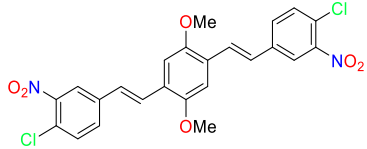
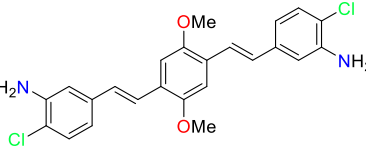
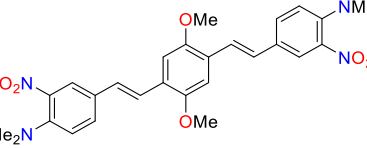
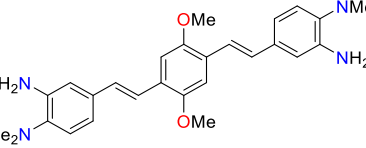
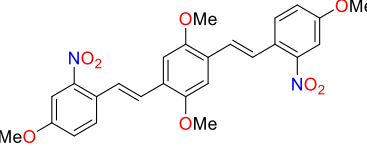
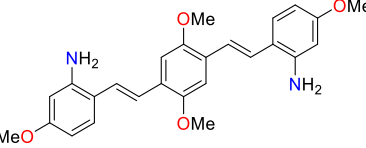
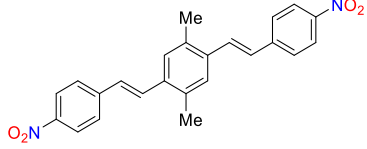
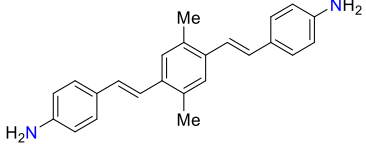
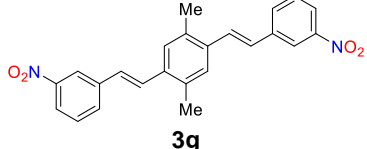
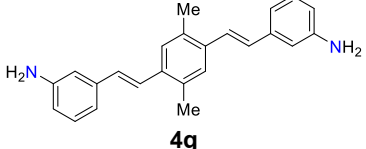
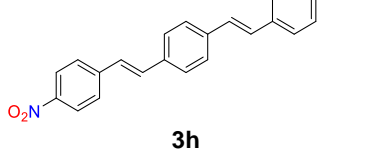
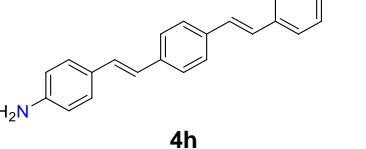


All nitro OPV products were obtained as stable solids. Noteworthy, the *E*-stereoselective preparation of compounds **3a** and **3b** was successfully achieved employing the Mizoroki-Heck reaction as an alternative route to classic Wittig conditions, whereas a mixture of *cis* and *trans* isomers was obtained as reported by Saikachi and coworkers.¹⁴⁷ Moreover, no significant yield variation was observed regardless of the electronic and steric nature of the styrene and 1,4-dihalide arene precursors. All these nitro-OPV compounds were brought into the Na₂S/pyridine reaction conditions (**Table 2-4**).

Complete reduction of the -NO₂ group was achieved in all cases in moderate to high yields (**Appendix 7.2** and **7.3**). The reaction of nitro-OPVs **3d** and **3g** required a minor procedure modification to enhance solubility and consisted in heating the reacting mixture (**3d/3g**, pyridine, and Na₂S) at 100 °C on a capped vial for 12 hours, after which the reaction crude was also poured into water and the target product recovered by filtration. It should be noted that the insertion of additional substituents around the OPV scaffold (compounds **4c-e**) led to a significant decrease in the reduction reaction yields, although no side-products were observed by TLC.

Interestingly, the reduction reaction with OPVs containing the nitro group in the central ring gave a mixture of products as confirmed by MALDI-MS and NMR experiments (**Figure 2-2**). Reports indicate that the use of sulfide as a reducing agent for *p*-substituted nitrobenzenes promotes the formation of azo and azoxy compounds as by-products.¹⁴⁸ Upon thorough examination of the MALDI spectrum, a self-radical unimolecular induced fragmentation pattern is observed for all signals due to the presence of the amino group. However, signals at 592 and 502 *m/z* confirm the presence of the azo compound and its subsequent double bond cleavage product along with the desired amino OPV with the corresponding [M+H]⁺ ion signal at 298 *m/z* (**Figure 2-3**).

Table 2-4: Sodium sulfide/pyridine reduction of other nitro OPV systems.

Entry	Nitro-OPV	Product	Yield, %
1	 NO₂-OPV (3a)	 OPV-3 (4a)	82
2	 3b	 4b	76
3	 3c	 4c	36
4	 3d	 4d	43
5	 3e	 4e	39
6	 3f	 4f	96
7	 3g	 4g	93
8	 3h	 4h	75

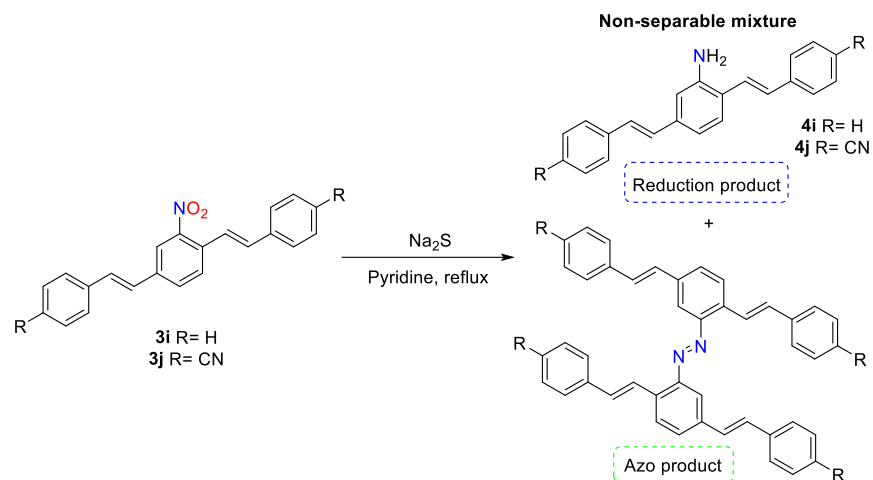


Figure 2-2. Products observed under the evaluated reaction conditions for nitro-OPVs **3i** and **3j**.

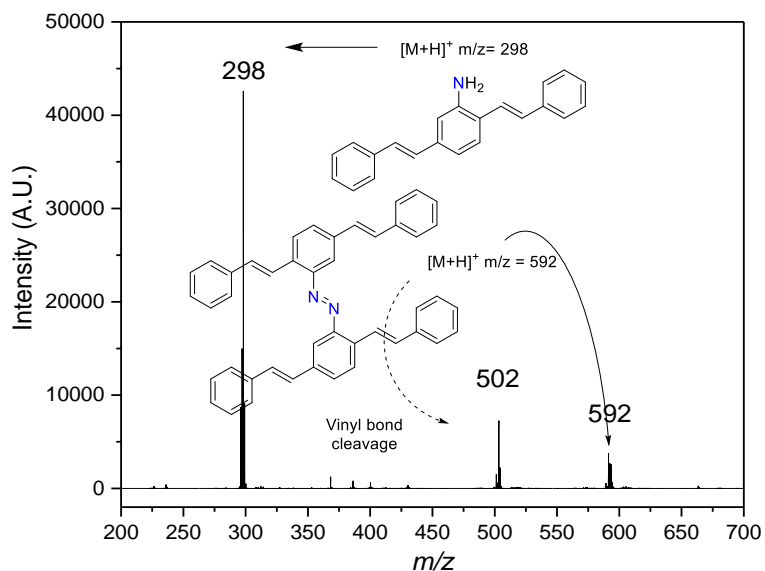


Figure 2-3. MALDI-ToF spectrum of purified fraction for **3i** reduction product.

Despite the efforts that were made to isolate the major amino OPV products **4i** and **4j** via recrystallization and purification by column chromatography, HPLC and NMR results indicate the side-product remains in a 0.28:1 ratio (**Figure 2-4**). The formation of the azo compound can be ascribed to the reaction between the nitrosyl reduction intermediate¹⁴⁹ and a preformed amine molecule in the medium, as depicted in **Figure 2-5**. The azo dimerization starts with the addition of the amine on the nitrosyl group, and then the elimination of water affords the N=N bond.

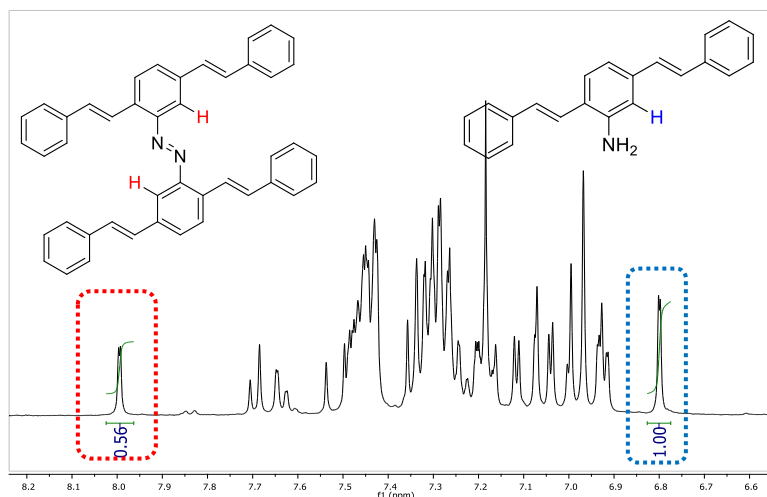


Figure 2-4. $^1\text{H-NMR}$ expanded aromatic region of **3i** reduction products.

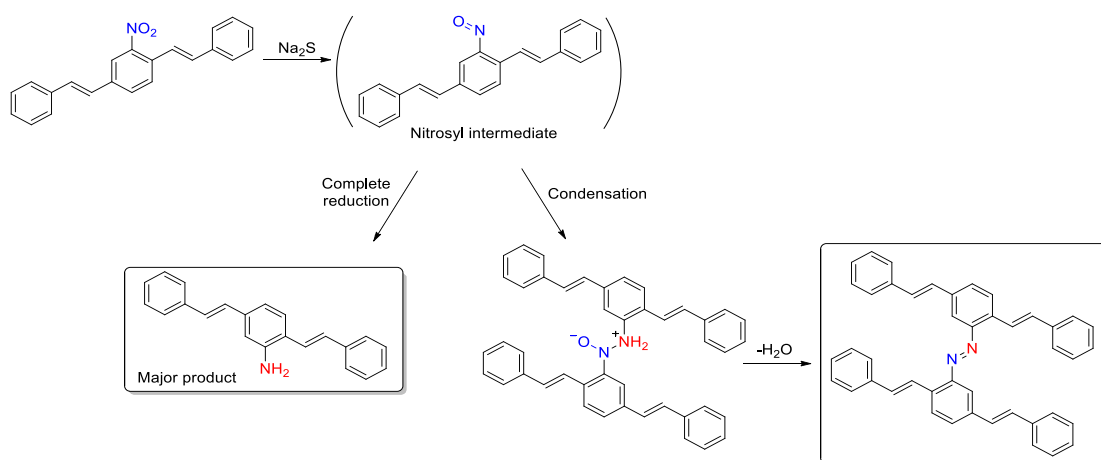


Figure 2-5. Proposed mechanism of OPV azo-dimerization.

Monitoring the reduction of compound **3j** by HPLC confirms the coelution of two substances with different UV-Vis absorption spectra. MALDI-MS showed the $[\text{M}+\text{H}]^+$ ion of the expected amino-OPV at 348 m/z as well as other peaks at 590 and 522 m/z that can be assigned to the azo by-product fragmentation ions. It should be highlighted that under the employed reduction conditions, the nitrile group was unaffected, and the formation of possible thioamide-type side-products was not observed in the MS spectrum.¹⁵⁰ The overall experimental data shows that placing the nitro group in the central ring of the OPV moiety seems to stabilize the reduction nitrosyl intermediate due to the electron-donating character of the styrene substituents, thus favoring the formation of the azo by-product.

▪ Structural characterization of target OPVs

Preliminary IR examination of the target products shows signals between 3000–3050 cm^{-1} and vibrational bands between 1665–1680 cm^{-1} that are characteristic of aromatic C-H and alkene C=C conjugated bonds, respectively. Additional C-H stretch aliphatic bands in the range of 2915–2950 cm^{-1} are observed as evidence of the -OMe groups in the central aryl ring. Moreover, signals attributed to *trans* C=C deformation mode between 955–980 cm^{-1} were observed, clearly indicating the desired *E-E* OPV scaffold formation in all cases (**Figure 2-6**).

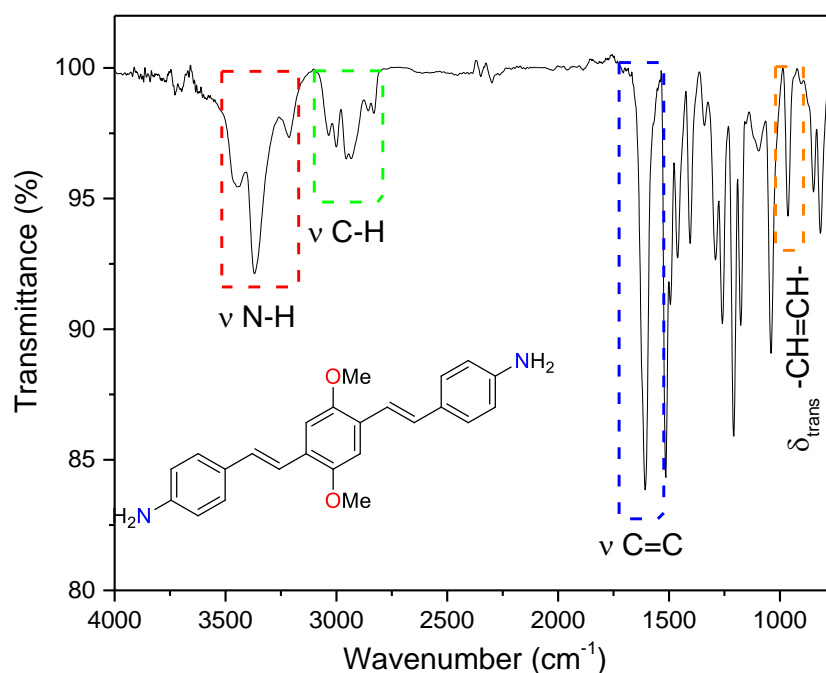


Figure 2-6. IR spectrum of compound **OPV 3**.

Due to the molecular weight range of the prepared OPV materials and their poor solubility in the most commonly used organic solvents, MALDI-ToF MS was employed as a characterization technique. LDI experiments show, for all OPVs, the characteristic $[\text{M}-\text{H}]^+$, $[\text{M}]^+$, and $[\text{M}+\text{H}]^+$ ions (**Figure 2-7**), corroborating the successful formation of the target OPV structures. ^1H -NMR analyses displayed 3J values between 12–18 Hz for the alkene groups, serving as evidence of the *E-E* stereochemistry in all OPV materials, which is maintained even after hydrolysis and reduction reactions. (**Figure 2-8**). ^{13}C -NMR results are in accordance with the synthesized structures where molecular symmetry simplifies the carbon atoms' assignment. A summary of the ^1H and ^{13}C -NMR signals can be found in **Tables 2-5** and **2-6**.

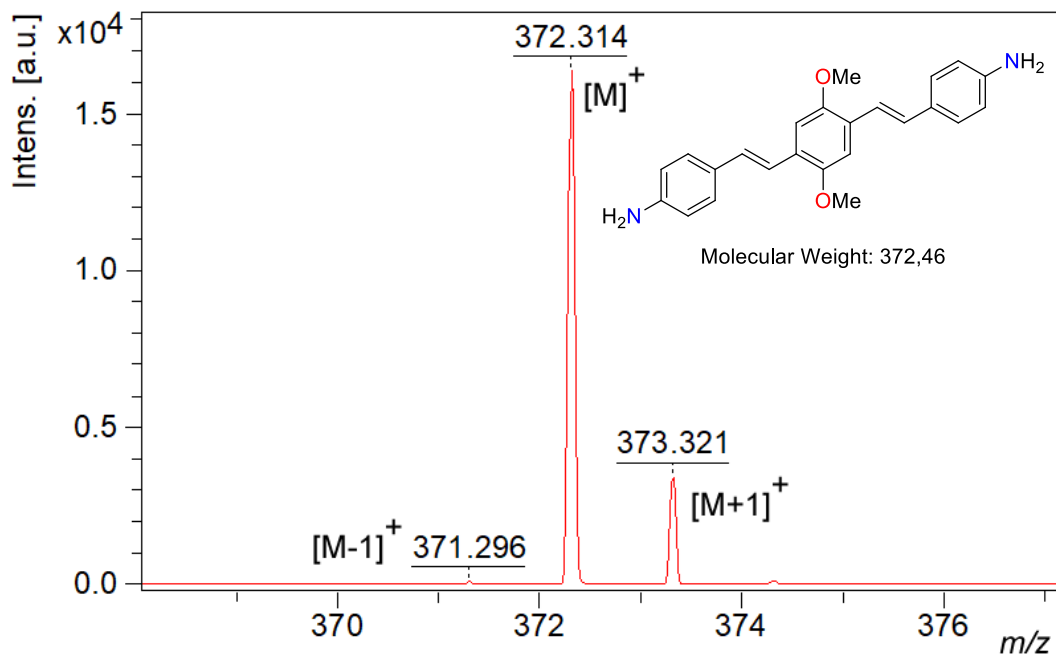


Figure 2-7: MALDI-ToF MS spectrum of compound **OPV 3**.

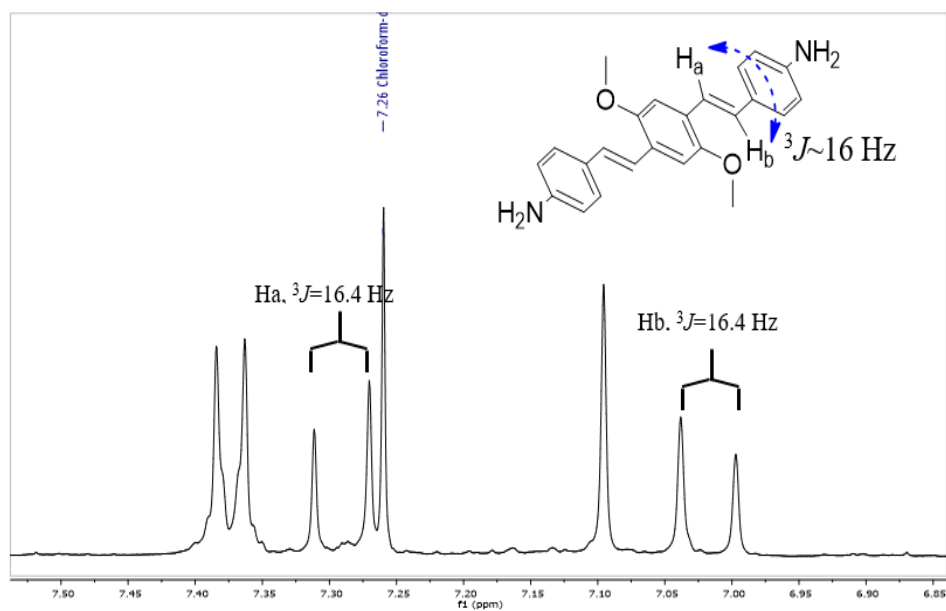
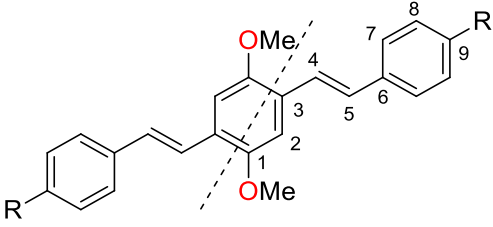
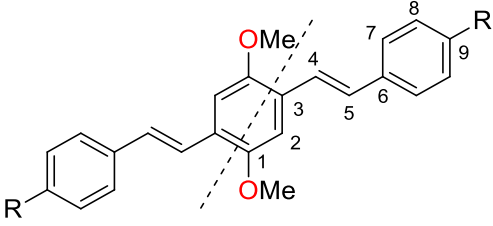


Figure 2-8: $^1\text{H-NMR}$ spectrum for compound **OPV 3**, aromatic region (6.85–7.55 ppm) expansion.

Table 2-5: $^1\text{H-NMR}$ signals (ppm) for OPVs.


Compound	H-2	H-4	H-5	H-7	H-8	-OMe	R
OPV 1 (DMSO-d6)	7.39 (s)	7.57 (d, $J=16.5$ Hz)	7.44 (d, $J=16.5$ Hz)	7.69 (d, $J=8.4$ Hz)	7.95 (d, $J=8.4$ Hz)	3.92 (s)	COOH, 12.89 (bs)
OPV 2 (DMSO-d6)	7.20 (s)	7.22 (d, $J=18.7$ Hz)	7.22 (d, $J=18.7$ Hz)	7.40 (d, $J=8.1$ Hz)	6.78 (d, $J=8.1$ Hz)	3.87 (s)	OH, 9.58 (s)
OPV 3 (CDCl ₃)	7.10 (s)	7.29 (d, $J=16.4$ Hz)	7.02 (d, $J=16.4$ Hz)	7.37 (d, $J=8.5$ Hz)	6.67 (d, $J=8.5$ Hz)	3.90 (s)	NH ₂ , 3.73 (bs)
OPV 4 (CDCl ₃)	7.16 (s)	7.65 (d, $J=16.4$ Hz)	7.19 (d, $J=16.4$ Hz)	7.70 (d, $J=8.0$ Hz)	7.88 (d, $J=8.0$ Hz)	3.96 (s)	CHO, 10.00 (s)

Table 2-6: $^{13}\text{C-NMR}$ signals (ppm) for OPVs (table continues in next page).


Compound	1	2	3	4	5	6	7
OPV 1 (DMSO-d6)	151.3	109.6	125.9	125.0	128.3	141.8	126.3
OPV 2 (DMSO-d6)	150.7	108.8	125.6	119.3	128.6	128.6	127.7
OPV 3 (CDCl ₃)	151.3	108.9	126.6	119.7	128.7	128.7	127.8
OPV 4 (CDCl ₃)	152.0	109.5	126.8	126.8	128.2	144.0	127.2

Compound	8	9	-OMe	R
OPV 1 (DMSO-d6)	129.8	129.4	56.2	(COOH) 167.0
OPV 2 (DMSO-d6)	115.6	157.2	56.1	---
OPV 3 (CDCl ₃)	115.2	146.0	56.4	---
OPV 4 (CDCl ₃)	130.4	135.4	56.4	(CHO) 191.7

2.3.2 Optoelectronic characterization of target OPVs

Absorption and emission spectra of OPVs were acquired in MeCN solution (**Figure 2-9**) and, in solid-state, to obtain relevant optoelectronic characterization (**Table 2-7**). All OPVs in solution displayed a double band absorption due to the expected π - π^* transition ascribed to the OPV conjugated backbone. An additional n - π^* transition was originated by the -OMe group bonded to the central aryl ring.

Also, a double band emission is observed only for OPVs containing -OH and -NH₂ as electron-donating groups (EDG) on the flanking aryl rings, indicating a significant modification of the vibronic states in these molecules. Interestingly, the λ_{\max} and λ_{em} values undergo a bathochromic shift in **OPVs 1** and **4** because of the presence of the electron-withdrawing groups (EWG) COOH and CHO, respectively. The optical ΔE values for OPVs in solution indicate that photocatalytic activity can be achieved even under blue visible light irradiation. Furthermore, the low to moderate fluorescence quantum yields (Φ_f) suggests deficient radiative charge recombination, implying that photocatalysis and related surface reactions might be favored as an alternative relaxation pathway.¹⁵¹

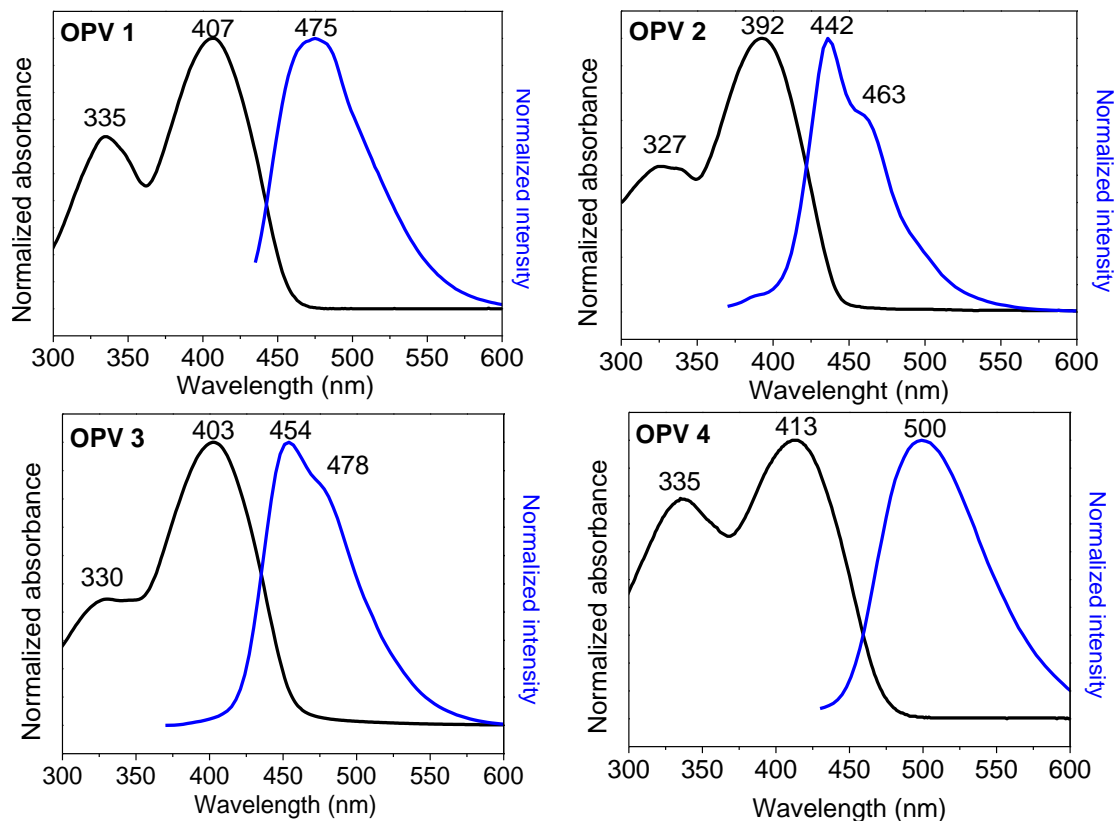


Figure 2-9: Normalized absorption and emission spectra for **OPVs 1-4** in MeCN.

Table 2-7: Optoelectronic properties of **OPVs 1-4** in MeCN solution and in solid state.

OPV		1	2	3	4
MeCN solution	λ_{\max} (nm)	407	392	403	413
	λ_{em} (nm)	475	442	454	500
	ΔE (eV)	2.67	2.83	2.71	2.59
	Φ_f^*	0.25	0.58	0.10	0.21
Solid state	ΔE (eV)	2.41	2.70	2.35	2.32
	λ_{em} (nm)	540	483	574	568

*Perylene was used as standard

To provide a complete overview of the absorption and emission profile of **OPVs 1-4**, the Excitation Emission Matrices (EEM) were acquired (**Figure 2-10**). Such surfaces clearly show a broader emission region for OPVs bearing EWG substituents (**OPVs 1** and **4**), while a much narrower fluorescence is observed for compounds with EDG (**OPVs 2** and **3**). These results suggest that the electron-withdrawing character of -COOH and -CHO substituents distribute the vibrational

energy levels in S_0 , so they are closely spaced, enabling a range of photon energies to match the $S_1 \rightarrow S_0$ transition.

Regarding solid-state optoelectronic properties (**Figure 2-11**), diffuse reflectance spectra revealed a broad absorption for all OPVs starting in the visible region. The Kubelka-Munk function was calculated from the reflectance spectra to estimate the ΔE values for all the materials. The observed shift of the ΔE to lower energies in solid OPVs, compared to the values in MeCN solution, might be the result of solid-state non-covalent interactions such as $\pi \cdots \pi$ stacking, where the HOMO-LUMO energy gap can decrease due to orbital overlapping of the oligomers (**Table 2-8**).¹⁵² At the same time, all OPVs exhibited moderate fluorescence emission when excited under 370 nm light. It is worth noting that all the λ_{em} values are redshifted when compared to the spectra acquired in MeCN solution, serving as evidence for the existence of the above-mentioned $\pi \cdots \pi$ stacking interactions.

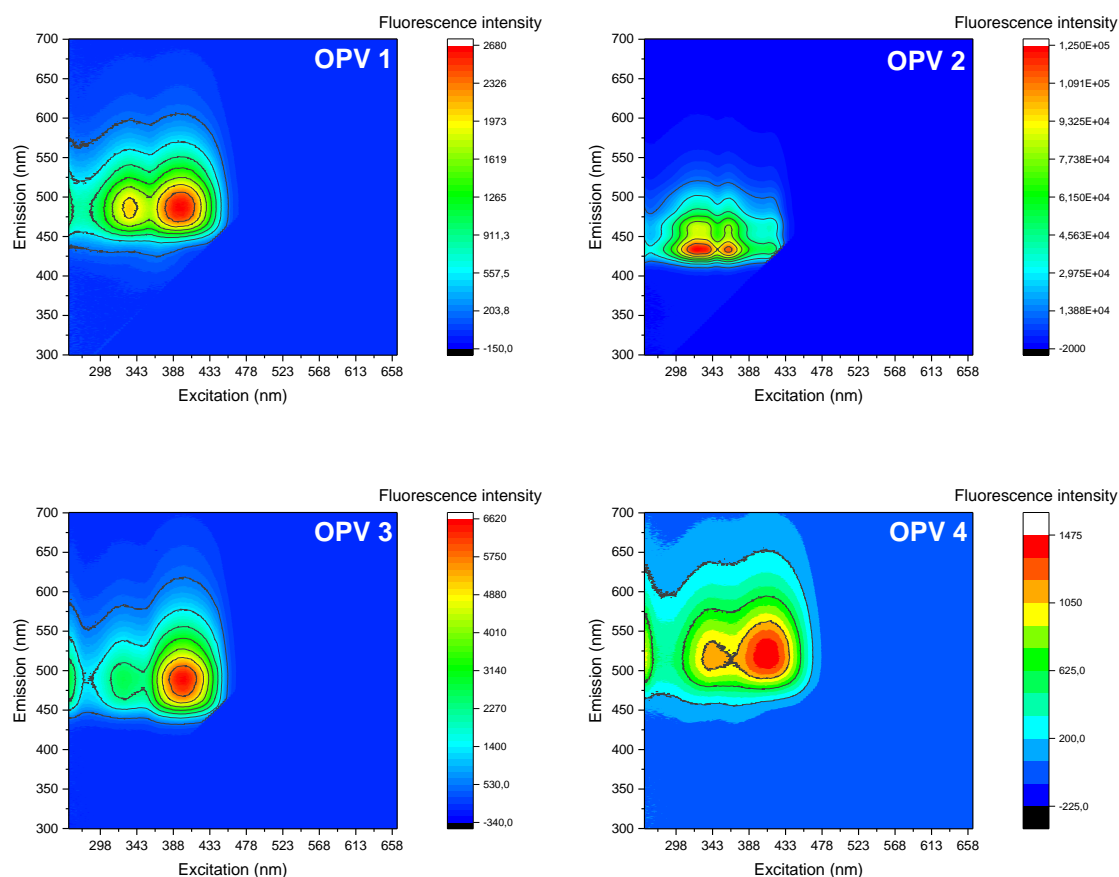


Figure 2-10: Excitation-Emission Matrices (EEM) for OPVs 1-4 in MeCN.

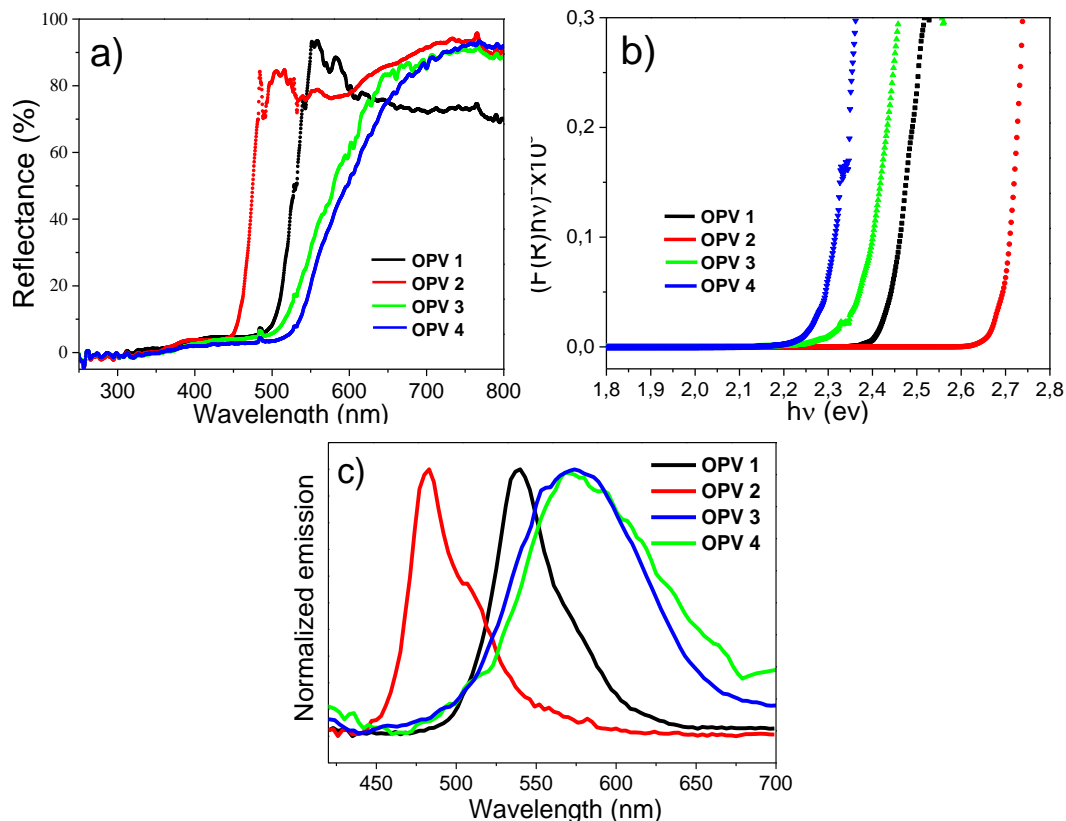


Figure 2-11: (a) Diffuse reflectance spectra of OPVs, (b) Kubelka-Munk function of OPVs, and (c) solid-state emission spectra for OPVs.

Cyclic voltammetry was employed to estimate the OPVs' HOMO-LUMO energy levels. The onset reduction (E_{red}) and oxidation (E_{ox}) peak potentials (**Table 2-8**) were determined directly from the electrochemistry experiments (**Figure 2-12**) and correlated to ferrocene.¹⁵³

Table 2-8: Electrochemical data obtained for OPVs 1-4.

OPV	E_{ox} (V)	E_{red} (V)	E_{HOMO} (V vs. NHE)	E_{LUMO} (V vs. NHE)
1	1.31	-1.09	1.81	-0.59
2	0.83	-1.82	1.33	-1.32
3	0.68	-1.80	1.18	-1.30
4	1.18	-1.30	1.68	-0.80

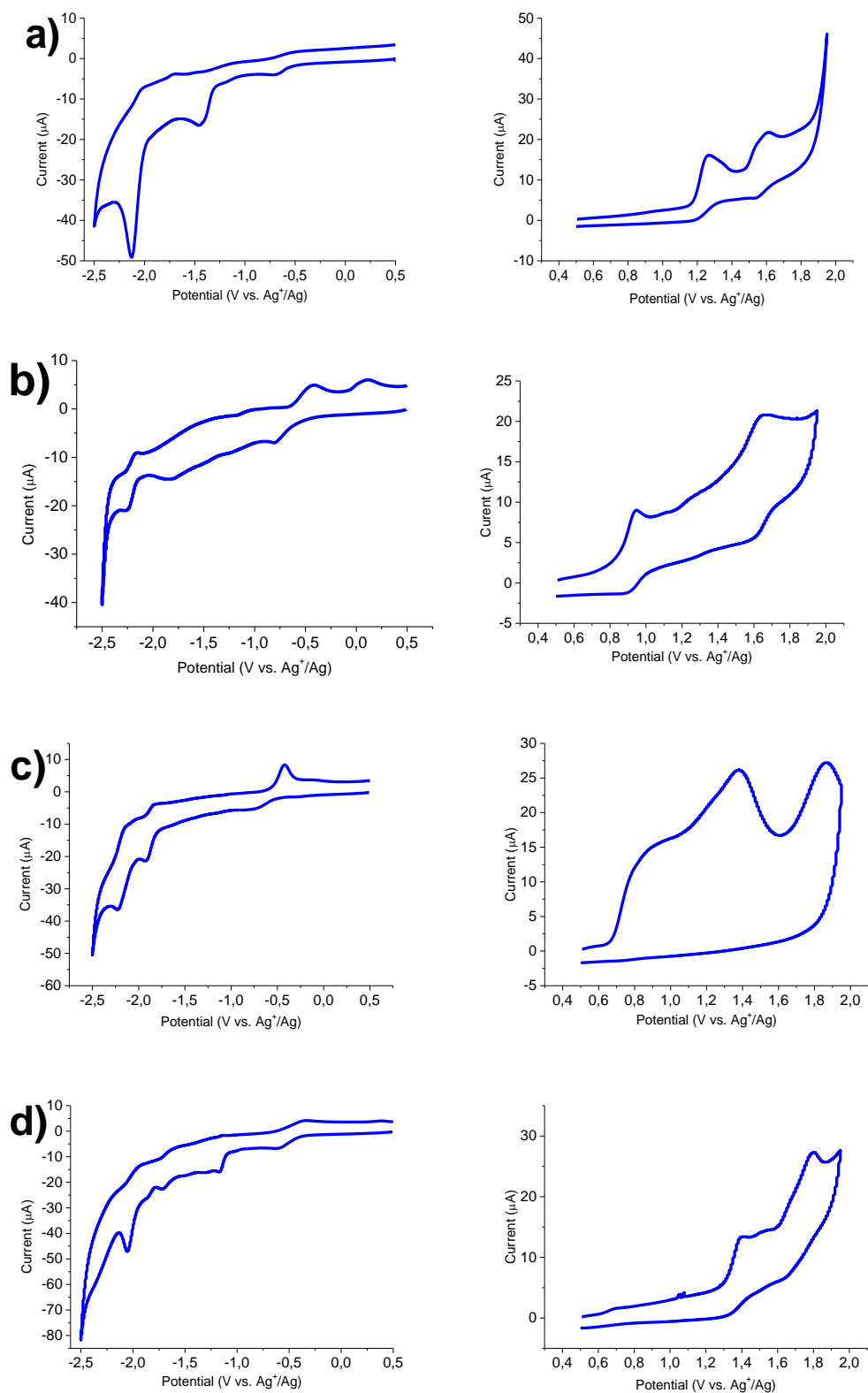


Figure 2-12: Cathodic (left) and anodic (right) scans for OPVs 1 (a), 2 (b), 3 (c) and 4 (d).

A marked influence in the HOMO level is observed when electron-withdrawing groups are placed around the OPV backbone (**OPV 1** and **4**), changing the frontier orbital potentials to more positive values. Noteworthy, all E_{HOMO} levels fall in the range of 1.18 to 1.81 eV (vs. NHE) providing sufficient driving force to carry out some oxidation reactions. Likewise, the presence of EWG in the flanking aryl rings of the OPV (**OPV 1** and **4**) causes the LUMO level to shift to more positive potential values compared to EDG.

Finally, with this information in hand, an energy level diagram is proposed for all OPVs as a valuable tool to predict their photochemical behavior. The LUMO position was estimated by adding the experimental optical ΔE value (**Figure 2-13**).

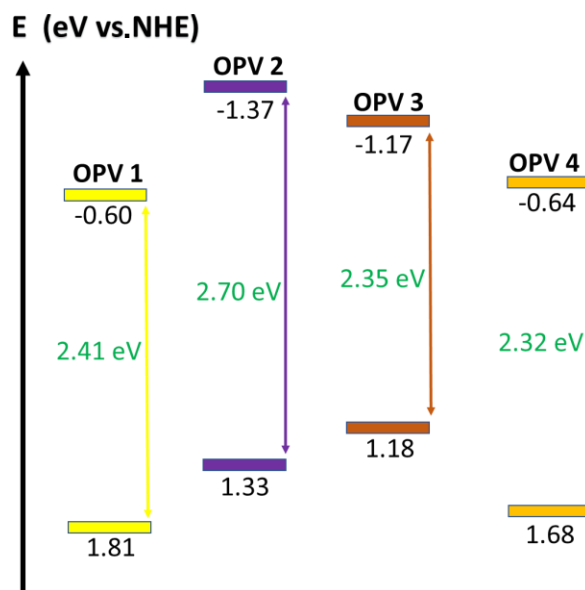


Figure 2-13: Relative HOMO-LUMO levels alignment for OPVs (vs. NHE).

2.4 Conclusions

Four target OPVs were prepared by the Mizoroki-Heck reaction in moderate to good yields providing excellent *E-E* double bond stereoselectivity. **OPV 1** was first prepared employing commercially available 4-vinylbenzoic acid as starting material, resulting in a simpler and more expedited synthetic route towards this compound. Moreover, after a comprehensive reduction conditions evaluation, Na_2S /pyridine was demonstrated to be an effective and efficient alternative to access amino OPV derivatives from their nitro analogs.

The optoelectronic properties of the OPVs in MeCN solution showed that EWG led to a bathochromic shift in both absorption and emission spectra. Also, the low to moderate fluorescence quantum yields (Φ_f) determined for the OPV compounds suggest that photocatalysis can be favored as a relaxation pathway. Regarding solid-state optoelectronic properties, the absorption spectra revealed that photoexcitation could be achieved even under visible light near 500 nm, as confirmed by the ΔE values. This behavior, explained by a $\pi \cdots \pi$ stacking interaction, indicates that the radiative requirement is reduced for heterogeneous photocatalysis applications. Finally, cyclic voltammetry allowed to set the HOMO-LUMO levels of the OPVs as an effective strategy to predict the electrons flow in photocatalytic applications.

3. Assessment of OPVs photocatalytic activity in the degradation of indigo carmine dye

Abstract

The mechanism and fate of phenylene vinylene systems when applied to the heterogeneous photocatalytic degradation of indigo carmine (IC) dye in aqueous media were explored. The stability, mechanism, and photodegradation activity of the OPV systems over aqueous IC were investigated using radical scavengers, a singlet oxygen ($^1\text{O}_2$) trap, and ESI-IT-MS. It was confirmed that superoxide radical ($\text{O}_2^{\cdot-}$), $^1\text{O}_2$, and direct oxidation are responsible for dye degradation. Hydroxide radical formation, under neutral pH conditions, does not occur, and it was corroborated by the HOMO and LUMO levels of the photocatalysts. Additionally, the use of oxalic acid as an electron sacrificial donor was demonstrated as an effective approach to enhance the OPVs photocatalytic activity.

3.1 Introduction

Organic dyes are widely employed in the global textile industry for the manufacture of denim fabrics and other materials, including paper and plastics, which are incorporated in daily-use apparel.^{154,155} Especial attention has been placed on indigo carmine (3,3-dioxo-2,2-bis-indolyden-5,5-disulfonic acid disodium salt), an indigoid-type compound discharged into industrial wastewaters, due to their well-known toxicity and high impact over aquatic environments, since this compound reduces sunlight penetration, favoring eutrophication.¹⁵⁶ Although indigo carmine (IC) can be used for medical diagnostic purposes,¹⁵⁷ many health concerns regarding skin and eye irritation, carcinogenicity, and reproductive toxicity have been established.¹⁵⁸ Considering this set of negative effects, the removal or degradation of IC has become a significant concern for the scientific community.

Several strategies have been explored to address this problem. Physical processes such as adsorption based on low-cost natural materials, including chitin, chitosan, and hen feathers, have been investigated.^{159,160} However, further treatments are required to remove IC from the solid adsorbent, increasing the operative costs of dye removal. Alternatively, biological,¹⁶¹ electrochemical,⁹ and advanced oxidation processes (AOPs) have been employed as a feasible choice for IC degradation.^{163,164} Out of all these treatment options, photocatalytic degradation has emerged as the method of choice for environmental remediation for soluble organic pollutants, including IC, due to the low-cost scaling to industrial level.^{157,165,166}

Similarly, inorganic TiO₂-based materials have been subject to research over the last decades for the mineralization of contaminants via heterogeneous photocatalysis¹⁶⁷.¹⁶⁷ However, their high bandgap values represent a severe limitation considering that the incident solar spectrum contains a high percentage of visible light.¹⁶⁸ On the other hand, organic compounds and polymers arise as a metal-free approach for photocatalytic applications offering easily tunable properties and lowering the radiative requirements taking advantage of a wide range of synthetic pathways available for their construction.²

Examples of heterogeneous organic and polymeric photocatalysts for pollutants degradation in aqueous media have been described before, some displaying distinct π -conjugation structures embedded in hetero-aromatic rings and alternated double bonds.^{46,169,170} Thus, phenylene vinylenes (PV) as conjugated systems serve as promising molecular models for heterogeneous photocatalysis, as demonstrated by several applications involving two-photon excitation singlet oxygen production,⁹³ Orange G dye degradation,⁵ and light-promoted oxidative hydroxylation of aryl boronic acids.¹⁷¹ In all this, the participation of radical reactive species such as OH \cdot and O₂⁻ have been described. However, detailed studies on photocatalytic properties, for example, the determination of HOMO-LUMO levels by redox behavior in poly-PVs have not been extendedly performed, considering that direct study of high-molecular weight poly-conjugated systems is often restricted by low solubility and heterogeneity.

As a consequence, the oligomer approach is presented as a useful and expedite tactic to perform extensive characterization -including optoelectronic-, predict reactivity and provide key information to understand the photocatalytic degradation process.^{9,172} Oligo (phenylene vinylene)s (OPVs), as model π -conjugated systems, can be easily prepared by the Mizoroki-Heck reaction in a highly stereoselective fashion,¹³² where structural and chemical diversity around the

conjugated scaffold offers a wide range of controllable properties for light absorption and photocatalytic applications.^{42,134} Although small molecules and oligomers are challenging models for heterogeneous photocatalysis due to photostability requirements,⁶⁹ it has been demonstrated that long-term stability and recyclability can be achieved.¹⁷³

In this chapter, we examine the synthesis, optoelectronic properties, stability, and heterogeneous photocatalytic performance of four OPVs for the treatment of aqueous IC. Also, the radical oxygen species and their role in the degradation mechanism are discussed as the basis for the future development of novel photostable poly-PV-based heterogeneous materials.

3.2 Experimental section

3.2.1 Materials

Sigma-Aldrich was used as a supplier unless otherwise indicated. OPVs were synthesized according to the procedure described in Chapter 2. Indigo carmine (C.I. 73015) for clinical diagnosis (>98%) was supplied from Panreac. TiO₂ Degussa P25 Aeroxide® (<45 microns, S_{BET} 35-65 m²/g) was obtained from Acros Organics. Silica gel 60 (Macherey-Nagel GmbH & Co., 0.063-0.200 mm, S_{BET} 480-540 m²/g) was employed for photocatalyst preparation. Oxygen-sensitive reactions were performed under an atmosphere of dry argon or nitrogen. Distilled, deionized (MilliQ purification systems) water was used for photocatalytic and ESI-IT MS experiments.

3.2.2 Analytical techniques

An Amazon X (Bruker) ESI-IT, operating in alternate positive/negative ion modes at 300°C and 4500V in the capillary, was used for MS data collection. Nitrogen was used as nebulizer gas with an influx of 8 L/min and 30 psi. MeCN (HPLC grade) was used for sample dilution. ¹H-NMR spectra (400 MHz) were obtained from an Ultrashield-400 Bruker spectrometer using DMSO-d₆ as solvent. Chemical shifts are reported in ppm (δ). The absorption spectra were recorded using a Thermo Scientific Evolution 300 UV-Vis spectrophotometer. The emission spectra were measured using a PTI QuantaMaster™ 40 spectrofluorometer adapted to an integrating sphere. Diffuse reflectance measurements were performed on an Ocean Optics spectrometer adapted to a reflection probe. The EEM was acquired using the Horiba Duetta Fluorescence and Absorbance

Spectrometer, and inner-filter effects and Rayleigh scattering were corrected using EzSpec™ software.

3.2.3 Photocatalyst preparation

SiO₂-adsorbed OPVs

The photocatalysts were prepared by the wet impregnation method dissolving 5 mg of the corresponding OPV in 10 mL of chloroform under sonication. Then, 500 mg of silica gel was added, keeping the mixture under a constant flow of air at 50 °C for complete solvent evaporation. It must be disclosed that SiO₂ was chosen as an inert support for the evaluation of OPVs as photocatalysts to increase surface area, promoting mass transfer in the photocatalytic process by improving the surface wetness and providing stabilization.¹⁷⁴ This strategy also contributes to catalyst reuse, allowing easy separation from the reaction products and solvent.

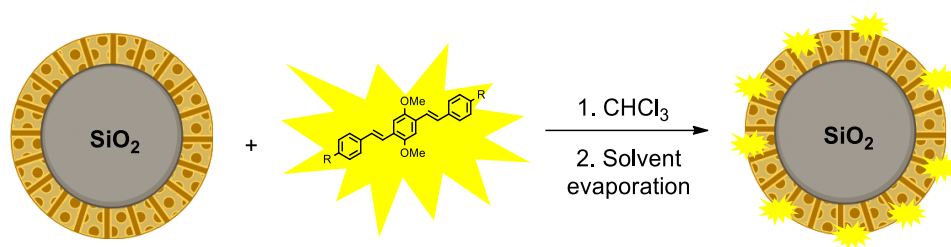


Figure 3-1: Schematic preparation of OPVs photocatalyst by the wet impregnation method.

3.2.4 Photocatalytic IC degradation

The IC degradation reactions were performed on an LED-based panel type photoreactor equipped with a 3W LED array as irradiation source within the UVA and visible portion of the spectrum (350-450 nm). In a typical dye degradation experiment, 20 mg of catalyst was suspended on 3 mL of 50 μM aqueous IC solution on the UV-vis cuvette to facilitate direct monitoring of the color intensity. The mixture was then left for 15 min in darkness to ensure the adsorption equilibrium is reached. The temperature was maintained constant at 20 °C using circulated water and, the experiments were performed under a low-stirring regime (100 rpm).

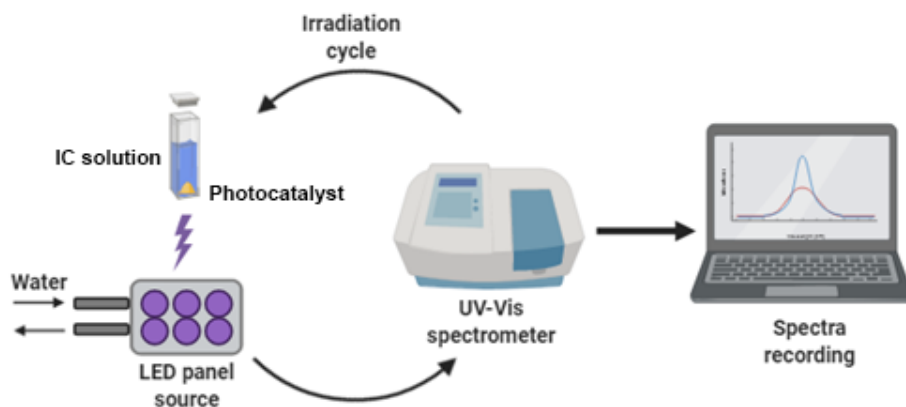


Figure 3-2: Experimental set-up for IC degradation.

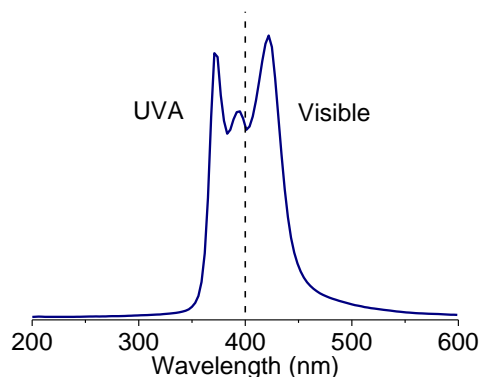


Figure 3-3: LED panel emission spectrum.

3.2.5 Photostability experiments

The stability of OPVs was monitored employing UV-Vis and $^1\text{H-NMR}$ spectroscopy. The change in the OPVs absorption under inert atmosphere (nitrogen) was directly monitored in a septum-sealed quartz cuvette after the corresponding irradiation cycles for a MeCN solution (1×10^{-5} M). For the $^1\text{H-NMR}$ experiments, 2.0 mg of the compound with 0.5 mL of DMSO- d_6 were added to the tube and vortexed until complete dissolution was achieved. To ensure an inert atmosphere, the NMR tube was septum-capped and purged for 15 minutes with nitrogen through a 27 Gauge needle. Then, after 1 hour of irradiation with the LED panel, the $^1\text{H-NMR}$ spectrum was acquired. The same experiments were conducted under open atmosphere (cap removed) for comparative purposes.

3.2.6 Singlet oxygen quantum yield determination

The singlet oxygen quantum yield (Φ_{Δ}) was estimated employing a modification of the chemical acceptor methodology described in the literature.¹⁷⁵ The Φ_{Δ} determination experiments were carried out by following the decay in the furfuraldehyde absorption band at 270 nm. Even though furfuraldehyde exhibits a chemical reaction towards $^1\text{O}_2$ that is around 17 times slower compared to other furane-based trapping agents such as furfuryl alcohol,^{176,177} it was selected as a suitable singlet oxygen acceptor considering that it does not absorb light in the 350-450 nm range, its absorption profile does not entirely overlap with the employed photosensitizers, and it has been widely used as a reference for the determination of singlet oxygen reaction rates.^{178,179} This signal was completely isolated by placing a solution of the corresponding sample/reference material, with the same concentration (around 10^{-5} M), in the reference beamline of the spectrophotometer. The spectra set were collected after irradiation of both, sample solution (sample + furfuraldehyde), and reference solution (sample) with a 3W LED panel (350-450 nm) at specified time intervals under constant stirring (200 rpm). 1*H*-Phenalen-1-one (PN) was used as singlet oxygen reference photosensitizer ($\Phi_{\Delta} = 1.00$).¹⁸⁰ The PN absorbance at 380 nm and the OPV absorbance at λ_{max} were matched at a value of approximately 0.160. The absorbance difference (ΔOD) value was calculated using the $t=0$ s absorbance value of furfuraldehyde at 270 nm as reference. The linear fit slope of the ΔOD vs. time plot was then used to calculate the Φ_{Δ} ,¹⁸¹ employing equation 1, where the correction factors I_{Ref} and I_{Sample} include the sum of total light intensities $I = I_0(1 - 10^{-\text{Abs}})$ absorbed by reference and sample within the irradiation range (350-450 nm), respectively.^{182,183}

$$\Phi_{\Delta}^{\text{Sample}} = \frac{\text{Slope}_{\text{Sample}} \times I_{\text{Ref}}}{\text{Slope}_{\text{Ref}} \times I_{\text{Sample}}} \Phi_{\Delta}^{\text{Ref}} \quad (1)$$

3.3 Results and discussion

3.3.1 Optoelectronic properties of SiO₂ adsorbed OPVs

Diffuse reflectance spectra for SiO₂-adsorbed OPVs revealed a broad absorption for all OPVs starting in the visible region (**Figure 3-4**). The Kubelka-Munk function was also calculated for

SiO₂-adsorbed OPVs from the reflectance spectra to estimate the ΔE values, where an increase in the gap starting from 0.15 eV was observed because of the ineffective overlapping of OPV molecules caused by the loss of $\pi \cdots \pi$ stacking interactions when dispersed on the silica surface (**Table 3-1**). Moreover, this lack of aggregation led to a blueshift in the emission maxima compared to the pure solid OPV samples. This phenomenon has already been described and can be attributed to a restricted molecular reorientation caused by the adsorption interactions with the SiO₂ surface, causing the radiative relaxation to occur from a higher energy level.¹⁸⁴

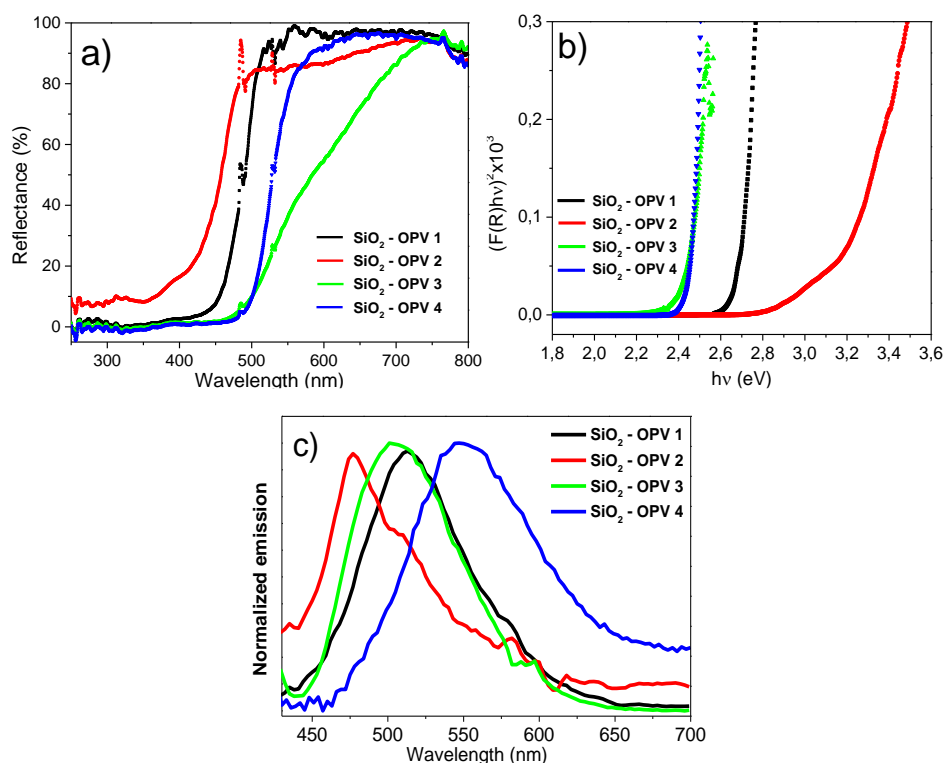


Figure 3-4: (a) Diffuse reflectance spectra, (b) Kubelka-Munk function, and (c) solid-state emission spectra of OPVs adsorbed in SiO₂.

Table 3-1: Comparative optoelectronic properties of **OPVs 1-4** in solid-state and adsorbed in SiO₂.

OPV		1	2	3	4
Solid state	ΔE (eV)	2.41	2.70	2.35	2.32
	λ_{em} (nm)	540	483	574	568
Adsorbed on SiO ₂	ΔE (eV)	2.69	3.15	2.51	2.47
	λ_{em} (nm)	513	477	501	547

3.3.2 Photostability of OPV systems

Preliminary assessment of OPVs stability was performed by direct irradiation of MeCN solutions (1×10^{-5} M) while monitoring the absorbance decrease of each compound at the λ_{\max} value. The experiments were carried out in an open atmosphere and under an inert atmosphere of N_2 , as depicted in **Figure 3-5**.

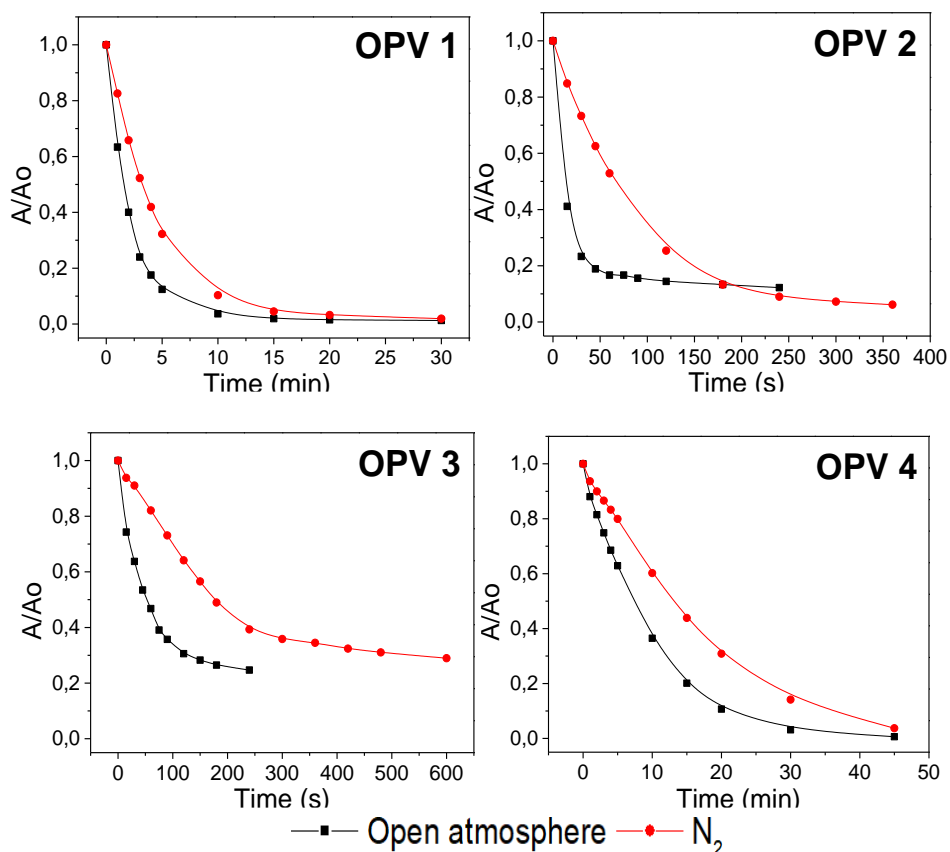


Figure 3-5: Absorption decay profile at λ_{\max} for **OPVs 1-4** in MeCN solution.

For experiments under nitrogen, a decrease in the rate of discoloration was observed, suggesting that oxygen plays an important role in molecular photodegradation for all OPV materials. Moreover, the presence of EWG (**OPVs 1** and **4**) in the flanking aryl rings of the OPV moiety seems to significantly delay the OPV photodegradation process compared to OPVs bearing EDG (**OPVs 2** and **3**).

Complete disappearance of the main visible absorption band for **OPVs 1** and **4**, was achieved after 20 minutes of irradiation, yielding a colorless solution. Upon examination of the UV-Vis

spectra for these solutions, an absorption band at 306 nm was observed, suggesting the presence of less-conjugated photoproducts or fragments. Oddly, **OPVs 2**, and **3** decreased their λ_{\max} absorbance in the visible region to a constant, but much lower value after only 200 seconds of irradiation along with the notorious formation of bands at 270 and 348 nm for **OPV 2**, and one band at 312 nm for **OPV 3** (**Figure 3-6**). This outcome clearly indicates that the initial **OPVs 2** and **3** are being rapidly transformed into other visible light-absorbing conjugated products as a result of the electronic effect exerted by -OH and -NH₂ groups in the OPV scaffold.

In all cases, the main absorption bands decreased upon irradiation. In contrast, new absorptions appeared in the UV region, creating isosbestic points for **OPVs 2**, **3**, and **4** as evidence of a clean interconversion towards photoproducts (**Figure 3-7**). However, for **OPV 1** a distortion in the isosbestic point is observed, suggesting different simultaneous photodegradation pathways. Moreover, the isosbestic points for the spectra sets under aerobic and anaerobic conditions do not match, except for **OPV 4**. This result is probably due to the formation of other products with different absorption profiles, once again indicating different photodegradation pathways.

¹H-NMR experiments confirmed the complete disappearance of the OPV peaks after irradiation, yielding a complex mixture of aromatic and deshielded aliphatic signals, also demonstrating the formation of multiple products. Additionally, the NMR spectra for experiments performed under aerobic and anaerobic conditions were not identical, confirming different photodegradation pathways (**Figure 3-8**).

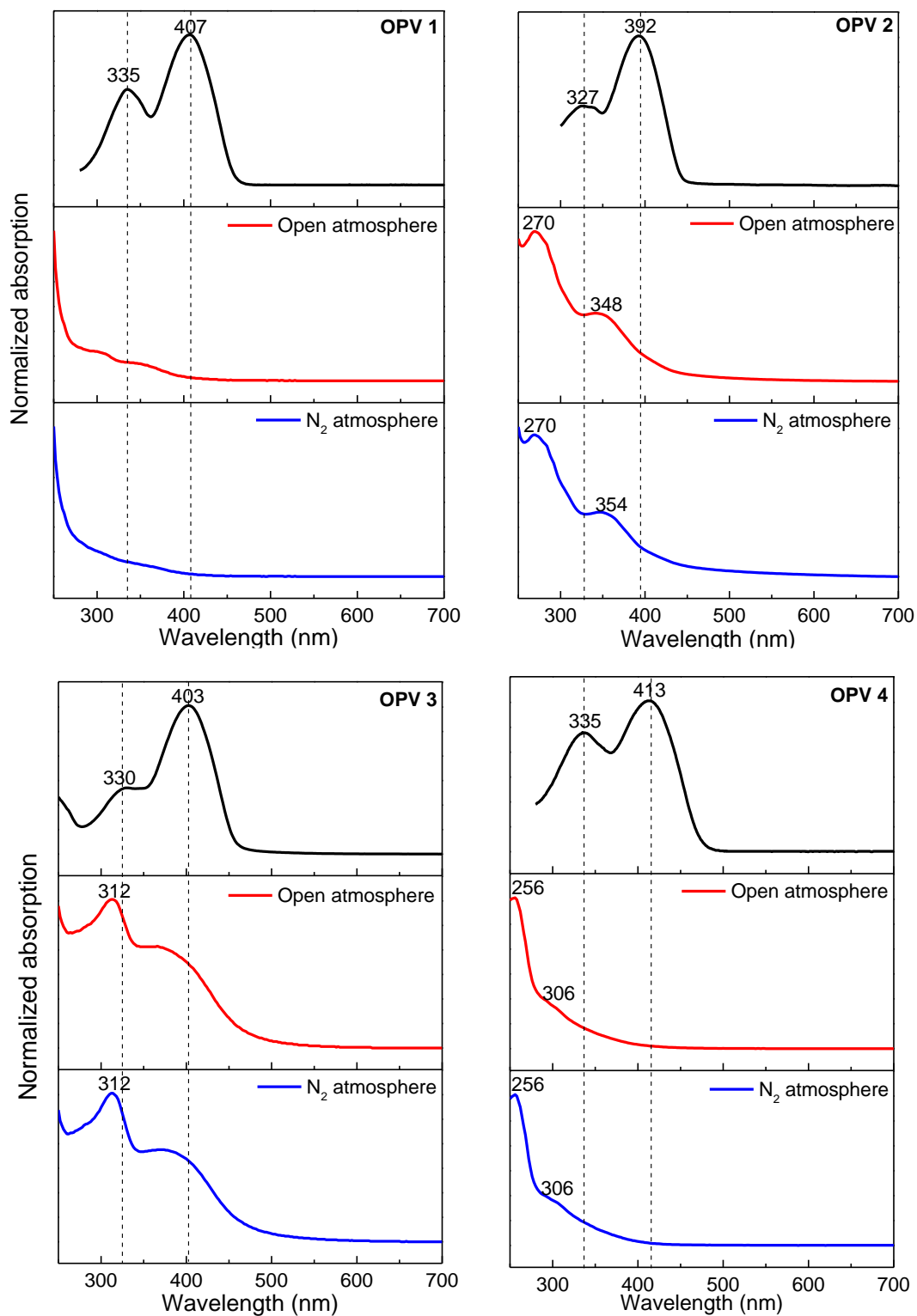


Figure 3-6: UV-Vis monitoring of stability for **OPVs 1-4** upon irradiation. Initial and final UV-vis spectra are shown for comparative purposes.

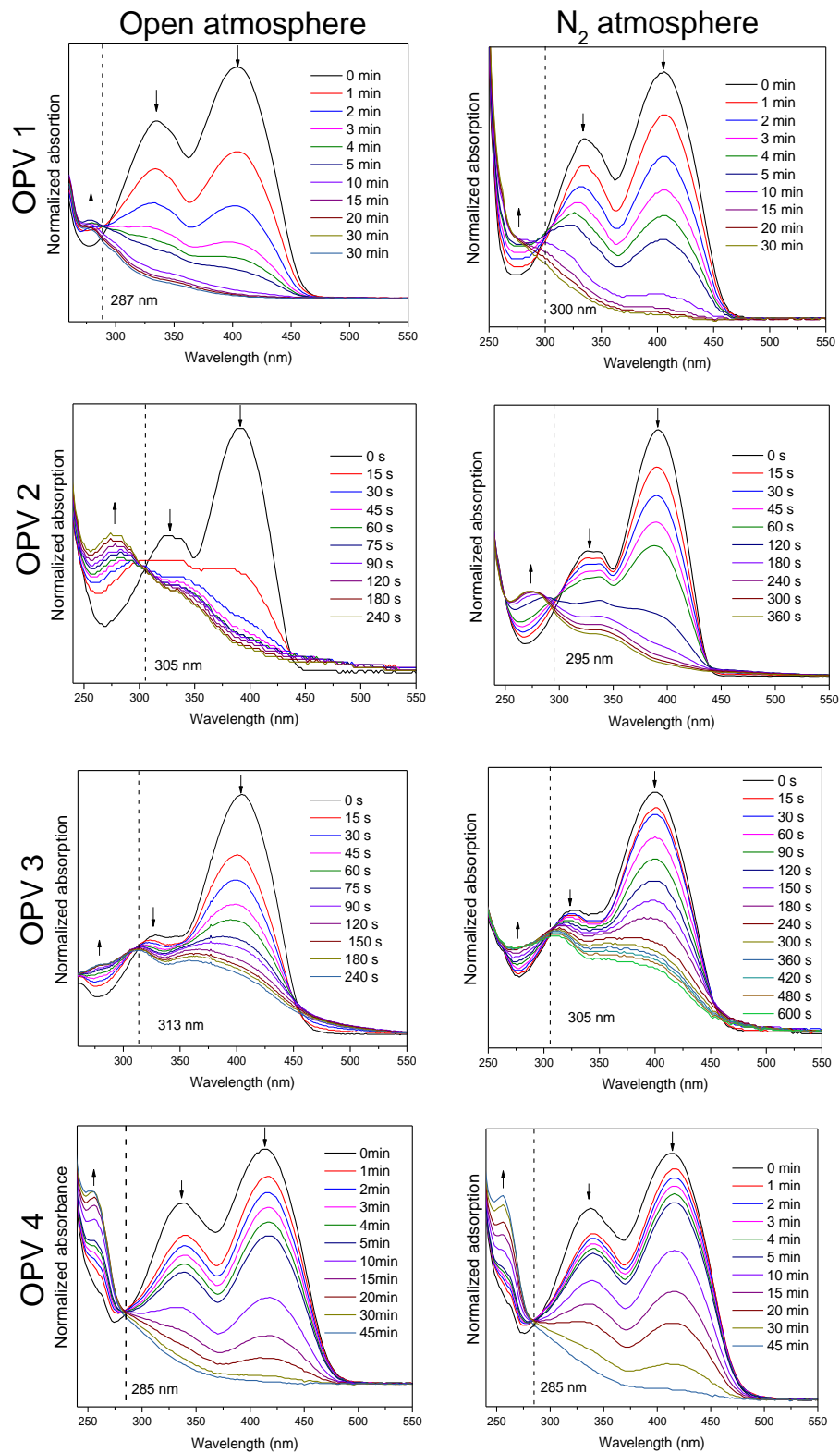


Figure 3-7: Spectral changes observed at various times for **OPVs 1-4** upon irradiation under open and nitrogen atmosphere. Isosbestic points are highlighted.

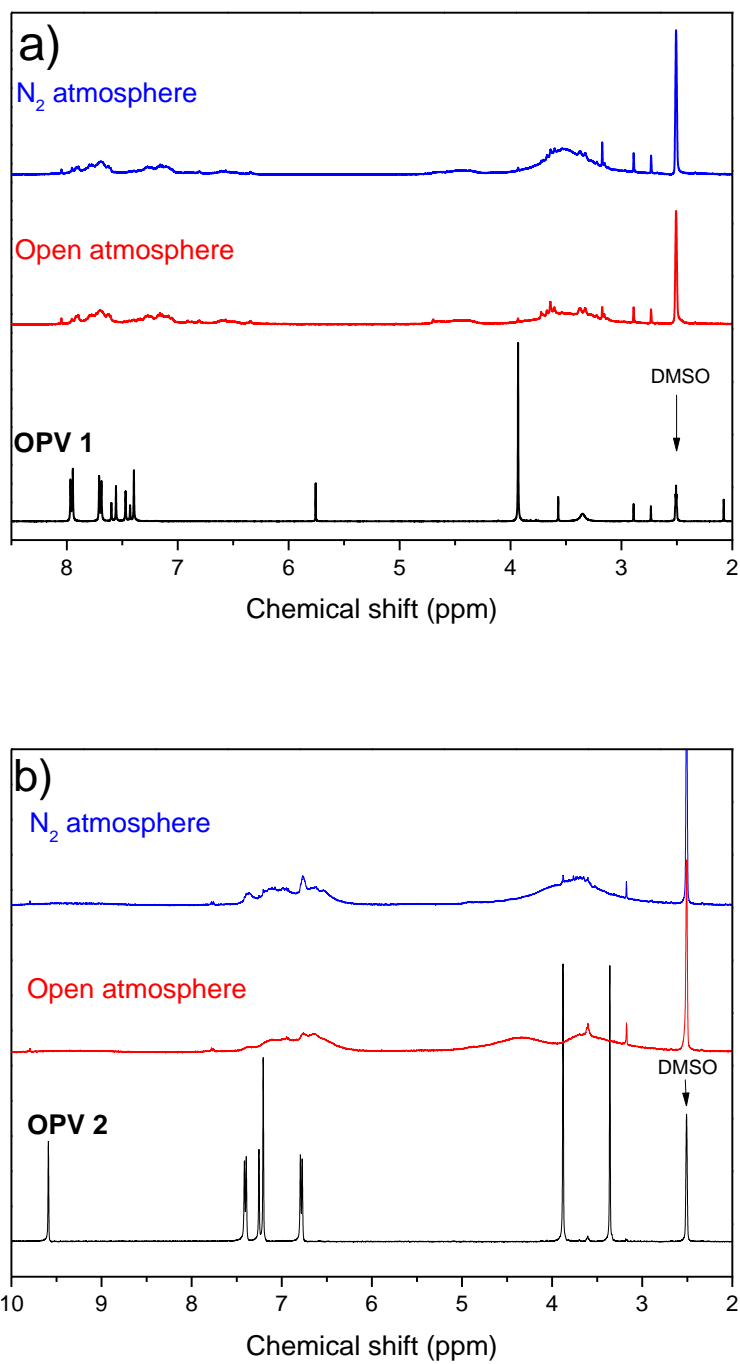


Figure 3-8: $^1\text{H-NMR}$ spectrum of (a) **OPV 1**, and (b) **OPV 2** after irradiation in open (red spectra) and nitrogen atmosphere (blue spectra).

ESI-IT-MS experiments were performed as an attempt to identify possible photodegradation products. For **OPV 1**, irradiated under open atmosphere, ions at 339, 325, 311, and 297 m/z confirmed OPV double bond cleavage reactions mediated by reactive oxygen species (ROS), with the formation of carbonyl and related compounds¹⁸⁵ along with the characteristic fragmentation of the methoxy group (**Figure 3-9**). MS spectrum for **OPV 1** irradiated under N₂ atmosphere provided similar peaks with a significantly decreased intensity, making the identification of other photodegradation products very challenging.

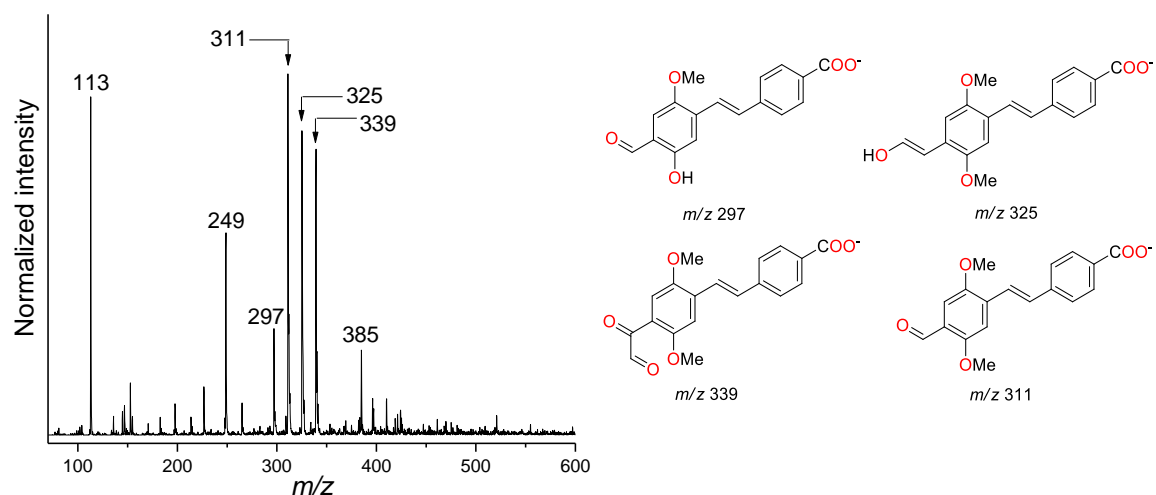


Figure 3-9: ESI (-)IT mass spectrum of **OPV 1** after irradiation under open atmosphere and structure of the identified degradation products.

Interestingly, for **OPV 3**, positive ion ESI-MS confirmed the formation of a unique OPV derivative, possibly a nitroso compound (**Figure 3-10**). This photoinduced transformation explains the remaining visible-light absorption observed in **Figure 3-5**. Also, the MS spectrum of the solution irradiated under N₂ shows unnumbered low-intensity peaks; in consequence, we were unable to provide chemical identification of additional degradation products under these conditions. A very similar chemical behavior was observed for **OPVs 2** and **4**, where the number of different products generated after irradiation for both aerobic and anaerobic experiments prevented us from obtaining an accurate description of the photodegradation process.

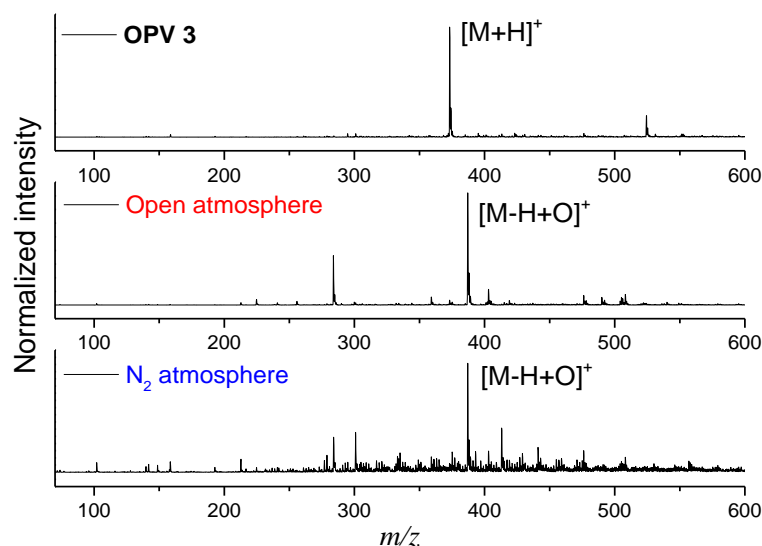


Figure 3-10: ESI (+)-IT mass spectra of **OPV 3** before and after irradiation under aerobic and anaerobic conditions.

3.3.3 Photocatalytic performance of OPVs

First, to evaluate the photostability of aqueous IC, a 50 μM solution was directly irradiated with the LED panel (350-450 nm, 3W). No change in the dye absorption profile was observed after 60 minutes, indicating that IC is stable under the employed irradiation conditions (**Figure 3-11a**, control). An additional control experiment was performed, adding silica gel to the IC solution, displaying no significant dye-adsorption (**Figure 3-11a**, SiO_2).

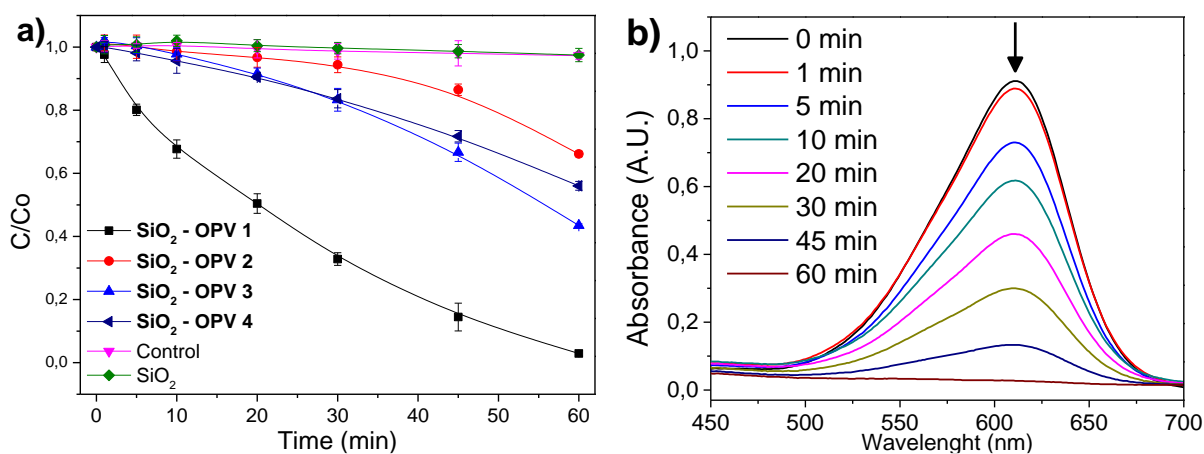


Figure 3-11: (a) SiO_2 -OPVs induced photodegradation of IC dye and (b) dye degradation profile at λ_{max} employing SiO_2 -OPV 1 as photocatalyst.

As expected, only when SiO₂-OPV systems were employed in the reaction, a decrease in the concentration of dye was observed, confirming the photocatalytic ability arises exclusively from the OPVs. Noteworthy, **SiO₂-OPV 1** exhibited the best photocatalytic performance among all the evaluated compounds, reaching a 98% dye removal within 60 minutes, yielding a colorless solution (**Figure 3-11a, SiO₂-OPV 1**). The time-dependent absorption spectrum of IC dye in the presence of **SiO₂-OPV 1** under irradiation is depicted in **Figure 3-11b**. The maximum absorption band for IC around 610 nm gradually decreases with irradiation following pseudo-first-order kinetics with a k_{ap} value of 0.041 min⁻¹, suggesting that the dye undergoes a degradation process that affects the molecular integrity of the chromophoric fragment.

To determine the chemical species involved in the photodegradation, benzoquinone (BZ, 2 mM) and potassium iodide (KI, 2 mM) were employed as scavengers for superoxide radical (O₂⁻) and holes (h⁺), respectively.¹⁸⁶ A decrease in the efficiency of the process using **SiO₂-OPV 1** was observed for both experiments, especially for BZ, suggesting that the process comprises superoxide radical as the main active species responsible for IC degradation (**Figure 3-12**). Hydroxyl radical (OH[•]) scavengers¹⁸⁷ (2 mM); isopropanol (i-PrOH), ethanol (EtOH), and methanol (MeOH) were also employed, unexpectedly achieving an improvement in the degradation process. This observation clearly indicates that these substances act as sacrificial electron donors, thus enhancing the electron/hole separation efficiency and promoting the electron transfer from **OPV 1** LUMO to dissolved oxygen molecules.¹⁸⁸

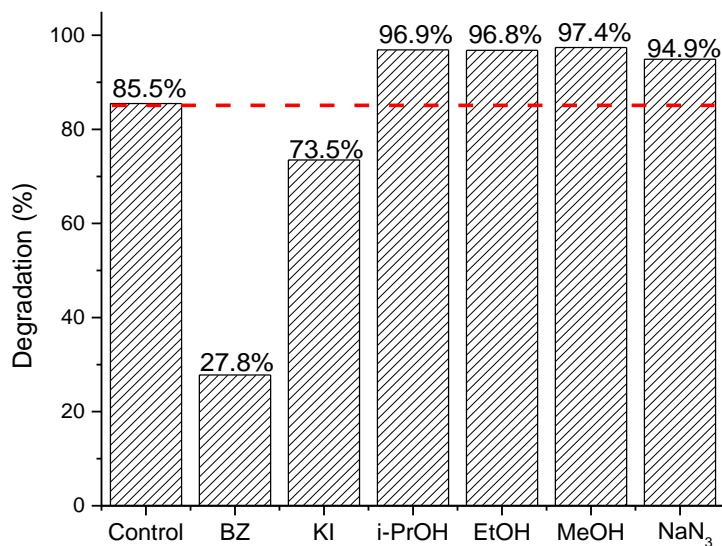


Figure 3-12: Scavengers effect on IC degradation with **SiO₂-OPV 1** after 45 minutes of reaction. Control: **SiO₂-OPV 1** without the addition of any scavenger.

To validate this hypothesis regarding the regeneration of the OPV HOMO level, an additional experiment was performed employing oxalic acid (2 mM), a well-known and very efficient sacrificial electron donor in photocatalysis.¹⁸⁹ A remarkable decrease in the reaction time was observed, achieving 97% degradation in only 5 minutes of irradiation (**Figure 3-13**). The efficiency of this OPV photocatalytic system in the IC discoloration is superior to that of TiO₂ (Degussa P25, 0.2 mg/3 mL) and follows an apparent zeroth-order reaction ($k_{ap}=0.22 \text{ mol}\cdot\text{L}^{-1}\cdot\text{min}^{-1}$). This indicates that the rate is now limited by a constant oxygen mass transfer from the solution to the photocatalyst surface, as a result of a significant increase in the regeneration of the HOMO level for **OPV 1** by means of oxalic acid oxidation.¹⁹⁰

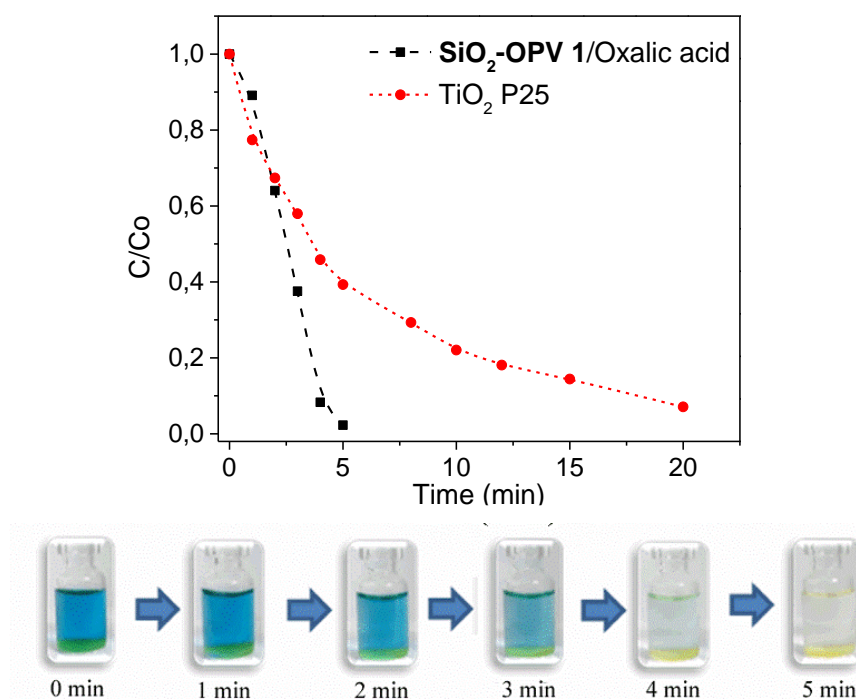


Figure 3-13: Color degradation profile of IC in the presence of **SiO₂-OPV 1** and oxalic acid (2 mM) as sacrificial electron donor.

Considering that singlet oxygen is a very reactive intermediate, specie previously reported as produced by analog OPV structures,^{93,191} its generation, was initially evaluated employing sodium azide (NaN₃) as a scavenger (**Figure 3-12**). However, an unexpected increase in the degradation efficiency suggested that ¹O₂ is not the main active species involved in the reaction. Moreover, it simultaneously prevented us from satisfactory establishing it as one of the photogenerated products.¹⁹² This particular phenomenon encouraged us to use 2-furoic acid as an alternative singlet oxygen probe.^{193,194} Method that involves a [2+4] cycloaddition reaction between the furan

moiety and singlet oxygen, generating an endoperoxide that decomposes into 5-hydroxy-5H-furan-2-one (**Figure 3-14**).¹⁹⁵

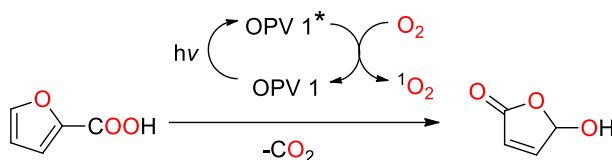


Figure 3-14: Reaction of 2-furoic acid with singlet oxygen.

The reaction can be followed by UV-vis using the furoic acid absorption maximum at 246 nm. After 30 minutes of irradiation of a furoic acid solution (1.0 mM) in a 3:1 water-methanol mixture, and **OPV 1** presence, a slight decrease (11%) in the absorption was achieved, suggesting that singlet oxygen is being generated in small amounts (**Figure 3-15**). The production of $^1\text{O}_2$ by **OPV 1**, as an additional mechanism that explains its photocatalytic ability, is attributed to the presence of the carbonyl group within the chromophore structure. It is well-known that C=O groups boost the efficiency of the $S_1 \rightarrow T_1$ intersystem crossing (ISC) according to El-Sayed's rules (e.g., $^1n, \pi^* \rightarrow ^3\pi, \pi^*$ is faster than $^1n, \pi^* \rightarrow ^3n, \pi^*$) which, in turn, results in the more efficient production of singlet oxygen via triplet state energy transfer.¹⁹⁶

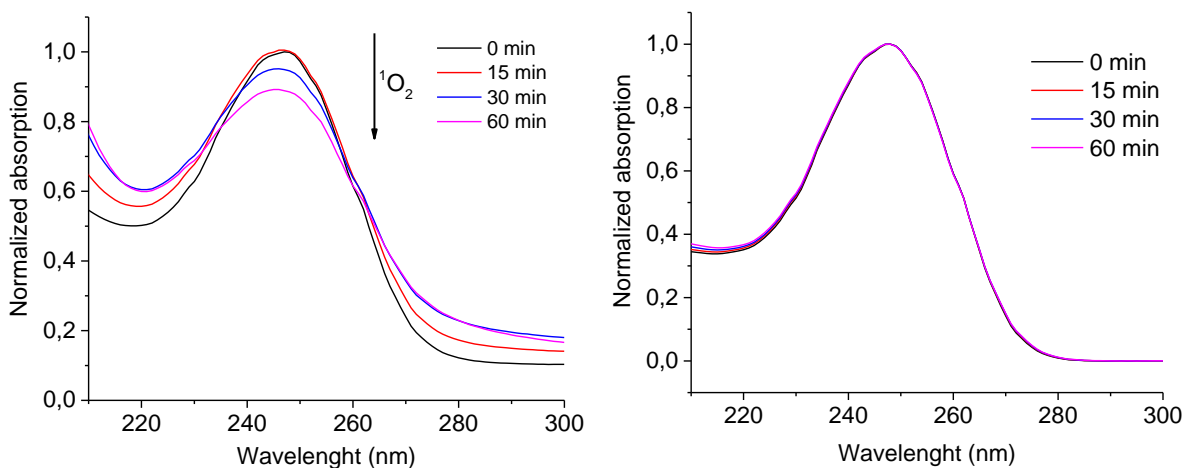


Figure 3-15: Singlet oxygen mediated degradation of furoic acid. Left: With **SiO₂-OPV 1**; Right: Control experiment (no photocatalyst).

To additionally corroborate this assumption, the Φ_{Δ} values estimated employing furfuraldehyde as chemical acceptor are summarized in **Table 3-2**. The results clearly indicate that **OPV 1**

exhibits the greatest $^1\text{O}_2$ production (**Appendix 7.5**). This outcome supports the observed photocatalytic behavior for this OPV system and reassures the pivotal role of this photogenerated substance in the degradation of the IC dye.

Table 3-2: Singlet oxygen quantum yields determined for **OPVs 1-4** in MeCN solution.

OPV	1	2	3	4
Φ_{Δ}	0.14±0.01	N.D.*	N.D.*	0.10±0.01

*N.D. Not determined. Fast photodegradation (50% in about 45 s) prevented the estimation of the Φ_{Δ}

To provide additional insight into the IC degradation pathway, negative mode ESI-MS was employed as a characterization technique. Initial analysis of pure IC was performed for comparative purposes showing ions at 210, 421, and 443 m/z associated with $[\text{IC}-2\text{Na}]^{2-}$, $[\text{IC}+\text{H}-2\text{Na}]^{-}$ and $[\text{IC}-\text{Na}]^{-}$, respectively (**Figure 3-16**). The colorless solution obtained after 60 minutes of irradiation established isatin-5-sulfonic acid (226 m/z) as the major IC degradation product. Tandem MS experiments confirmed the identity of this compound. Also, fragments at 216 and 244 m/z were identified as 4-amino-3-carboxybenzenesulfonate and 4-amino-3-(carboxycarbonyl) benzenesulfonate, respectively.^{197,198} No IC characteristic ions remained after the irradiation cycle, indicating total dye-degradation.

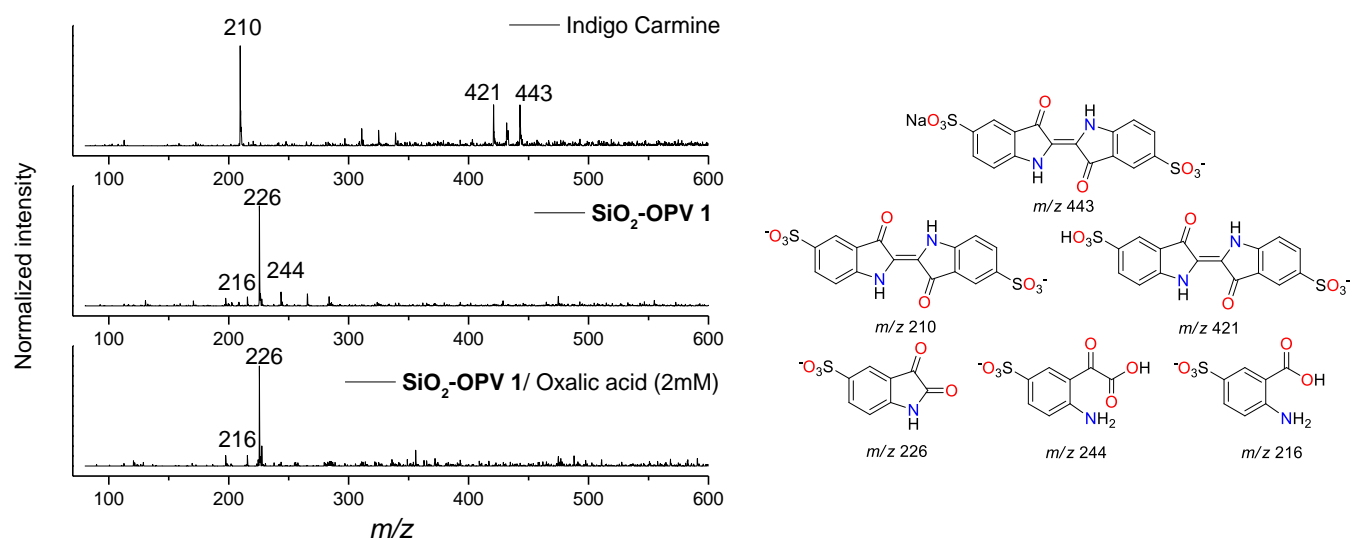


Figure 3-16: Negative mode ESI-MS spectra of IC and its photo-irradiated solutions in the presence of **SiO₂-OPV 1** and structure of most abundant ions observed in MS spectra.

A similar MS profile was obtained for the solution where oxalic acid was employed as a sacrificial electron donor for the photocatalytic process (with just 5 minutes of irradiation), being the isatin-5-sulfonic acid (226 m/z) the primary degradation product as well. Although oxalic acid may also modify the pH of the IC solution, promoting the superoxide chemical transformation into hydroxide radicals, no hydroxylated products were observed on the MS spectra for any of the experiments. Thus, the photocatalyzed formation of OH^\cdot radicals and their role in the IC degradation under the employed experimental conditions can be disregarded.

The photocatalytic activity of **SiO₂-OPV 1** was also tested in the absence of oxygen (**Figure 3-17**). The degradation profile under nitrogen atmosphere indicated that IC maintains a constant discoloration rate, attributed to a direct interaction of the dye with the excited molecular state of the OPV.

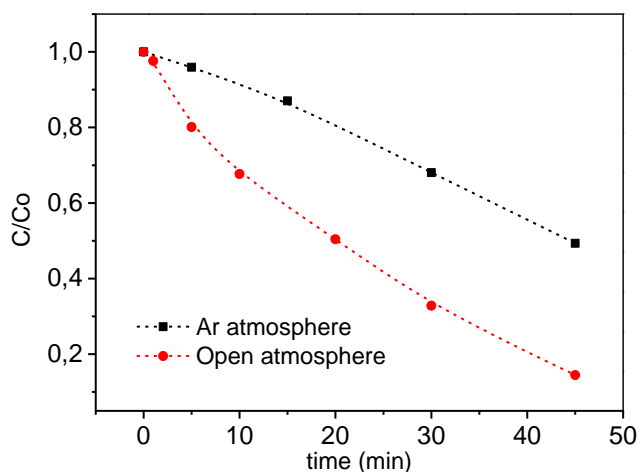


Figure 3-17: Effect of oxygen in the degradation profile of IC for **SiO₂-OPV 1**.

To accurately determine the nature of the process, ESI-IT MS was employed to establish the structure of the products after irradiation of the IC solution in the presence of **SiO₂-OPV 1** under an inert atmosphere (**Figure 3-18**). Interestingly, isatin-5-sulfonic acid (226 m/z) was again detected as the major photodegradation product along with a compound at 202 m/z with a considerable intensity that has not been previously detected in the experiments that were carried out under open atmosphere. This degradation product corresponds to the ion formed after continuous oxidative degradation of isatin-5-sulfonic acid (**Figure 3-18**) as it has been previously reported by Combariza *et al.*¹⁹⁸ This outcome suggests that direct and continuous oxidation of IC and its subsequent degradation products by **OPV 1** HOMO is contributing to the overall observed

dye degradation. Also, the absence of reduction products in the MS spectrum indicates that direct electron transfer from **OPV 1** to the IC dye does not occur. Nevertheless, the MS spectrum includes ions that belong to **OPV 1** and its degradation products, indicating desorption and migration of the photocatalyst to the aqueous phase is occurring, making the covalent functionalization of SiO_2 with the OPV moiety a plausible strategy to prevent this phenomenon and eventually help to maintain the molecular integrity in the conjugated scaffold.

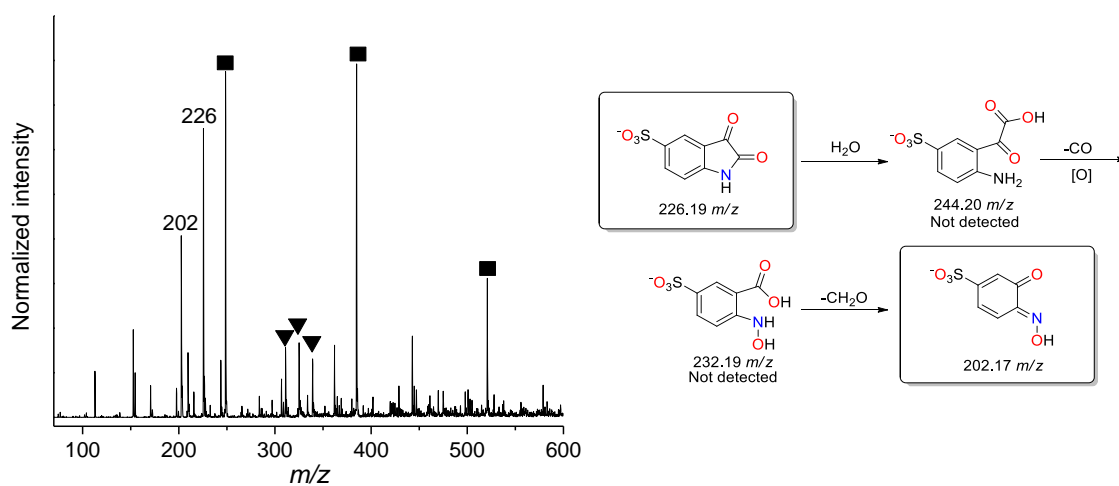


Figure 3-18: ESI (-)-IT mass spectrum of IC irradiated under inert atmosphere for **SiO₂-OPV 1** and proposed direct oxidative degradation pathway for isatin-5-sulfonic. Marked peaks belong to desorbed **OPV 1** (■) and **OPV 1** degradation products (▼).

The cyclic voltammetry results (**Table 2-6**) were employed to corroborate the absence of OH^\cdot radicals during the photocatalytic reaction. It can be seen that the formation of OH^\cdot is not possible, considering that the oxidation of water at pH 7 occurs at 2.31 eV (vs. NHE) and all the OPVs HOMO levels are located at more negative potentials (<1.81 eV vs. NHE) making the required electron transfer thermodynamically unfavored.¹⁹⁹ This finding indicates that these OPV materials are unsuitable for the mineralization of aqueous organic pollutants under the employed conditions (**Figure 3-19**).²⁰⁰

Likewise, all OPVs E_{LUMO} levels are located at lower potentials compared to the reduction of oxygen (-0.18 eV vs. NHE). Hence, an effective transformation of O_2 into superoxide radicals can be achieved in all cases. However, the proximity of the oxygen reduction potential and the LUMO level for **OPV 1**, implies that the electron transfer rate is the main factor for determining the

observed IC degradation efficiency. Interestingly, the HOMO-LUMO levels for IC, that were previously calculated by El-Mansy employing a DFT/B3LYP/SDD basis set,²⁰¹ indicate that the electron transfer from the dye to **OPV 1** and **OPV 4** is favored. This corroborates the experimental observation where IC oxidation can occur even under anaerobic conditions (**Figure 3-17**). This additional direct oxidative pathway clearly explains why **SiO₂-OPV 1** resulted in the best photocatalytic system for degrading indigo carmine.

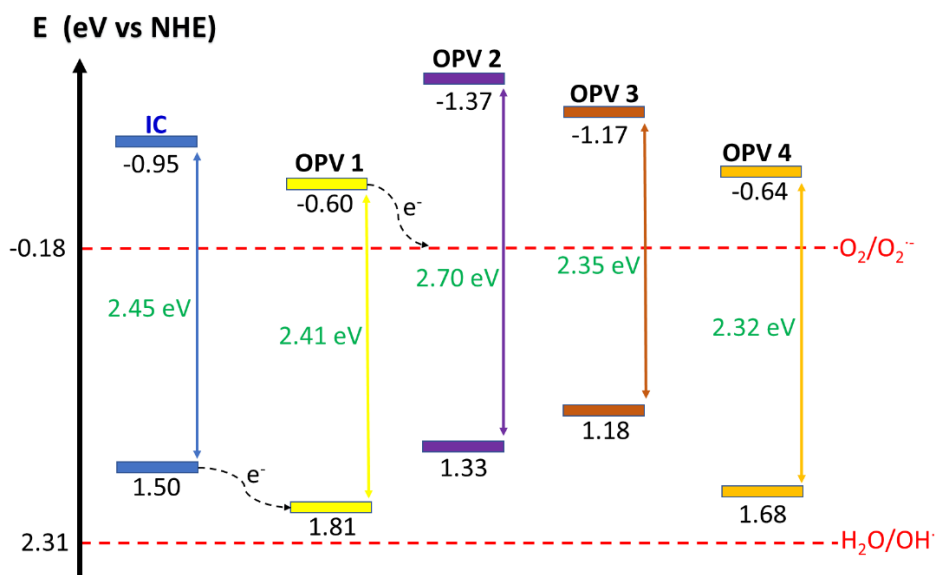


Figure 3-19: Relative HOMO-LUMO levels alignment for OPVs (vs. NHE) and IC. The LUMO position was estimated by adding the experimental ΔE value.

Moreover, these results help to understand better the previous experimental observation where KI was employed as a scavenger for holes (h^+). If effective hole regeneration takes place, the recombination rate of charge carriers decreases, prompting the electron transfer from the LUMO level of the excited **OPV 1** to O_2 . This increases the dye degradation performance via superoxide and singlet oxygen generation, as observed for alcohols and oxalic acid. In addition, since the release of OH^\bullet radicals at the HOMO level by direct oxidation of water does not occur, as previously demonstrated, the observed decrease in the IC degradation efficiency when KI is added to the mixture (**Figure 3-12**) cannot be attributed to the suppression of such radical species, but to the generation of oxidation products in the photocatalyst surface such as IO_3^- and I_2 . Species that could directly oxidize the OPV skeleton, decreasing its photocatalytic efficiency.¹⁸⁶ With all this information in hand, a schematic degradation pathway under aerobic conditions for indigo carmine is proposed (**Figure 3-20**). After irradiation and generation of the OPV excited

state, the photogenerated electron in the LUMO is transferred to oxygen, creating the superoxide radical. At the same time, IC oxidation can occur due to direct interaction with the HOMO. On the other hand, the excited OPV can also generate singlet oxygen by acting as a photosensitizer transferring energy from the triplet state.²⁰² Both oxygen species, superoxide radical and singlet oxygen, react with the IC causing cleavage of the double bond. Finally, adding oxalic acid to the solution rapidly regenerates the half-vacant HOMO via oxidation, making the OPV readily available for another irradiation cycle.

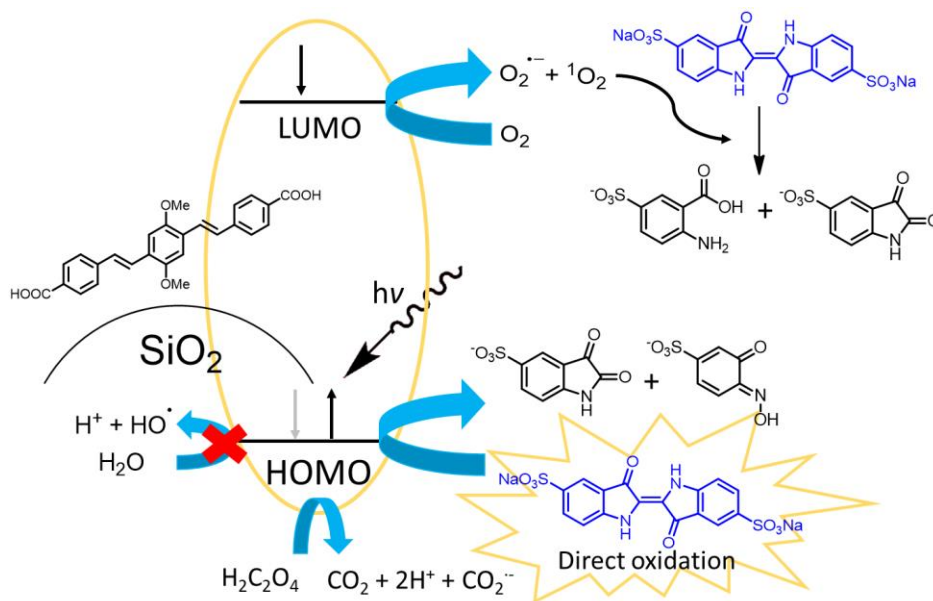


Figure 3-20: Photocatalytic schematic pathway for IC degradation in the presence of **SiO₂-OPV 1** and oxalic acid as sacrificial electron donor.

In addition to the photocatalytic performance, the reusability of **SiO₂-OPV 1** was evaluated by recycling experiments employing the best reaction conditions found in this study (**OPV 1** and oxalic acid, 2 mM). As shown in **Figure 3-21**, the dye degradation percentage is dramatically lowered after each irradiation cycle reaching only 20% for the third test. Although oxalic acid addition reduces the time exposure of the OPV to the photogenerated superoxide radical and singlet oxygen, the catalyst activity is strongly compromised due to molecular degradation.

By the results, it is evident that further stability improvements are required to enhance the efficiency of the photocatalyst after several irradiation cycles. Therefore, strategies such as chemical immobilization on solid supports and polymerization are proposed as rational approaches to overcome this issue. Notwithstanding, OPVs proved to be useful and interesting models for heterogeneous photocatalytic applications allowing easy and complete elucidation of the dye-degradation process.

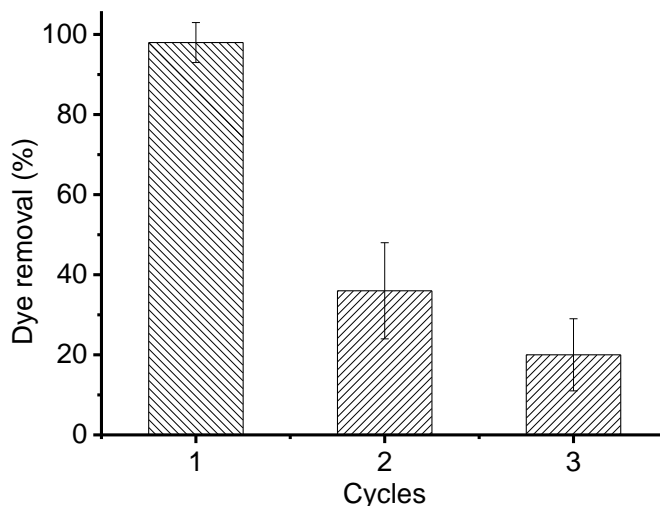


Figure 3-21: Reusability of **SiO₂-OPV 1** in the degradation of 50 μM IC aqueous solution.

3.4 Conclusions

Oligo (phenylene vinylene)s, adsorbed on silica gel, were evaluated for the first time as heterogeneous photocatalysts in the degradation of indigo carmine dye as the basis to provide a deeper understanding of the photochemical behavior for phenylene vinylene systems. The stability experiments indicated that ROS induce cleavage of the OPV conjugated structure. However, this feature can be improved by the insertion of EWG around the OPV scaffold.

It was demonstrated that the degradation of IC dye proceeds via the generation of superoxide radicals, singlet oxygen, and direct oxidation at the HOMO level of the OPV. Moreover, the addition of oxalic acid as a sacrificial electron donor provides a drastic improvement in the time required for the dye photodegradation by rapid HOMO regeneration, achieving superior discoloration efficiency compared to TiO_2 .

The HOMO energetic levels, estimated by cyclic voltammetry, indicated that the formation of hydroxyl radicals does not occur as corroborated by the organic products observed in the ESI-MS spectra and radical trapping assays. Thus, these materials are unsuitable for the mineralization of other organic pollutants under the employed conditions. However, the reusability tests, along with the identification of OPV double bond-cleavage fragments, and the use of sacrificial electron donors, served as the basis for ongoing research aimed to develop other phenylene vinylene systems with significant stability enhancement for dye-contaminated and other water treatment applications.

4. Photostability enhancement in OPV systems

Abstract

Chemical immobilization and polymerization were evaluated as strategies to enhance both the stability and photocatalytic performance of the best OPV system found in Chapter 3 (**OPV 1**). All the prepared materials were characterized and tested as photocatalysts in the degradation of indigo carmine dye under different irradiation conditions. All the prepared materials, except for **SiO₂/OPV 1**, displayed an improvement in the photodegradation process, where **TiO₂/OPV 1** exhibited a remarkable photocatalytic activity under white light illumination. It was also confirmed that superoxide radical ($O_2^{\cdot-}$), 1O_2 , and direct oxidation are responsible for dye degradation in most cases. However, for **TiO₂/OPV 1** an additional direct reductive degradation pathway for IC was identified. The reusability tests established that **TiO₂/OPV 1** and **Pol-1** materials retain up to 84% and 96% of their photocatalytic activity throughout the first five cycles, respectively.

4.1 Introduction

Despite the easily tunable optoelectronic properties of pure-organic photocatalytic systems that have led to exceptionally lower radiative requirements when compared to TiO₂-based materials, several photostability issues, including photobleaching or solvolytic attack in the reaction medium, arise as the major limitation that has prevented these metal-free systems from being widely explored for light-driven catalysis.²⁰³ In this sense, phenylene vinylenes are not the exception considering that the vinyl bridging bond makes them prone to a rapid conjugation loss via interaction with reactive oxygen species and the generation of alkoxy radicals.^{49,52,55} Additionally, regarding fully conjugated PPVs, it has been demonstrated that the singlet oxygen reaction rate increases when the chain length is enlarged.⁵¹

Some strategies to improve the photostability of PV systems have been studied and consist mainly in the insertion of EWG such as -CN, -F, -NO₂ and -CF₃ around the conjugated scaffold,^{61,63,64,66} and the sp³-bridged rigidification of the PV backbone,⁶⁸ as techniques to reduce

the ROS reaction rate. Moreover, the preparation of blends with inorganic materials such as TiO₂ via physical methods successfully prevented the oxidation of the vinyl fragments acting as oxygen diffusion barriers.^{6,82} Surprisingly, the above-mentioned approaches have been chiefly implemented and projected as elements of design for PV-based photovoltaic cells, lasers, LEDs, and other sensory applications. Thus, the assessment of their influence in the PV photocatalytic activity remains markedly unexplored.

In this chapter, the grafting of **OPV 1** (the best photocatalytic system found in previous chapters) onto SiO₂ and TiO₂ surfaces and the copolymerization of this same OPV scaffold with aromatic and aliphatic molecular spacers are explored as stability, and reusability enhancement approaches towards the photochemical degradation of indigo carmine dye.

4.2 Experimental section

4.2.1 Materials

Sigma-Aldrich was used as a supplier unless otherwise indicated. OPVs were synthesized according to the procedure described in Chapter 2. Indigo carmine (C.I. 73015) for clinical diagnosis (>98%) was supplied from Panreac. TiO₂ Degussa P25 Aeroxide® (<45 microns, S_{BET} 35-65 m²/g) was obtained from Acros Organics. Silica gel 60 (Macherey-Nagel GmbH & Co., 0.063-0.200 mm, S_{BET} 480-540 m²/g) was employed for photocatalyst preparation. Oxygen-sensitive reactions were performed under an atmosphere of dry argon or nitrogen. Distilled, deionized (MilliQ purification systems) water was used for photocatalytic experiments.

4.2.2 Analytical techniques

An Amazon X (Bruker) ESI-IT, operating in alternate positive/negative ion modes at 300°C and 4500 V in the capillary, was used for MS data collection. Nitrogen was used as nebulizer gas with an influx of 8 L/min and 30 psi. MeCN and MeOH (HPLC grade) were used for sample dilution. ¹H-NMR spectra (400 MHz) were obtained from a Ultrashield-400 Bruker spectrometer using DMSO-d₆ as solvent. Chemical shifts are reported in ppm (δ). The absorption spectra were recorded using a Thermo Scientific Evolution 300 UV-Vis spectrophotometer. The emission spectra were measured using a PTI QuantaMaster™ 40 spectrofluorometer adapted to an integrating sphere. Diffuse reflectance measurements were performed on an Ocean Optics spectrometer adapted to a reflection probe. IR spectra were recorded on an FTIR Thermo

Scientific Nicolet iS10 spectrophotometer employing the KBr pellet method for transmission measurements. Raman spectra were recorded using a Thermo Scientific DXR Raman Microscope equipped with an excitation laser at 532 nm or 780 nm with a power level of 20 mW. The laser beam was focused on the sample using a 50x objective. The EEM was acquired using the Horiba Duetta Fluorescence and Absorbance Spectrometer, and inner-filter effects and Rayleigh scattering were corrected using EzSpec™ software. The N₂ adsorption-desorption analysis was carried out with an ASAP 2020 MICROMERITICS equipment at 77 K with a previous degassing of the sample at 300 °C for 4 h. The BET model ($0.05 \leq P/P^\circ \leq 0.20$) was used to calculate the specific surface area of the materials. The mean pore diameter was estimated by the BJH method applied to the adsorption branch. The total pore volume was determined from the isotherms at $P/P^\circ = 0.95$. Thermogravimetric analyses (TGA) were performed on a TA instrument Q50 with a heating rate of 10 °C/min under nitrogen atmosphere (60 mL/min). DSC was performed on a TA Instruments DSC Q-2000 using cooling and heating rates of 10 °C/min. X-ray diffraction was performed in a BRUKER D8-ADVANCE diffractometer. GPC (HPLC) analyses were performed on a Thermo Scientific™ Ultimate™ 3000 LC system (Thermo Fisher Scientific, Milan, Italy), coupled to a variable wavelength detector Dionex UltiMate 3000 fixed at 400 nm. The samples were separated by passage through a Phenogel 1000 Å column (5 µm, 300 x 7.8 mm, Phenomenex, Torrance, CA, USA). The temperature of the column was kept at 35 °C. The mobile phase was HPLC-grade THF (Merck Millipore) at a flow rate of 1.0 mL/min, using 200 µL as the injection volume. Micrographs were obtained with a TESCAN VEGA 3 Scanning Electron Microscope (SEM). Solid-state ¹³C CP/MAS NMR spectra were acquired in a Varian UI300 spectrometer at a ¹³C resonance frequency of 75.47 MHz with a 4-mm probe. The CP technique was applied during Magic Angle Spinning (MAS) of the rotor at 10 kHz. The contact time was 1 ms and 3500 scans were accumulated using a 2 s delay. XPS spectra were measured on a Leybold-Heraeus EA 11 spectrometer equipped with a monochromatic Al Kα X ray source (1486.6 eV) operating at 350 W. The peak positions were referenced by adjusting the binding energy of the Ti2p_{3/2} peak of TiO₂ at 458.8 eV and the Si2p peak of SiO₂ at 103.3 eV to correct for the charging effect during acquisition.^{204,205}

4.2.3 Chemical modifications of OPV 1

As previously outlined, to address the photostability issues inherent to the OPV framework, the initially proposed structural modification embodies the chemical immobilization of **OPV 1** into SiO₂ and TiO₂, as solid supports. The materials preparation methodology is herein presented.

Drying process of solid supports

The specified amount of SiO₂ or TiO₂ was added to a Schlenk flask containing a magnetic stirrer followed by heating at 150 °C under vacuum (33 kPa) for 24 hours and 250 rpm. Then, the flask was filled with argon and allowed to cool to ambient temperature. The solids were immediately employed in the surface modification reactions.

OPV 1 grafted SiO₂ (SiO₂/OPV 1)

A toluene solution (30 mL) containing 1.07 mL (0.829 g, 5.14 mmol) of HMDA was added to previously dried SiO₂ (1.0 g, estimated 2.57 mmol of -OH/g). The suspension was stirred at 110 °C for 24 h, filtered and the resulting solid was washed thoroughly with toluene (3 x 30 mL) and dried under vacuum. This recovered white solid was then suspended in 30 mL of dry 1,4-dioxane under inert atmosphere and 1.106 g (2.57 mmol) of **OPV 1** were added. The mixture was stirred at 100 °C for 24 h. The light-yellow solid product was filtered, washed with 1,4-dioxane (3 x 30 mL) and dried under vacuum. FTIR (KBr, cm⁻¹): 1726 (C=O), 1629 (ν_{as} COO), 1396 (ν_s COO). Loading: 0.056 mmol/g of OPV determined by TGA.

OPV 1 grafted TiO₂ (TiO₂/OPV 1)

A toluene solution (30 mL) containing 0.21 mL (0.161 g, 1 mmol) of HMDA was added to previously dried TiO₂ (1.0 g, estimated 0.5 mmol of -OH/g). The suspension was stirred at 110 °C for 24 h, filtered and the resulting solid was washed thoroughly with toluene (3 x 30 mL) and dried under vacuum. This recovered white solid was then suspended in 30 mL of dry 1,4-dioxane under inert atmosphere and 0.215 g (0.5 mmol) of **OPV 1** were added. The mixture was stirred at 100 °C for 24 h. The yellow solid product was filtered, washed with 1,4-dioxane (3 x 30 mL) and dried under vacuum. FTIR (KBr, cm⁻¹): 1709 (C=O), 1622 (ν_{as} COO), 1384 (ν_s COO). Loading: 0.049 mmol/g of OPV determined by TGA.

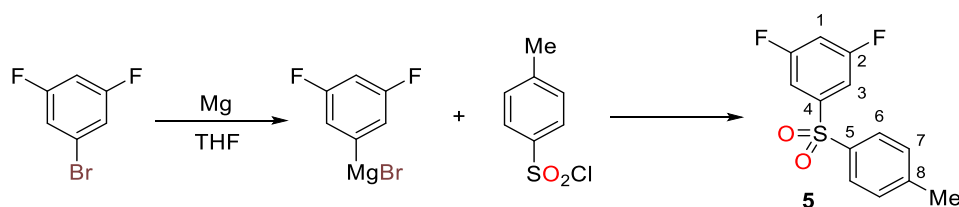
The second photostability enhancement approach entails the **OPV 1** copolymerization with rigid and flexible spacers. The synthesis of one of the rigid polymerization precursors and the complete copolymerization methodology are displayed as follows.

Polymerization

Synthesis of 1,3-difluoro-5-tosylbenzene, precursor 5

Metallic magnesium (0.210 g, 8.66 mmol), previously grounded in a mortar, was added to a 100 mL round bottom flask under nitrogen and covered with dry THF (approx. 10 mL). Then, a small portion (approx. 1 mL) of a 1-bromo-3,5-difluorobenzene (1.594 g, 8.25 mmol) solution in 5 mL of

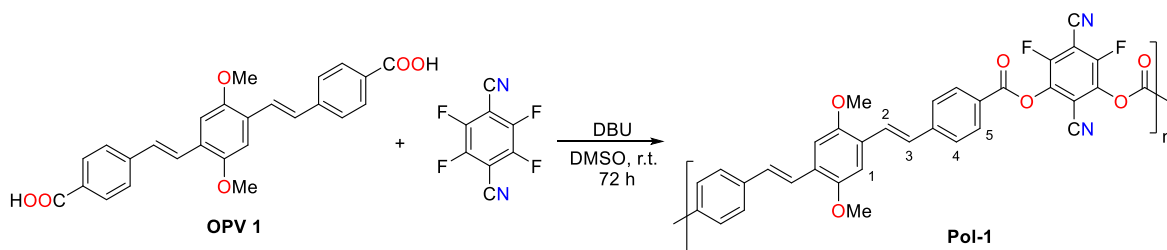
THF was slowly added. To initiate the reaction, a gentle warm was provided. Once the reaction had started, complete and very slow addition of the 1-bromo-3,5-difluorobenzene was carried out. The reaction mixture was then stirred at room temperature for 4 h. Next, a solution of tosyl chloride (1.484 g, 7.8 mmol) in 6 mL of THF was added, and the mixture was stirred for 12 h at room temperature and then heated to reflux for an additional 2 h (**Scheme 4-1**). After reaction completion, the flask was cooled to room temperature and 50 mL of water was poured. The crude product was extracted with diethyl ether (3 x 20 mL) followed by washing cycles with HCl (2%), NaHCO₃ (5%) and distilled water. The combined organic layers were dried over anhydrous MgSO₄ and the solvent was removed in vacuum. The product was then purified by column chromatography employing SiO₂ and a n-hexane/ ethyl acetate 6:1 mixture as eluent. White solid. m.p. 116-118 °C (Lit. 111-112 °C)²⁰⁶; yield 1.075 g (51%). IR (ATR, cm⁻¹): 3086, 2970, 1601, 1328 (ν S-O), 1153 (ν S-O), 985, 860, 810. ¹H-NMR (400 MHz, CDCl₃) δ (ppm): 2.42 (s, 3H Me), 6.98 (tt, $J=8.4$; 2.2 Hz, 1H H-1), 7.34 (d, $J=8.2$ Hz, 2H H-7), 7.41-7.48 (m, 2H H-3), 7.82 (d, $J=8.2$ Hz, 2H H-6). ¹³C-NMR (100 MHz, CDCl₃) δ (ppm): 21.7 Me, 108.8 (t, $J=25.1$ Hz) C-1, 111.2 (dd, $J=19.7$; 8.3 Hz) C-3, 128.2 C-6, 130.4 C-7, 137.4 C-5, 145.3 C-8, 145.6 (t, $J=8.1$ Hz) C-4, 163.0 (dd, $J=255.2$; 11.5 Hz) C-2 (**Appendix 7.4**).



Scheme 4-1: Synthesis of precursor 5.

Synthesis of Pol-1

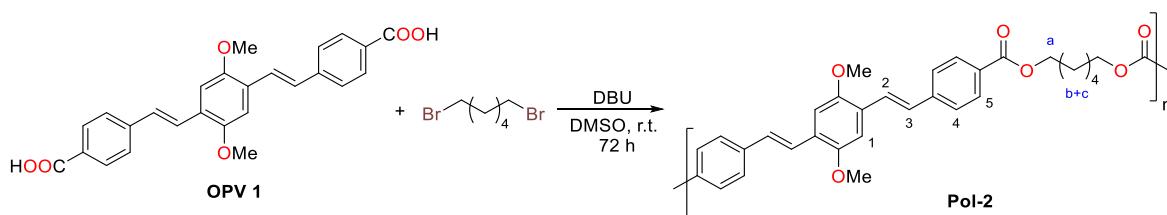
In a Schlenk-type 50 mL round bottom flask **OPV 1** (0.259 g, 0.6 mmol) and tetrafluoroterephthalonitrile (0.120 g, 0.6 mmol) were dissolved in 3 mL of DMSO. After 5 minutes of nitrogen purge, the flask was septum capped. Then, 1,8-diazabicyclo[5.4.0]undec-7-ene (DBU) (0.182g, 1.2 mmol) was slowly added via syringe. The reacting mixture was stirred for 72 h at room temperature (**Scheme 4-2**). After the reaction was completed, 15 mL of water was added to induce precipitation of a yellow solid that was filtered, thoroughly washed with distilled water (3 x 15 mL) and dried for 6 hours at 80 °C. Yield: 0.324 g. IR (ATR, cm⁻¹): 3045, 2936, 2226 (ν CN), 1703 (ν C=O), 1601, 1491, 1242, 1209, 1176, 1041, 968. ¹H-NMR (400 MHz, DMSO-d₆) δ (ppm): 3.92 (s OMe), 7.33-7.64 (m H_{1,2,3}), 7.70 (d H₄), 7.95(d H₅). Elemental analysis C, 68.8%; H, 5.3%; N, 4.4%.



Scheme 4-2: Synthesis of **Pol-1**.

Synthesis of Pol-2

In a Schlenk-type 50 mL round bottom flask **OPV 1** (0.259 g, 0.6 mmol) and 1,6-dibromohexane (0.146 g, 0.6 mmol) were dissolved in 3 mL of DMSO. After 5 minutes of nitrogen purge, the flask was septum capped. Then, DBU (0.182 g, 1.2 mmol) was slowly added via syringe. The reacting mixture was stirred for 72 h at room temperature (**Scheme 4-3**). After the reaction was completed, 15 mL of water was added to induce the formation of a yellow suspension. The formed solid was recovered by centrifugation (25000 rpm, 10 min), redissolved in THF and precipitated by the addition of diethyl ether. The final product was recovered after freeze-drying. Yield: 0.247 g. IR (ATR, cm^{-1}): 3049, 2931, 2856, 1711 (ν C=O), 1601, 1493, 1464, 1410, 1273 (ν C-O_{ester}), 1211, 1176, 1103 (ν C-O_{ester}), 1039, 964. $^1\text{H-NMR}$ (400 MHz, CDCl_3) δ (ppm): 1.40-1.85 (m $\text{H}_{\text{b+c}}$), 3.91 (s O_{Me}), 4.34 (s H_{a}), 7.08-7.16 (m $\text{H}_{1+\text{H}3}$), 7.50-7.62 (m $\text{H}_{2+\text{H}4}$), 8.00 (d H_5). Elemental analysis C, 62.8%; H, 7.2%.

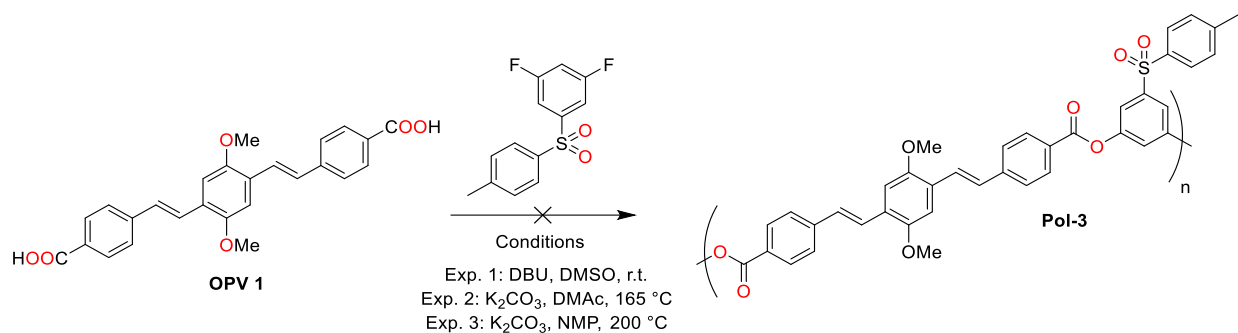


Scheme 4-3: Synthesis of **Pol-2**.

Synthesis of Pol-3

In a Schlenk-type 50 mL round bottom flask **OPV 1** (0.259 g, 0.6 mmol) and precursor **5** (0.161 g, 0.6 mmol) were dissolved in 3 mL of DMSO. After 5 minutes of nitrogen purge, the flask was septum capped. Then, DBU (0.182 g, 1.2 mmol) was slowly added via syringe. The reacting mixture was stirred for 72 h at room temperature (**Scheme 4-4**). After the reaction was completed, 15 mL of water was added. Nevertheless, no product was observed and only the starting materials

were recovered after the process. Additional efforts were made to force reactivity and included the use of K_2CO_3 as base and the use of NMP and DMAc as solvents in combination with temperatures of 200 and 165°C, respectively. Regardless of the harsh reaction conditions, no **Pol-3** product was recovered.



Scheme 4-4: Attempts for **Pol-3** synthesis.

4.2.4 Photocatalytic IC degradation

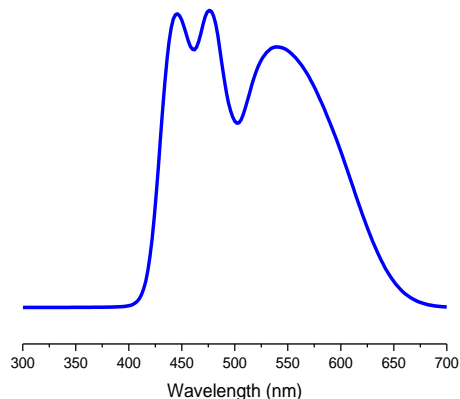


Figure 4-1: White LED panel emission spectrum.

The IC degradation reactions were performed on an LED-based panel type photoreactor equipped with: 1) a 3 W white LED array as irradiation source within the visible portion of the spectrum (400-700 nm) as shown in **Figure 4-1**, or 2) a 3W UV-Vis LED array (350-450 nm) previously used in Chapter 3. In a typical dye degradation experiment, the specified amount of catalyst was suspended on 3 mL of 50 μM aqueous IC solution. For **SiO₂/OPV 1** catalyst, the experiments were carried out on a UV-Vis quartz cuvette to facilitate direct irradiation and monitoring of the IC solution color intensity. For **TiO₂/OPV 1** and polymer catalysts, 4 mL glass

vials were employed. After irradiation, the catalyst was allowed to settle in darkness for 30 seconds and 1 mL of the supernatant solution was extracted via syringe and filtered employing 0.22 μm PTFE membranes prior to the absorbance measurement (**Figure 4-2**). The irradiated solution in each glass container was measured only once. Thus, different vials were employed to follow the color intensity of the IC solution at each time interval. In all cases, the suspension was left for 15 min in darkness to ensure the adsorption equilibrium was reached preceding irradiation. The temperature was maintained constant at 20 °C using circulated water, and the experiments were performed under a continuous low-stirring regime (100 rpm).

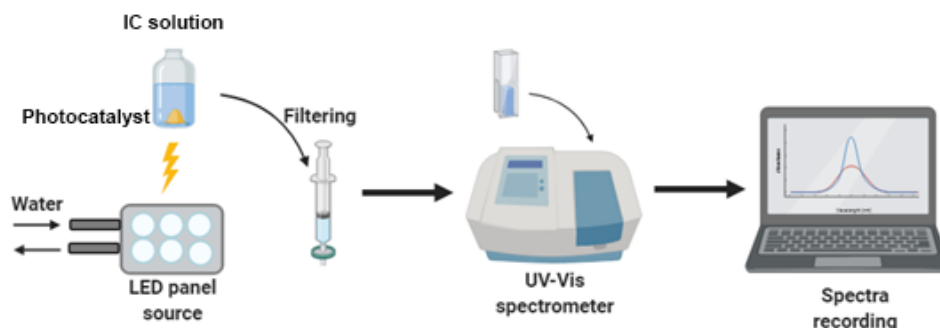
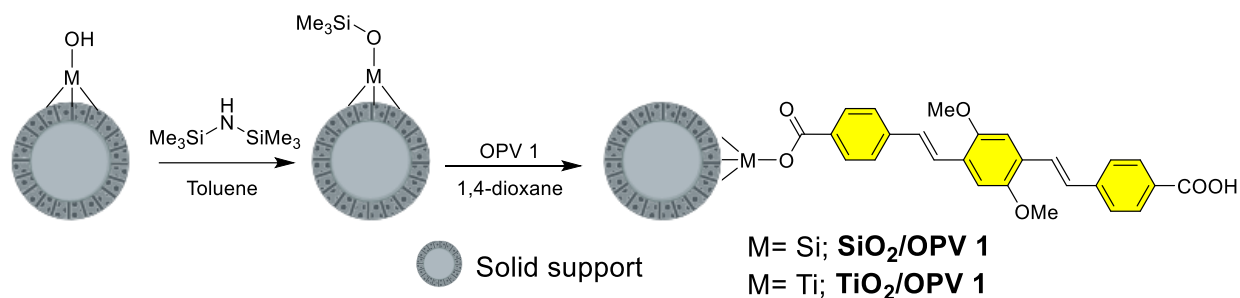


Figure 4-2: Experimental set-up for IC degradation employing $\text{TiO}_2/\text{OPV 1}$ and polymer catalysts.

4.3 Results and discussion

4.3.1 Synthesis and characterization of OPV grafted SiO_2 and TiO_2

Considering that **OPV 1** displayed the best photocatalytic performance in the IC degradation (Chapter 3), it was selected to be grafted onto SiO_2 and TiO_2 surfaces as a strategy to prevent migration of the conjugated material to the aqueous dye solution and simultaneously enhance its (photo)stability and reusability. The synthetic procedure involved the modification of the surface via trimethylsilylation of -OH groups by reaction with hexamethyldisilazane (HMDS) and subsequent reaction of the solid material with the OPV as depicted in **Scheme 4-5**.²⁰⁷



Scheme 4-5: Synthesis of **OPV 1** grafted SiO_2 and TiO_2 .

Evidence of the OPV anchoring onto the SiO_2 and TiO_2 surfaces is provided by the FTIR spectra (**Figure 4-3**). The carbonyl ($\text{C}=\text{O}$) group stretch signal in the decorated surfaces is broadened and shifted to higher wavenumber values when compared to the $\text{C}=\text{O}$ vibration band found for **OPV 1**, suggesting the formation of an ester-type bond. Moreover, the symmetric ν_s and asymmetric ν_{as} stretching modes of the carboxylate group were observed, and their difference ($\Delta\nu_{as-s}$) value $> 200 \text{ cm}^{-1}$ clearly suggest a monodentate binding mode in both cases as expected.²⁰⁸

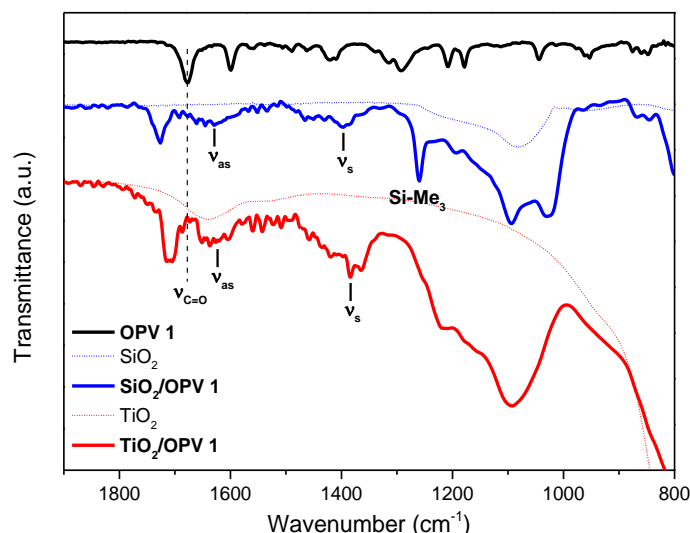


Figure 4-3: FTIR spectra (KBr disc) of **OPV 1**, modified SiO_2 and TiO_2 (solid lines) and pristine SiO_2 and TiO_2 (dashed lines).

Table 4-1: FTIR (KBr disc) carbonyl vibrations for **OPV 1** and prepared photocatalysts.

FTIR signals (cm^{-1})		$\nu_{\text{C}=\text{O}}$	$\nu_{as}(-\text{COO})$	$\nu_s(-\text{COO})$	$\Delta\nu_{as-s}$
	OPV 1	1676	---	---	---
OPV derivative	$\text{SiO}_2/\text{OPV } 1$	1726	1629	1396	233
	$\text{TiO}_2/\text{OPV } 1$	1709	1622	1384	238

Raman spectroscopy is a powerful tool to characterize the crystalline quality of TiO_2 (**Figure 4-4**). The anatase phase has a tetragonal structure with six active Raman modes: E_g (144, 197, and 639 cm^{-1}), B_{1g} (399 and 519 cm^{-1}), and A_{1g} (519 cm^{-1}) clearly identified in the Raman spectra. A very low-intensity band at 455 cm^{-1} was also observed, related to the E_g mode of the rutile phase.^{209,210} These five Raman peaks are characteristic of TiO_2 P25, as a mixture of anatase (80%) and rutile (20%).^{211,212} The Raman spectrum for **TiO₂/OPV 1** contains vibration bands associated with the carbonyl group (C=O) around 1632 cm^{-1} and one signal of the carboxylate stretching mode of the OPV structure along with the characteristic vibrations bands of the TiO_2 support. The observed shift from 1413 cm^{-1} in pure **OPV 1** to 1407 cm^{-1} in **TiO₂/OPV 1**, of the carboxylate stretching mode, suggests the formation of the desired unidentate configuration between the carboxylate and the Ti atom in the surface.²¹³ Interestingly, the Raman spectrum for **SiO₂/OPV 1** did not display any OPV peaks. However, it should be disclosed that the SiO-H signal's disappearance at 2437 cm^{-1} suggests an efficient modification of the surface hydroxyl groups after reaction with HMDA.²¹⁴ Moreover, signals around 3000 cm^{-1} , attributed to the unreacted $-\text{SiMe}_3$ groups, reveal incomplete grafting of the OPV moiety once again. The absence of OPV-related bands in the spectrum ascribed to the low concentration of molecules in the surface can only be surpassed by employing methods such as surface-enhanced Raman scattering (SERS).

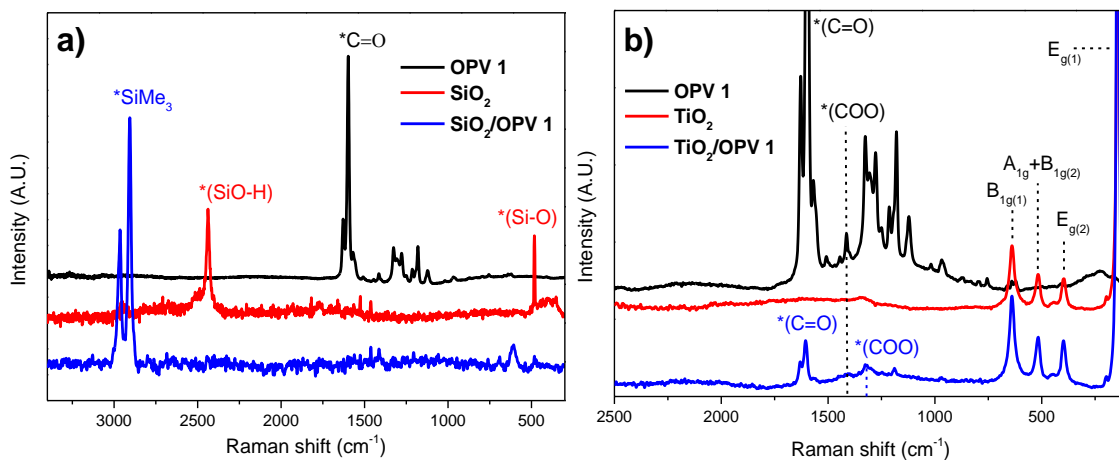


Figure 4-4: Comparative Raman spectra of (a) **SiO₂/OPV 1** and (b) **TiO₂/OPV 1**.

Solid-state ^{13}C CP/MAS NMR spectroscopy was also employed as an additional attempt to validate the **OPV 1** grafting onto the solid supports. However, no OPV signals were observed for the prepared photocatalysts and only the peak ascribed to unreacted $-\text{SiMe}_3$ groups at 0.8 ppm for **SiO₂/OPV 1** was recognized (**Figure 4-5**).

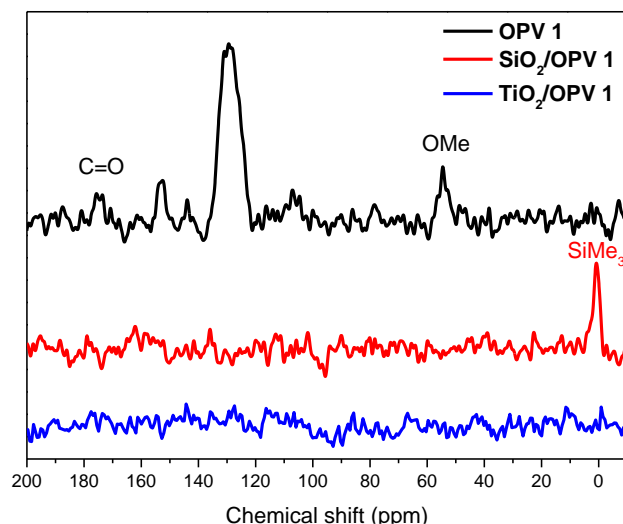


Figure 4-5: Comparative solid-state ^{13}C CP/MAS NMR spectra for **OPV 1** and prepared **$\text{SiO}_2/\text{OPV 1}$** and **$\text{TiO}_2/\text{OPV 1}$** photocatalysts.

Therefore, high-resolution XPS was used to explore the photocatalysts' surface chemistry further. In **$\text{TiO}_2/\text{OPV 1}$** , only two peaks assigned to the Ti spin-orbit splitting ($2p_{3/2}$ and $2p_{1/2}$) were discerned for the entire Ti2p region (**Figure 4-6a**).²¹⁵ This observation suggests no significant effect of the OPV on the chemical environment for the Ti. The O1s core level region (**Figure 4-6b**) displays a strong peak at 529.8 eV, which is typical for oxygen in the bulk TiO_2 structure. Moreover, two peaks at 530.5 and 533.1 eV appeared, suggesting a predominantly monodentate binding geometry for the OPV through the formation of the Ti-O-CO bond, in which the two oxygen atoms of the carboxylate are not chemically identical.²⁰⁴ Finally, the C1s signal (**Figure 4-6c**) displays two peaks at 285.0 and 285.3 eV attributed to C-C sp^2 and sp^3 bonds, respectively. In addition, C-O and C=O bonds were also identified, with peaks at 285.8 and 286.6 eV. An additional peak at 289.1 eV can be correlated with the Ti-carboxylate bond, which is a pivotal spectroscopic feature that confirms the successful grafting of the OPV onto the TiO_2 surface.²¹⁶ Finally, a broad peak at 292.6 eV matches a $\pi\text{-}\pi^*$ transition as a result of a delocalized conjugation in the OPV structure.²¹⁷

Similar XPS spectra features were observed for **$\text{SiO}_2/\text{OPV 1}$** . The deconvolution of the Si2p region displayed four peaks (**Figure 4-7a**). A major peak at 103.3 eV corresponds to Si atoms in the bulk SiO_2 structure. Additional peaks at 102.0 and 101.1 eV are consistent with Si-C and Si-O-C bonds, respectively.^{218–220} This experimental observation validates the successful grafting of the OPV along with the presence of unreacted SiMe_3 groups on the surface. An additional peak with very

low intensity at 99.7 eV may be attributed to the presence of residual elemental silicon on the SiO₂ surface. It should be noted that no peaks around 104.5 eV were observed, indicating a complete reaction of the surface silanol (Si-OH) groups.²²¹

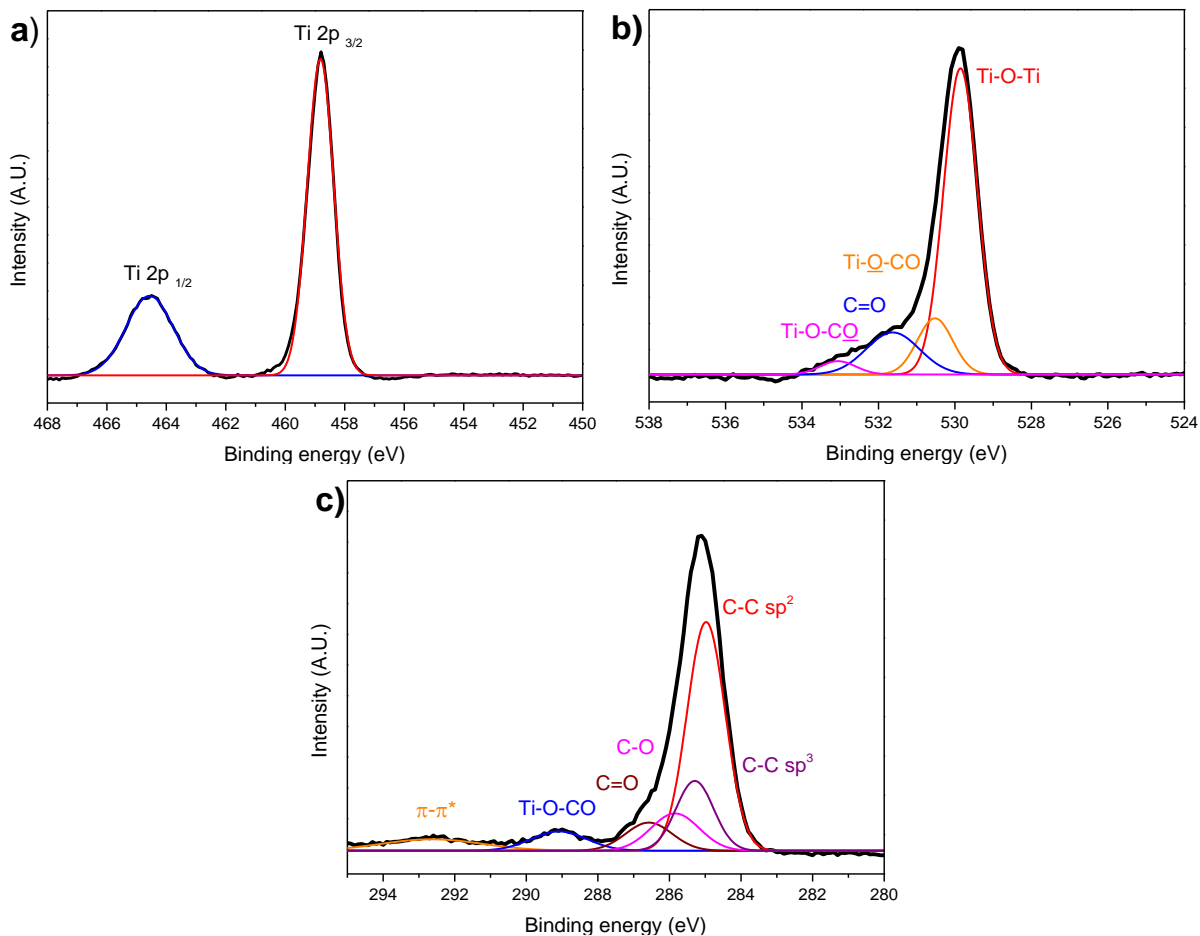


Figure 4-6: Deconvoluted XPS spectra of (a) Ti2p, (b) O1s, and (c) C1s regions for TiO₂/OPV 1.

The O1s core level region consists of three peaks located at 532.0, 530.7, and 528.7 eV (**Figure 4-7b**). The most intense was assigned to the Si-O bonds in the bulk SiO₂. The binding energy of the second peak is in agreement with the presence of Si-O-C and C=O bonds that cannot be individually distinguished.²²² Finally, the very low-intensity peak can be attributed to contamination of the surface with an unknown metal oxide.²²³ Thorough investigation of the C1s region (**Figure 4-7c**) confirms the presence of the OPV sp² C-C bonds with a peak at 282.7 eV. In addition, a peak corresponding to sp³ C-C bond at 283.9 eV exhibits a greater intensity due to unreacted SiMe₃ groups. C-O and C=O bonds are also present as evidenced by the peaks at 286.2 and 288.3 eV, respectively.²²¹ Finally, the last two peaks at 285.4 eV can be associated with C-Si

bonds in the unreacted SiMe_3 groups and C-O-Si bonds, which confirms the OPV grafting onto the SiO_2 surface.²²⁰

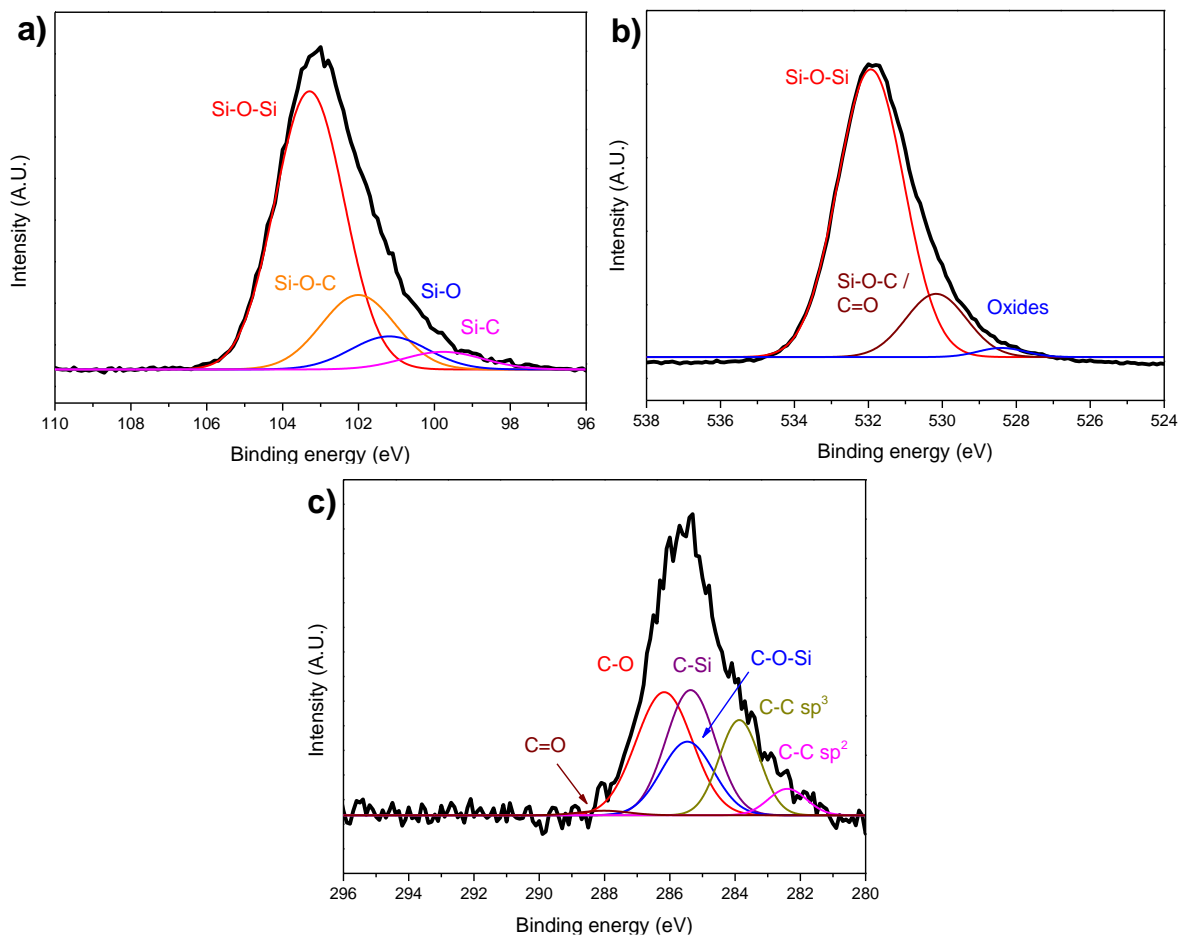


Figure 4-7: Deconvoluted XPS spectra of (a) Si2p, (b) O1s, and (c) C1s regions for $\text{SiO}_2/\text{OPV 1}$.

Additionally, powder XRD was employed to examine the crystal structure of the TiO_2 throughout the synthetic procedure (**Figure 4-8**). As anticipated, both $\text{TiO}_2/\text{SiMe}_3$ intermediate and $\text{TiO}_2/\text{OPV 1}$ final product retained the same crystallographic features exhibited by unaltered TiO_2 , demonstrating once more that the light-absorption and semiconductive properties of the solid bulk support were not affected.

The thermal stability of the prepared materials was determined employing TGA analyses. For $\text{TiO}_2/\text{OPV 1}$ material, three domains of weight loss are identified and were designated based on a comparison between the TGA curves for TiO_2 , $\text{TiO}_2/\text{SiMe}_3$ (TiO_2 after reaction with HMDA) and the pure **OPV 1** TGA curve as depicted in **Figure 4-9**.

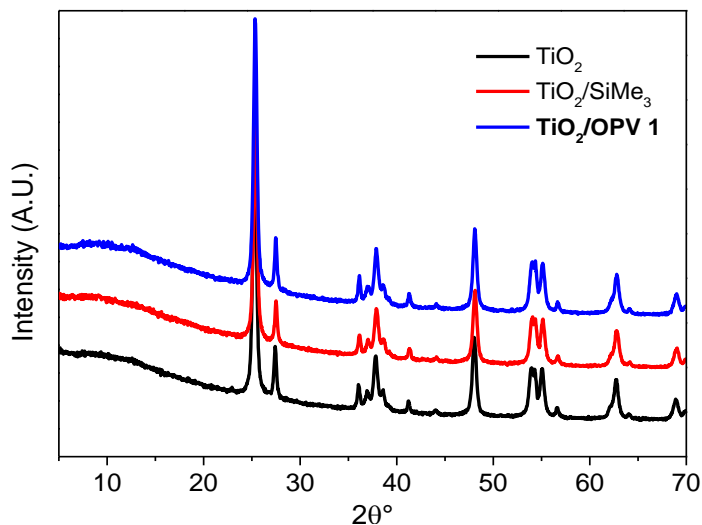


Figure 4-8: Comparative XRD traces for TiO_2 , $\text{TiO}_2/\text{SiMe}_3$ and, $\text{TiO}_2/\text{OPV 1}$

A weight loss of approximately 0.6 wt% in the range of 20-150 °C was attributed to the loss of physisorbed water, solvent, or residual by-product from the synthesis process. A second step between 220 and 610 °C (2.1 wt%) corresponds to the OPV moiety decomposition. And finally, the last decomposition step exhibiting a marked temperature onset between 690 and 880 °C (1.3 wt%) corresponds to the loss of the remaining $-\text{SiMe}_3$ groups and other impurities on the TiO_2 surface.

For $\text{SiO}_2/\text{OPV 1}$, four weight loss domains were recognized. The first one between 20 and 100 °C (4.0 wt%) for the loss of adsorbed water. The second and most prominent temperature onset, observed between 125 and 270 °C (4.7 wt%) attributed to the loss of solvent (dioxane) trapped in the porosities of the silicon oxide after the surface modification reaction. A third domain between 270 and 640 °C (2.4 wt%) is associated with the OPV decomposition, and the last one between 640 and 880 °C (1.0 wt%) for the loss of the remaining $-\text{SiMe}_3$ groups. The number of OPV molecules grafted on the material's surface was estimated by TGA and presented in **Table 4-2**. It should be noted that the degree of surface coverage with non-metallic compounds is difficult to be accurately determined by chemical analyses. Thus assessment of OPV content via TGA provides only an approximation²²⁴

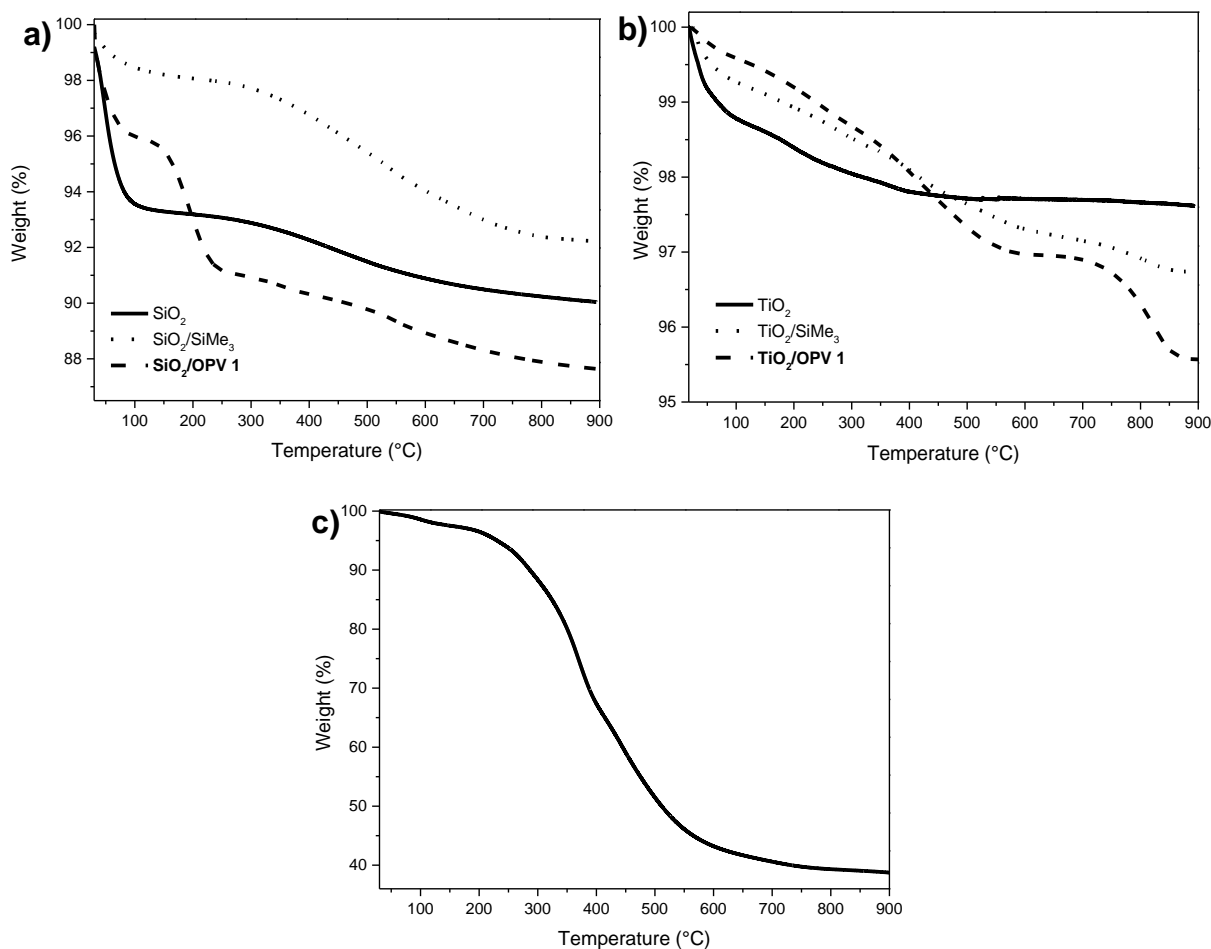


Figure 4-9: TGA curves for (a) silica gel (solid line), trimethylsilylated SiO₂ (dots) and SiO₂/OPV 1 material (dashed lines), (b) TiO₂ P25 (solid line), trimethylsilylated TiO₂ (dots) and TiO₂/OPV 1 material (dashed lines), and (c) OPV 1

Comparative N₂ adsorption/desorption isotherms of the photocatalysts and solid supports are presented in **Figure 4-10**. In the case of SiO₂ and SiO₂/OPV 1, the obtained isotherms confirmed the mesoporous structure of silicon oxide with H1-type hysteresis loops presenting a narrow range of uniform mesopores²²⁵. A decrease in the pore volume and pore size was observed when SiO₂/OPV 1 was compared to pristine SiO₂, which is attributable to the presence of the conjugated organic compound on the surface (**Table 4-2**). Conversely, the TiO₂ sorptometric results showed its non-porous nature, which is evidenced by a type III isotherm according to the IUPAC classification²²⁶. As expected, the grafting of the OPV on the titanol and silanol surface resulted in the decrease of the surface area when compared to the parent solid supports for both materials²⁰⁷.

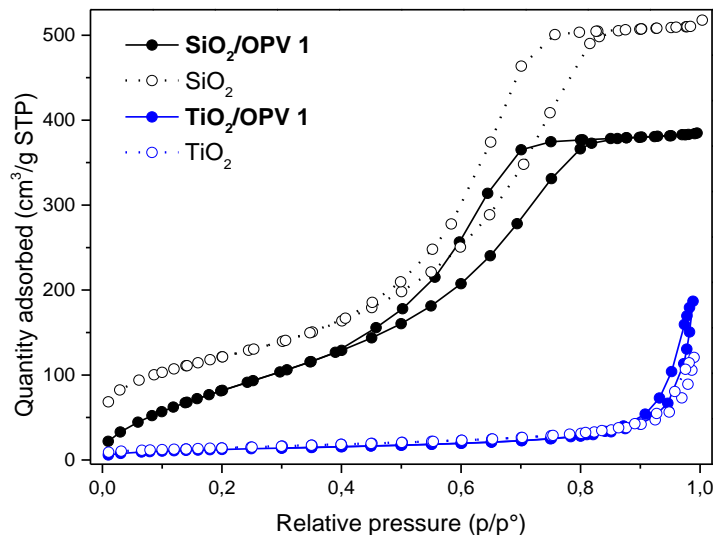


Figure 4-10: Nitrogen adsorption/desorption isotherms for (a) **SiO₂/OPV 1**, and (b) **TiO₂/OPV 1** materials.

Table 4-2: Results of nitrogen sorption and OPV loading for prepared photocatalysts.

Photocatalyst	Loading (mmol OPV/g) ^a	S _{BET} (m ² /g)	Pore volume (cm ³ /g)	Pore size (nm)
SiO ₂	---	438.6	0.80	5.72
SiO ₂ /OPV 1	0.056	353.4	0.59	4.73
TiO ₂	---	50.7	---	---
TiO ₂ /OPV 1	0.049	45.5	---	---

^aDetermined by TGA

Regarding the optoelectronic properties, an appreciable absorption in the UV-Vis region is observed for **TiO₂/OPV 1** photocatalyst compared with the diffuse reflectance spectrum of the unmodified TiO₂ support (**Figure 4-11a**). A similar absorption feature was ascertained for **SiO₂/OPV 1** photocatalyst. The bandgap (ΔE) value obtained from the Kubelka-Munk function (**Figure 4-11b**, **Table 4-3**) for **SiO₂/OPV 1** resulted in an increase of the direct energy gap value by 0.44 eV compared to pure OPV. In contrast, **TiO₂/OPV 1** (estimated employing the Kubelka-Munk function for an indirect bandgap material) displayed two consecutive linear increases ascribed to energy gap values of 2.39 eV and 3.20 eV and correspond to **OPV 1** and TiO₂, respectively.²²⁷

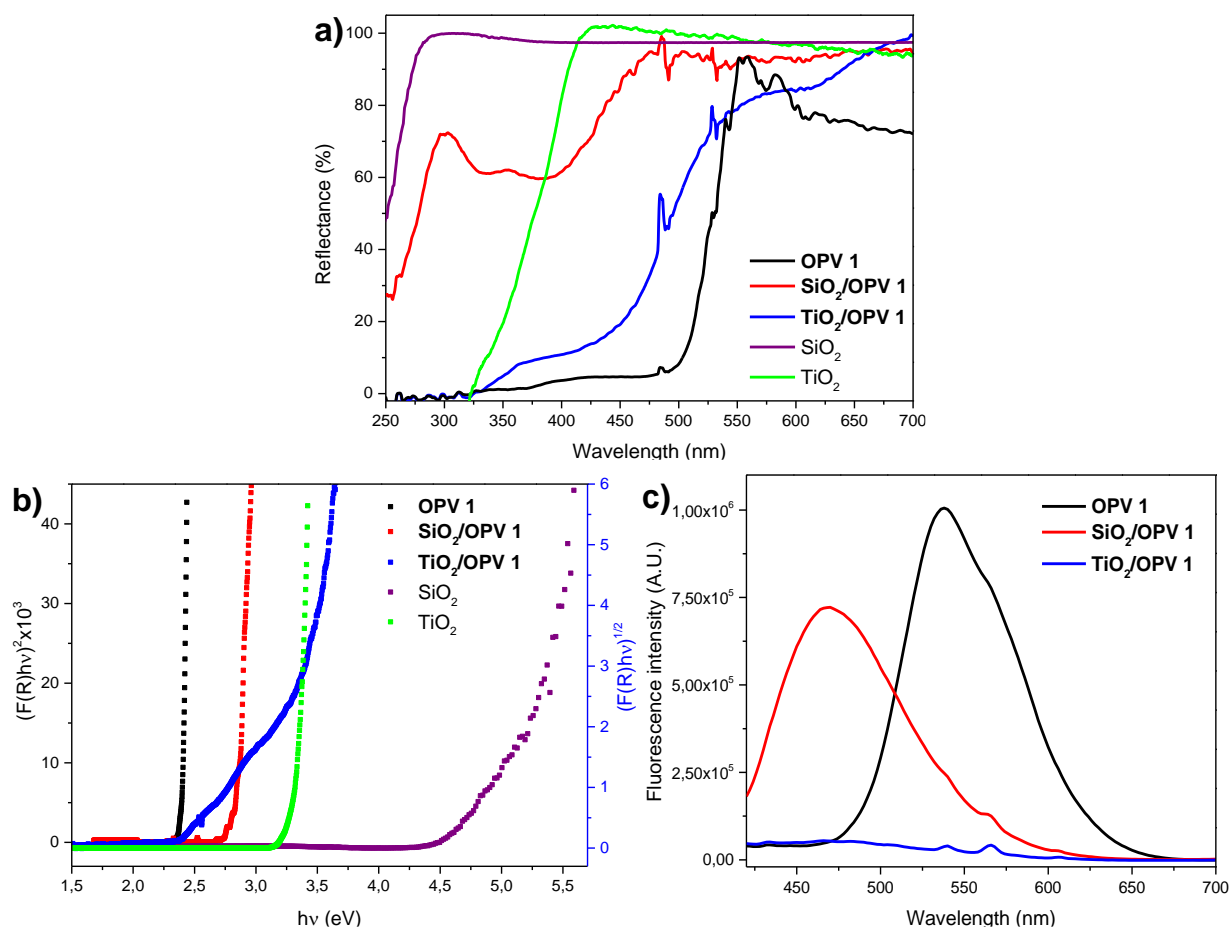


Figure 4-11: (a) Diffuse reflectance spectra, (b) Kubelka-Munk function and (c) solid-state emission spectra for **OPV 1** grafted materials.

Meanwhile, **SiO₂/OPV 1** solid-state emission exhibits a decrease in photoluminescence intensity of almost 25%, accompanied by a 70 nm redshift compared to pure OPV material. It can be rationalized that such photoluminescence bathochromic shift is the result of an excited state stabilization prompted by the interaction between the carbonyl groups in the OPV and the unreacted silanol groups on the SiO₂ surface.²²⁸ Conversely, **TiO₂/OPV 1** displayed a negligible emission (**Figure 4-11c**) that can be correlated to quenching of the OPV excited-states population. The energetic positions of the OPV LUMO and the TiO₂ conduction band, obtained from cyclic voltammetry experiments and previous literature reports, suggest a thermodynamically favored electron transfer.^{229,230} Thus, it can be inferred that the OPV moiety is acting as a light harvester to produce excited electrons that are injected into the conduction band of TiO₂ (**Figure 4-12**). This charge transfer phenomenon explains the deactivation of the molecular fluorescence considering the regeneration of the OPV HOMO occurs now via a back electron transfer

process.¹¹⁵ In the case of **SiO₂/OPV 1** photocatalyst, the more negative potential of the conduction band for SiO₂ entirely prevents an electron transfer, prompting the radiative route as the dominant relaxation pathway after OPV excitation. It should be noted that the bandgap for pure amorphous SiO₂ has been measured in the range of 8.0 – 11.0 eV, employing photoconductivity, optical transmission, reflectivity, and electron spectroscopy.^{231,232} Therefore, UV-Vis diffuse reflectance spectroscopy does not provide an accurate estimation of the bandgap for this material.²³³ Thus, a value of 8.9 eV was used to construct the SiO₂ relative energy levels for conduction and valence bands in **Figure 4-12**.²³¹

Table 4-3: Optoelectronic properties of **OPV 1** grafted materials.

OPV derivative		OPV 1	SiO ₂ /OPV 1	TiO ₂ /OPV 1
Solid state	ΔE (eV)	2.41	2.85	2.39
	λ_{em} (nm)	540	470	N.E.*

*N.E. No appreciable emission was observed.

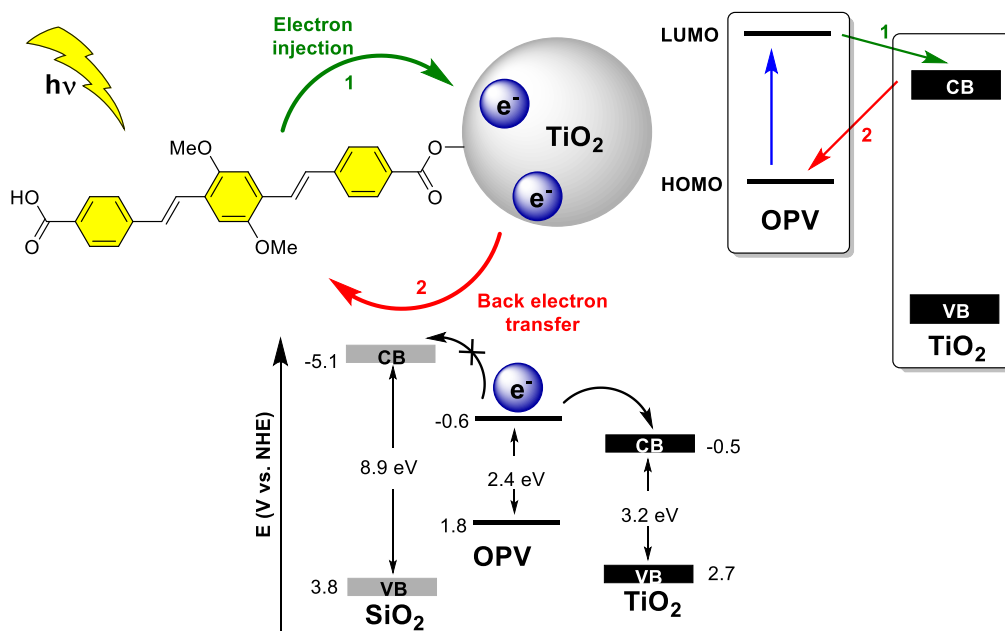
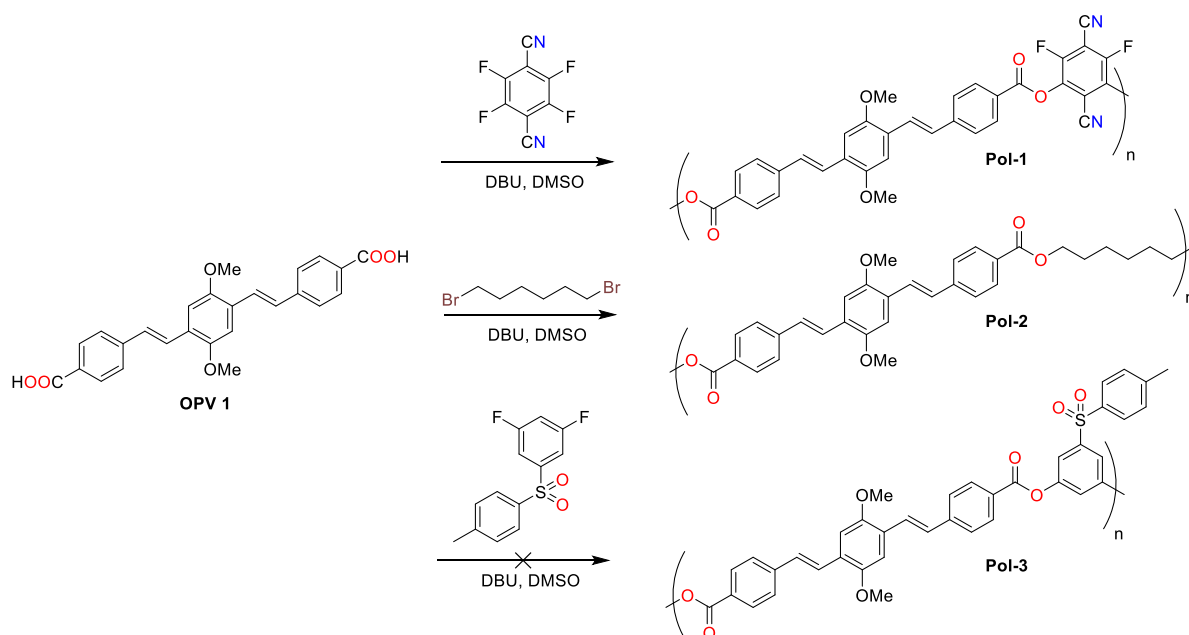


Figure 4-12: Molecular representation of interfacial electron transfer reactions and relative energy levels for **OPV 1** (HOMO and LUMO), TiO₂ and SiO₂ (conduction band: CB, and valence band: VB).

4.3.2 Synthesis and characterization of OPV 1 copolymers

Experiments to achieve the copolymerization of **OPV 1** were carried out employing DBU as base and DMSO as solvent, as depicted in **Scheme 4-6**. Nevertheless, the formation of **Pol-3** material was not observed even after modification of the reaction conditions that included the use of NMP and DMAc as solvents, K_2CO_3 as base and temperatures up to 200 °C, as previously described in the literature for analogous S_NAr -based polymerization.²³⁴



Scheme 4-6: Synthesis of **OPV 1** polymeric derivatives.

Evidence of the successful polymerization reactions was initially obtained from FTIR spectroscopy (**Figure 4-13**). For **Pol-1**, a notorious band at 2225 cm^{-1} clearly suggests the presence of the -CN group in the polymeric backbone. Alternatively, for **Pol-2**, the increase in the intensity of signals at 2935 cm^{-1} and 2858 cm^{-1} are associated with the presence of additional C-H groups from the C_6 aliphatic chain spacer. Moreover, the typical C-O stretch vibrations for ester groups are observed at 1273 and 1103 cm^{-1} .

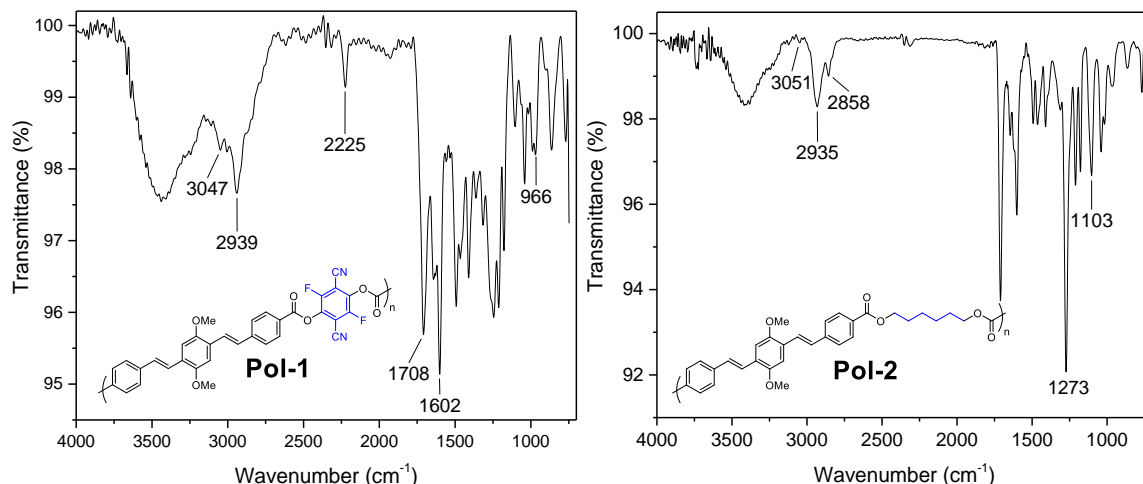


Figure 4-13: FTIR spectra of polymeric materials **Pol-1** and **Pol-2**.

The $^1\text{H-NMR}$ spectrum for **Pol-1** (**Figure 4-14**) shows a broadening in the signals as a result of the motion and rotation restrictions in the polymeric chain. However, all the peaks associated with the OPV moiety are easily identified. As expected, no additional proton signals appear in the spectrum due to the insertion of the difluoro terephthalonitrile fragment. Moreover, the characteristic carboxylic acid hydrogen signal around 12 ppm has completely disappeared, indicating the successful formation of the polymer.

On the other hand, the $^1\text{H-NMR}$ spectrum for **Pol-2** clearly displays the presence of the aliphatic protons in the aliphatic spacer chain labeled as a, b and c (**Figure 4-15**). It should be noted that the area ratio between the -OMe signal and the methylene protons a corresponds to a 6:4 value, respectively, indicating a 1:1 ratio between the OPV and the C_6 chain moieties. Likewise, all the signals of the phenylene vinylene system are displayed except for the hydrogen of the starting carboxylic acid group, once again suggesting that the desired reaction took place. Moreover, a small signal around 3.7 ppm might suggest that some terminal C_6 chains retained the Br atom after the reaction.

The resulting polymers were also characterized by GPC to estimate the molecular weight distribution. It should be noted that these analyses were carried out only as a semiquantitative tool since polystyrene, the employed standard, significantly differs from the synthesized structures and an important deviation in the molecular weight values is anticipated. As displayed in **Figure 4-16**, bimodal distributions were obtained with dispersity indices (DI) between 1.20 and 1.68 (**Table 4-4**).

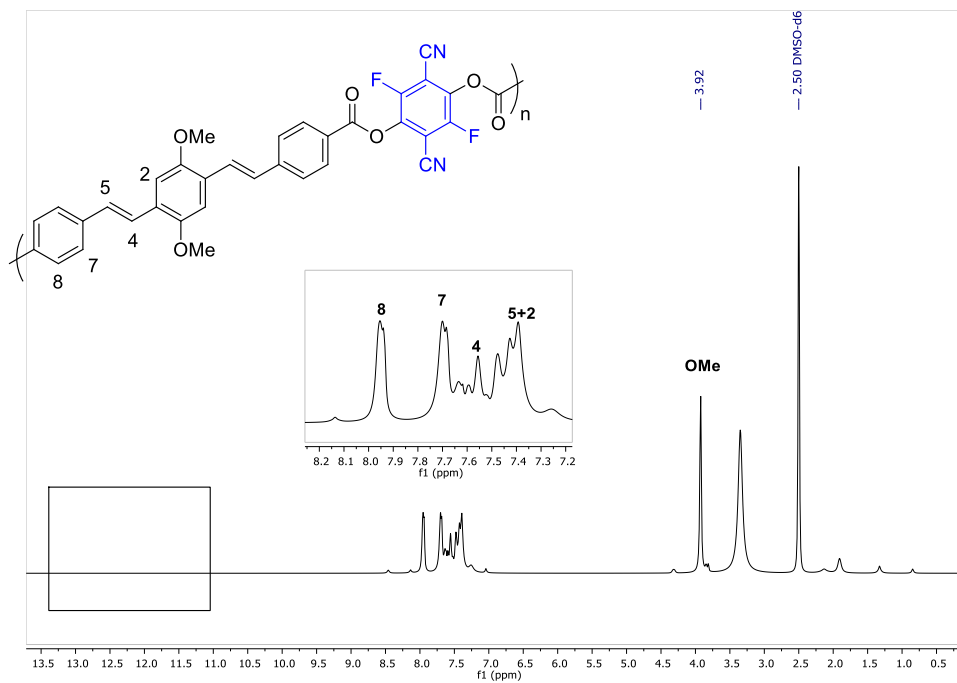


Figure 4-14: ¹H-NMR (DMSO-d₆) spectrum for Pol-1.

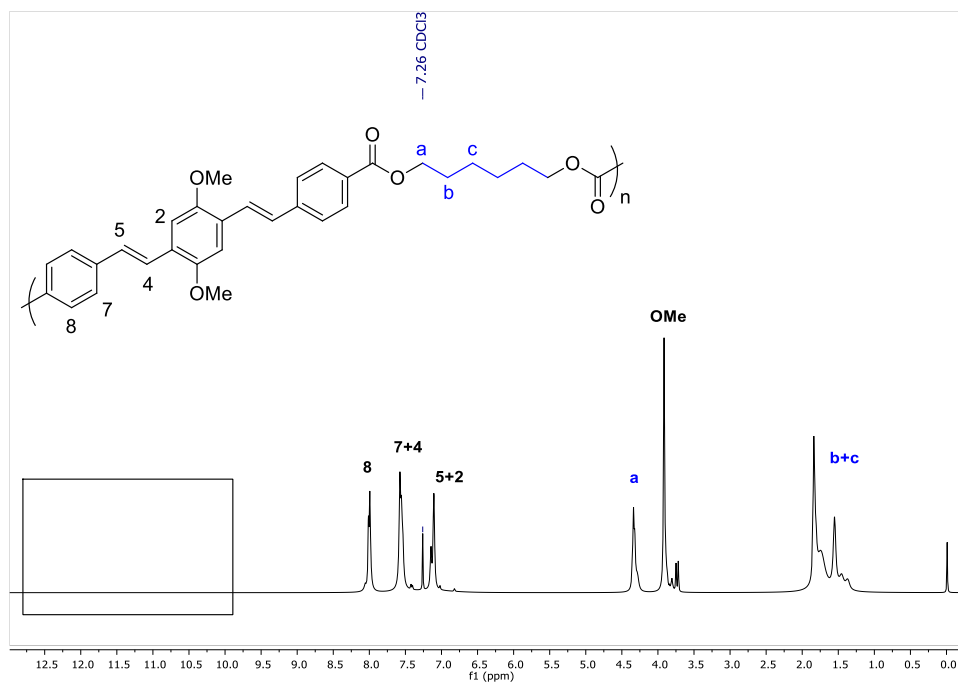


Figure 4-15: ¹H-NMR (CDCl₃) spectrum for Pol-2.

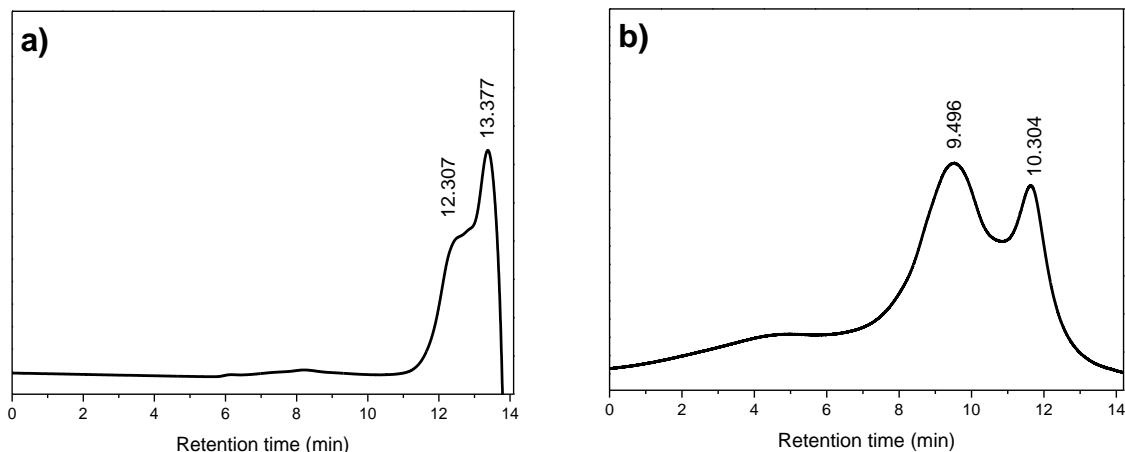


Figure 4-16: GPC traces of (a) Pol-1, and (b) Pol-2.

Table 4-4: GPC data of OPV-1 copolymers.

Polymer	t_R (min)	M_n	M_w	DI
Pol-1*	12.307	369	607	1.65
	13.377	---	---	1.20
Pol-2	9.496	7057	11843	1.68
	10.304	1100	1380	1.25

*Chromatographic peaks above retention time (t_R) of lowest MW PS standard (<2500).

To corroborate the molecular weight distribution, ESI-MS experiments confirmed that **Pol-1** consists of a mixture of dimers and trimers (Figure 4-17a), validating the observed GPC chromatographic behavior. For **Pol-2**, the ESI-MS spectrum displayed a single major distribution along with a pattern of a sequential loss of 232 and 281 m/z .

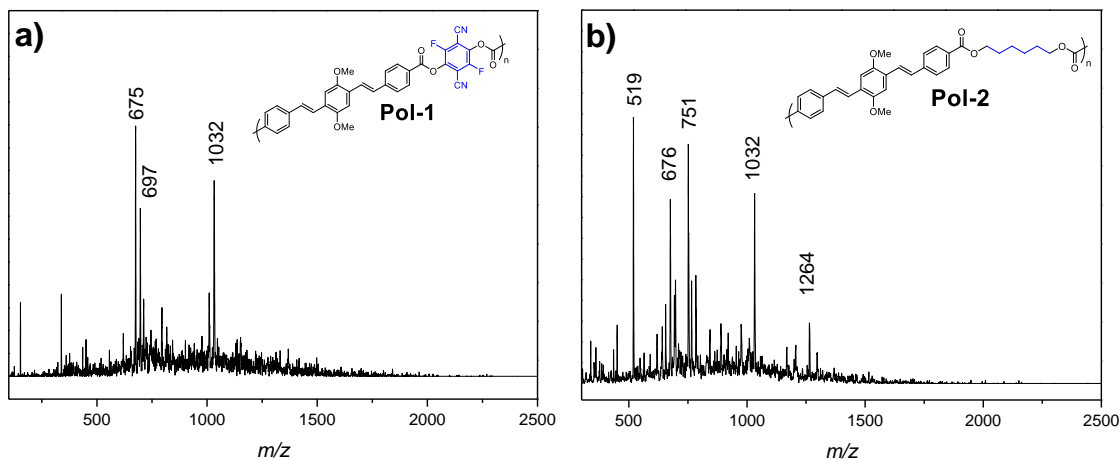


Figure 4-17: ESI-MS spectra set for (a) Pol-1, and (b) Pol-2.

The correlation of the observed peaks with the GPC results allowed to establish a charge of +7 for the molecular weight distribution in the mass spectrum (**Figure 4-17b**). The estimation of the adducts chemical structure with the most intense peaks is shown in **Table 4-5**. The estimated structures of the adducts for **Pol-2** keep correlation with the $^1\text{H-NMR}$ data where a 1:1 ratio between **OPV 1** and the C_6 chain spacer was identified. Furthermore, some structures were assembled considering that the Br atom in the terminal C_6 chain was unaffected throughout the reaction, and once more, this consideration is consistent with the information gathered from the $^1\text{H-NMR}$ spectrum.

Table 4-5: Estimated chemical structure of polymer adducts.

Polymer	Peak (m/z)	Adducts
Pol-1	675	$[\text{PV}_1\text{T}_1 + \text{MeCN} + \text{Na}]^+$
	697	$[\text{PV}_1\text{T}_1 + \text{MeCN} + 2\text{Na} - \text{H}]^+$
	1032	$[\text{PV}_2\text{T}_1 + \text{K} - \text{HCN}]^+$
Pol-2	519	$[\text{PV}_7\text{Hex}_7 + \text{MeOH} + 7\text{H}]^{+7}$
	676	$[\text{PV}_9\text{Hex}_9 + \text{MeCN} + 3\text{Na} + 4\text{H}]^{+7}$
	751	$[\text{PV}_{10}\text{Hex}_{10} - \text{OH} + \text{Br} + \text{MeOH} + \text{Na} + 6\text{H}]^{+7}$
	1032	$[\text{PV}_{14}\text{Hex}_{14} + \text{MeOH} + 7\text{H}]^{+7}$
	1264	$[\text{PV}_{17}\text{Hex}_{17} - \text{OH} + \text{Br} + \text{MeOH} + \text{Na} + 6\text{H}]^{+7}$

Building blocks PV: **OPV-1**; T: difluoroterephthalonitrile; Hex: C_6 chain

The thermal stability of the materials was examined using TGA (**Figure 4-18a**). **Pol-1** exhibits remarkable stability up to approximately $280\text{ }^\circ\text{C}$, where the onset of a marked weight loss domain is observed. However, **Pol-2** displays poor thermal stability defined by a rather constant mass loss domain starting from nearly $90\text{ }^\circ\text{C}$. The DSC thermogram (**Figure 4-18b**) for **Pol-1** revealed a broad heat absorption starting at $128\text{ }^\circ\text{C}$ associated with the overlapping of multiple melting peaks. Alternatively, **Pol-2** showed a single endothermic fluctuation that corresponds to a T_g at $54.3\text{ }^\circ\text{C}$ that can only be observed during the first heating cycle. Interestingly, it should be disclosed that both materials exhibit a good film-forming ability after solvent casting (THF), regardless of their molecular weight and chemical composition (**Figure 4-18a**, inset).

The polymers were also characterized by scanning electron microscopy (**Figure 4-19**). The micrographs for **Pol-1** show the presence of agglomerates exhibiting an irregular morphology with flake-like structures. For **Pol-2**, the observed agglomerates are assembled with quasi-spherical particles in the micrometric scale. It should be noted that none of the materials displayed any porosity features that may lead to an enhancement of the photocatalytic process. Additionally, nitrogen adsorption/desorption isotherms analyses confirmed that these materials have a S_{BET}

value lower than $5.0 \text{ cm}^2/\text{g}$, which is within the estimation error of the measurement and is accordant with the SEM observations.

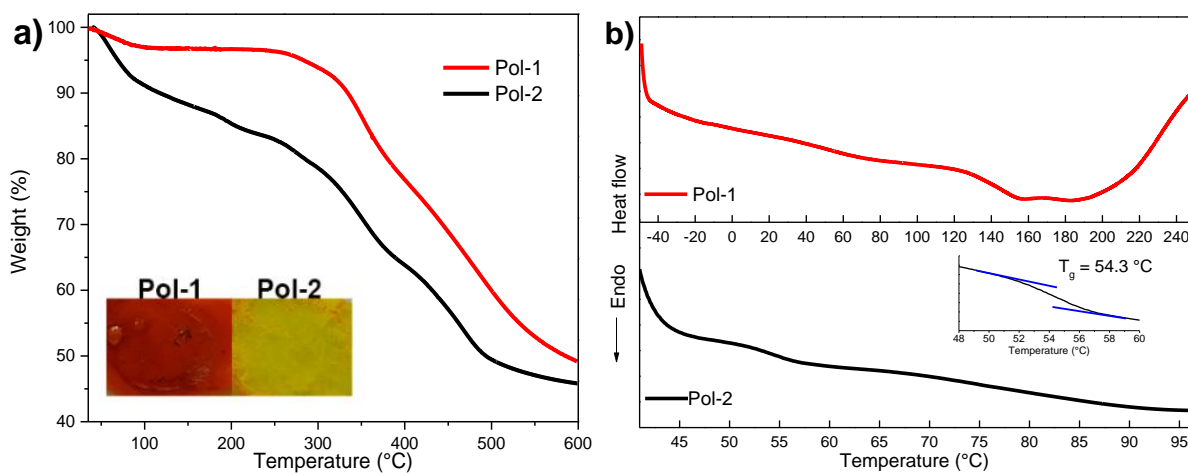


Figure 4-18: (a) TGA (inset: **Pol-1** and **Pol-2** films obtained after solvent casting) and (b) DSC heating curves obtained for **Pol-1** and **Pol-2**.

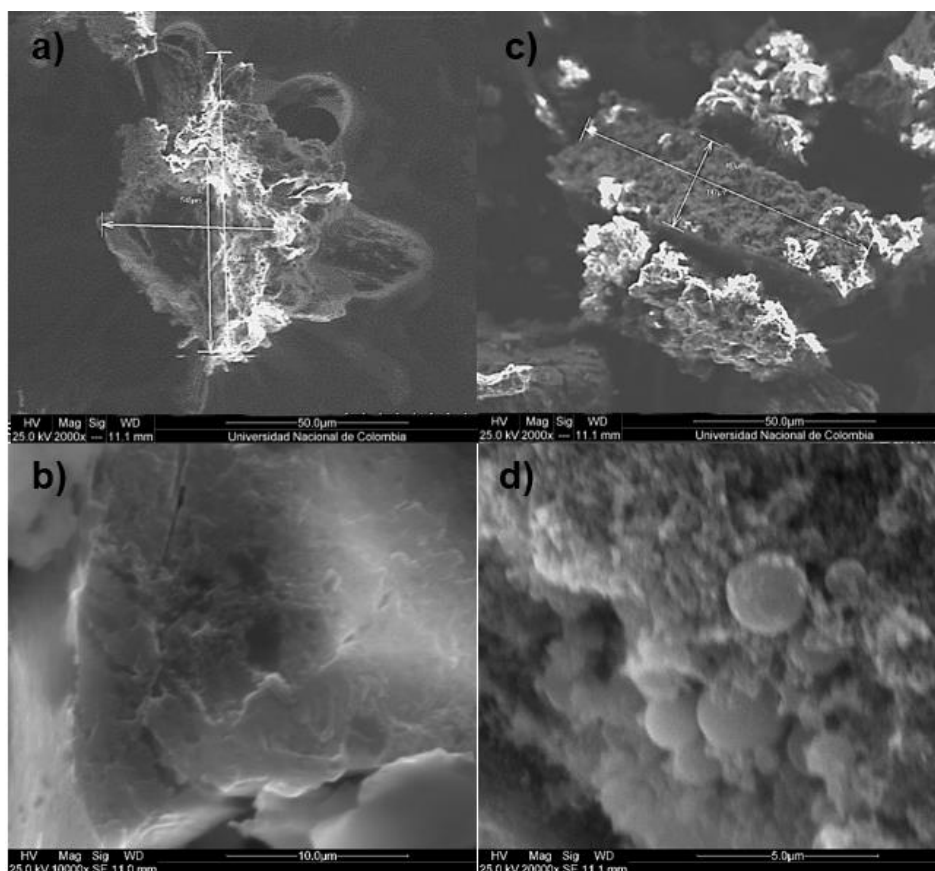


Figure 4-19: SEM micrographs of **Pol-1** (a,b) and **Pol-2** (c,d) particles.

The optoelectronic characterization of the polymers initially involved the measurement of the UV-Vis and fluorescence spectra in MeCN (**Figure 4-20**). It should be noted that both polymers displayed similar absorption and emission features, considering that the OPV chromophore was not altered during the reaction. This effect was also confirmed by the EEM measurements, which, at the same time, exhibited high similarity with **OPV 1** as shown in **Figure 4-21**.

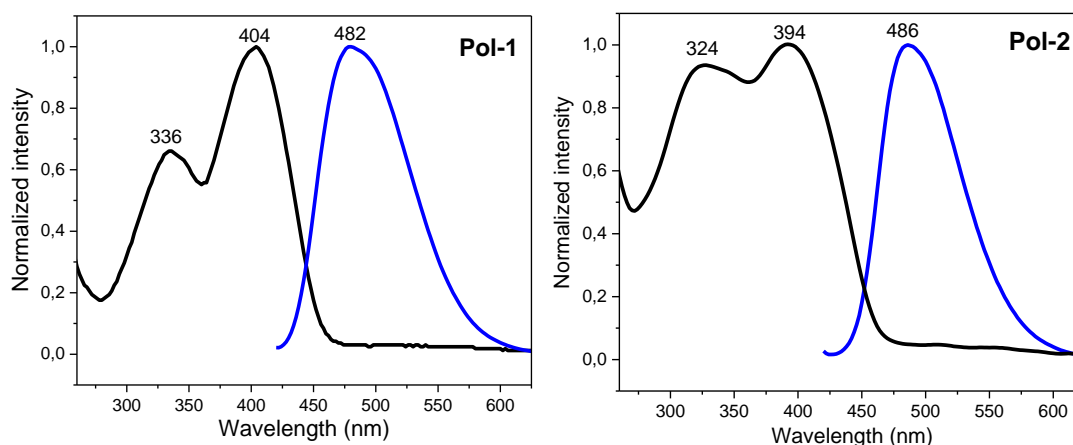


Figure 4-20: Normalized absorption (black) and emission (blue) spectra for **Pol-1** and **Pol-2**.

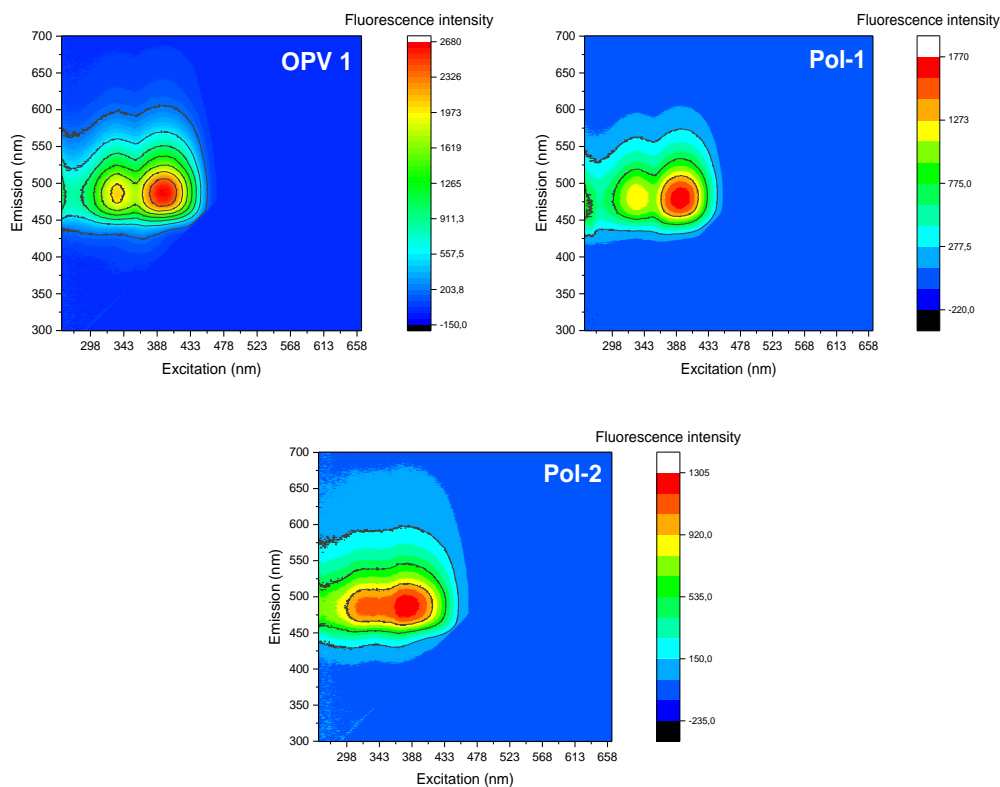


Figure 4-21: Excitation-Emission Matrices (EEM) for **OPV 1** and materials **Pol-1** and **Pol-2**.

All the experimental values for the optoelectronic characterization, including the Φ_{Δ} are summarized in **Table 4-6**, where no major differences in the λ_{\max} , λ_{em} , and ΔE were found between **OPV 1** and its polymeric derivatives. Interestingly, the relative fluorescence quantum yield ϕ_f increased approximately twofold from 0.25 to 0.47. Such behavior can be explained in terms of the molecular motion restriction of the excited state induced by the bulkiness of the building blocks and the polymer chain length, that deactivates non-radiative relaxation pathways, thus promoting the emission mechanism in solution.^{235,236} Also, **Pol-1** retained a likewise essentially identical Φ_{Δ} value to that obtained for **OPV 1**, implying that the singlet oxygen is generated exclusively by the OPV moiety.

Table 4-6: Optoelectronic properties of **OPV 1** polymeric derivatives.

OPV derivative	OPV 1	Pol-1	Pol-2	
MeCN solution	λ_{\max} (nm)	407	404	394
	λ_{em} (nm)	475	482	486
	ΔE (eV)	2.67	2.71	2.68
	ϕ_f^*	0.25	0.47	0.43
	Φ_{Δ}^{\ddagger}	0.14±0.01	0.11±0.01	N.D.
Solid state	ΔE (eV)	2.41	2.21	2.22
	λ_{em} (nm)	540	532	542

*Perylene as standard. †Phenalenone as standard. || N.D. Not determined due to fast degradation of the polymer.

Regarding solid-state optoelectronic properties (**Figure 4-22** and **Table 4-3**), the diffuse reflectance spectra of polymers show a broad absorption starting in the visible region. Additionally, the Kubelka-Munk function was calculated to estimate the ΔE values for the materials. It should be disclosed that the polymeric materials exhibited a more pronounced low-energy absorption gap (ΔE) compared to **OPV 1**. This can be attributed to an orbital overlapping prompted by a larger extent of intermolecular interactions of the chromophore moieties in the polymeric chains as a result of forced proximity and aggregation in the solid-state.^{152,237} Nevertheless, the λ_{em} values for the polymers and the OPV precursor are not quite different ($\Delta\lambda_{\text{em}} < 8$ nm), suggesting no significant modification in the excited state geometry as a result of no change in the chromophore conjugation. Alternatively, the major impact of the polymerization process in photoluminescence pertains a marked decrease in the emission intensity, where an aggregate-based self-quenching phenomenon is consistent with the experimental observations where the fluorescence intensity for **Pol-1** and **Pol-2** are respectively 14-fold and 2.5-fold lower when compared to **OPV 1** emission.²³⁸

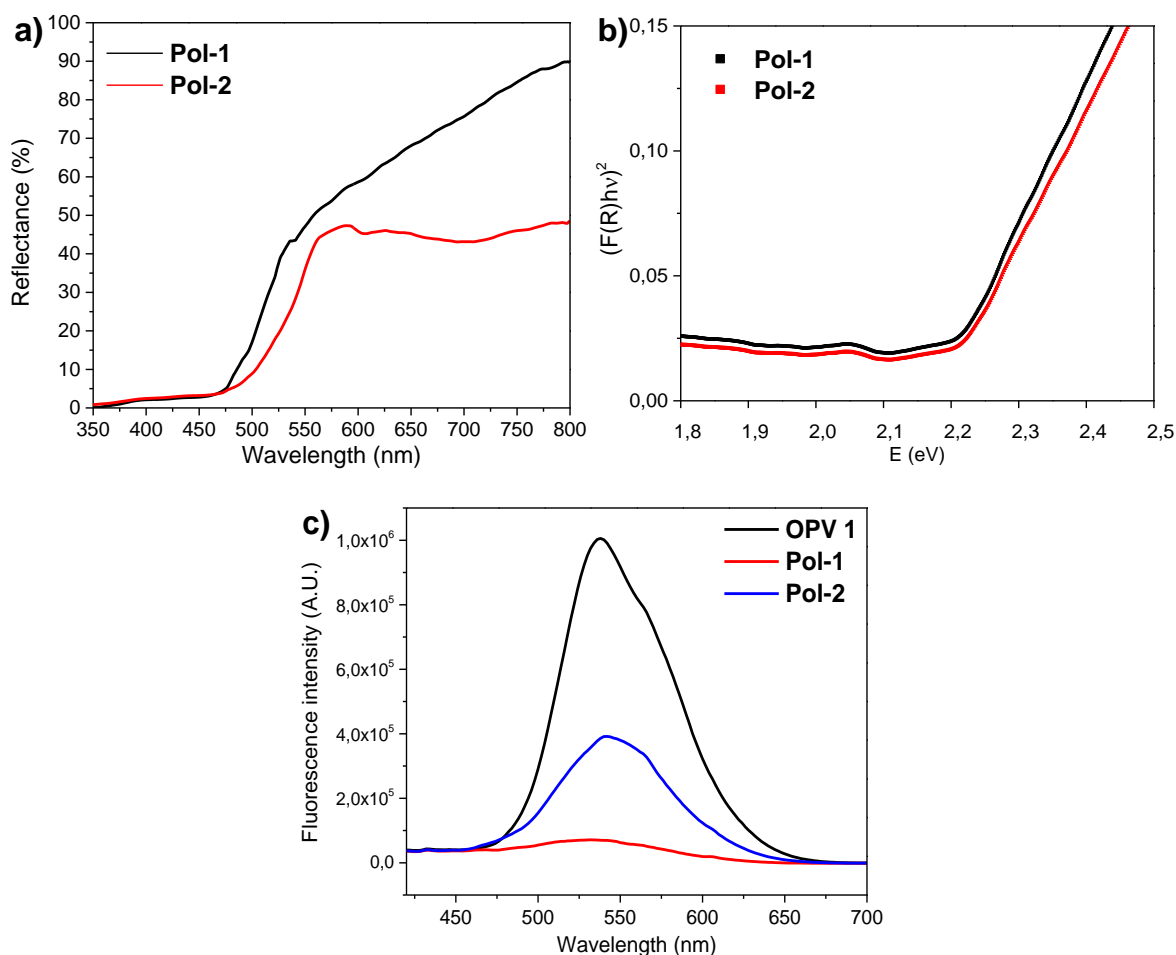


Figure 4-22: (a) Diffuse reflectance spectra, (b) Kubelka-Munk function, and (c) solid-state emission spectra for polymers **Pol-1** and **Pol-2**. Emission of **OPV 1** was included in (c) for comparative purposes.

4.3.3 Photocatalytic performance of OPV 1 derivatives

The prepared materials were assessed as photocatalysts in the degradation of aqueous IC dye. For each experiment, 3 mg of material were employed, and the efficiency of the discoloration was compared for both white LEDs and UVA-Vis LEDs, as sources of irradiation (**Figure 4-23**). An initial control experiment carried out in the absence of catalyst under visible light irradiation (white LEDs) confirmed that IC is stable under these reaction conditions. IC stability under UVA-Vis irradiation was previously validated in Chapter 3.

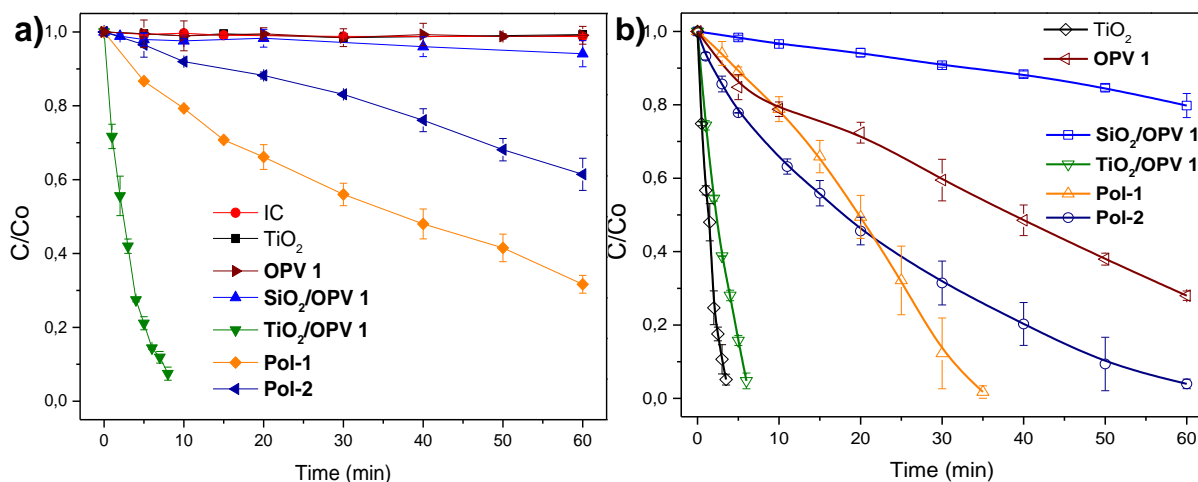


Figure 4-23: Degradation profile of **OPV 1** derivatives employing (a) white LEDs and (b) UVA-Vis LEDs (350-450 nm).

As expected, when pure TiO_2 was employed as a catalyst, no dye degradation was observed since the radiation emitted by white LEDs is not capable of inducing charge separation on this semiconductor material. Pure **OPV 1** was also used as a control and displayed only a 2% IC degradation. For materials **SiO₂/OPV 1**, **Pol-1**, and **Pol-2** a dye degradation of 6%, 68%, and 38%, respectively, was observed within 60 minutes of irradiation. Interestingly, for **TiO₂/OPV 1** a 93% of IC degradation was achieved in only 8 minutes of photocatalytic treatment.

Alternatively, when the UVA-Vis LED panel (350-450 nm) was employed the **OPV 1**, **SiO₂/OPV 1**, and **Pol-2** materials enhanced their photocatalytic activity by achieving 72%, 20% and 96% dye degradation within 60 minutes of reaction, respectively. Moreover, **Pol-1** displayed a 97% dye removal in only 35 minutes of irradiation. Such improvement in the photocatalytic process is attributed to the coverage of a broader region in the absorption profile which promotes a more efficient excitation of the OPV moiety in the materials (**Figures 4-11** and **4-22**). For this polymeric derivative, the notorious increase in the error bars can be ascribed to the observed uneven agglomeration of the material over time, decreasing the surface area initially available to carry out the catalytic process. For **TiO₂/OPV 1**, a 95% of dye removal was achieved in only 6 minutes of irradiation. However, a superior efficiency was observed for pure TiO_2 , which displayed an identical result in only 3.5 minutes. These outcomes indicate that an effective charge separation is being carried out in the TiO_2 as a result of the UVA light, and that the reactive oxygen species generated by both phases in **TiO₂/OPV 1** are competing to degrade not only the IC but also the supported **OPV 1**, thus requiring more time to provide a similar dye degradation percentage.

In summary, **TiO₂/OPV 1** provided superior IC photodegradation efficiency using white LEDs as a source of irradiation. Moreover, under 350-450 nm irradiation the polymeric materials **Pol-1** and **Pol-2** displayed the best photocatalytic performance achieving a higher IC degradation percentage when compared to pure **OPV 1**. Altogether, the experimental data confirms that the decoration of TiO₂ surface with **OPV 1** and the polymerization approach comprise effective strategies to boost the activity of the OPV moiety as a photocatalyst.

The assessment of the catalytic behavior also involved the kinetic parameters for the evaluated materials, which are summarized in **Table 4-7**. Starting with **SiO₂/OPV 1**, it should be noted that the kinetic data fit an apparent zero-order reaction for both sources of irradiation. Despite the 6.6-fold increase in the K_{ap} value when UVA irradiation is employed, the reaction order remained unchanged, suggesting that the reaction is governed by a diffusional regime possibly ascribed to the hydrophobicity of the surface as a result of unreacted SiMe₃ sites, which prevent an effective mass transfer of the dye and molecular oxygen in the employed aqueous media.¹⁹⁰

Table 4-7: Kinetic parameters determined for IC photodegradation experiments.

OPV derivative	White light (400-700 nm)		UVA-Vis light (350-450 nm)	
	Observed pseudo-order	K_{ap}	Observed pseudo-order	K_{ap}
SiO₂/OPV 1	Zero	0.024 $\mu\text{M}\cdot\text{min}^{-1}$	Zero	0.160 $\mu\text{M}\cdot\text{min}^{-1}$
TiO₂/OPV 1	First	0.319 min^{-1}	First	0.357 min^{-1}
Pol-1	First	0.018 min^{-1}	Zero	1.451 $\mu\text{M}\cdot\text{min}^{-1}$
Pol-2	Zero	0.312 $\mu\text{M}\cdot\text{min}^{-1}$	First	0.039 min^{-1}

In the case of **TiO₂/OPV 1**, no change in the order of reaction was observed for the different light sources. A slight increase in the K_{ap} value under UVA irradiation indicates the dye degradation is occurring faster. However, as previously outlined, this outcome derives from the combination in reactivity of the OPV moiety and the TiO₂ semiconductor support, making these reaction conditions unattractive considering the anchored **OPV 1** is also being degraded by the presence of TiO₂.

For **Pol-1**, the reaction order changed from pseudo-first to pseudo-zero when the white LEDs were changed to UVA-Vis LEDs. Such modification in the kinetic parameters was accompanied by an enhancement in the IC degradation time, denoting that the light absorption barrier was surpassed. However, the pseudo-zero reaction order for the disappearance of IC under 350-450

nm LEDs clearly suggests that the photodegradation may be restricted by the diffusion rate of molecular oxygen, that limits the generation of active oxidant species on the polymer surface. Finally, **Pol-2** photocatalytic performance favorably overcame all the light absorption and diffusion limitations when the light source was adjusted, as ascertained by the increase in the reaction order.

To provide a deeper understanding of the photocatalytic process for the materials that have shown the best performance (**TiO₂/OPV 1**, **Pol-1** and **Pol-2**), some radical scavengers (2 mM) were employed to investigate the formation of the active species involved in the degradation of the IC dye. Starting with **TiO₂/OPV 1** under white LEDs illumination, a significant decrease in the dye degradation percentage was observed in the presence of benzoquinone (Bz), confirming the formation of superoxide radicals (**Figure 4-24**). Additionally, the use of sodium azide (NaN₃) also exhibited a decrease in the IC degradation, indicating that singlet oxygen is also being generated by the system.²³⁹ As expected, a significant decrease in the photocatalytic activity was displayed when the reaction is carried out under nitrogen atmosphere, which indicates that oxygen and its derivatives provide the major contribution towards the IC degradation.

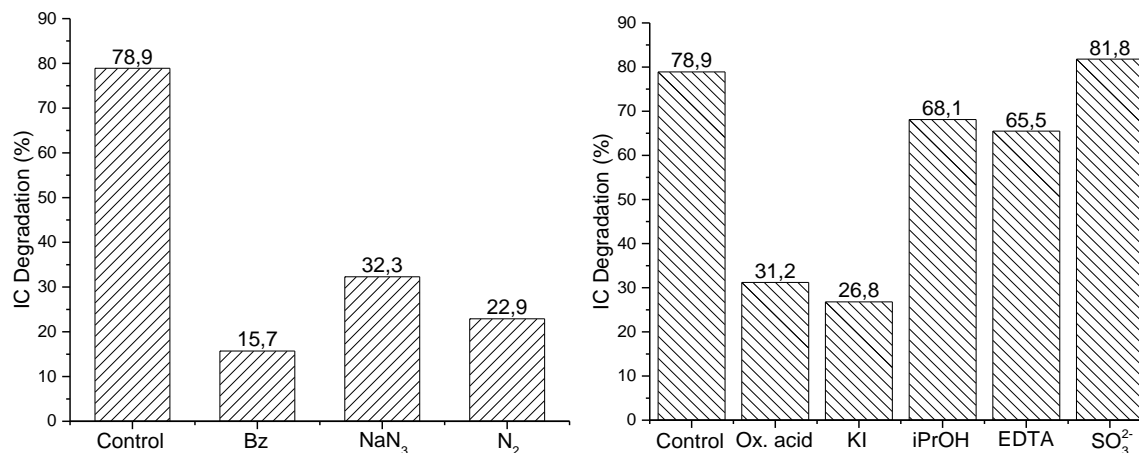


Figure 4-24: (a) Effect of scavengers and (b) electrons donors in the IC photodegradation mediated by **TiO₂/OPV 1**.

Surprisingly, the use of oxalic acid (Ox. Acid in Figure 4-24) as an electron donor exerted a negative effect on the IC degradation performance. Further investigation with other sacrificial reducing agents bearing more negative oxidation potentials (iPrOH: isopropanol, EDTA: ethylenediaminetetraacetic acid disodium salt) led only to a moderate improvement, but never surpassed the results of the control experiment, despite the thermodynamic feasibility of the OPV

regeneration reaction.^{240–242} The data presented is closely related to the electron donor's role and the charge transfer process between the excited OPV and the TiO_2 (**Figure 4-25**). The reducing agent ions or molecules (D , e.g., oxalic acid) contribute to a significant TiO_2 surface coverage prompting a competition with oxygen for reactive adsorption sites. Therefore, inducing a delay in the rate of singlet oxygen and superoxide radical formation, and a simultaneous disruption in the IC dye degradation. Moreover, the increase in OPV regeneration rate via direct oxidation of D barely compensates for the oxygen reduction on the TiO_2 surface, explaining the lack of a marked effect in the overall photodegradation. With this information in hand, it is clear that the use of substances acting as electrons donors does not significantly enhance the photocatalytic activity of $\text{TiO}_2/\text{OPV 1}$ under the employed reaction conditions.

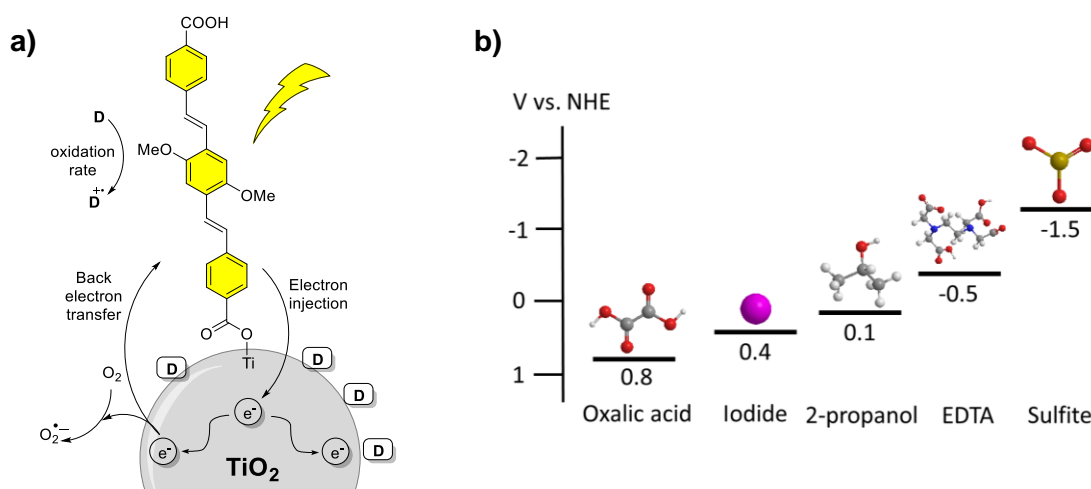
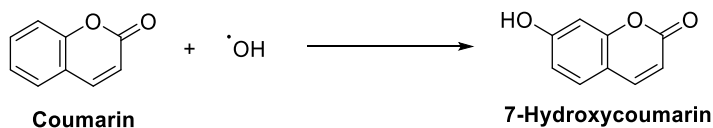


Figure 4-25: Schematic representation of (a) the electron donor (D) effect on the photocatalyst surface, and (b) oxidation potential values of the employed electrons donors.

The generation of OH radicals was also investigated for $\text{TiO}_2/\text{OPV 1}$ photocatalyst, employing coumarin as selective chemical probe (**Scheme 4-7**).²⁴³ The control experiments carried out employing an aqueous coumarin solution (1×10^{-5} M) displayed no major modification of the fluorescence spectra (**Figure 4-26**). When $\text{TiO}_2/\text{OPV 1}$ was suspended in the coumarin solution and irradiated under visible light for 8 minutes, no evidence of coumarin hydroxylation was observed, either. This outcome validates that $\text{TiO}_2/\text{OPV 1}$ photocatalyst is incapable of generating hydroxyl radicals under the employed conditions. An additional positive control experiment that involved TiO_2 P25 as photocatalyst under UV light irradiation was performed, where a major modification of the emission spectrum consisting in the appearance of a band at 455 nm ascribed

to the generation of 7-hydroxycoumarin was observed, as a result of the well-known OH^\cdot generation ability for this material.



Scheme 4-7: Reaction of coumarin with OH radicals.

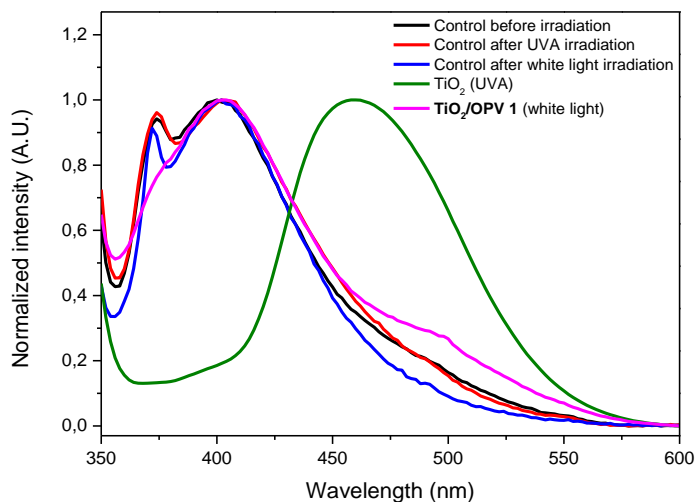


Figure 4-26: Emission spectra of coumarin solutions after irradiation in control and photocatalysis experiments.

With all this information in hand, UV-Vis spectroscopy was then employed to follow the IC photodegradation process. The spectra set within 8 minutes of irradiation clearly shows the disappearance of the dye absorption band at 610 nm (**Figure 4-27**). However, a small band at 550 nm is being formed throughout the process providing a light pink color for the treated solution at the end of the reaction.

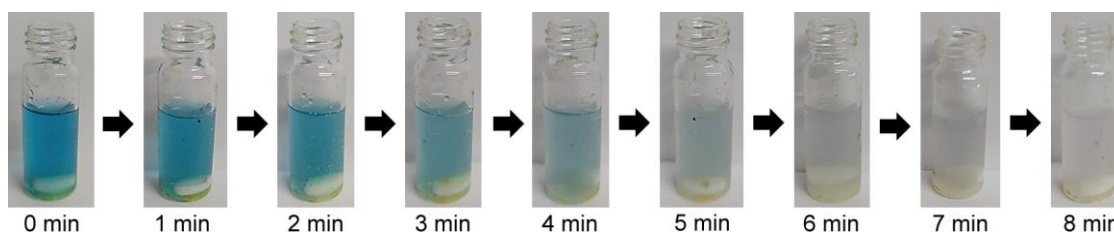
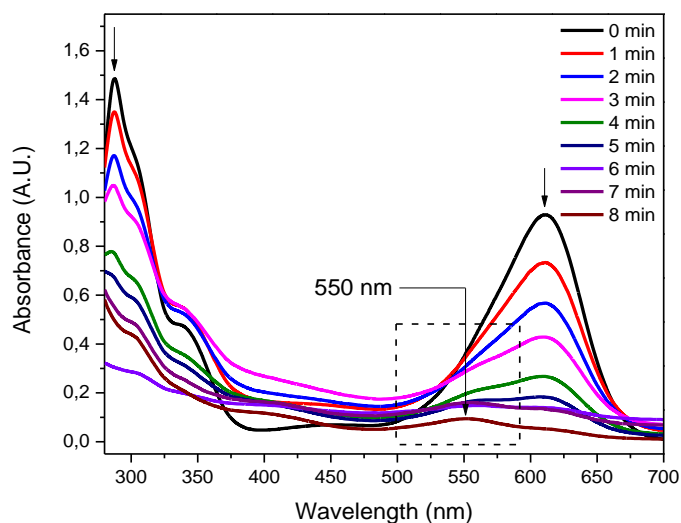


Figure 4-27: Degradation of the IC solution (50 μM) employing $\text{TiO}_2/\text{OPV 1}$ as photocatalyst under visible light.

The appearance of an absorption band at 553 nm has already been described and corresponds to a reduction anionic radical intermediate (**Figure 4-28**).²⁴⁴ Such intriguing finding provides evidence of a simultaneous direct reductive pathway that is contributing to the IC dye degradation when this $\text{TiO}_2/\text{OPV 1}$ photocatalyst is employed.

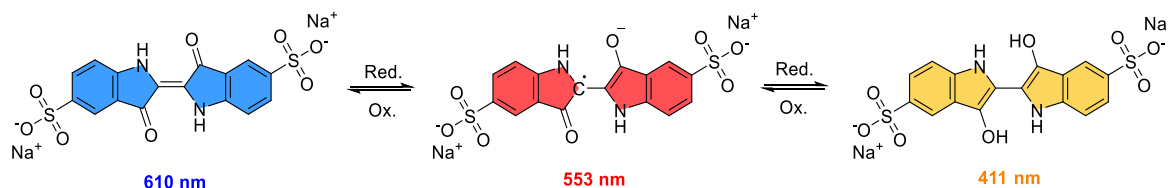


Figure 4-28: Reversible redox reaction of IC and the λ_{max} value for each specie.

To validate this hypothesis, ESI-MS experiments were conducted on the treated IC solutions (**Figure 4-29**). The mass spectrum of the light pink solution (after treatment with $\text{TiO}_2/\text{OPV 1}$ under open atmosphere) displays a peak at 421 m/z that corresponds to the previously outlined

IC anionic radical intermediate (MW = 422.38, $[M-H]^- = 421.38$). Moreover, peaks at m/z 226 and 216 are attributed to isatin-5-sulfonic acid, and 4-amino-3-carboxybenzenesulfonate as IC oxidation products, respectively. Furthermore, the ESI-MS spectrum of the IC solution treated with $\text{TiO}_2/\text{OPV 1}$ under inert atmosphere shows again a peak at m/z 226, consistent with isatin-5-sulfonic acid as IC oxidation product, and a peak at m/z 198 that corresponds to indoline sulfonic acid, an IC reduction product that has been previously identified by mass spectrometry.¹⁵⁵

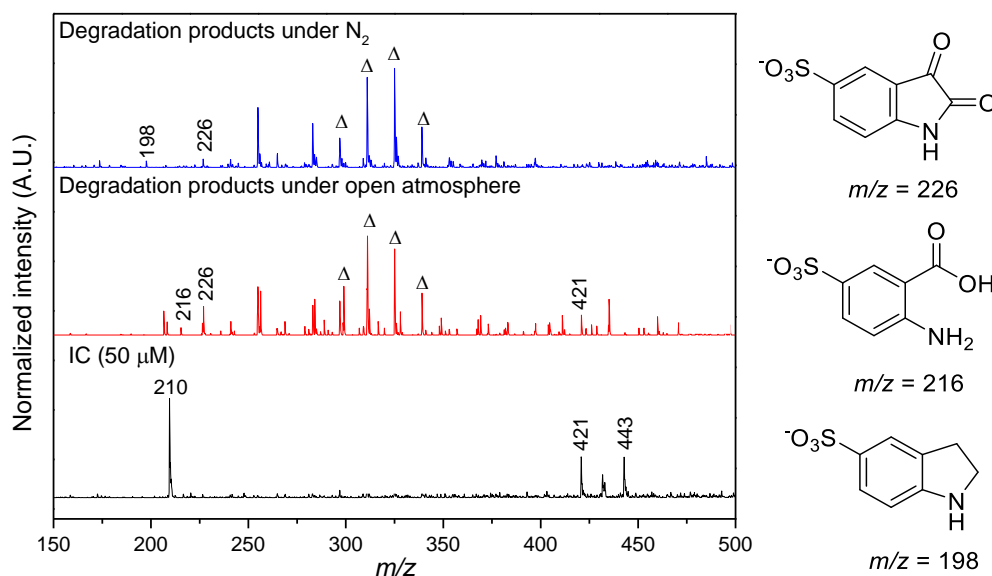


Figure 4-29: Mass spectra set for the degradation of 50 μM IC aqueous solution under different conditions using $\text{TiO}_2/\text{OPV 1}$ as photocatalyst. Marked peaks (Δ) correspond to previously identified OPV degradation products.

In all cases, peaks at m/z 297, 311, 325, and 339 associated with **OPV 1** degradation products were observed, suggesting that the conjugated grafted material is, to some extent, being affected by the ROS generated during the photocatalytic process. Furthermore, considering the previous results, it is evident that the IC photodegradation proceeds via a simultaneous oxidative/reductive pathway when $\text{TiO}_2/\text{OPV 1}$ is employed as a photocatalyst under visible light illumination. In this regard, **Figure 4-30** provides a schematic IC degradation pathway that merges the oxidative degradation of the dye via reaction with superoxide radical (Route 1), and the direct reduction of the pollutant (Route 2), after the electron injection from the visible light excited **OPV 1** to the TiO_2 conduction band.

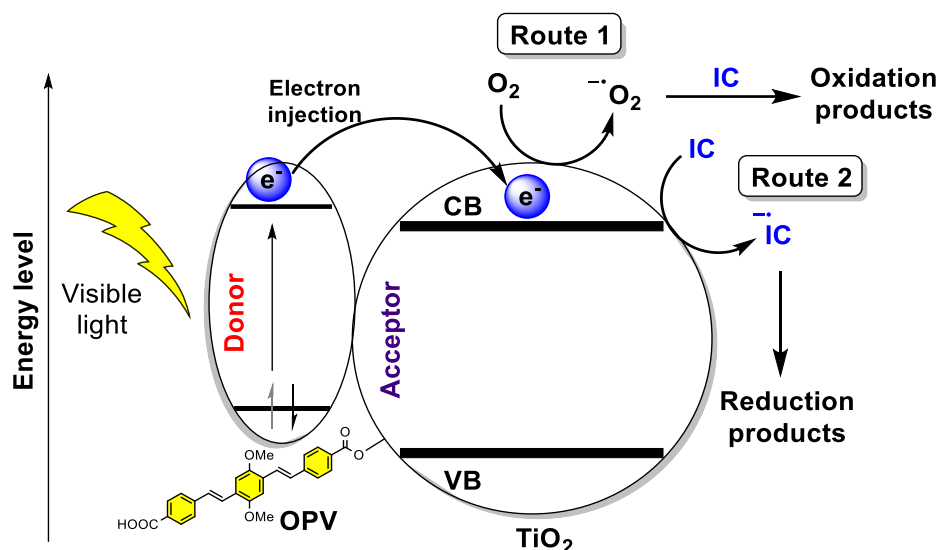


Figure 4-30: Photocatalytic schematic IC degradation pathway, employing TiO_2/OPV 1 and visible light.

An analogous approach to assess the generated species employing radical scavengers was also explored for materials **Pol-1** and **Pol-2** under 350-450 nm light irradiation (**Figure 4-31**). The outcomes indicate that the polymers can generate superoxide radicals and singlet oxygen as oxidant species. Additionally, their release can be suppressed by the effect of benzoquinone (Bz) and azide scavengers, respectively. With this information, a direct degradation pathway analogous to the one observed in SiO_2 adsorbed **OPV 1** material explored in Chapter 3 can be inferred, considering that the degradation keeps taking place under inert atmosphere. Furthermore, the addition of oxalic acid significantly improved the dye degradation process by rapidly regenerating the vacant LUMO level in the polymer, suggesting the use of electron donors can serve as a strategy to boost the IC discoloration.

In contrast to TiO_2/OPV 1 material, a simultaneous reductive pathway for the polymers was not conceived based on the experimental evidence that confirms not only a complete loss of the IC absorption band at 610 nm, but the absence of additional bands in the visible region that might have been formed throughout the photocatalytic process (**Figure 4-32**).

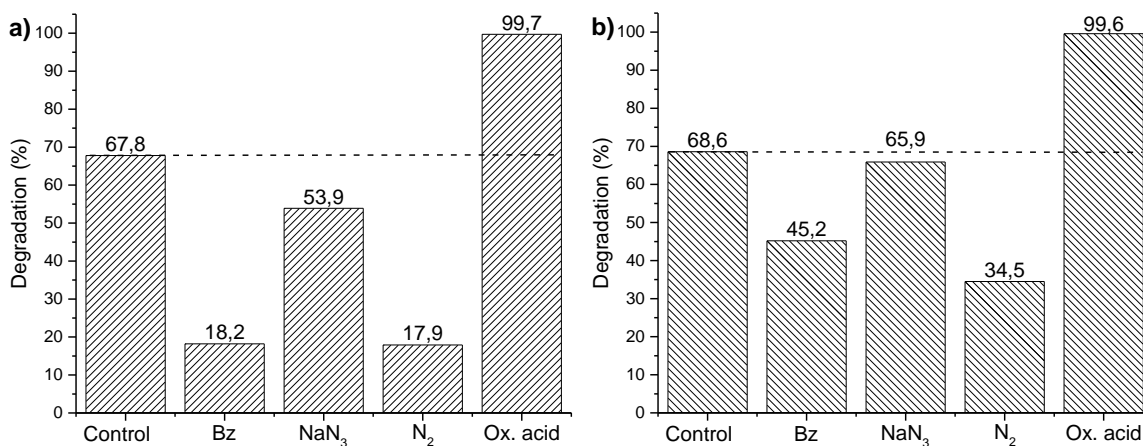


Figure 4-31: (a) Effect of scavengers and electrons donors in the IC photodegradation for **Pol-1** at 25 min, and (b) **Pol-2** at 30 min.

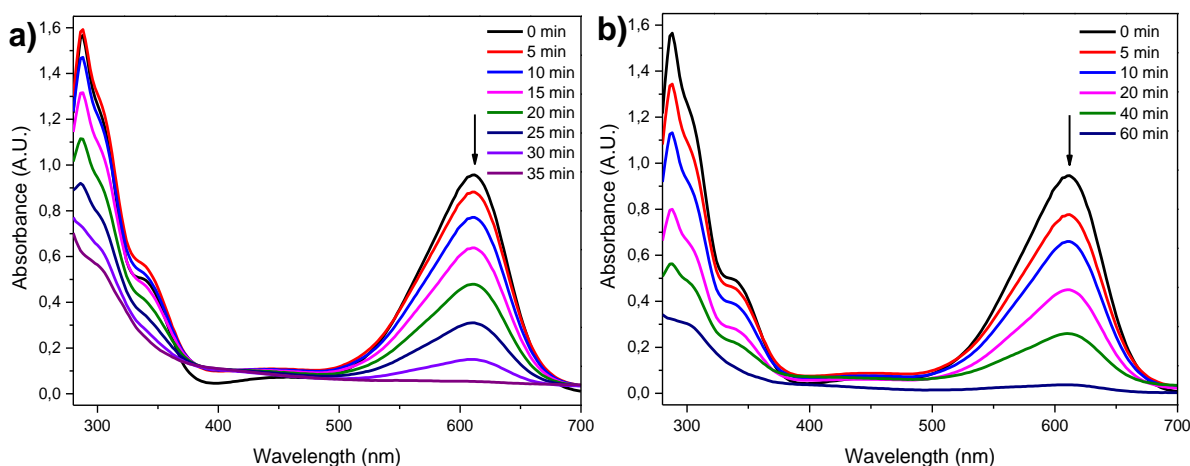


Figure 4-32: Degradation of the IC solution (50 μM) employing (a) **Pol-1**, and (b) **Pol-2** as photocatalysts.

Additionally, the reusability of the materials was evaluated as an approach to estimate their stability as heterogeneous photocatalyst compared to the SiO₂ adsorbed **OPV 1** studied in Chapter 3. As shown in **Figure 4-33**, a significant improvement was achieved for **TiO₂/OPV 1** and **Pol-1** materials, displaying a decrease in their photocatalytic activity to 84% and 96% after five cycles of use, respectively. In contrast, **Pol-2** showed a dramatic reduction of photocatalytic activity achieving only a 33% value in the fourth cycle. Moreover, **OPV 1** adsorbed onto TiO₂ (**TiO₂/OPV 1** (adsorbed), 0.049 mmol/g) was evaluated as reference material and displayed only a 28% degradation efficiency after the third reuse cycle. This result ratifies that the stability of **TiO₂/OPV 1** arises directly from the covalent grafting process, which prevents lixiviation and

simultaneous degradation of the organic framework. It should be disclosed that the reuse of **OPV 1** was also assessed. However, poor reproducibility and significant variation of the IC degradation percentage between cycles were observed as a result of deficient surface wettability, which prevents homogeneous adsorption of reactants on the surface.

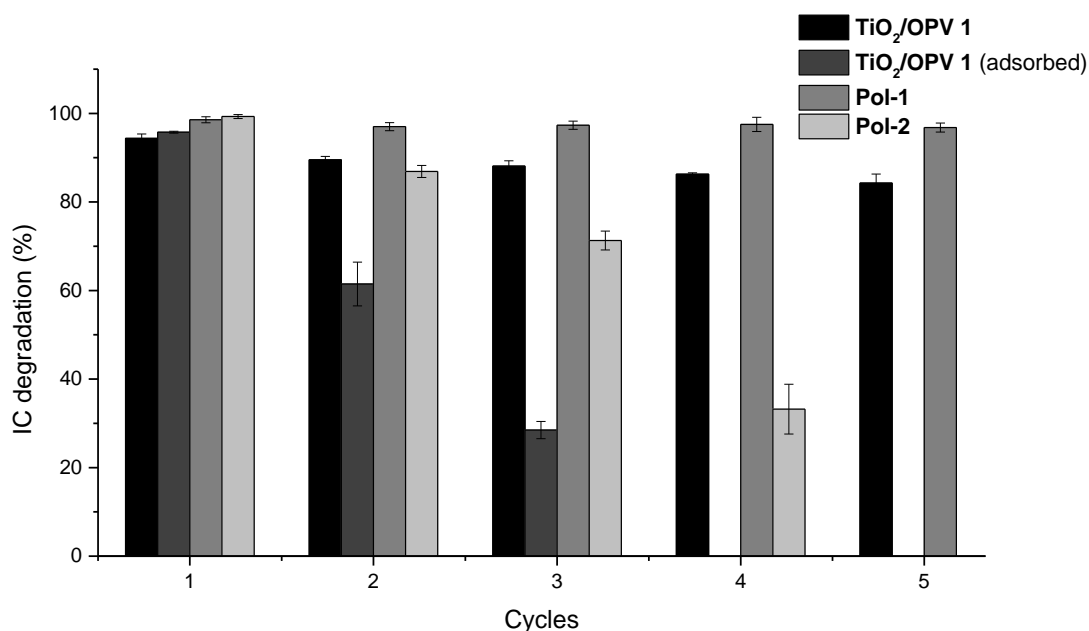


Figure 4-33: Reusability of **TiO₂/OPV 1**, **Pol-1** and **Pol-2** in the degradation of 50 μM IC aqueous solution.

Finally, Raman scattering and IR spectroscopy were chosen as techniques to assess the OPV molecular integrity in **TiO₂/OPV 1** and **Pol-1** materials along with the grafting endurance on the TiO₂ surface after 5 photocatalytic cycles. The comparative Raman spectra set (**Figure 4-34a**) displays no change in the TiO₂ anatase phase vibrational modes. However, a nearly 50% intensity decrease in the signals ascribed to the grafted-OPV material clearly suggests a combination of partial lixiviation and degradation of the photosensitizer. This outcome confirms once more that the OPV immobilization on TiO₂ represents an effective strategy to reduce its photodegradation, taking into consideration that ROS generation now occurs principally on the surface of TiO₂, and not directly on the OPV moiety. In consequence, the chance of the vinyl bridge scission through the heterogeneous photocatalytic process is remarkably minimized.

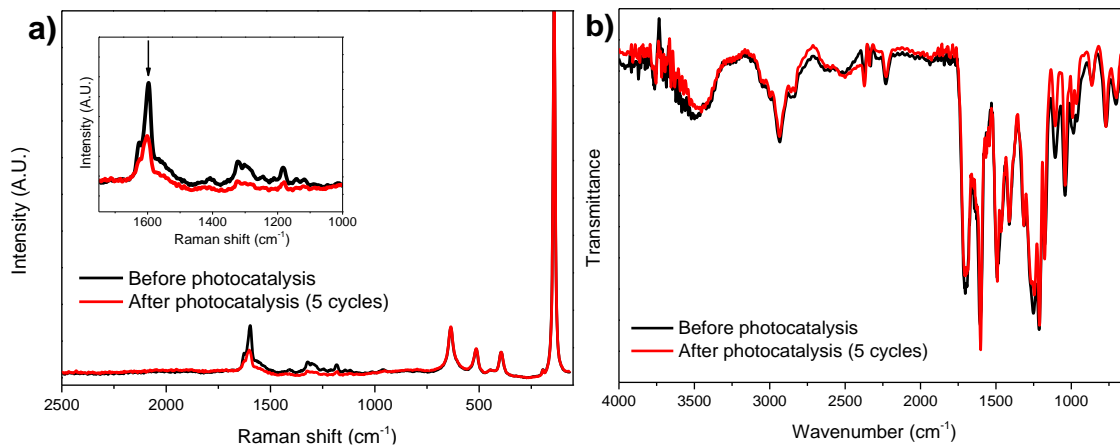


Figure 4-34: (a) Raman spectra set for **TiO₂/OPV 1**, and (b) IR spectra set for **Pol-1** before photocatalysis and after 5 photocatalytic cycles.

Likewise, an attenuation in the intensity of the signals in 1710 and 1105 cm⁻¹ for **Pol-1** was observed (**Figure 4-34b**). These bands, ascribed to C=O and C-O bond vibrations, suggest the gradual degradation of the OPV moiety in the structure. Such delayed chemical decomposition can be related to the insertion of the aromatic spacer, which renders superior π -conjugation and simultaneously secures the conformational rigidity required to lower the alkene scission via ¹O₂ and superoxide reaction.⁶⁸

Further investigation of the **OPV 1** grafted content in **TiO₂/OPV 1** after five photocatalytic cycles was performed by comparing the TGA profiles as illustrated in **Figure 4-35**. The purpose of this comparison was to determine the OPV amount removed from the TiO₂ surface throughout the photocatalytic process. Noteworthy, the thermal behavior between the photocatalyst before use and after five reaction cycles remains almost identical, suggesting no significant changes in the chemical composition of the surface. Consequently, it was established that only a difference of 1.6% in the degree of surface coverage was achieved because of OPV lixiviation or ROS-induced degradation processes.

All the information gathered through this research confirms that the OPV immobilization on TiO₂ and the copolymerization, employing a rigid spacer, comprise effective strategies to reduce the conjugated backbone fragmentation as a result of its reaction with the generated ROS throughout the heterogeneous photocatalytic process.

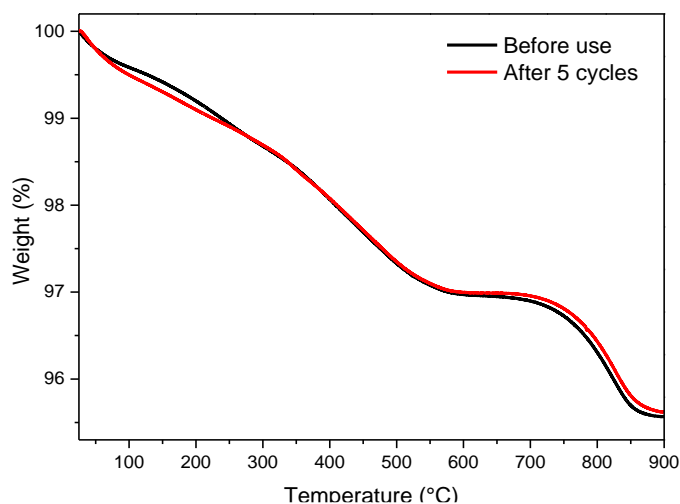


Figure 4-35: Comparative TGA profiles of the $\text{TiO}_2/\text{OPV 1}$ photocatalyst before use, and after five photocatalytic cycles.

4.4 Conclusions

It was demonstrated that the grafting of the carboxylic acid **OPV 1** derivative in the commercially available TiO_2 Degussa P25 via trimethylsilylation of the surface titanol groups, and **OPV 1** copolymerization employing tetrafluoroterephthalonitrile, serve as effective methodologies to develop more efficient and stable PV-based heterogeneous photocatalysts for the degradation of indigo carmine dye. For $\text{TiO}_2/\text{OPV 1}$, the scavenging experiments confirmed that the photodegradation proceeds mainly via the generation of superoxide radicals and singlet oxygen after electron injection from the excited OPV to the TiO_2 conduction band. Moreover, a direct reductive pathway was found to participate in this reaction. It was also confirmed that electrons donors play a negligible role in boosting photocatalytic efficiency. Alternatively, for **Pol-1**, the photocatalysis proceeds only via superoxide radicals, singlet oxygen and direct oxidation, resembling the activity of **OPV 1** (Chapter 3). Finally, the reusability study confirmed an outstanding improvement in the stability of the OPV conjugated system up to 84% for $\text{TiO}_2/\text{OPV 1}$ and up to 96% for **Pol-1** in the fifth photocatalytic cycle, validating that such chemical modifications preserve the organic conjugated motif throughout photocatalysis.

5. Other photocatalytic applications

Abstract

Considering that **TiO₂/OPV 1** and **Pol-1** materials have stood out as the most promising OPV-based photocatalysts throughout this research, additional applications concerning the treatment of a real textile wastewater sample, and the control of aqueous 17β-estradiol (E2) were explored. This approach revealed a partial decolorization of the wastewater sample, behavior ascribed to the resistance of some dyes to directly react with the excited photocatalyst and the oxygen species released in the process. Alternatively, complete removal of E2 hormone was observed for both photocatalysts. Remarkably, the appearance of a dehydroxylated reaction product when **TiO₂/OPV 1** was used, endorses the prospect of future applications for this material in visible-light-driven organic photochemical synthesis. Finally, as a contribution to assessing potential environmental risks associated with poultry farming activities, E2 was identified in poultry litter samples collected in the Santander region.

5.1 Introduction

The textile industry is considered one of the most profitable sectors in Colombia's economy. The companies within this economic group are dedicated not only to the merchandising of finished apparels but to the production and chemical treatment of fibers and fabrics. This manufacture is strongly related to the use of synthetic dyes such as indigo and indigo carmine, for which at least 50% of the water used in the dyeing process is then discharged directly on rivers, deteriorating the water quality. Surprisingly, textile wastewater effluents could display a dye content as high as 50 %.²⁴⁵

Another important activity with a remarkable economic impact in Colombia, especially in the Santander region, is poultry production.²⁴⁶ Recent research has demonstrated that poultry farms are responsible of discharging a wide variety of emerging contaminants that include pesticides, pharmaceutical formulations, and sex esterooids.²⁴⁷ These hormones are produced naturally by birds as part of their metabolism, and are released to the environment in their manure. Especial attention has been placed on 17 β -estradiol (E2), estrone (E1) and testosterone (T) for their well-known and serious physiological and reproductive effects in several living organisms, including humans (**Figure 5-1**).^{248,249} Such biogenic compounds can spread across the environment as a result of chicken bed cleaning activities, inappropriate wastewater management, and the use of chicken manure compost as a soil amendment in crops.²⁵⁰

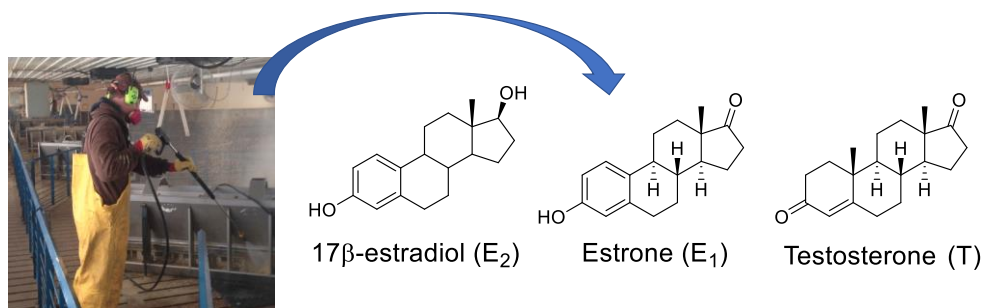


Figure 5-1: Hormones released by poultry farming activities.

Undoubtedly, the lack of adequate and affordable wastewater treatment technologies to be integrated as part of textile and poultry industries boosts light-driven processes as a low-cost and effective alternatives to counteract this problem and, simultaneously, prevent any further contamination of water resources.²⁵¹ As a result, several photocatalysts have been explored for dye degradation of textile wastewater and estrogen control; especially, those materials capable of absorbing light in the visible region of the spectrum.^{252–254}

In this chapter, the efficiency of **TiO₂/OPV 1**, and **Pol-1** materials in the photocatalytic treatment of a real textile wastewater sample and aqueous solutions of E2 was determined by monitoring the color change and the hormone concentration using UV-Vis spectroscopy and HPLC, respectively. The identification of reaction intermediates allowed to establish a transformation mechanism for E2 when **TiO₂/OPV 1** was used as photocatalyst under visible light irradiation. Moreover, poultry litter extracts of samples obtained in Santander were analyzed by HPLC to validate the presence of E2. Finally, all the obtained results are

discussed based on the photodegradation pathway identified for each material in previous chapters.

5.2 Experimental section

5.2.1 Materials

The wastewater sample was provided by a Colombian textile manufacturer, and it was collected at the outfall of the dyeing process. The dye composition of the sample is unknown. The dried poultry litter sample was collected from multiple egg production farms located in Santander, Colombia. The sample was grounded to generate a homogeneous particulate material that was subsequently frozen until analysis. 17β -estradiol was purchased from Merck. Distilled, deionized (MilliQ purification systems) water was used for HPLC experiments.

5.2.2 Analytical techniques

High-Performance Liquid Chromatography (HPLC) analyses were performed on a Thermo Scientific™ Ultimate™ 3000 LC system (Thermo Fisher Scientific, Milan, Italy) coupled to a variable wavelength detector Dionex UltiMate 3000, fixed at 281 nm. The chromatographic column employed was a reversed-phase 4.6 x 150 mm Zorbax SB-C18 (Agilent, USA) with 5 μ m particles.

HPLC method to assess 17β -estradiol photodegradation: The isocratic method consisted of methanol–formic acid (0.1 % in water) (70:30, v/v) as a solvent mixture with a flow rate of 1.0 mL/min, using 20 μ L as the injection volume, and comprises a minor modification of the method originally reported by Yilmas *et al.*²⁵⁵ The temperature of the column was kept at 25 °C. E2 standards of 50, 125, 250, 500, 750, 1000, and 2500 ng/mL were employed to construct the calibration curve (**Appendix 7.6**).

Alternative HPLC method for 17β -estradiol identification in poultry litter extracts: The isocratic method consisted of an acetonitrile-water mixture (50:50, v/v) with a flow rate of 1.0 mL/min, using 20 μ L as the injection volume according to the method originally reported

by Alqahtani *et al.*²⁵⁶ The temperature of the column was kept at 25 °C. UPLC-MS analyses of poultry litter extracts were performed on a LC-MS QTOF 9030, Nexera X2 (Shimadzu®, Duisburg, Germany) system at Pontificia Universidad Javeriana. The separation was performed on a Shimpak XR-ODS II column (150 mm x 2.0 mm, 2.2 µm) with a gradient elution program of methanol and 0.1% formic acid as the mobile phase structured as follows at a flow rate of 0.40 mL/min: 10% methanol for 1 min; to 55% methanol in 3 min; to 100% methanol in 10.5 min and until chromatographic run completion (15 min). The temperature of the column was kept at 35 °C. Electrospray ionization was applied and operated in the negative ion mode. The absorption spectra were recorded using a Thermo Scientific Evolution 300 UV-Vis spectrophotometer. The emission spectra were measured using a PTI QuantaMaster™ 40 spectrofluorometer.

5.2.3 Preparation of poultry litter extracts

The dried poultry litter sample was collected from a poultry farm located in Santander-Colombia, and kept frozen until analysis. The extracts were prepared based on a previously reported methodology.²⁵⁷ Two poultry litter leachate solutions were obtained by adding 0.5 g of thawed litter homogenate in 200 mL of HPLC-grade water (solution 1), or methanol (solution 2), and stirred at 500 rpm at 37 °C for 24 h. Then, the solutions were filtered through a filter paper (Whatman No. 1) using a Buchner funnel. These solutions were immediately analyzed to assess the 17β-estradiol content by HPLC and UPLC-MS.

5.2.4 Photocatalytic experiments

In a typical dye degradation experiment, the specified amount of catalyst was suspended on 3 mL of wastewater sample or 2.5 µg/mL 17β-estradiol solution. It should be disclosed that 2.5 µg/mL was selected as the reference concentration for E2, considering that it provides a sharp and well-defined chromatographic peak to follow its disappearance easily. For **TiO₂/OPV 1** (irradiated with white light) and **Pol-1** (irradiated with UV light) catalysts, 4 mL glass vials were employed. After irradiation, the catalyst was allowed to settle in darkness for 30 seconds, and 1 mL of the supernatant solution was extracted via syringe and filtered employing 0.22 µm PTFE membranes before the absorbance measurement or HPLC injection. The irradiated solution in each glass container was measured only once. Thus, different vials were employed to follow the color intensity of the IC solution at each

time interval. In all cases, the suspension was left for 15 min in darkness to ensure the adsorption equilibrium was reached preceding irradiation. The temperature was maintained constant at 20 °C using circulated water, and the experiments were performed under a continuous low-stirring regime (100 rpm).

5.3 Results and discussion

5.3.1 Discoloration of an actual textile wastewater sample

Preliminary characterization of the wastewater sample employing UV-Vis absorption spectroscopy was carried out to select a suitable λ_{\max} value in the visible region to monitor the photocatalytic process. The spectrum (**Figure 5-2**) clearly displays an absorption band with a maximum at 598 nm. Additional relevant chemical characterization of the wastewater sample is summarized in **Table 5-1**. It should be noted that the pH value is very close to 7.0, which allowed the direct use of the photocatalysts without any additional adjustment of the H^+ ions concentration; therefore, ensuring identical experimental conditions to those previously described in Chapter 4.

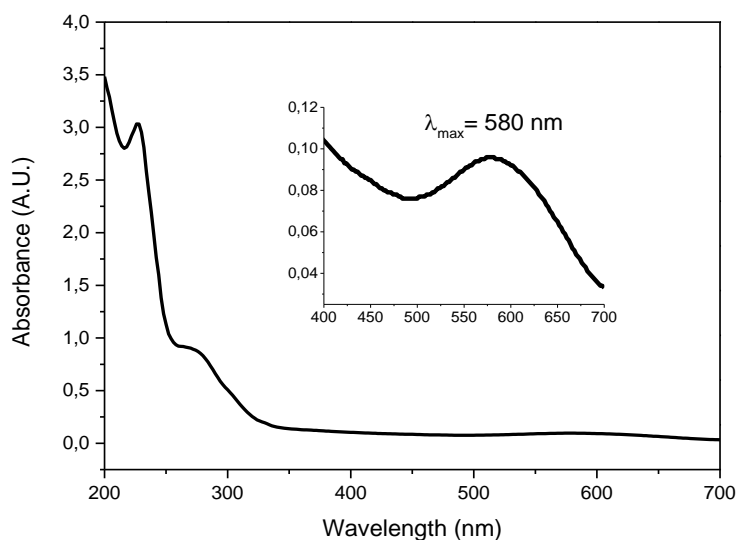


Figure 5-2: UV-Vis spectrum of the 1:5 diluted wastewater sample. Inset displays a close-up of the absorption band within the visible region.

Table 5-1: Textile wastewater sample chemical analysis results.

Analysis item	Unit	Value
pH	pH units	7.18
Total suspended solids	mg/L	5.65
Sulfate	mg/L SO ₄ ²⁻	461.0
Sulfide	mg/L S ²⁻	1.0
Total alkalinity	mg/L CaCO ₃	103.0
Chloride	mg/L Cl ⁻	19.7
COD	mg/L O ₂	354

An initial examination of **TiO₂/OPV 1** performance under visible light was carried out, where a 46% discoloration efficiency was achieved in 14 minutes of irradiation (**Figures 5-3 and 5-4**). Experiments in the absence of photocatalyst corroborate the dye stability in the sample under the employed irradiation conditions. Moreover, dark experiments displayed no major modification of the color intensity in the wastewater sample.

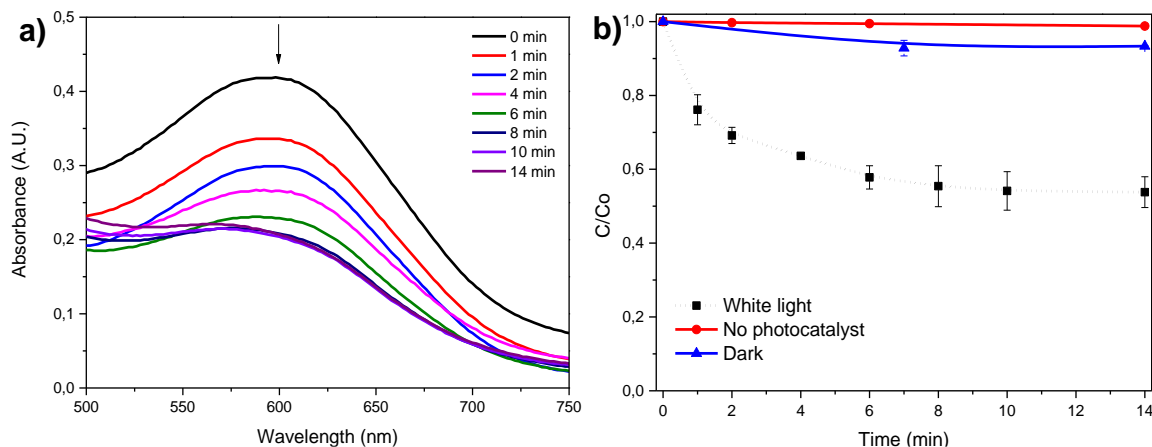


Figure 5-3: (a) Induced discoloration of wastewater, and (b) discoloration profile at wastewater λ_{\max} employing **TiO₂/OPV 1** as photocatalyst under white light irradiation.

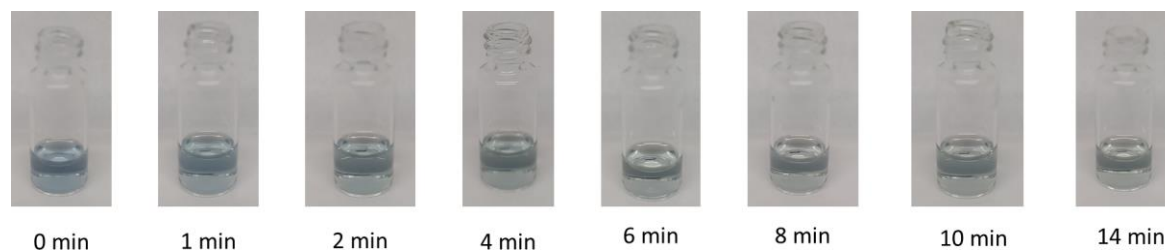


Figure 5-4: Color degradation profile of the wastewater sample during the photocatalytic process.

Noteworthy, the real-sample conditions and the possible presence of highly nucleophilic substances prompted the cleavage of the **OPV 1** from the TiO_2 surface, as evidenced from the increase in the fluorescence intensity of the solution, which matches the emission profile of the **OPV 1** moiety (**Figure 5-5**). This experimental observation can be attributed to a photocatalyst deactivation, which explains the plateau observed in the color degradation profile (**Figure 5-3**). It should be disclosed that **OPV 1** alone does not exhibit any photocatalytic activity under white light illumination (**Figure 4-23**).

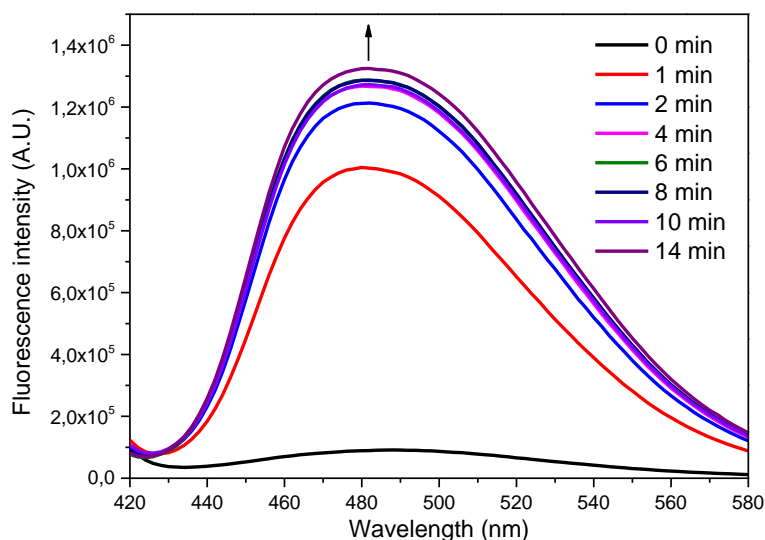


Figure 5-5: Fluorescence intensity increase of the wastewater sample during the photocatalytic process with $\text{TiO}_2/\text{OPV 1}$ under visible light.

Furthermore, **Pol-1** was also evaluated as a photocatalyst in the treatment of the same wastewater sample (**Figure 5-6**). In contrast, only a 25% discoloration efficiency was achieved within 40 minutes of irradiation (350-450 nm). The same plateau behavior was observed, suggesting a major chemical modification of the **Pol-1** photocatalyst surface. Thus, leading to a significant decrease in the photocatalytic activity. Moreover, the 21% difference in discoloration efficiency of **Pol-1** when compared to $\text{TiO}_2/\text{OPV 1}$ may be ascribed to the lack of the additional direct reductive pathway observed in the grafted solid material. Once more, dark experiments and those in the absence of photocatalyst indicate the sample does not undergo photolysis under the employed irradiation conditions and that light is required to initiate the dye degradation process.

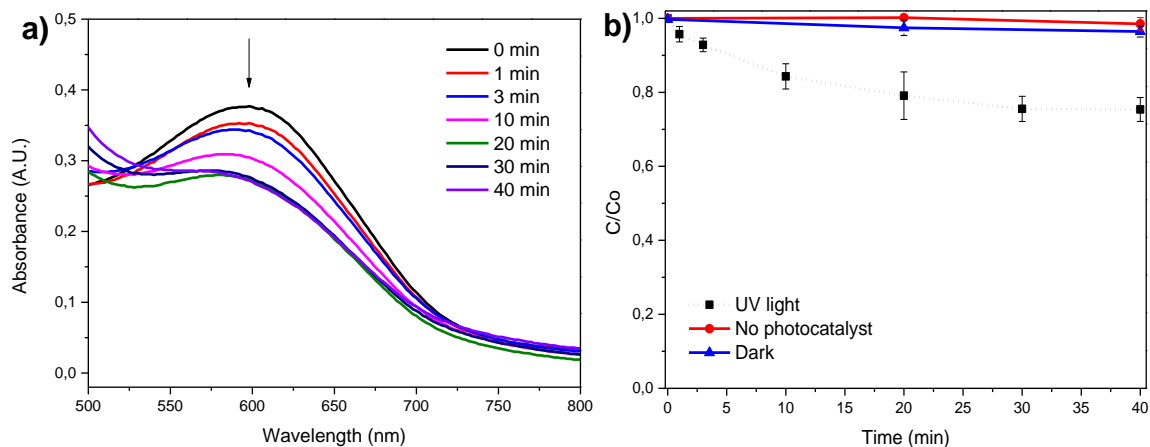


Figure 5-6: (a) Induced discoloration of wastewater, and (b) discoloration profile at wastewater λ_{\max} (b) employing **Pol-1** as photocatalyst under UV irradiation (350-450 nm).

With this information in hand, it is evident that **TiO₂/OPV 1** exhibited the best photocatalytic performance among the materials evaluated, with the advantage of using visible light to trigger the process. However, it is necessary to combine additional treatment strategies such as adsorption, coagulation, or electrochemical oxidation to achieve complete decolorization of the wastewater sample.

5.3.2 Control of aqueous 17- β estradiol

An exploratory assessment of the UV absorption profile for 17- β estradiol in methanol was initially carried out to determine its λ_{\max} value, and therefore maximize the instrumental response, taking into consideration that our HPLC system is coupled to a UV detector. It was confirmed that 281 nm corresponds to the maximum absorption wavelength for the analyte, and it was used as the default configuration to measure the absorbance in the chromatographic system (**Figure 5-7**).

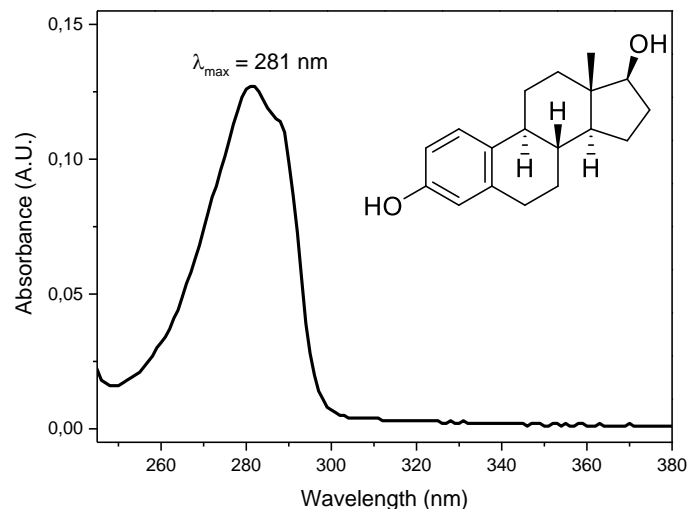


Figure 5-7: UV spectrum of 17- β estradiol.

The photodegradation experiments employing **TiO₂/OPV 1** as photocatalyst under white light illumination displayed a 97% decrease in the concentration of E2 after seven minutes of reaction (**Figure 5-8**). Moreover, additional experiments confirmed that this hormone does not undergo decomposition when white LEDs (without any photocatalyst) are used and that the reaction does not occur in darkness. Thus, validating a photocatalytic transformation pathway. Remarkably, after comparing the HPLC traces of the photocatalytic process with the blank experiment (irradiation of **TiO₂/OPV 1** in type-I water), the formation in time of a major reaction product with $T_R=2.6 \text{ min}$ was clearly identified (**Figure 5-9**).

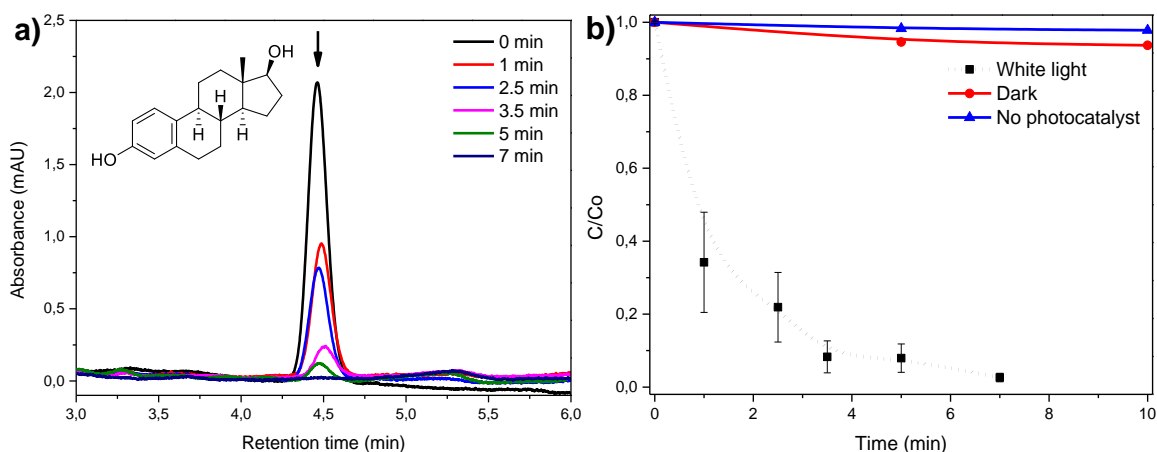


Figure 5-8: (a) HPLC traces of a E2 solution (2500 ng/mL) throughout photodegradation, and (b) degradation profile employing **TiO₂/OPV 1** as photocatalyst under white light irradiation.

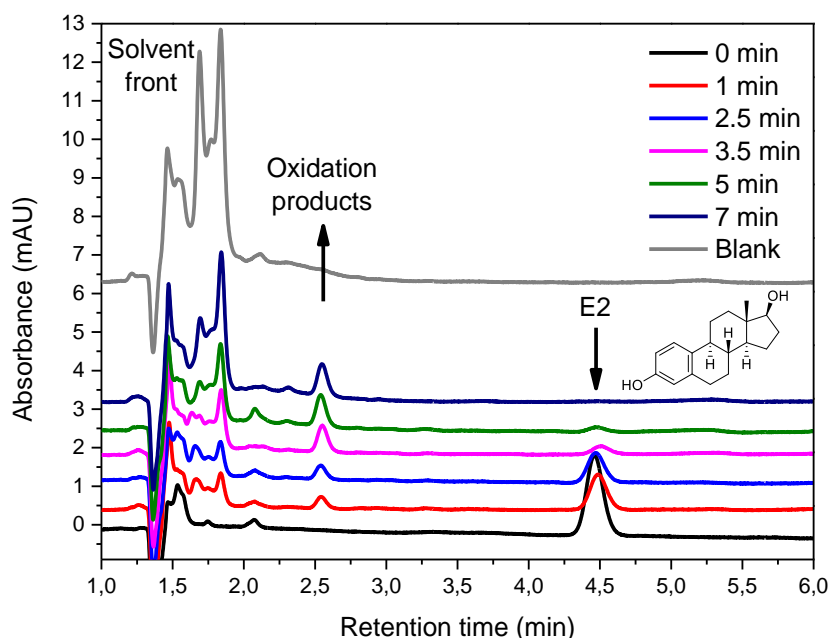


Figure 5-9: Total HPLC chromatograms of an E2 solution (2500 ng/mL) during photocatalysis with $\text{TiO}_2/\text{OPV 1}$ under white light irradiation.

To unveil the chemical identity of the observed major product, UPLC-MS (negative mode) was employed to monitor $[\text{M}-\text{H}]^-$ ions that have been previously identified in literature during E2 photocatalytic degradation (**Figure 5-10**).^{258,259} Exact coincidences were found for m/z 255, 285, and 303, which displayed five different chromatographic peaks. The plausible structure of the products can be found in **Table 5-2**. As expected, the identified compounds for m/z 285 and 303 can be attributed to the reaction of E2 with the generated superoxide radicals, and singlet oxygen, through an oxidative pathway. However, the structure associated to m/z 255 corresponds to a dehydroxylated reduction product, validating the dual oxidation/reduction character of $\text{TiO}_2/\text{OPV 1}$ photocatalyst. It should be disclosed that the earlier appearance of the peak at $T_R=2.6$ min in the HPLC-UV chromatogram (**Figure 5-9**) indicates a more polar character of the eluted compounds. Thus, it can be ascertained that this new chromatographic signal corresponds to either a single E2 oxidation product or the coelution of the oxygenated identified substances. Moreover, the absence of the less polar dehydroxylated product in the HPLC-UV chromatogram can be explained in terms of the unsuccessful identification at 281 nm, as a result of a blueshift in the absorption maximum for this compound after the loss of the OH group in the aromatic ring.

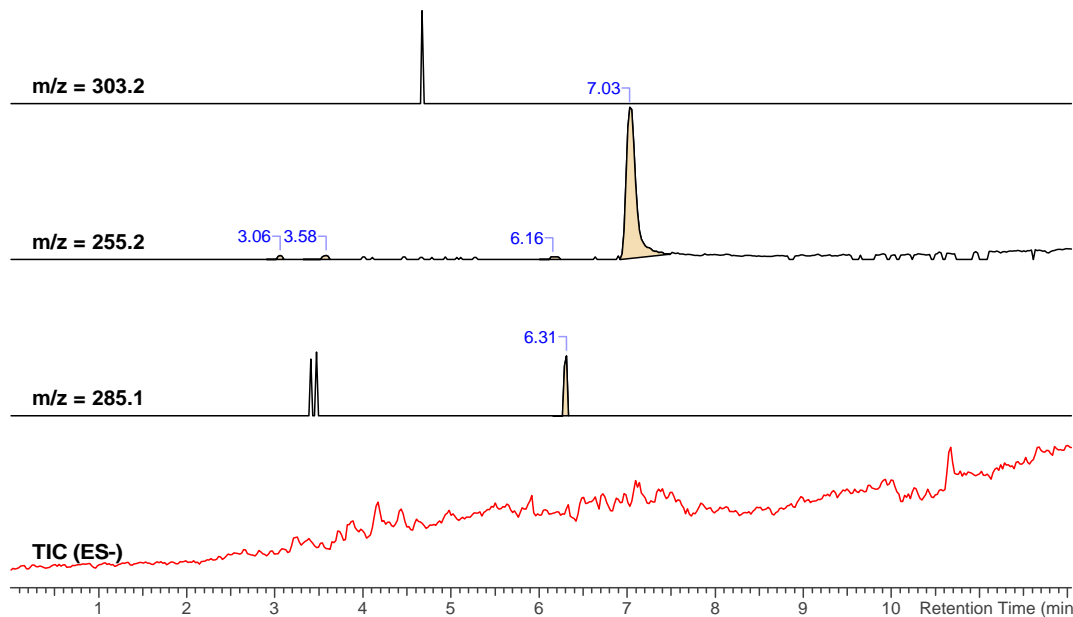


Figure 5-10: TIC trace and single ion curves of the ions at m/z 255, 285 and 303 for the E2 solution (2500 ng/mL) after five minutes treatment with $\text{TiO}_2/\text{OPV 1}$ under white light illumination.

Table 5-2: Probable structures of products after photocatalytic treatment of aqueous E2 with $\text{TiO}_2/\text{OPV 1}$.

m/z [M-H] ⁻	Probable products
255.2	 MW 256,39
285.1	 MW 286,37 MW 286,37 MW 286,37
303.2	 MW 304,39

On the other hand, when **Pol-1** was used as a photocatalyst, the E2 concentration decreased 96% approximately after 10 minutes of illumination with 350-450 nm light (**Figure 5-11**). Once again, experiments without photocatalyst confirm that E2 is very stable under the employed irradiation conditions. Moreover, although a 20% decrease in E2 concentration is observed when **Pol-1** was used in dark conditions, the reaction with **Pol-1** under UV light undoubtedly corresponds to a photocatalytic transformation.

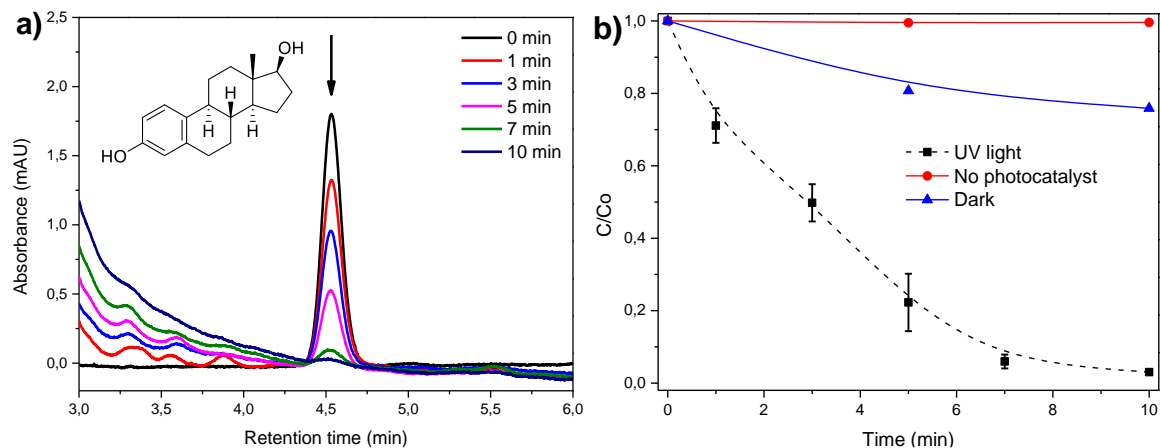


Figure 5-11: (a) HPLC traces of an E2 solution (2500 ng/mL) throughout photodegradation, and (b) degradation profile employing **Pol-1** as photocatalyst under UVA light irradiation.

Noteworthy, despite the E2 chromatographic peak is disappearing over time, no isolated additional signal related to a degradation product for this hormone is distinguishable when comparing the HPLC traces with the blank experiment, where **Pol-1** photocatalyst was irradiated while immersed in type-I water (**Figure 5-12**). Considering that **Pol-1** photocatalysis chiefly involves the generation of $O_2^{\cdot-}$, the same chromatographic peak attributed to oxidation products at 2.6 min was expected. However, it was completely overlapped by the elution of **Pol-1** degradation fragments.

As previously established, both **TiO₂/OPV 1** and **Pol-1** photocatalyst can significantly reduce the concentration of E2 in water samples. Although these materials can't generate OH radicals to prompt mineralization of the organic pollutants, it has been demonstrated that the E2 photocatalytic oxidation products exhibit a negligible estrogenic activity compared to their parent compound.²⁶⁰ Therefore, the treatment of poultry wastewater samples with these photocatalysts is expected to control the severe effects in living organisms caused by the release of hormones to the environment.

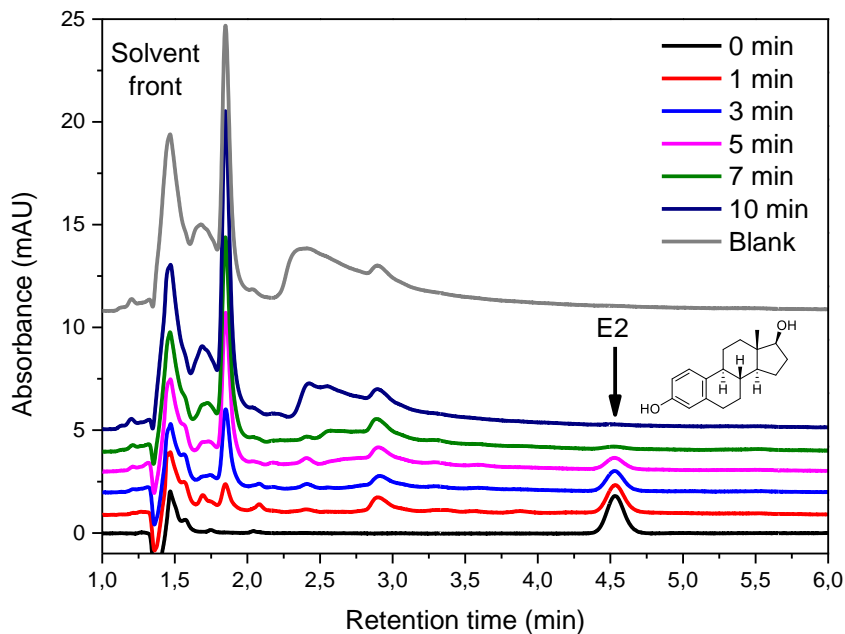


Figure 5-12: Total HPLC chromatograms of a 17 β -estradiol solution (2500 ng/mL) during photocatalysis with **Pol-1** under UVA light irradiation.

Finally, and as a contribution to the poultry industry in the Santander region (Colombia), a sample of dried poultry litter collected in different egg production farms was analyzed to determine the presence of E2 in this material and its potential migration to the environment. Although E2 concentration in litter leachates has been found to be up to 0.73 ng/mL (in other countries),²⁶¹ it has also been described that the amount of hormone can be directly related to the sample conditions (temperature, storage conditions, etc.) and geographic location.²⁵⁷

The hormone content examination involved the preparation of two different extracts, aqueous and alcoholic, that were injected into the HPLC system. The retention time of the obtained peaks was compared with a 17- β estradiol standard. The use of formic acid (0.1%)/methanol 30:70 %v/v as mobile phase displayed no exact coincidence of the retention time values of the chromatogram peaks (**Figure 5-13**). However, a peak at 4.79 min in the methanol extract was found to be within 10% variation range of the T_R for E2. Thus, a modification of the mobile phase was carried out as an attempt to verify the presence of E2 in the sample thoroughly.

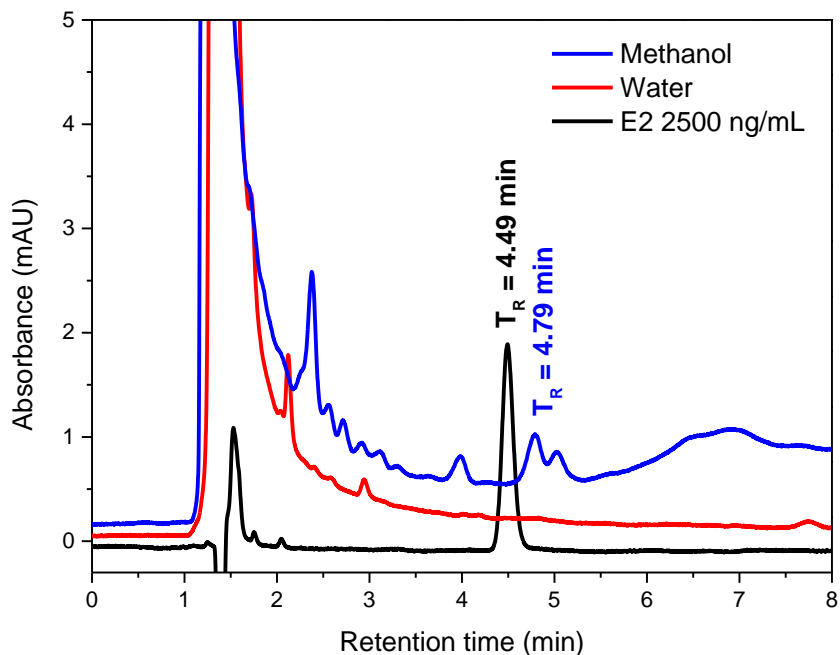


Figure 5-13: Comparative HPLC traces between 17- β estradiol standard and the obtained poultry litter solutions extracted with water and methanol (mobile phase: formic acid (0.1%)/methanol 30:70 %v/v).

With the new mobile phase arrangement (acetonitrile/water 50:50 %v/v), a difference of 11% in the T_R between the unknown peak and E2 was observed (**Figure 5-14**). Thus, it can be unequivocally demonstrated that 17- β estradiol was not detected under the employed chromatographic conditions.

The high-sensitivity technique UPLC-MS was additionally employed to assess the poultry litter extracts qualitatively. The results show a chromatographic peak for both solutions at the same retention time as that one displayed by the E2 standard (**Figure 5-15**). A thorough examination of the MS spectrum for each chromatographic peak at $T_R = 5.87 \pm 0.02$ min allowed an unequivocal confirmation of the presence of E2 in both aqueous and methanolic solutions (**Appendix 7.7**). All the MS spectra in the extracts exhibit the same m/z peaks observed in the E2 standard, and correspond to the $[M-H]^-$ (m/z 271.30), $[M+Na-2H]^-$ (m/z 293.25) and $[M+Br]^-$ (m/z 351.2) adducts. Therefore, it was proven and first reported that 17- β estradiol is present in poultry litter samples from Santander and that this hormone can migrate to water streams jeopardizing aquatic ecosystems in the region.

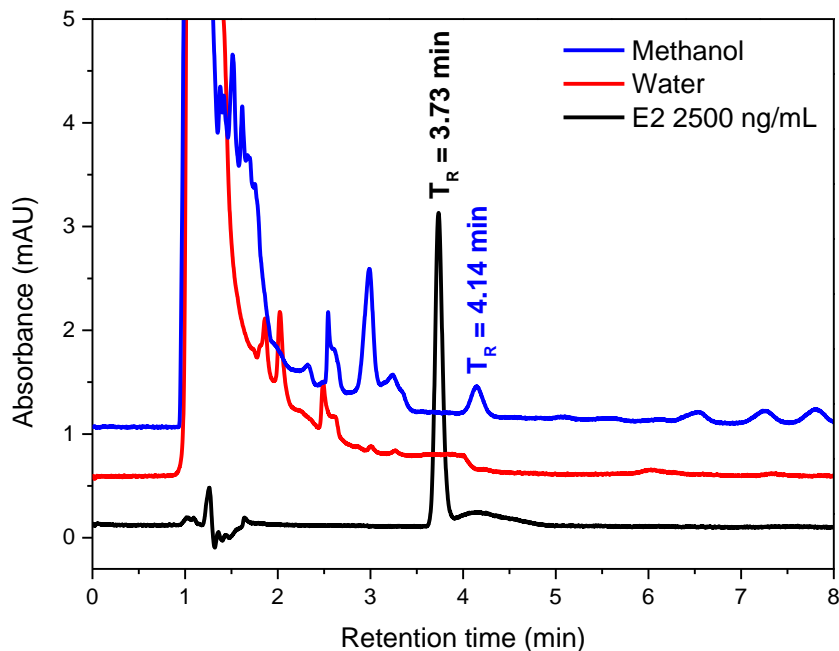


Figure 5-14: Comparative HPLC traces between 17- β estradiol standard and the obtained poultry litter solutions extracted with water and methanol (mobile phase: acetonitrile/water 50:50 %v/v).

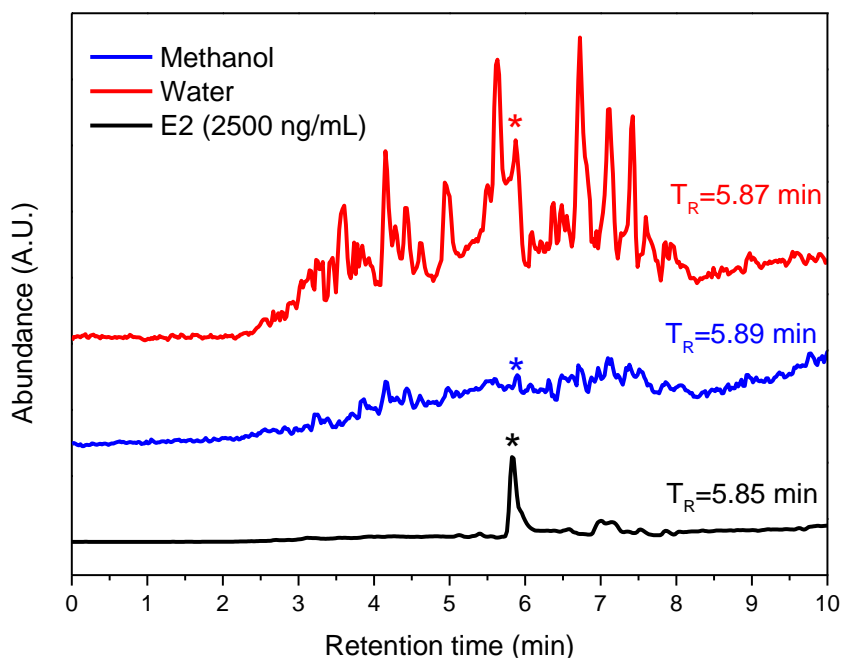


Figure 5-15: Comparative UPLC-MS TIC traces between the 17- β estradiol standard and the obtained poultry litter solutions extracted with water and methanol.

5.4 Conclusions

The efficacy of **TiO₂/OPV 1** and **PoI-1** photocatalysts in the control of an actual textile industry wastewater sample and aqueous 17- β estradiol was successfully assessed. Both materials displayed moderate discoloration when applied to the textile wastewater sample, ascribed to the deactivation of the photocatalysts under the real sample conditions. Also, **TiO₂/OPV 1** showed an additional 21% discoloration capacity which can be related to the additional direct reductive photocatalytic pathway unveiled for this material. Alternatively, a remarkable control of the E2 content and inherent estrogenicity was observed for both photocatalysts, where some oxidation and reduction products were identified by UPLC-MS. It should be noted that these outcomes validate once more the previously established oxidative/reductive character of **TiO₂/OPV 1**. The obtained results also suggest that **TiO₂/OPV 1** and **PoI-1** materials can serve as a starting point to develop innovative photocatalytic systems that can be implemented within the poultry industry to reduce the environmental impact of this economic activity. Moreover, the qualitative identification of E2 in poultry litter extracts from samples gathered in the Santander region allows recognizing the potential environmental threat as a result of poultry farming activities.

6. Perspectives

The OPV derivatives prepared in this work have demonstrated an outstanding potential as heterogeneous photocatalysts in the control of aqueous pollutants including an example of the so-called emerging contaminants. It should be disclosed that this contribution comprises the first attempt of Macromolecules research group to improve the performance and photostability of the OPV conjugated moiety for heterogeneous photocatalytic applications and may become the starting point for the future development of other OPV-based materials with enhanced photocatalytic properties. However, further studies are still required to broaden their applicability.

A thorough survey of the impact of adding other EWG, not only in the flanking aryl rings but in the central ring and vinyl bridges, in the photostability of the OPV backbone should be performed as an important step forward in the development of organic photocatalytic materials. Moreover, the modification of the *E-E* geometry within the OPV conjugated framework may provide unprecedented optoelectronic and photocatalytic properties, in view of a possible modification of the effective π -conjugation along the structure.

The preparation of OPV-copolymers with different chain lengths and miscellaneous spacers of different chemical nature could provide a more accurate insight of the effect of molecular composition on photostability and photocatalytic properties for these materials. For this purpose, additional synthesis tactics to expand the chemical diversity of OPV-copolymers using alternative rigid and flexible spacers and entailing an accurate control of the molecular weight of the polymeric chain should be examined.

To further explore the impact of the OPV-grafted content on the TiO₂ solid support, additional synthetic methodologies should be investigated to provide a meticulous and tailored degree of surface coverage. This, as an attempt to maximize the photocatalytic response in function of the surface OPV concentration. Moreover, the effect in the photocatalytic properties of analogous materials containing different TiO₂ supports with

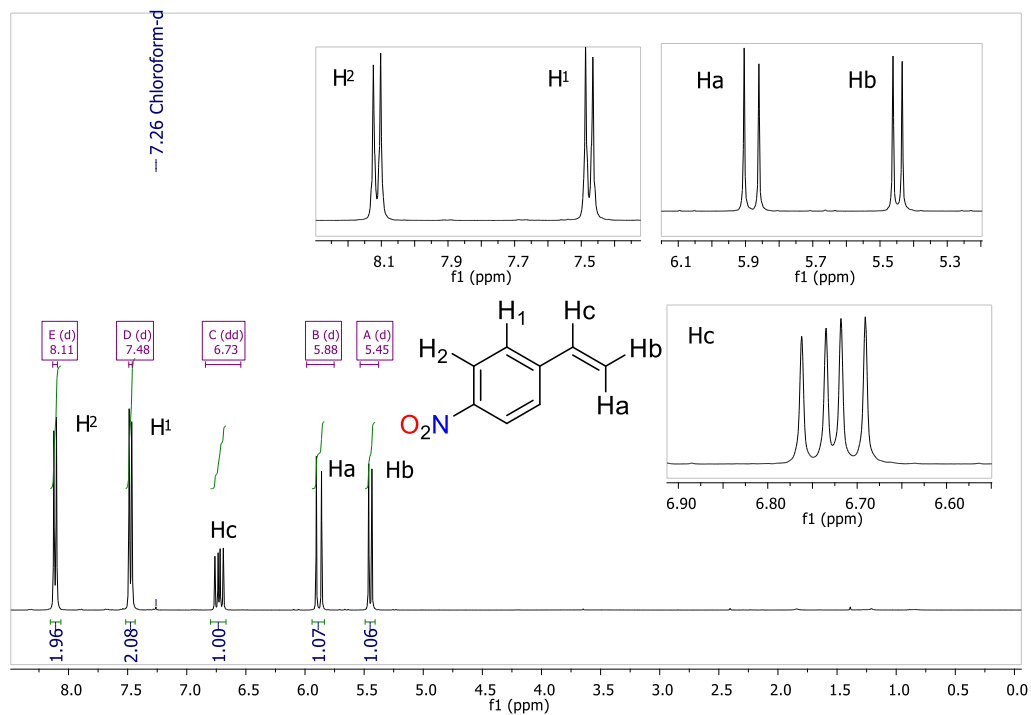
enhanced textural properties should be evaluated to boost the design of novel visible light-active photocatalysts.

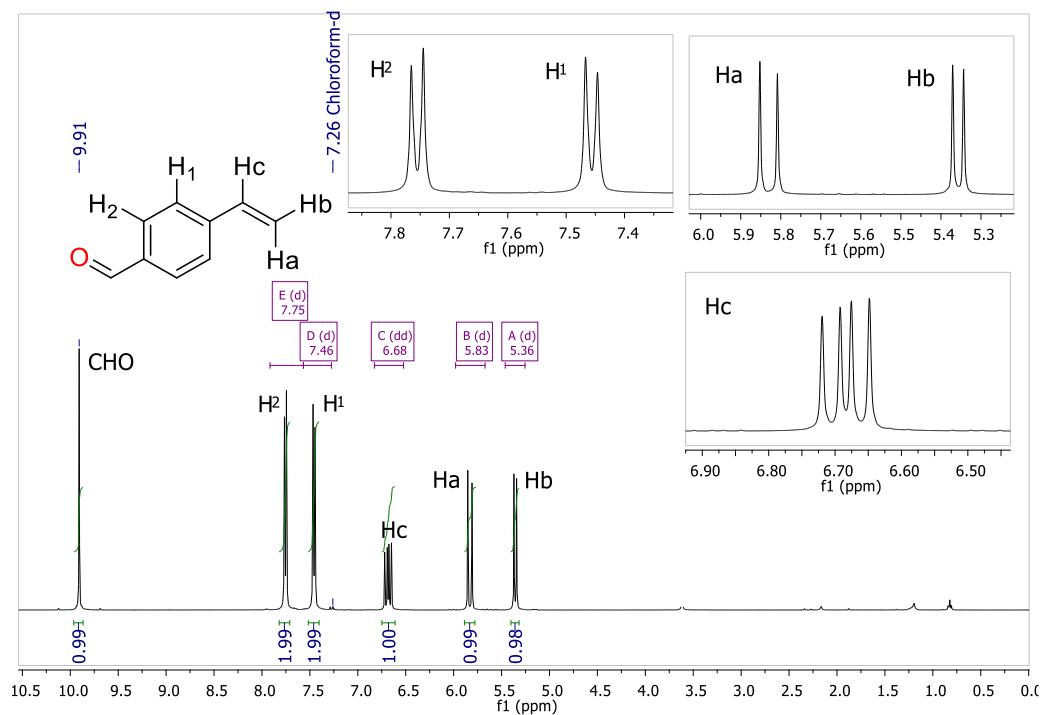
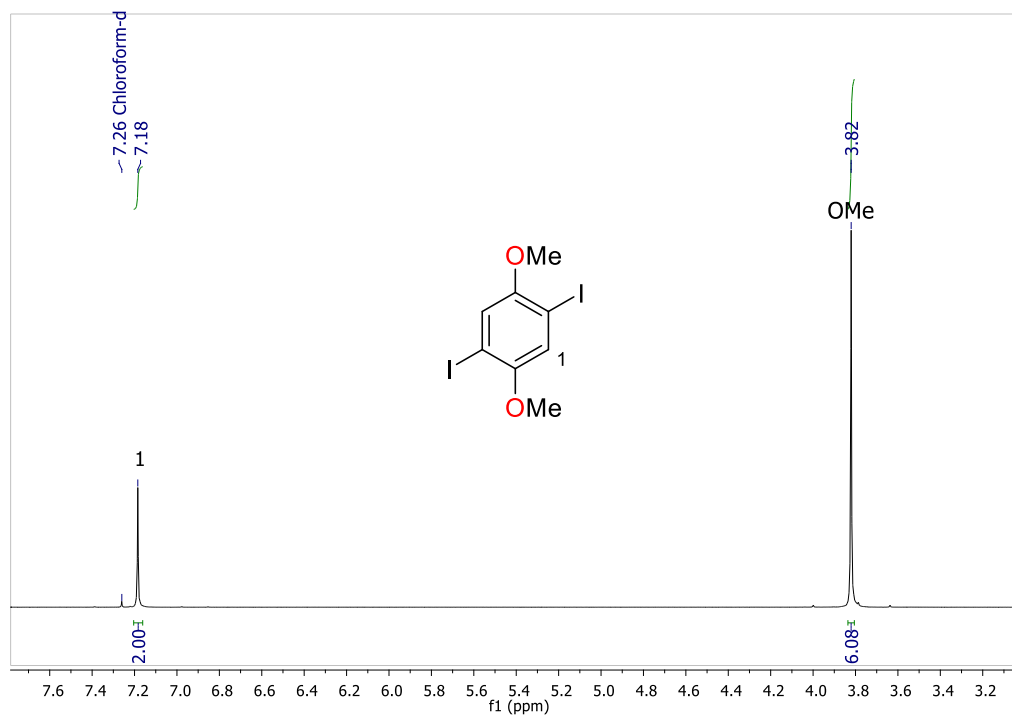
Finally, the herein prepared materials should be used as photocatalyst in the control of additional organic pollutants not only to expand their environmental applicability but to validate their stability. Furthermore, taking advantage of the superoxide generation capacity of the OPV-based photocatalysts in aqueous media, experiments involving the light-driven synthesis of small molecules should be performed as a contribution to design greener chemical synthetic processes and to acquire a deeper understanding of the mechanistic aspects involved in OPV-photocatalyzed organic transformations.

7. Appendices

7.1 Spectroscopic characterization of precursors and target OPVs 1-4.

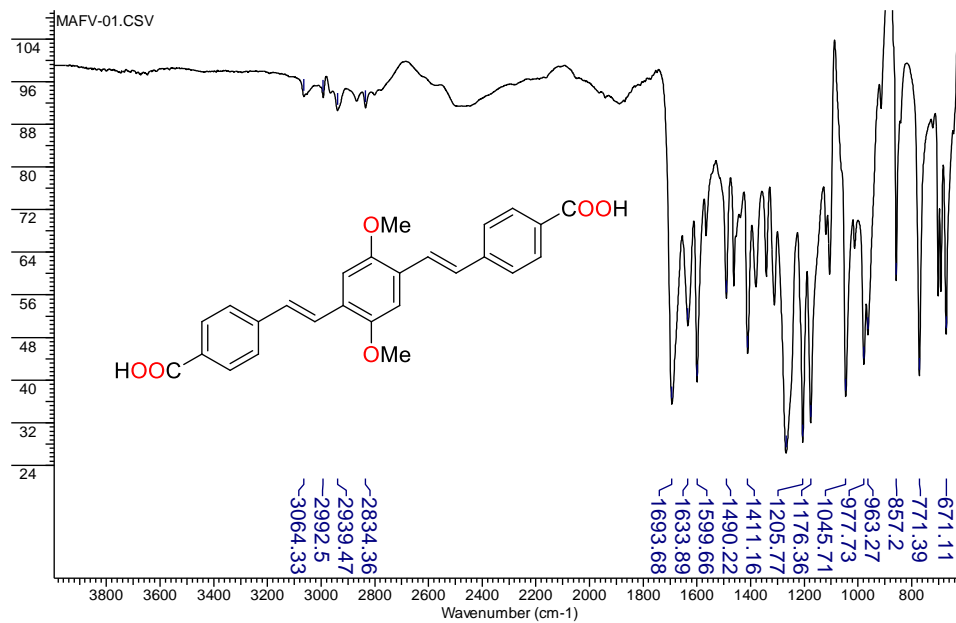
Appendix 7-1A. $^1\text{H-NMR}$ (CDCl_3) spectrum for compound **1c**



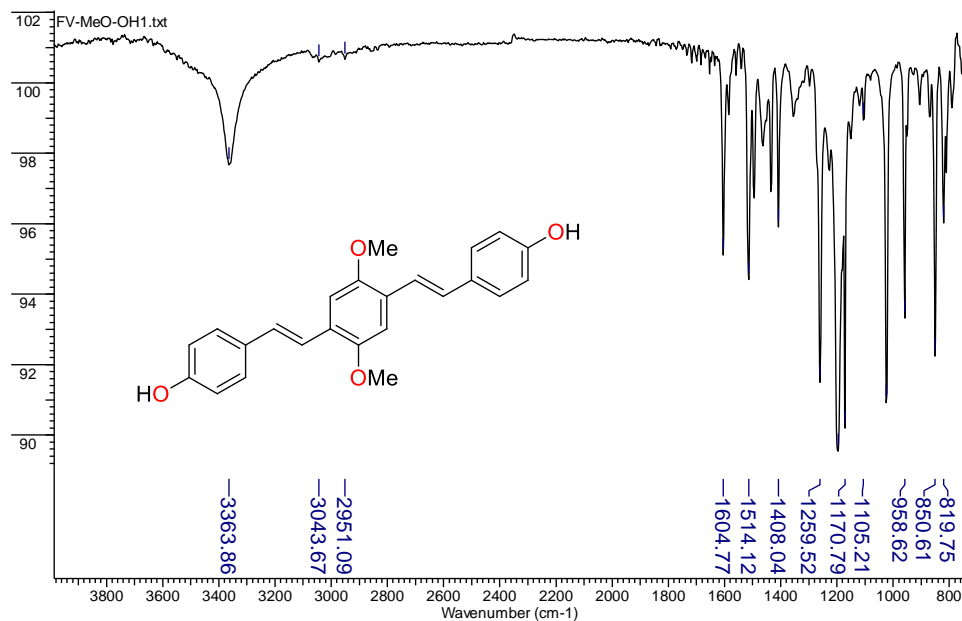
Appendix 7-1B. $^1\text{H-NMR}$ (CDCl_3) spectrum for compound **1d**

Appendix 7-1C. $^1\text{H-NMR}$ (CDCl_3) spectrum for compound **2a**


Appendix 7-1D. ATR FT-IR spectra for OPVs

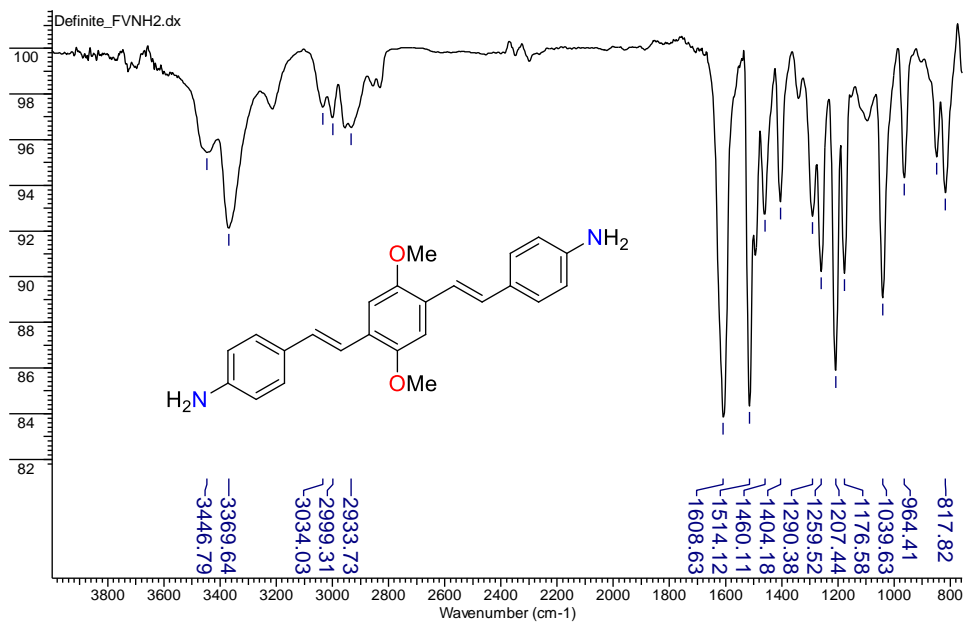
OPV 1



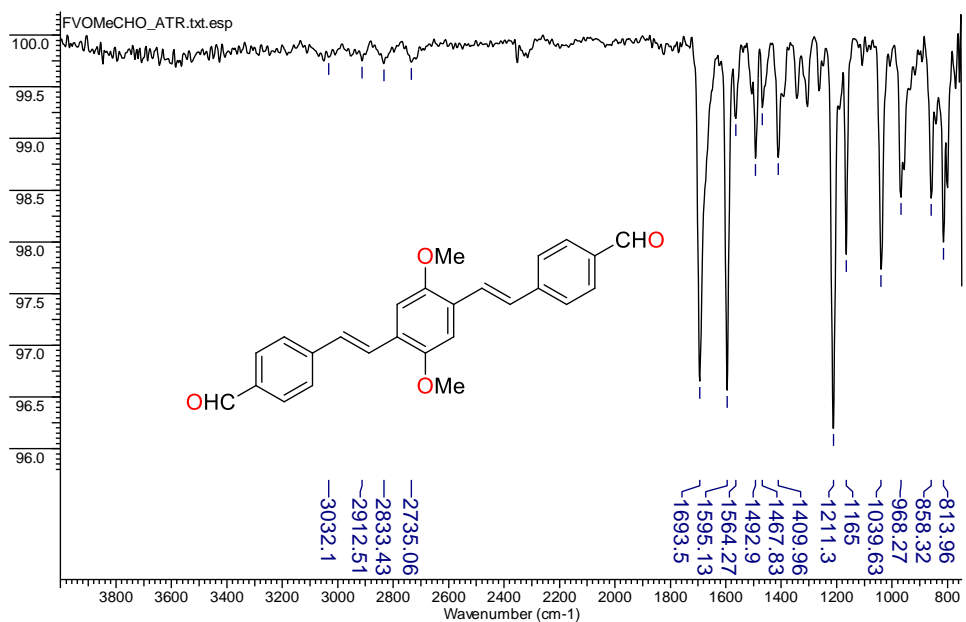
OPV 2

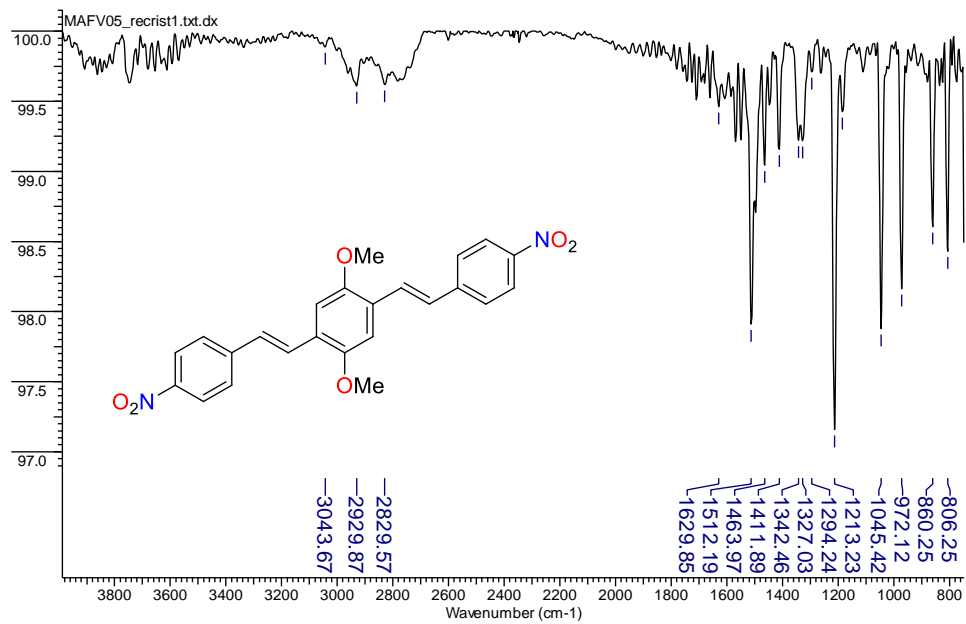


OPV 3

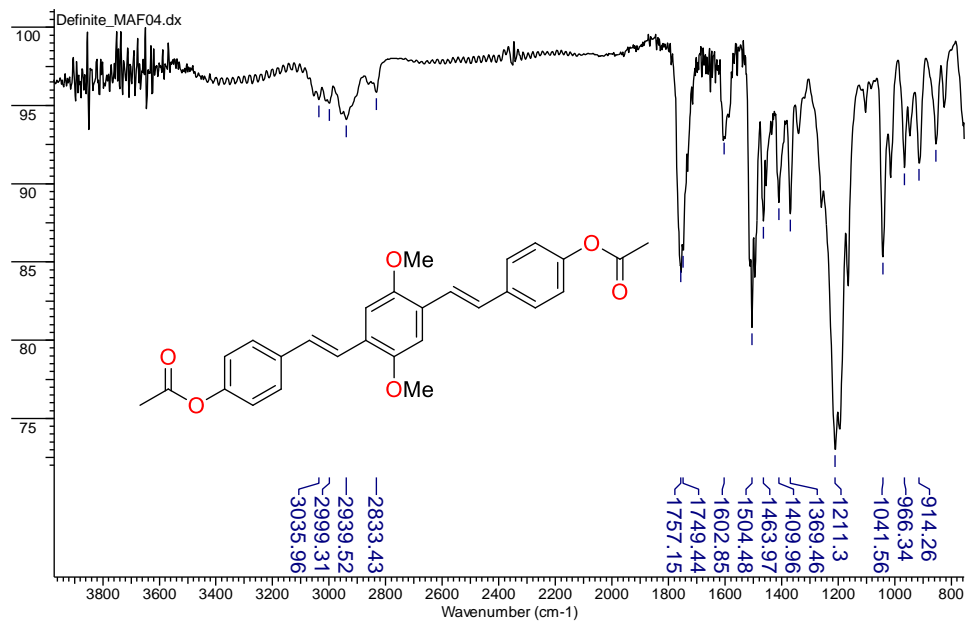


OPV 4

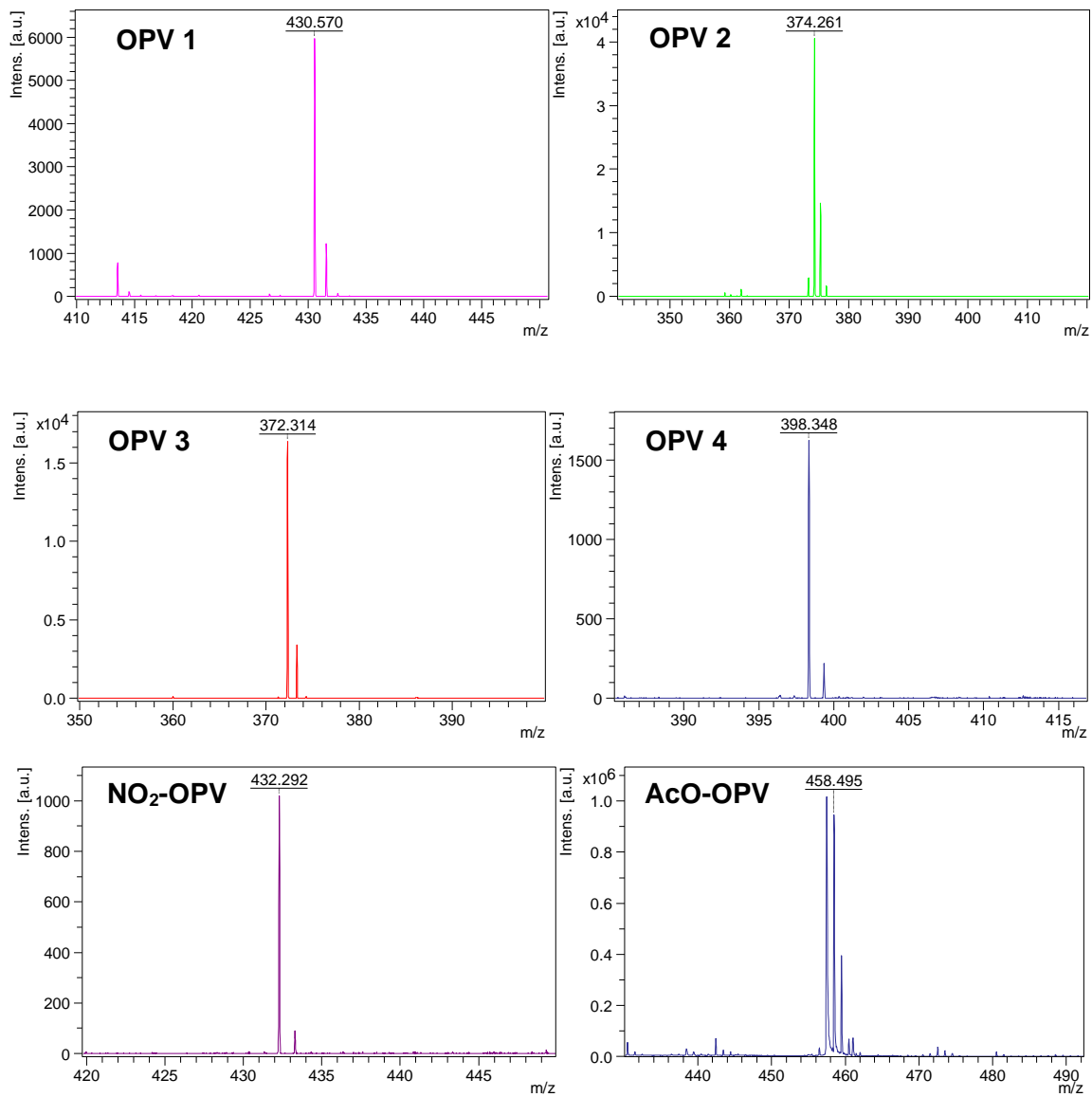


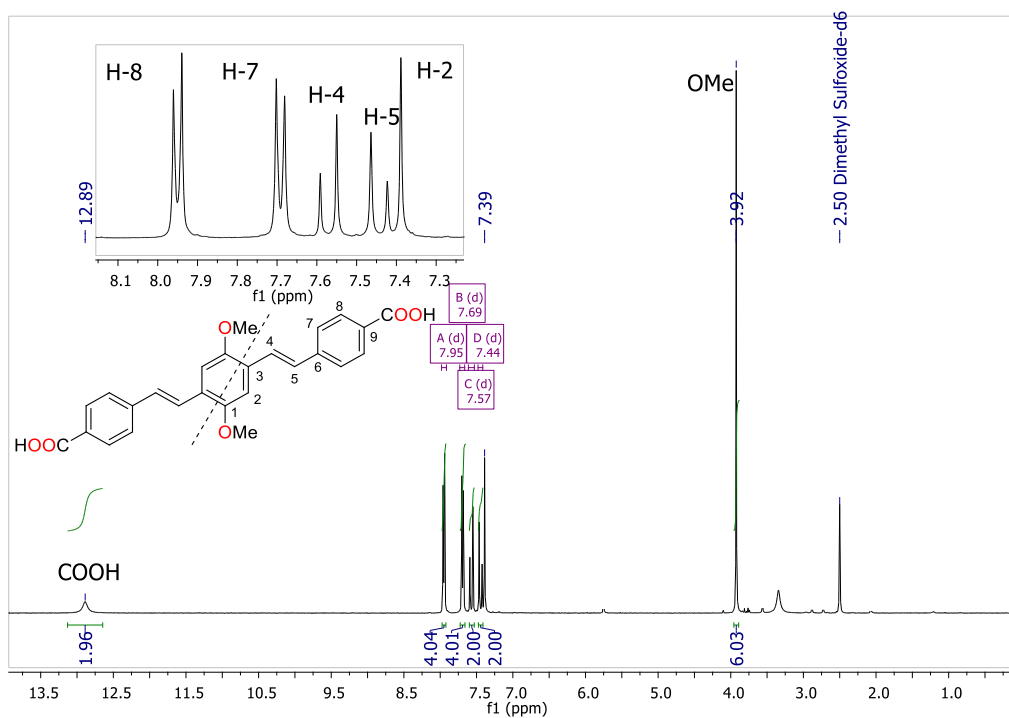
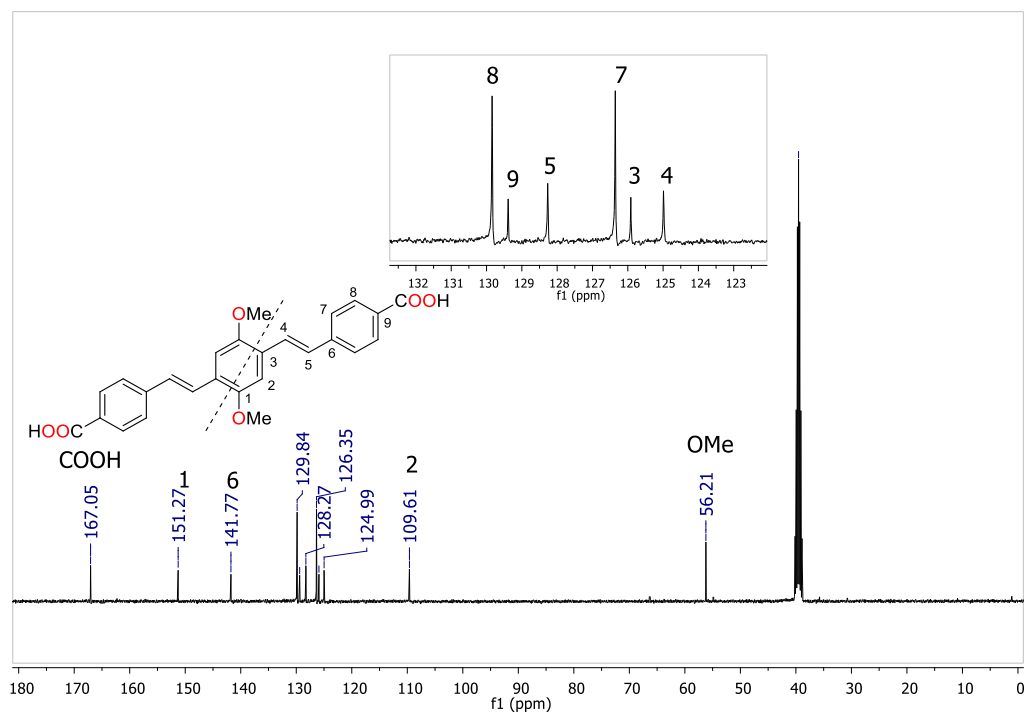
NO₂-OPV

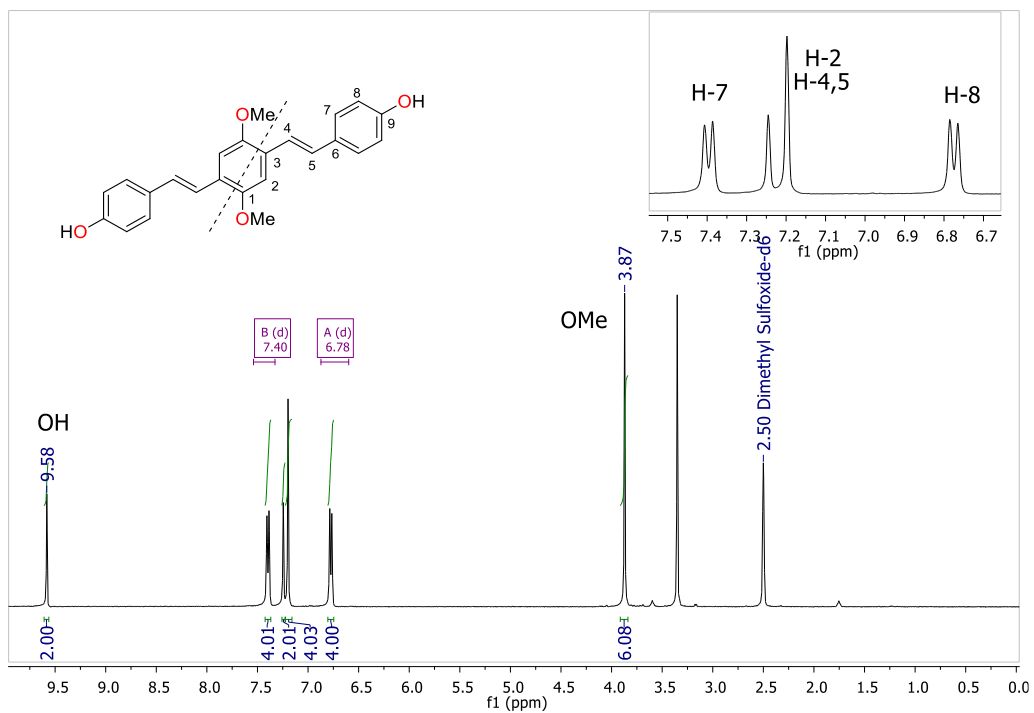
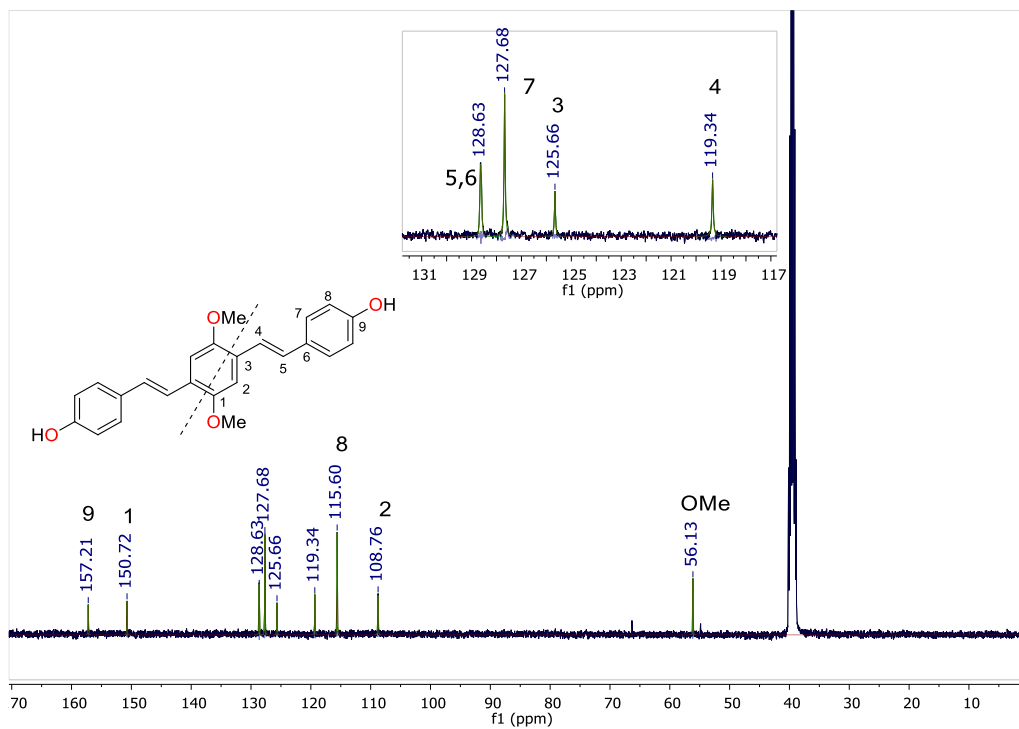
AcO-OPV

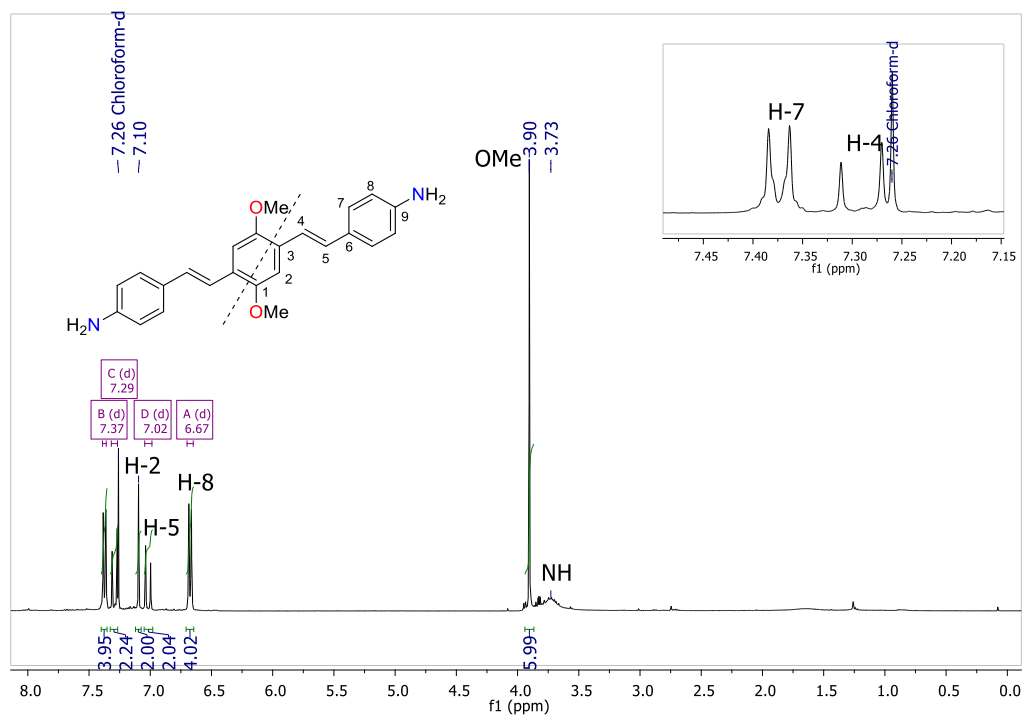
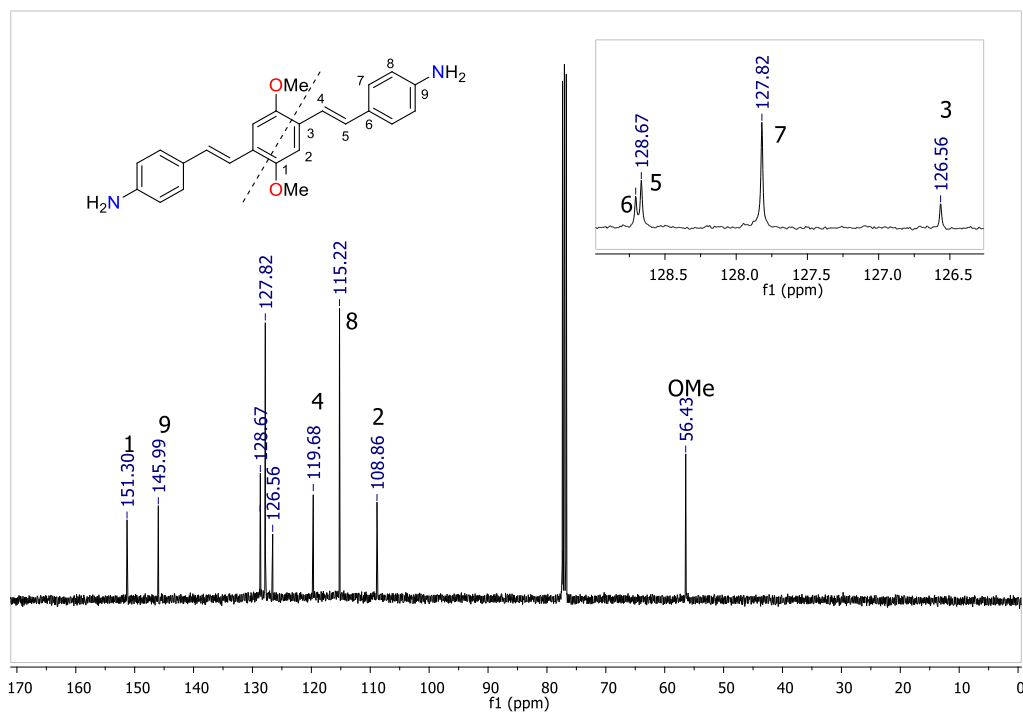


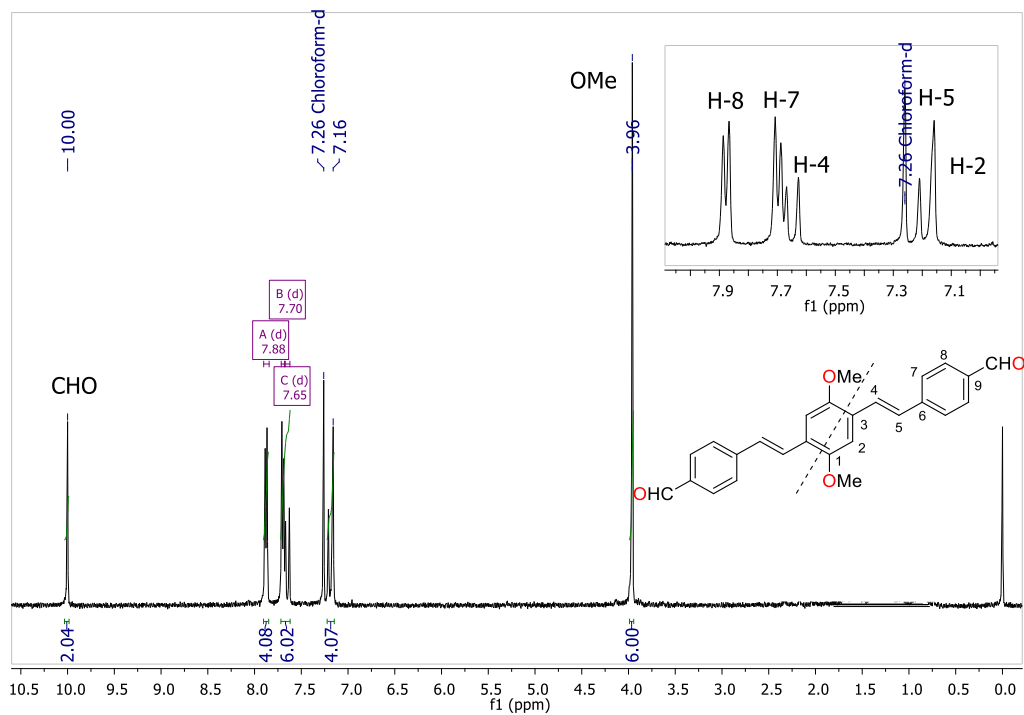
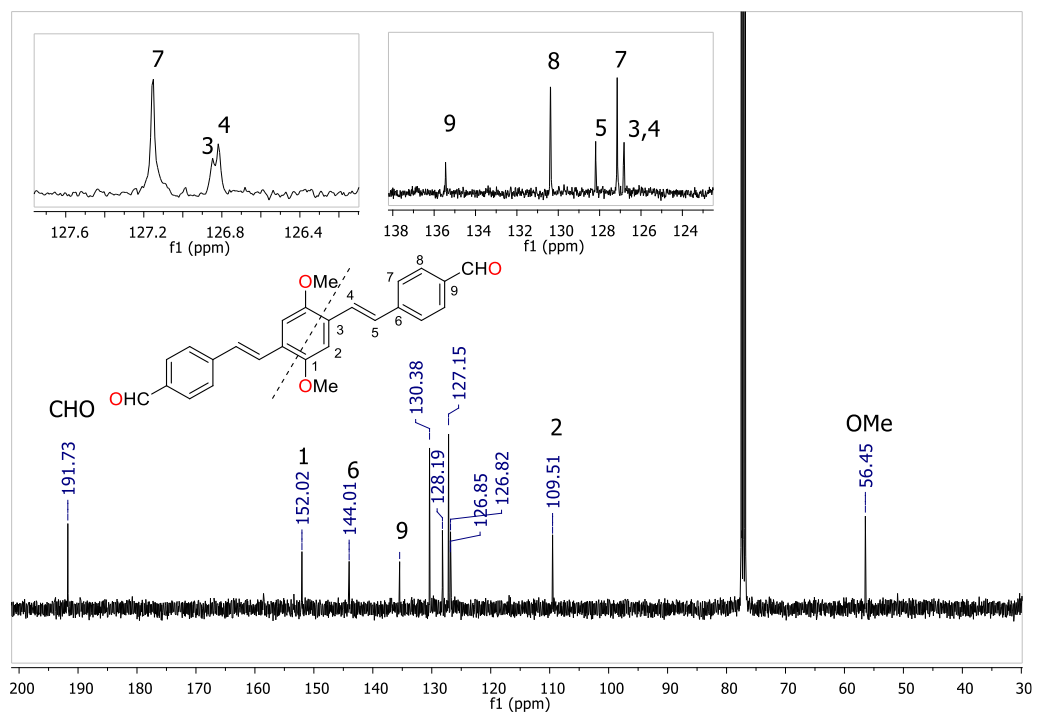
Appendix 7-1E. MALDI-ToF MS spectra for OPVs

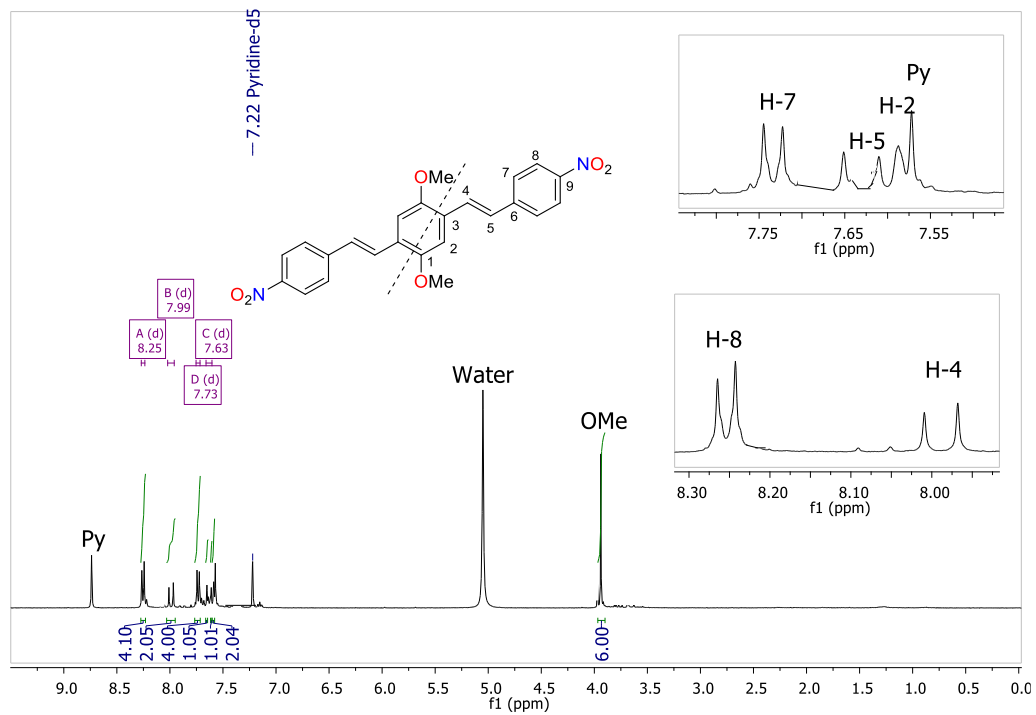
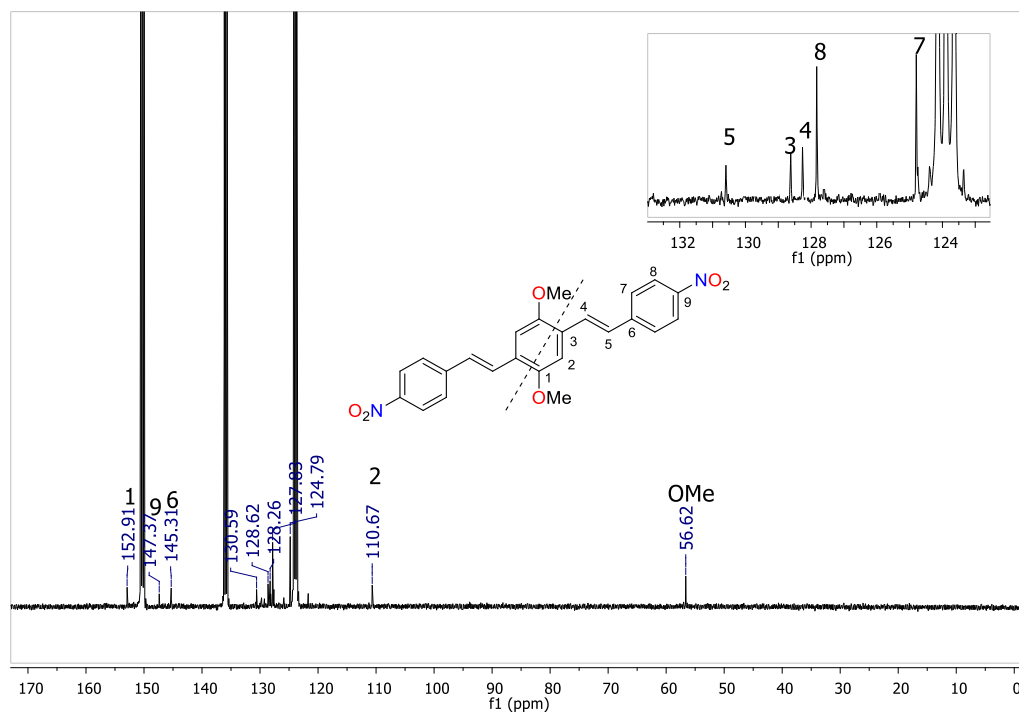


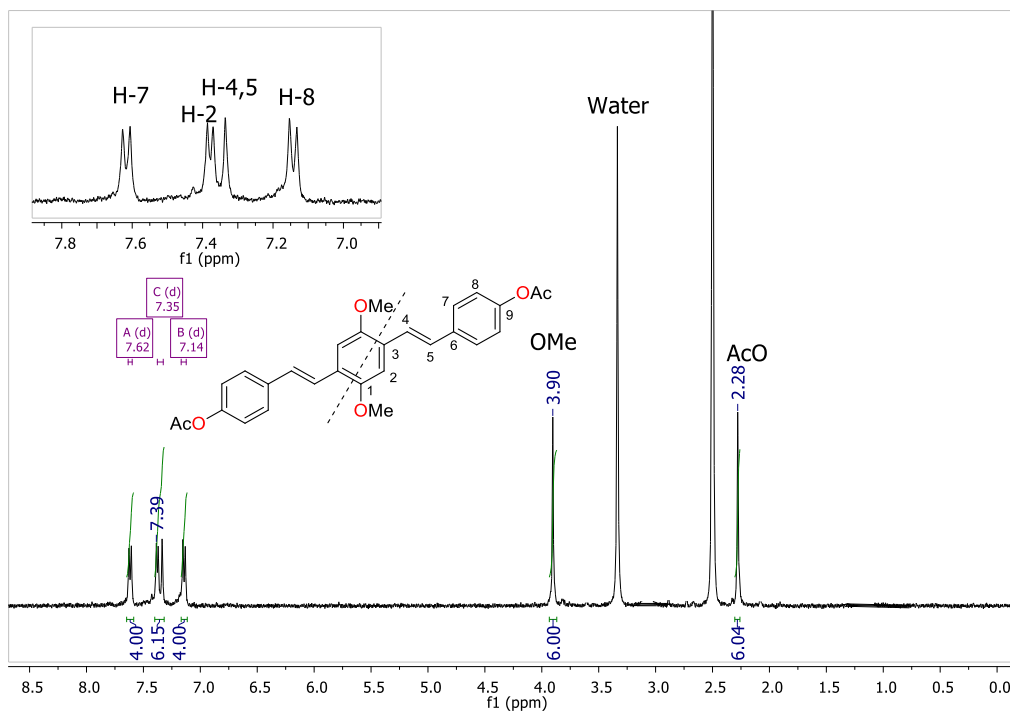
Appendix 7-1F. $^1\text{H}/^{13}\text{C}$ NMR spectra for OPVs ^1H -NMR (DMSO- d_6) for OPV 1 ^{13}C -NMR (DMSO- d_6) for OPV 1

¹H-NMR (DMSO-d₆) for OPV 2**¹³C-NMR (DMSO-d₆) for OPV 2**

¹H-NMR (CDCl₃) for OPV 3**¹³C-NMR (CDCl₃) for OPV 3**

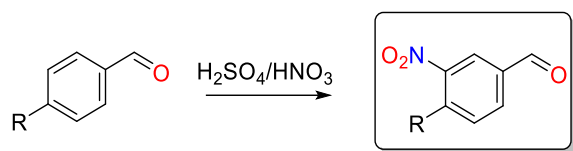
¹H-NMR (CDCl₃) for OPV 4**¹³C-NMR (CDCl₃) for OPV 3**

¹H-NMR (Pyridine-d₅) for NO₂-OPV**¹³C-NMR (Pyridine-d₅) for NO₂-OPV**

¹H-NMR (DMSO-d₆) for AcO-OPV

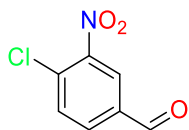
7.2 Synthetic procedures for nitro and amino-OPVs employed for Na₂S/pyridine reduction scope determination

7.2.1 General procedure for the synthesis of nitro benzaldehydes

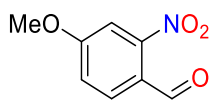


Nitration reactions were performed according to the methodology described by Chorev *et al.* with minor modifications.²⁶² A mixture of 5 mL concentrated sulfuric acid and 10 mmol of the corresponding benzaldehyde was cooled to 0 °C under vigorous stirring. Then, 1.2 equiv. of nitric acid, previously dissolved in 1 mL concentrated sulfuric acid, was slowly added. After addition is completed, the reaction mixture was then warmed to room

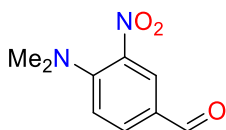
temperature and stirred for 1 additional hour. The crude was then poured into crushed ice, the solid product was recovered by filtration, washed with cold water and recrystallized from ethanol.



• **4-Chloro-3-nitrobenzaldehyde.** White solid, yield 1.090 g (59%) from 4-chlorobenzaldehyde (1.405g, 10 mmol); m.p. 60-62 °C. (Lit. 61-62 °C).²⁶³ The spectral data of the product are in agreement with those reported in literature. IR (ATR, cm^{-1}): 3099, 3071, 3035, 2859, 1701 (ν C=O), 1542 (ν NO₂), 1358 (ν NO₂), 1203, 831. ¹H-NMR (400 MHz, CDCl₃) δ (ppm): 7.77 (d, $J=8.3$ Hz, 1H), 8.05 (dd, $J= 8.3, 1.8$ Hz, 1H), 8.37 (d, $J=1.8$ Hz, 1H), 10.05 (s, 1H).



• **4-Methoxy-3-nitrobenzaldehyde.** Pale yellow solid, yield 1.583 g (87%) from 4-methoxybenzaldehyde (1.361 g, 10 mmol); m.p. 77-79 °C. (Lit. 61-62 °C).²⁶² The spectral data of the product are in agreement with those reported in literature. IR (ATR, cm^{-1}): 3075, 2947, 2845, 1706 (ν C=O), 1615, 1526 (ν NO₂), 1354 (ν NO₂), 1281, 829. ¹H-NMR (400 MHz, CDCl₃) δ (ppm): 4.08 (s, 3H), 7.26 (d, $J=8.7$ Hz, 1H), 8.10 (dd, $J= 8.7, 1.5$ Hz, 1H), 8.36 (d, $J=1.5$ Hz, 1H), 9.95 (s, 1H).

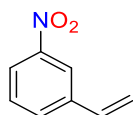


• **4-(Dimethylamino)-3-nitrobenzaldehyde.** Yellow solid, yield 1.436 g (74%) from 4-dimethylaminobenzaldehyde (1.491g, 10 mmol); m.p. 104-105 °C (Lit. 105 °C).²⁶⁴ The spectral data of the product are in agreement with those reported in literature. IR (ATR, cm^{-1}): 3069, 2979, 2931, 2853, 1677 (ν C=O), 1609, 1548 (ν NO₂), 1351 (ν NO₂), 1192, 803.

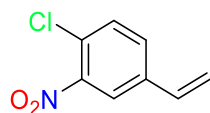
$^1\text{H-NMR}$ (400 MHz, CDCl_3) δ (ppm): 3.04 (s, 6H), 7.07 (d, $J=9.0$ Hz, 1H), 7.89 (dd, $J= 9.0$, 2.0 Hz, 1H), 8.26 (d, $J=2.0$ Hz, 1H), 9.80 (s, 1H).

7.2.2 Synthesis of styrene precursors

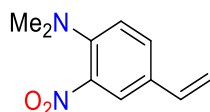
These compounds were prepared employing the Wittig reaction methodology described in Section 2.2.3.



• **1-Nitro-3-vinylbenzene 1g.** Light yellow oil; yield 0.556 g (35%) from of 3-nitrobenzaldehyde (1.600g, 10.58 mmol), methyl triphenylphosphonium bromide (4.536 g, 12.70 mmol) and potassium carbonate (2.339 g, 16.93 mmol). IR (ATR, cm^{-1}): 3090, 1595, 1528 (νNO_2), 1348 (νNO_2), 1097, 920. $^1\text{H-NMR}$ (400 MHz, CDCl_3) δ (ppm): 5.42 (d, $J=10.9$ Hz, 1H), 5.87 (d, $J=17.5$ Hz, 1H), 6.74 (dd, $J=10.9$, 17.5 Hz, 1H), 7.47 (t, $J=7,9$ Hz, 1H), 7.68 (d, $J=7.9$ Hz, 1H), 8.07 (d, $J=7.9$ Hz, 1H), 8.21 (s, 1H).

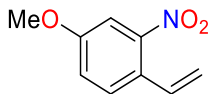


• **1-chloro-2-nitro-4-vinylbenzene 1h.** Yellow oil; yield 0.471 g (95%) from of 4-chloro-3-nitrobenzaldehyde (0.500 g, 2.69 mmol), methyltriphenylphosphonium bromide (1.155 g, 3.23 mmol) and potassium carbonate (0.596 g, 4.31 mmol). IR (ATR, cm^{-1}): 3096, 3073, 1538 (νNO_2), 1354 (νNO_2), 923. $^1\text{H-NMR}$ (400 MHz, CDCl_3) δ (ppm): 5.46 (d, $J=10.9$ Hz, 1H), 5.85 (d, $J=17.5$ Hz, 1H), 6.69 (dd, $J=17.5$, 10.9 Hz, 1H), 7.49 (d, $J=8.4$ Hz, 1H), 7.53 (dd, $J=8.4$, 2.0 Hz, 1H), 7.87 (d, $J= 2.0$ Hz, 1H).

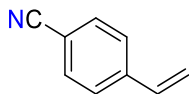


• ***N,N*-dimethyl-2-nitro-4-vinylaniline 1i.** Red oil; yield 0.629 g (91%) from 4-(dimethylamino)-3-nitrobenzaldehyde (0.700 g, 3.60 mmol), methyltriphenylphosphonium bromide (1.545 g, 4.32 mmol) and potassium carbonate (0.796 g, 5.76 mmol). IR (ATR, cm^{-1}

¹): 3091, 3071, 2938, 2893, 1618, 1525 (ν NO₂), 1344 (ν NO₂), 908. ¹H-NMR (400 MHz, CDCl₃) δ (ppm): 2.90 (s, 6H), 5.19 (d, J =10.9 Hz, 1H), 5.63 (d, J =17.5 Hz, 1H), 6.60 (dd, J =17.5, 10.9 Hz, 1H), 6.97 (d, J =8.7 Hz, 1H), 7.46 (dd, J =8.7, 2.1 Hz, 1H), 7.78 (d, J =2.1 Hz, 1H).

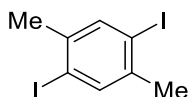


• **1-methoxy-3-nitro-4-vinylbenzene 1j**. Yellow oil; yield 0.488 g (62%) from of 4-methoxy-2-nitrobenzaldehyde (0.800 g, 4.41 mmol), methyltriphenylphosphonium bromide (1.893 g, 5.30 mmol) and potassium carbonate (0.975 g, 7.05 mmol). IR (ATR, cm⁻¹): 3089, 3013, 2951, 2847, 1620, 1529 (ν NO₂), 1356 (ν NO₂), 916. ¹H-NMR (400 MHz, CDCl₃) δ (ppm): 3.96 (s, 3H), 5.30 (d, J =10.9 Hz, 1H), 5.71 (d, J =17.6 Hz, 1H), 6.64 (dd, J =17.6, 10.9 Hz, 1H), 7.05 (d, J =8.7 Hz, 1H), 7.57 (dd, J =8.7, 2.1 Hz, 1H), 7.88 (d, J =2.0 Hz, 1H).



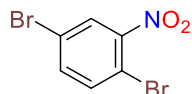
• **4-Vinylbenzonitrile 1l**. Colorless oil; yield 1.130 g (96%) from of 4-cyanobenzaldehyde (1.200g, 9.15 mmol), methyltriphenylphosphonium bromide (3.922 g, 10.98 mmol) and potassium carbonate (2.023g, 14.64 mmol). IR (ATR, cm⁻¹): 3068, 2226 (ν CN), 1604, 1506, 1219, 921, 844. ¹H-NMR (400 MHz, CDCl₃) δ (ppm): 5.39 (d, J =10.9 Hz, 1H), 5.82 (d, J =17.6 Hz, 1H), 6.66 (dd, J =10.9, 17.6 Hz, 1H), 7.42 (d, J =8.2 Hz, 2H), 7.54 (d, J =8.2 Hz, 2H).

7.2.3 Synthesis of 1,4-dihalide precursors



• **1,4-Diiodo-2,5-dimethylbenzene 2b**. To a 250 mL round bottom flask equipped with a condenser and a magnetic stirrer 1,4-dimethylbenzene (5.30 g, 50.00 mmol), iodine (10.15 g, 40.0 mmol) potassium periodate (3.900 g, 22.00 mmol), acetic acid (120 mL), sulfuric acid (1 mL) and deionized water (10 mL) were added. The reaction mixture was heated to

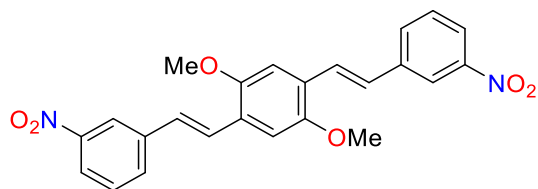
reflux for 24 hours. After reaction completion, the flask was cooled to room temperature and poured over 300 mL of a saturated sodium sulfite solution. The solid formed was filtered and washed with saturated sodium sulfite solution (5 x 20 mL) and cold ethanol (3 x 20 mL). The pink solid obtained was then recrystallized from cyclohexane. White solid; yield 14.56 g (81%), m.p. 102-104 °C (Lit. 102-103 °C).²⁶⁵ IR (ATR, cm⁻¹): 3064, 2972, 2908, 1467, 1427, 1041, 979, 877. ¹H-NMR (400 MHz, CDCl₃) δ(ppm): 2.34 (s, 6H), 7.64 (s, 2H).



• **1,4-Dibromo-2-nitrobenzene 2d.** To a 100 mL round bottom flask equipped with an addition funnel and a magnetic stirrer a mixture of 1,4-dibromobenzene (5.00 g, 21.2 mmol), dichloromethane (13.0 mL) and sulfuric acid (9.0 mL) was added. Then, a nitrating mixture containing nitric acid (63%, 2.97 g, 29.7 mmol) and sulfuric acid (3.5 mL) was added dropwise changing the color of the reaction from colorless to deep blue. After the addition is complete, the solution turns to yellow and it was stirred for 30 additional minutes at room temperature. The crude was quenched with 30 mL of a 25% NaOH solution, extracted with dichloromethane (3 x 20 mL) and dried over MgSO₄. The solvent was then removed under vacuo. Light yellow solid; yield 5.74 g (96%), m.p. 83-84 °C (Lit. 83-84 °C).²⁶⁶ IR (ATR, cm⁻¹): 3086, 1531 (ν NO₂), 1352 (ν NO₂), 1082, 1032, 873, 822. ¹H-NMR (400 MHz, CDCl₃) δ(ppm): 7.55 (dd, *J*=8.5, 2.2 Hz, 1H), 7.60 (d, *J*=8.5 Hz, 1H), 7.97 (d, *J*=2.2 Hz, 1H).

7.2.4 Synthesis of nitro OPVs 3b-j

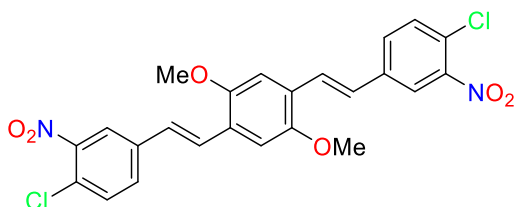
These compounds were prepared according to the procedure described in **Section 2.2.3**.



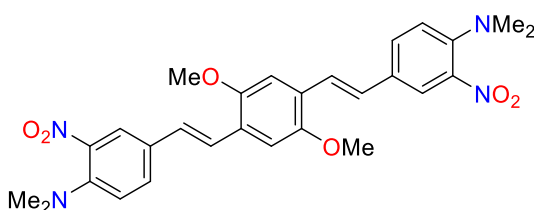
3,3'-((1E,1'E)-(2,5-dimethoxy-1,4-phenylene)bis(ethene-2,1-diyl))bis(nitrobenzene)

3b. Dark orange solid, m.p. 271-272 °C (Lit. 273-275 °C)¹⁴⁷; yield 0.442 g (69%) from 1-nitro-3-vinylbenzene (0.438 g, 2.94 mmol), 1,4-diiodo-2,5-dimethoxybenzene (0.573 g, 1.47 mmol), Pd(dba)₂ (33.8 mg, 0.058 mmol), P(PhO)₃ (82.1 mg, 0.26 mmol) and Et₃N (0.297 g, 2.94 mmol). IR (ATR, cm⁻¹): 3059, 2968, 2943, 1518 (ν NO₂), 1412, 1346 (ν NO₂), 1213,

1049, 958, 824. $^1\text{H-NMR}$ (400 MHz, Pyridine- d_5) δ (ppm): 3.95 (s, 6H), 7.46 (t, $J=8.0$ Hz, 2H), 7.57-7.64 (m, 4H), 7.93-7.95 (m, 2H), 7.94 (d, $J=16.6$ Hz, 2H), 8.11 (dd, $J=8.0, 1.7$ Hz, 2H), 8.48 (t, $J=1.7$ Hz, 2H). MALDI-MS Calc. for $\text{C}_{24}\text{H}_{20}\text{N}_2\text{O}_6$ 432.132; found $[\text{M}]^+$ 432.475. Anal. Calcd for $\text{C}_{24}\text{H}_{20}\text{N}_2\text{O}_6$: C, 66.66; H, 4.66; N, 6.48%. Found: C, 66.32; H, 4.73; N, 6.39%.

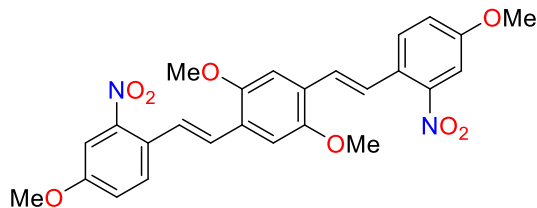


4,4'-((1E,1'E)-(2,5-dimethoxy-1,4-phenylene)bis(ethene-2,1-diyl))bis(1-chloro-2-nitrobenzene) 3c. Orange solid, m.p. 293-295 °C; yield 0.282 g (55%) from 1-chloro-2-nitro-4-vinylbenzene (0.378 g, 2.06 mmol), 1,4-diiodo-2,5-dimethoxybenzene (0.368 g, 1.03 mmol), $\text{Pd}(\text{dba})_2$ (23.7 mg, 0.041 mmol), $\text{P}(\text{PhO})_3$ (57.5 mg, 0.18 mmol) and Et_3N (0.208 g, 2.06 mmol). IR (ATR, cm^{-1}): 3058, 2957, 2918, 1626, 1530 (ν NO_2), 1414, 1347 (ν NO_2), 1213, 1057, 963, 815. $^1\text{H-NMR}$ (400 MHz, Pyridine- d_5) δ (ppm): 3.92 (s, 6H), 7.53 (s, 2H), 7.53 (d, $J=16.5$ Hz, 2H), 7.64 (d, $J=8.3$ Hz, 2H), 7.75 (d, $J=8.3$ Hz, 2H), 7.91 (d, $J=16.5$ Hz, 2H), 8.26 (s, 2H). MALDI-MS Calc. for $\text{C}_{24}\text{H}_{18}\text{Cl}_2\text{N}_2\text{O}_6$ 500.054; found $[\text{M}]^+$ 500.163. Anal. Calcd for $\text{C}_{24}\text{H}_{18}\text{Cl}_2\text{N}_2\text{O}_6$: C, 57.50; H, 3.62; N, 5.59%. Found: C, 57.82; H, 3.85; N, 5.71%.

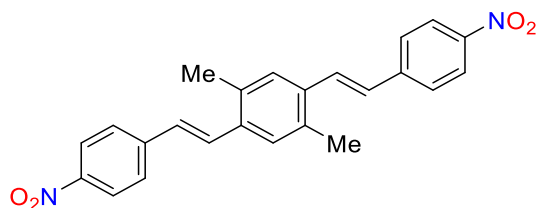


4,4'-((1E,1'E)-(2,5-dimethoxy-1,4-phenylene)bis(ethene-2,1-diyl))bis(N,N-dimethyl-2-nitroaniline) 3d. Red solid, m.p. 281-283 °C; yield 0.333 g (62%) from *N,N*-dimethyl-2-nitro-4-vinylaniline (0.396 g, 2.06 mmol), 1,4-diiodo-2,5-dimethoxybenzene (0.368 g, 1.03 mmol), $\text{Pd}(\text{dba})_2$ (23.7 mg, 0.041 mmol), $\text{P}(\text{PhO})_3$ (57.5 mg, 0.18 mmol) and Et_3N (0.208 g, 2.06 mmol). IR (ATR, cm^{-1}): 3052, 3002, 2943, 1612, 1528 (ν NO_2), 1408, 1354 (ν NO_2), 1212, 1047, 968, 817. Due to very poor solubility in DMSO- d_6 , pyridine- d_5 , DCl (35% in D_2O) and mixtures, no NMR data was collected. MALDI-MS Calc. for $\text{C}_{28}\text{H}_{30}\text{N}_4\text{O}_6$ 518.216;

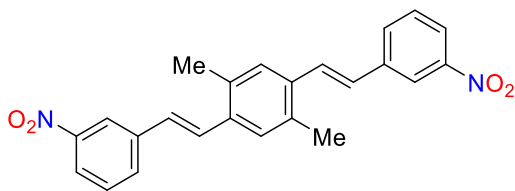
found $[M]^+$ 518.327. Anal. Calcd for $C_{28}H_{30}N_4O_6$: C, 64.85; H, 5.83; N, 10.80%. Found: C, 64.57; H, 5.96; N, 11.06%.



• **4,4'-((1E,1'E)-(2,5-dimethoxy-1,4-phenylene)bis(ethene-2,1-diyl))bis(1-methoxy-3-nitrobenzene) 3e.** Orange solid, m.p. 264-265 °C; yield 0.586 g (87%) from 1-methoxy-3-nitro-4-vinylbenzene (0.488 g, 2.72 mmol), 1,4-diiodo-2,5-dimethoxybenzene (0.530 g, 1.36 mmol), $Pd(dba)_2$ (31.0 mg, 0.054 mmol), $P(PhO)_3$ (74.0 mg, 0.24 mmol) and Et_3N (0.275 g, 2.72 mmol). IR (ATR, cm^{-1}): 3064, 2964, 2913, 2837, 1612, 1525 (ν NO_2), 1412, 1347 (ν NO_2), 1252, 1212, 1049, 1015, 963, 809. 1H -NMR (400 MHz, Pyridine- d_5) δ (ppm): 3.79 (s, 6H), 3.93 (s, 6H), 7.14 (d, $J=8.5$ Hz, 2H), 7.52 (d, $J=16.7$ Hz, 2H), 7.54 (s, 2H), 7.81 (d, $J=8.5$ Hz, 2H), 7.83 (d, $J=16.7$ Hz, 2H), 8.25 (s, 2H). MALDI-MS Calc. for $C_{26}H_{24}N_2O_8$ 492.153; found $[M]^+$ 492.306. Anal. Calcd for $C_{26}H_{24}N_2O_8$: C, 63.41; H, 4.91; N, 5.69%. Found: C, 63.65; H, 5.13; N, 5.92%.

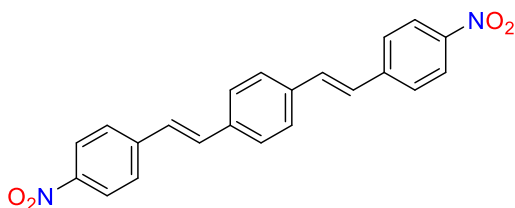


4,4'-((1E,1'E)-(2,5-dimethyl-1,4-phenylene)bis(ethene-2,1-diyl))bis(nitrobenzene) 3f. Brown-orange solid, decomposes at 263 °C (Lit. Decomposes)²⁶⁷; yield 0.230 g (56%) from 1-nitro-4-vinylbenzene (0.307 g, 2.06 mmol), 1,4-diiodo-2,5-dimethylbenzene (0.368 g, 1.03 mmol), $Pd(dba)_2$ (23.7 mg, 0.041 mmol), $P(PhO)_3$ (57.5 mg, 0.19 mmol) and Et_3N (0.208 g, 2.06 mmol). IR (ATR, cm^{-1}): 3016, 2922, 1589, 1510 (ν NO_2), 1336 (ν NO_2), 1107, 962, 860. 1H -NMR (400 MHz, Pyridine- d_5) δ (ppm): 2.53 (s, 6H), 7.36 (d, $J=16.2$ Hz, 2H), 7.71 (s, 2H), 7.76 (d, $J=16.2$ Hz, 2H), 7.83 (d, $J=8.7$ Hz, 4H), 8.30 (d, $J=8.7$ Hz, 4H). MALDI-MS Calc. for $C_{24}H_{20}N_2O_4$ 400.142; found $[M+DMF+2H]^+$ 475.602. Anal. Calcd for $C_{24}H_{20}N_2O_4$: C, 71.99; H, 5.03; N, 7.00%. Found: C, 71.87; H, 4.90; N, 7.17%.

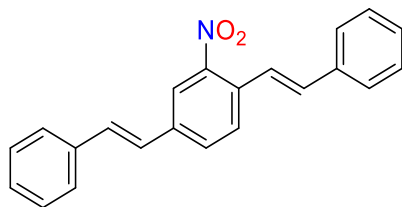


3,3'-((1E,1'E)-(2,5-dimethyl-1,4-phenylene)bis(ethene-2,1-diyl))bis(nitrobenzene) 3g.

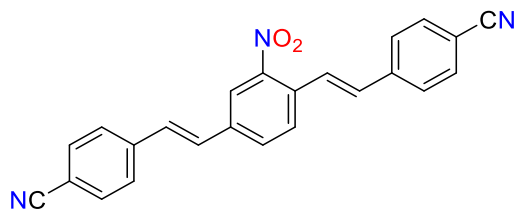
Yellow solid, m.p. 281-282 °C; yield 0.287 g (70%) from 1-nitro-3-vinylbenzene (0.307 g, 2.06 mmol), 1,4-diiodo-2,5-dimethylbenzene (0.368 g, 1.03 mmol), Pd(dba)₂ (23.7 mg, 0.041 mmol), P(PhO)₃ (57.5 mg, 0.19 mmol) and Et₃N (0.208 g, 2.06 mmol). IR (ATR, cm⁻¹): 3086, 2945, 2918, 1525 (ν NO₂), 1350 (ν NO₂), 970, 891, 800. ¹³C CP/MAS-NMR (100 MHz, KBr) δ(ppm): 19.9, 117.3, 122.7, 125.6, 128.5, 129.9(x₂), 134.1, 135.3(x₂), 139.0, 149.7. MALDI-MS Calc. for C₂₄H₂₀N₂O₄ 400.142; found [M]⁺ 400.205. Anal. Calcd for C₂₄H₂₀N₂O₄: C, 71.99; H, 5.03; N, 7.00%. Found: C, 72.09; H, 5.14; N, 6.89%.



1,4-bis((E)-4-nitrostyryl)benzene 3h. Orange solid, m.p. 290-292 (Lit 292-294 °C)⁴²; yield 0.398 g (40%) from 1-nitro-4-vinylbenzene (1.196 g, 8.02 mmol), 1,4-diiodobenzene (1.564 g, 4.01 mmol), Pd(dba)₂ (92.2 mg, 0.16 mmol), P(PhO)₃ (223.9 mg, 0.72 mmol) and Et₃N (0.811 g, 8.02 mmol). IR (ATR, cm⁻¹): 3020, 1589, 1506 (ν NO₂), 1332 (ν NO₂), 1105, 957, 849. ¹H-NMR (400 MHz, Pyridine-d₅) δ(ppm) 7.41 (d, J=16.4 Hz, 2H), 7.54 (d, J=16.4 Hz, 2H), 7.74 (d, J=8.8 Hz, 4H), 7.77 (s, 4H), 8.27 (d, J=8.8 Hz, 4H). MALDI-MS Calc. for C₂₂H₁₆N₂O₄ 372.111; found [M]⁺ 372.138. Anal. Calcd for C₂₂H₁₆N₂O₄: C, 70.96; H, 4.33; N, 7.52%. Found: C, 70.82; H, 4.41; N, 7.40%.



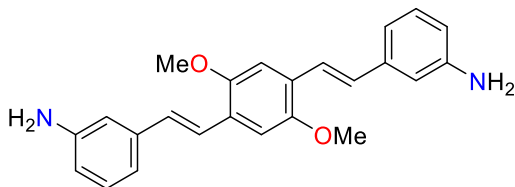
((1E,1'E)-(2-nitro-1,4-phenylene)bis(ethene-2,1-diyl)dibenzene 3i. Orange solid; m.p. 177-180 °C; yield 0.161 g (37%) from styrene (0.279 g, 2.68 mmol), 1,4-dibromo-2-nitrobenzene (0.376 g, 1.34 mmol), Pd(dba)₂ (30.8 mg, 0.054 mmol), P(PhO)₃ (74.8 mg, 0.24 mmol) and Et₃N (0.271 g, 2.68 mmol). IR (ATR, cm⁻¹): 3030, 1668, 1526 (ν NO₂), 1352 (ν NO₂), 962, 821. ¹H-NMR (400 MHz, CDCl₃) δ(ppm): 7.10 (d, *J*=16.3 Hz, 1H), 7.13 (d, *J*=16.1 Hz, 1H), 7.21 (d, *J*=16.3 Hz, 1H), 7.29-7.42 (m, 6H), 7.52-7.56 (m, 4H), 7.59 (d, *J*=16.1 Hz, 1H), 7.71 (dd, *J*= 8.3, 1.5 Hz, 1H), 7.77 (d, *J*= 8.3 Hz, 1H), 8.07 (d, *J*= 1.5 Hz, 1H). ¹³C-NMR (100 MHz, CDCl₃) δ(ppm): 122.3, 123.1, 125.9, 126.8, 127.1, 128.2, 128.5, 128.6, 128.8, 128.9, 130.4, 131.4, 133.6, 136.4, 136.6, 137.7, 148.5. MALDI-MS Calc. for C₂₂H₁₇NO₂ 327.125; found [M+H]⁺ 328.289. Anal. Calcd for C₂₂H₁₇NO₂: C, 80.71; H, 5.23; N, 4.28%. Found: C, 80.58; H, 5.35; N, 4.43%.



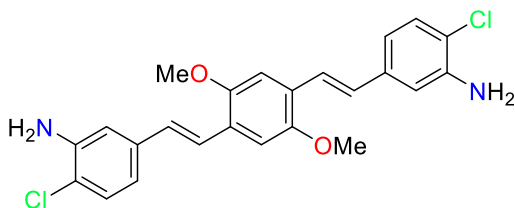
4,4'-((1E,1'E)-(2-nitro-1,4-phenylene)bis(ethene-2,1-diyl)dibenzonitrile 3j. Yellow solid; yield 0.247 g (50%) m.p. 276-277 °C. from 4-vinylbenzonitrile (0.346 g, 2.68 mmol), 1,4-dibromo-2-nitrobenzene (0.376 g, 1.34 mmol), Pd(dba)₂ (30.8 mg, 0.054 mmol), P(PhO)₃ (74.8 mg, 0.24 mmol) and Et₃N (0.271 g, 2.68 mmol). IR (ATR, cm⁻¹): 3061, 2220 (ν CN), 1600, 1521 (ν NO₂), 1354 (ν NO₂), 966, 950, 840, 823. ¹H-NMR (400 MHz, Pyridine-d₅) δ(ppm): 7.32 (d, *J*=16.2 Hz, 1H), 7.42 (d, *J*=16.6 Hz, 1H), 7.47 (d, *J*=16.6 Hz, 1H), 7.68-7.76 (m, 8H), 7.86 (d, *J*=16.2 Hz, 1H), 7.90 (d, *J*=8.4 Hz, 1H), 7.93 (dd, *J*=8.4, 1.2 Hz, 1H), 8.34 (d, *J*=1.2 Hz, 1H). MALDI-MS Calc. for C₂₄H₁₅N₃O₂ 377.116; found [M+H]⁺ 378.197. Anal. Calcd for C₂₄H₁₅N₃O₂: C, 76.38; H, 4.01; N, 11.13%. Found: C, 76.17; H, 3.92; N, 11.26.

7.2.5 Synthesis of amino OPVs 4b-h

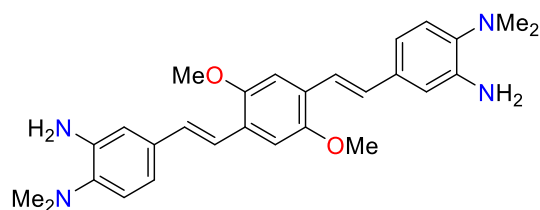
These compounds were prepared according to the procedure described in **Section 2.2.3**.



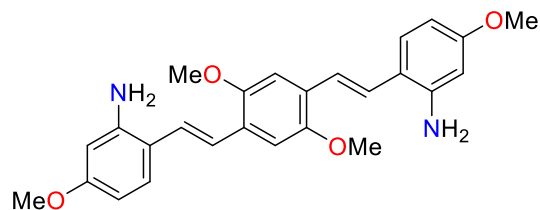
3,3'-((1E,1'E)-(2,5-dimethoxy-1,4-phenylene)bis(ethene-2,1-diyl))dianiline 4b. Dark yellow solid. Yield 0.056 g (76%) m.p. 213-215 °C; from OPV **3b** (0.087 g, 0.20 mmol) and Na₂S (0.156 g (60%), 1.2 mmol). IR (ATR, cm⁻¹): 3468 (ν NH₂), 3377 (ν NH₂), 3055, 2991, 2935, 1622, 1205, 1043, 960, 775. ¹H-NMR (400 MHz, Mixture of CDCl₃ and DMSO-d₆ 4:1) δ(ppm): 3.84 (s, 6H), 4.02 (bs, NH), 6.51 (d, *J*=8.2 Hz, 2H), 6.78-6.82 (m, 4H), 6.93 (d, *J*=16.4 Hz, 2H), 7.00-7.05 (m, 4H), 7.31 (d, *J*=16.4 Hz, 2H), 7.61 (s, 4H). ¹³C-NMR (100 MHz, Mixture of CDCl₃ and DMSO-d₆ 4:1) δ(ppm): 55.7, 108.5, 112.0, 113.9, 116.2, 122.0, 125.9, 128.6, 128.8, 138.0, 146.8, 150.8. MALDI-MS Calc. for C₂₄H₂₄N₂O₂ 372.183; found [M]⁺ 372.539. Anal. Calcd for C₂₄H₂₄N₂O₂: C, 77.39; H, 6.49; N, 7.52%. Found: C, 77.51; H, 6.64; N, 7.36%.



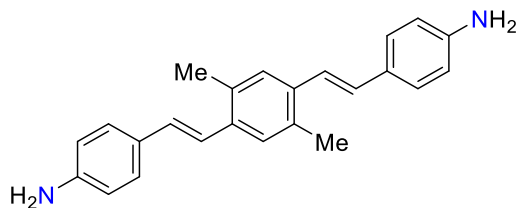
5,5'-((1E,1'E)-(2,5-dimethoxy-1,4-phenylene)bis(ethene-2,1-diyl))bis(2-chloroaniline) 4c. Yellow solid. Yield 0.016 g (36%) m.p. 278-280 °C; from OPV **3c** (0.050 g, 0.10 mmol) and Na₂S (0.078 g (60%), 0.6 mmol). IR (ATR, cm⁻¹): 3461 (ν NH₂), 3372 (ν NH₂), 3049, 2917, 2851, 1611, 1205, 1036, 952, 849. ¹H-NMR (400 MHz, DMSO-d₆) δ(ppm): 3.89 (s, 6H), 5.39 (s, NH), 6.76 (d, *J*=8.3 Hz, 2H), 7.03 (s, 2H), 7.18 (d, *J*=8.3 Hz, 2H), 7.18 (d, *J*=16.4 Hz, 2H), 7.31 (s, 2H), 7.32 (d, *J*=16.4 Hz, 2H). ¹³C-NMR (100 MHz, DMSO-d₆) δ(ppm): 56.2, 109.0, 112.4, 115.7, 116.5, 122.2, 125.6, 128.5, 129.2, 136.9, 144.7, 150.9. MALDI-MS Calc. for C₂₄H₂₂Cl₂N₂O₂ 440.106; found [M]⁺ 440.181. Anal. Calcd for C₂₄H₂₂Cl₂N₂O₂: C, 65.31; H, 5.02; N, 6.35%. Found: C, 65.11; H, 5.30; N, 6.66%.



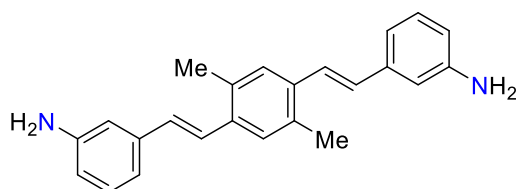
4,4'-((1E,1'E)-(2,5-dimethoxy-1,4-phenylene)bis(ethene-2,1-diyl))bis(N,N-dimethylbenzene-1,2-diamine) 4d. Orange solid. Yield 0.019 g (43%) m.p. 220-222 °C; from OPV **3d** (0.050 g, 0.09 mmol) and Na₂S (0.075 g (60%), 0.58 mmol). The reactants were added and stirred on a sealed 10 mL headspace crimp vial for 12 h at 100°C. IR (ATR, cm⁻¹): 3425 (ν NH₂), 3332 (ν NH₂), 3049, 2924, 2829, 1602, 1204, 1042, 960, 857. ¹H-NMR (400 MHz, CDCl₃) δ(ppm): 2.69 (s, 12H), 3.91 (s, 6H), 3.98 (bs, NH), 6.92 (d, *J*=8.1 Hz, 2H), 6.96-7.03 (m, 6H), 7.11 (s, 2H), 7.34 (d *J*=16.4 Hz, 2H) ¹³C-NMR (100 MHz CDCl₃) δ(ppm): 43.6, 56.5, 109.1, 112.6, 117.8, 119.2, 121.6, 126.7, 128.8, 133.8, 140.6, 141.3, 151.4. MALDI-MS Calc. for C₂₈H₃₄N₄O₂ 458.268; found [M]⁺ 458.312. Anal. Calcd for C₂₈H₃₄N₄O₂: C, 73.33; H, 7.47; N, 12.22%. Found: C, 73.12; H, 7.61; N, 11.97%.



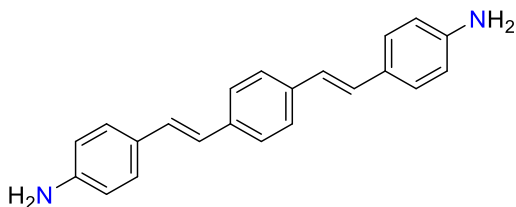
6,6'-((1E,1'E)-(2,5-dimethoxy-1,4-phenylene)bis(ethene-2,1-diyl))bis(3-methoxyaniline) 4e. Yellow solid. Yield 0.017 g (39%) m.p. 199-201 °C; from OPV **3e** (0.050 g, 0.10 mmol) and Na₂S (0.078 g (60%), 0.60 mmol). IR (ATR, cm⁻¹): 3446 (ν NH₂), 3352 (ν NH₂), 3049, 2916, 2850, 1615, 1589, 1207, 1030, 932, 762. ¹H-NMR (400 MHz, CDCl₃) δ(ppm): 3.87 (s, 6H), 3.90 (s, 6H), 3.90 (bs, NH), 6.76 (d, *J*=8.5 Hz, 2H), 6.89 (d, *J*=8.5 Hz, 2H), 6.98 (d, *J*=16.1 Hz, 2H), 6.99 (s, 2H), 7.09 (s, 2H), 7.29 (d, *J*=16.1 Hz, 2H). ¹³C-NMR (100 MHz, CDCl₃) δ(ppm): 55.7, 56.6, 109.1, 110.5, 112.4, 118.1, 121.0, 126.7, 128.8, 131.2, 136.4, 147.5, 151.5. MALDI-MS Calc. for C₂₆H₂₈N₂O₄ 432.205; found [M]⁺ 432.287. Anal. Calcd for C₂₆H₂₈N₂O₄: C, 72.20; H, 6.53; N, 6.48%. Found: C, 72.43; H, 6.79; N, 6.89%.



4,4'-((1E,1'E)-(2,5-dimethyl-1,4-phenylene)bis(ethene-2,1-diyl)dianiline 4f. Dark-orange solid. Yield 0.073 g (96 %), m.p. 211-213 °C; from OPV **3f** (0.090 g, 0.22 mmol) and Na₂S (0.175 g (60%), 1.35 mmol). IR (ATR, cm⁻¹): 3398 (ν NH₂), 3329 (ν NH₂), 3028, 2918, 1602, 1514, 1261, 960. ¹H-NMR (400 MHz, CDCl₃:Methanol-d₄ 5:1) δ(ppm): 2.41 (s, 6H), 3.72 (bs, NH), 6.71 (d, *J*=8.5 Hz, 4H), 6.93 (d, *J*=16.1 Hz, 2H), 7.11 (d, *J*=16.1 Hz, 2H), 7.34 (s, 2H), 7.37 (d, *J*=8.5 Hz, 4H). ¹³C-NMR (100 MHz, CDCl₃:Methanol-d₄ 5:1) δ(ppm): 19.5, 115.5, 122.6, 126.7, 127.7, 128.8, 129.1, 133.0, 135.4, 145.9. MALDI-MS Calc. for C₂₄H₂₄N₂ 340.194; found [M]⁺ 340.356. Anal. Calcd for C₂₄H₂₄N₂: C, 84.67; H, 7.11; N, 8.23%. Found: C, 85.00; H, 6.97; N, 8.07%.



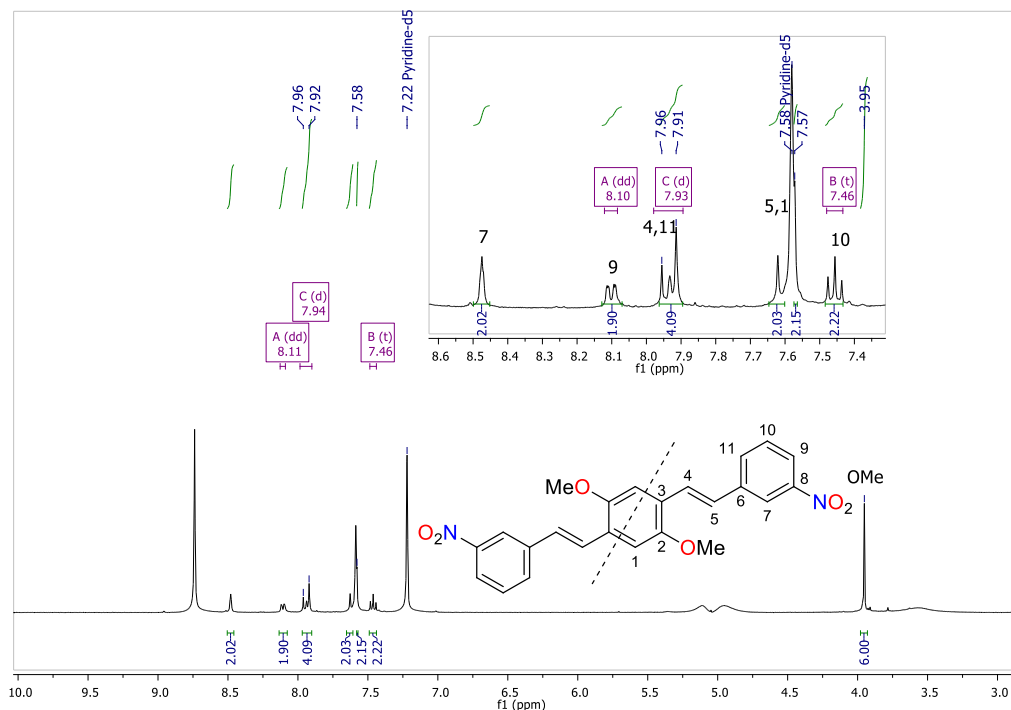
3,3'-((1E,1'E)-(2,5-dimethyl-1,4-phenylene)bis(ethene-2,1-diyl)dianiline 4g. Brown-yellowish solid. Yield 0.079 g (93%), starts decomposing at 190 °C. From OPV **3g** (0.100 g, 0.29 mmol) and Na₂S (0.228 g (60%), 1.76 mmol). The reactants were added and stirred on a sealed 10 mL headspace crimp vial for 12 h at 100°C. IR (ATR, cm⁻¹): 3437 (ν NH₂), 3344 (ν NH₂), 3045, 2991, 2945, 1597, 1159, 960, 775. ¹H-NMR (400 MHz, Mixture of CDCl₃ and Methanol-d₄ 4:1) δ(ppm): 2.42 (s, 6H), 6.68 (dd, *J*= 7.7, 1.5 Hz, 2H), 6.91-6.97 (m, 6H), 7.15 (t, *J*=7.7 Hz, 2H), 7.27 (d, *J*=16.2 Hz, 2H), 7.41 (s, 2H). ¹³C-NMR (100 MHz, Mixture of CDCl₃ and Methanol-d₄ 4:1) δ(ppm): 19.8, 114.1, 115.8, 118.1, 126.3, 127.7, 130.0, 130.2, 134.1, 136.1, 139.4, 147.5. MALDI-MS Calc. for C₂₄H₂₄N₂ 340.194; found [M]⁺ 340.209. Anal. Calcd for C₂₄H₂₄N₂: C, 84.67; H, 7.11; N, 8.23%. Found: C, 84.46; H, 7.19; N, 8.36%.

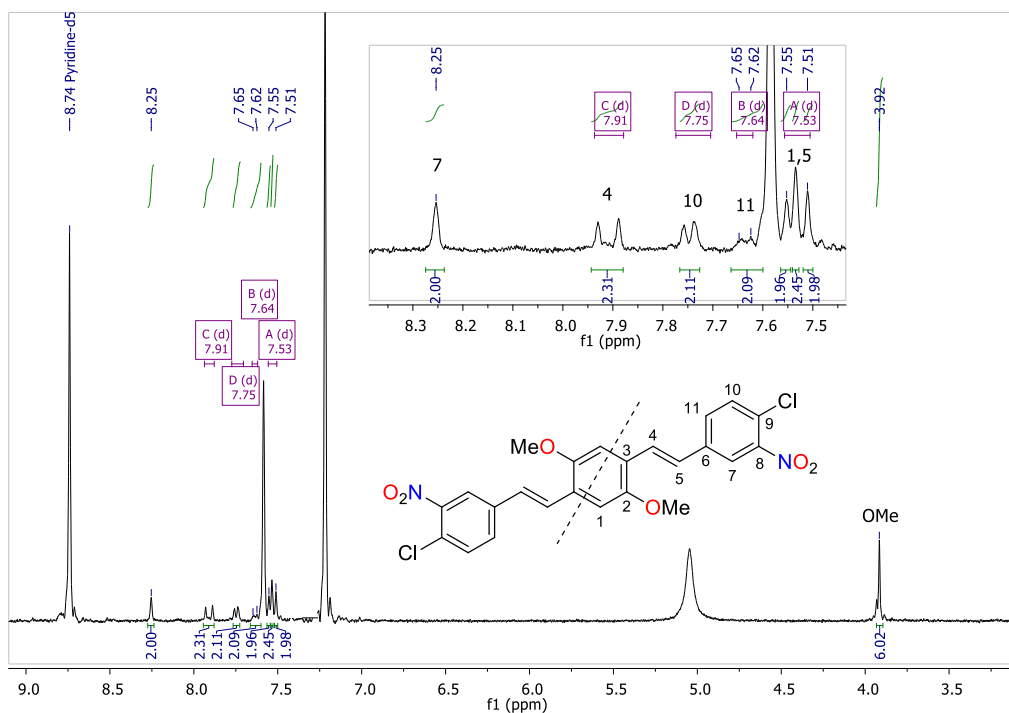
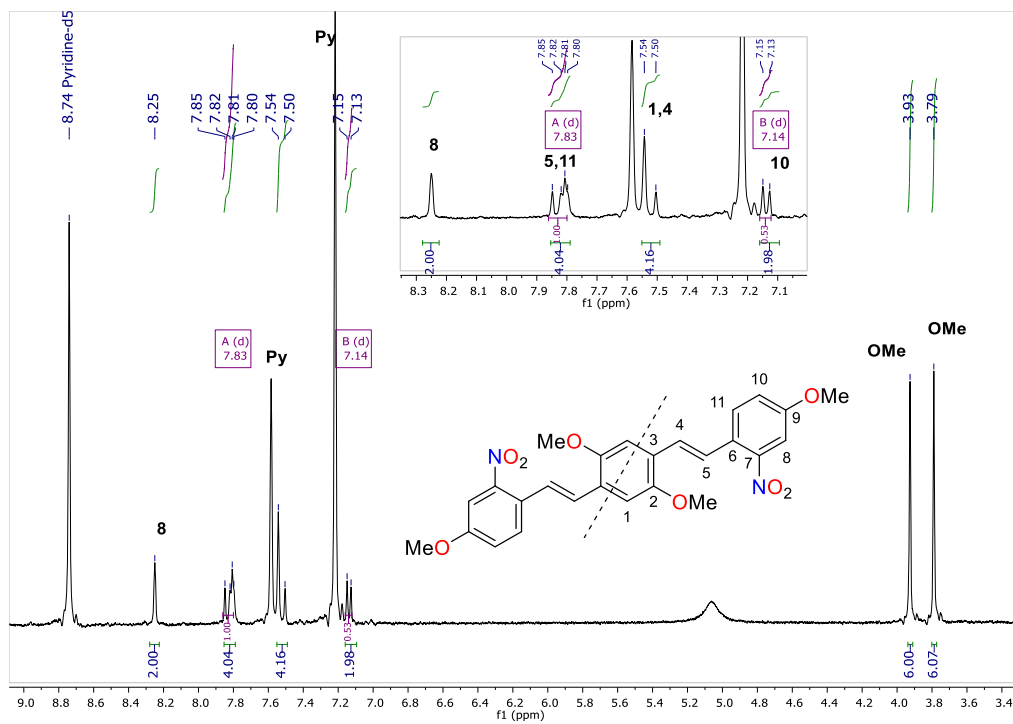


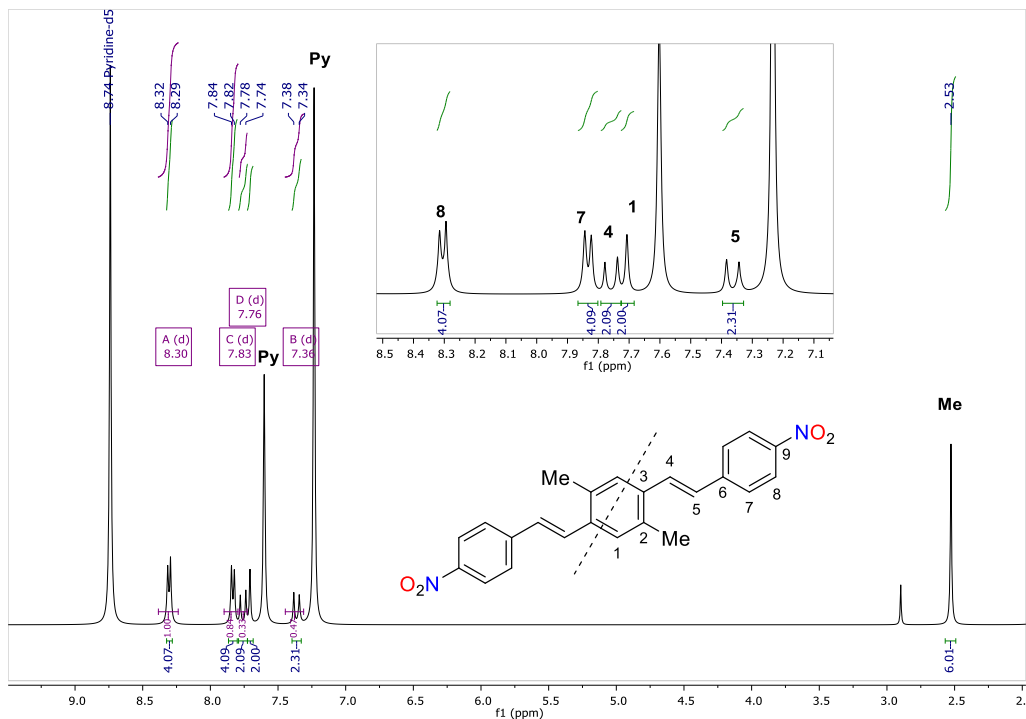
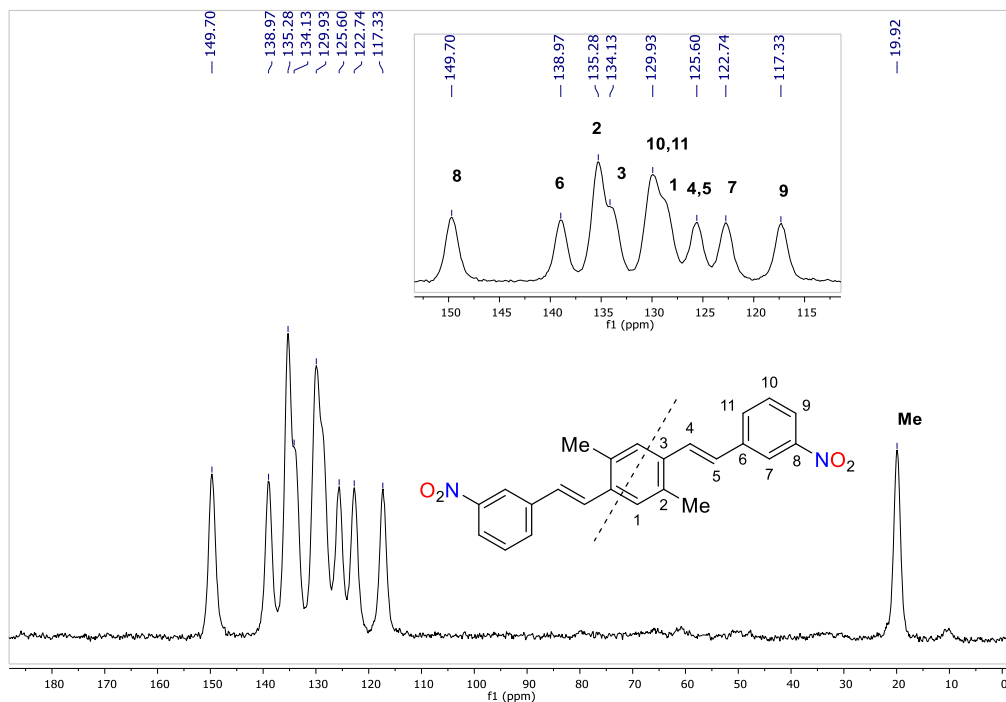
• **4,4'-((1E,1'E)-1,4-phenylenebis(ethene-2,1-diyl))dianiline 4h**. Light brown solid. Yield 0.249 (75%) m.p. 277-279 °C (Lit. 300-303 °C)²⁶⁸; from OPV **3h** (0.398 g, 1.07 mmol) and Na₂S (0.834 g (60%), 6.42 mmol). IR (ATR, cm⁻¹): 3431 (ν NH₂), 3337 (ν NH₂), 3205, 3021, 2920, 1600, 1513, 1266, 1176, 964. ¹H-NMR (400 MHz, pyridine-d₅) δ(ppm): 5.45 (bs, NH), 7.00 (d, *J*=8.3 Hz, 4H), 7.17 (d, *J*=16.4 Hz, 2H), 7.35 (d, *J*=16.4 Hz, 2H), 7.56 (d, *J*=8.3 Hz, 4H), 7.61 (s, 4H). ¹³C-NMR (100 MHz, pyridine-d₅) δ(ppm): 115.6, 124.5, 126.9, 127.3, 128.9, 129.7, 137.8, 150.0. MALDI-MS Calc. for C₂₂H₂₀N₂ 312.162; found [M]⁺ 312.299. Anal. Calcd for C₂₂H₂₀N₂: C, 84.58; H, 6.45; N, 8.97%. Found: C, 84.22; H, 6.33; N, 9.11%.

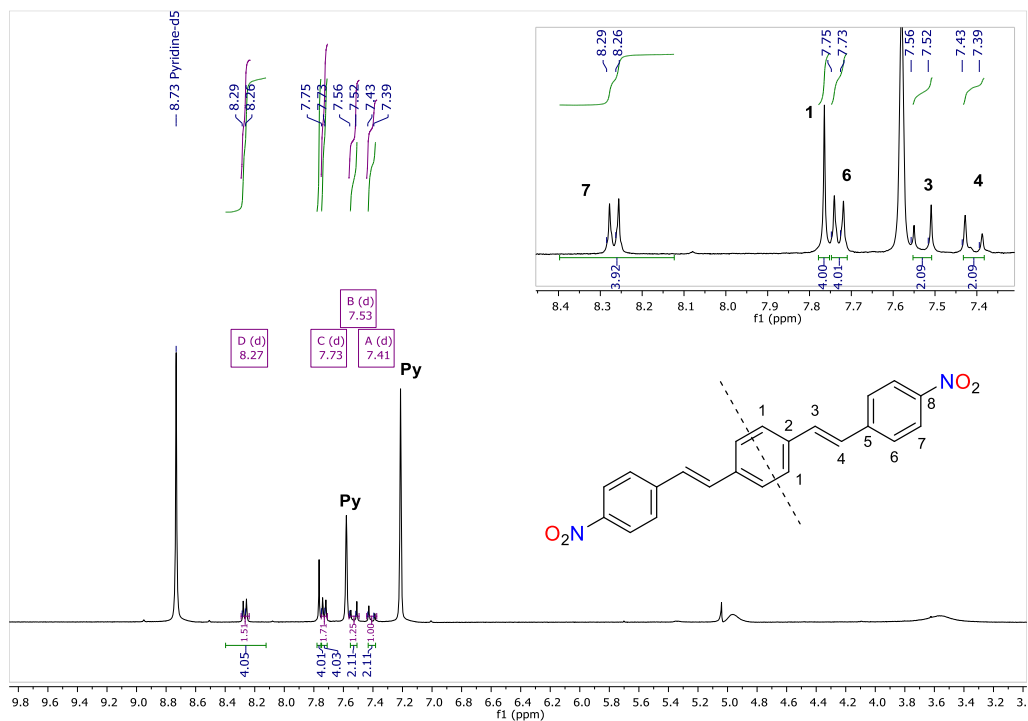
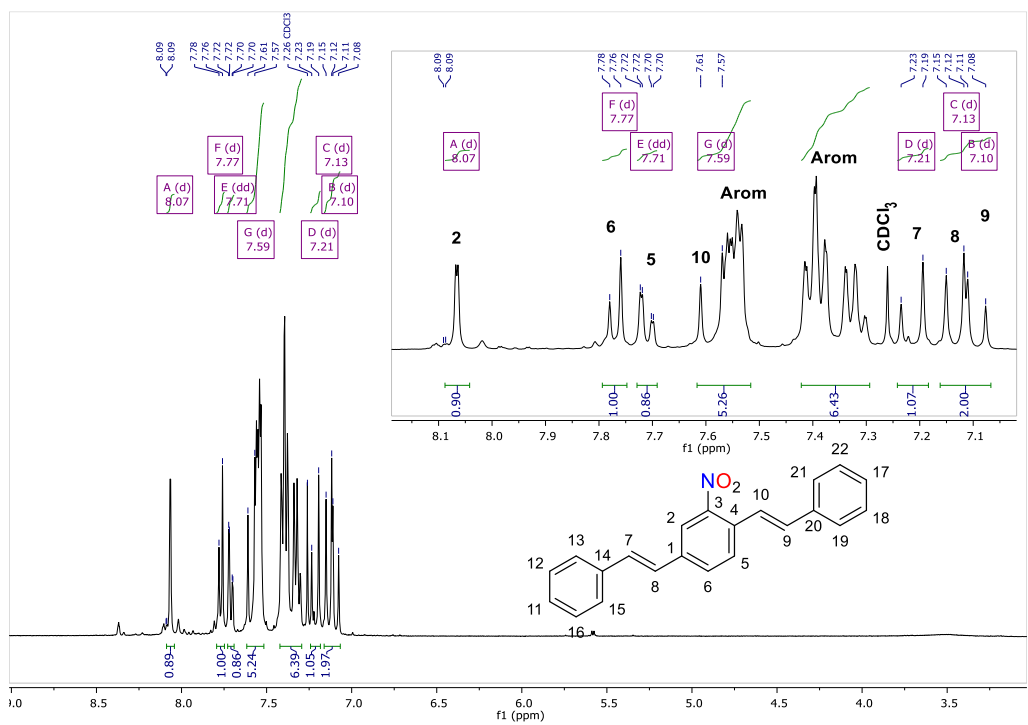
7.3 Experimental data for nitro and amino OPVs employed for Na₂S/pyridine reduction scope determination

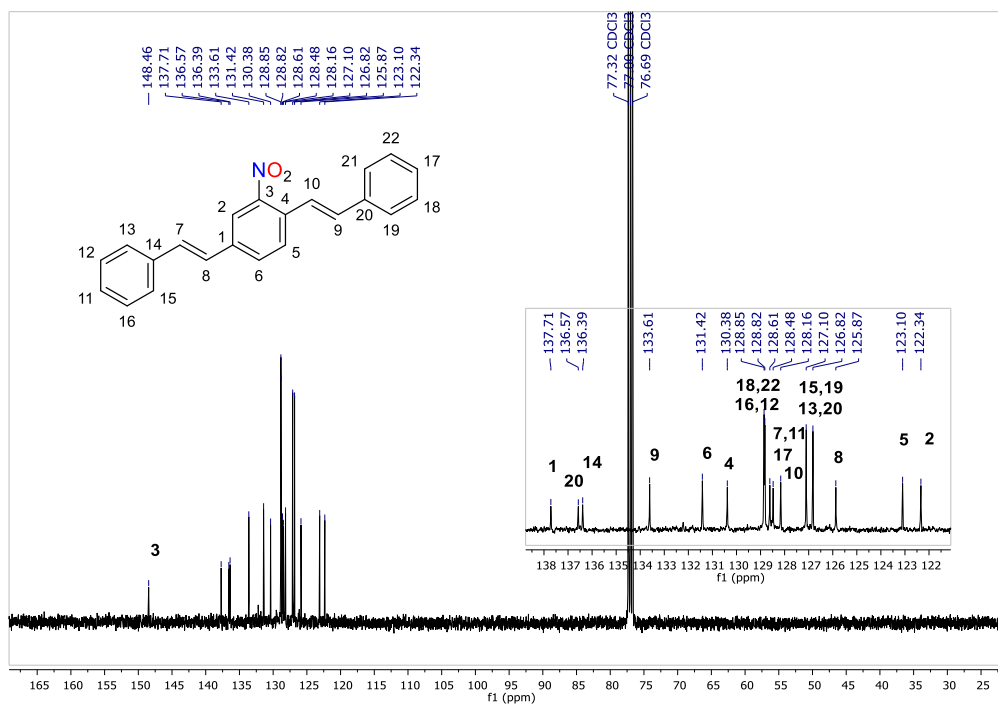
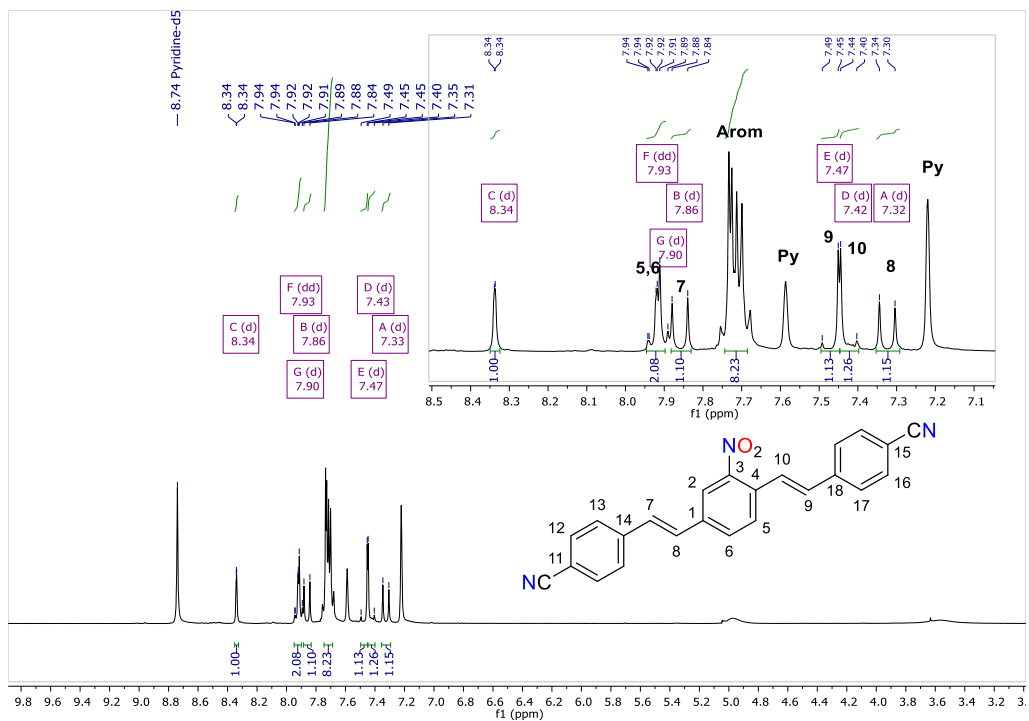
Appendix 7-3A. ¹H-NMR (Pyridine-d₅) spectrum for compound **3b**

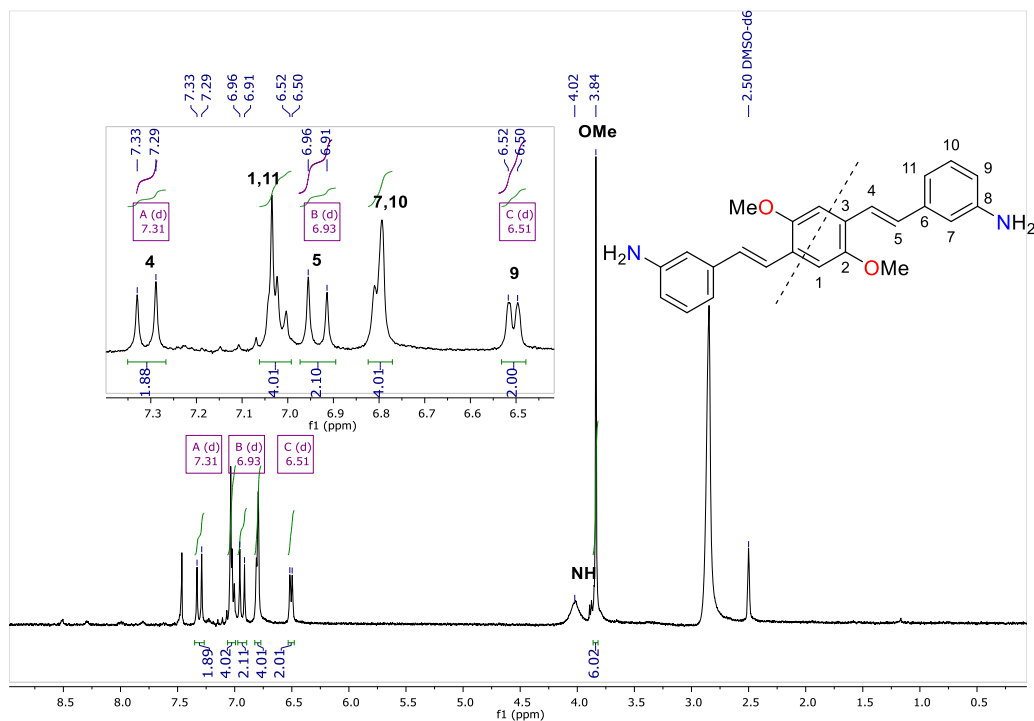
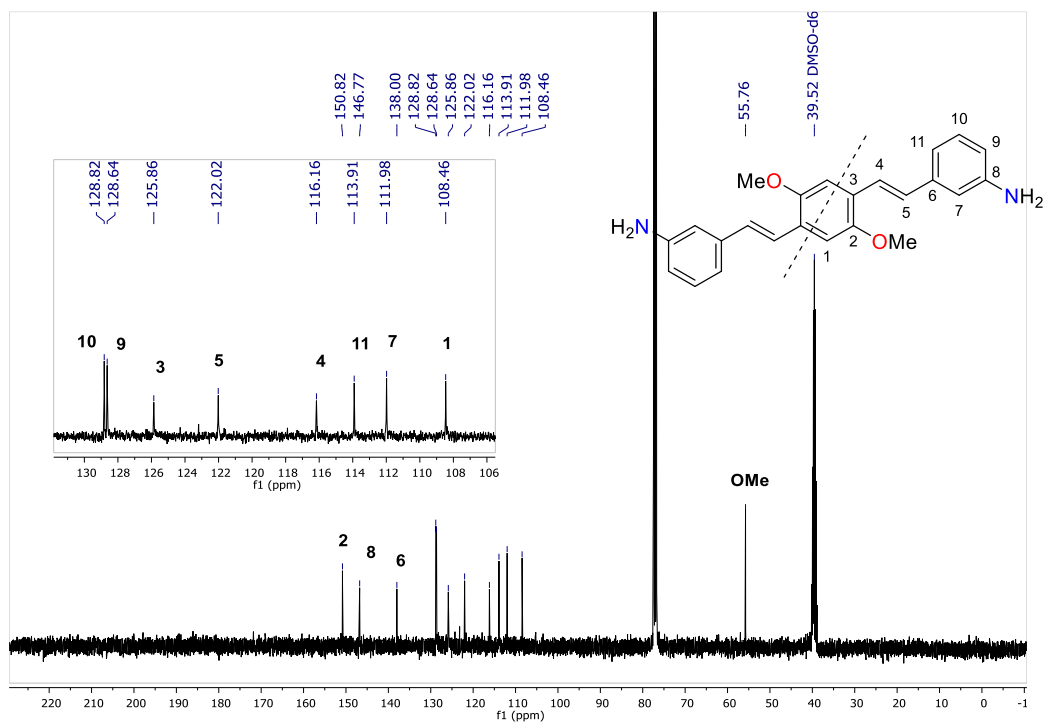


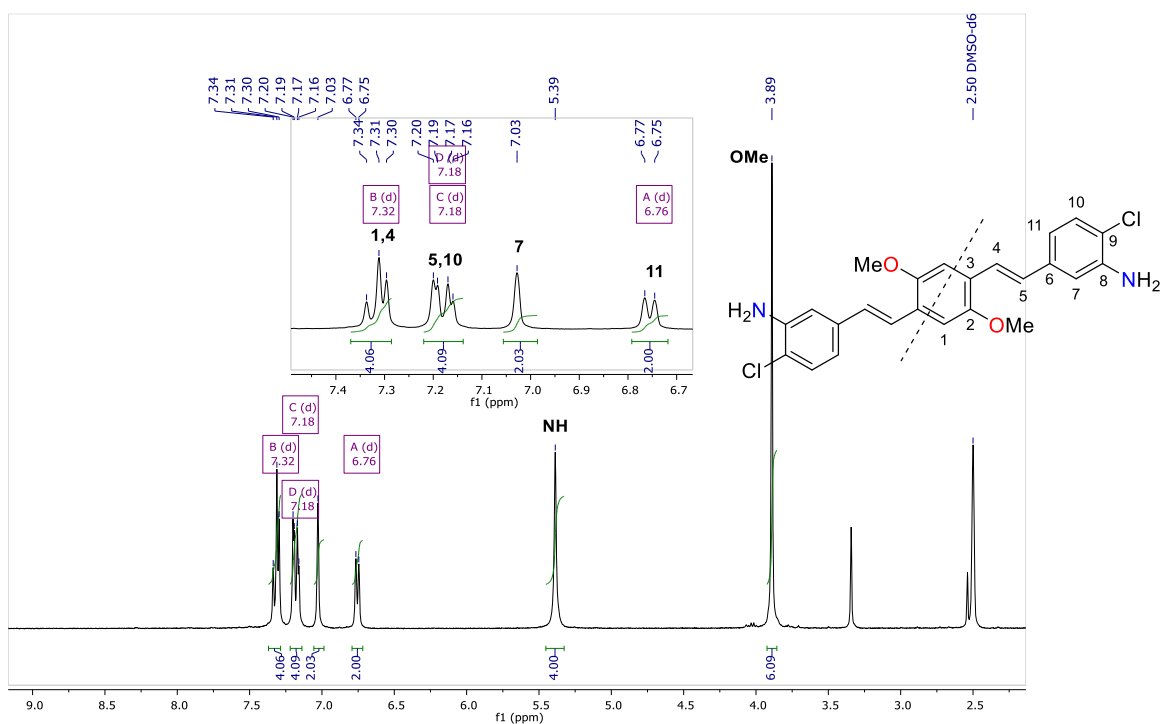
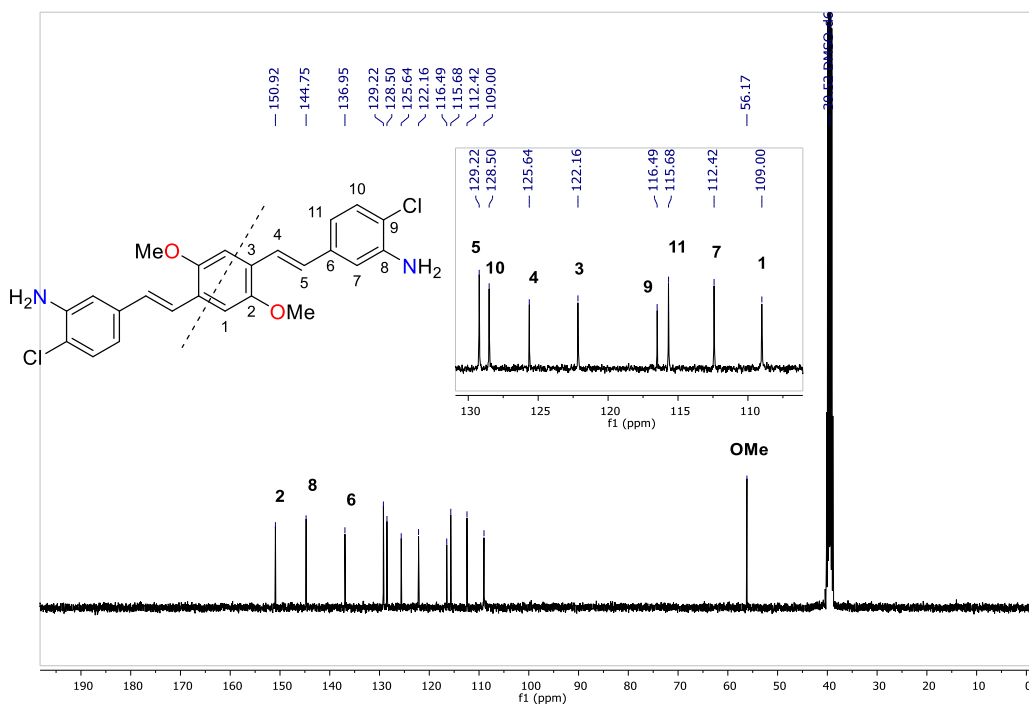
Appendix 7-3B. ¹H-NMR (Pyridine-d₅) spectrum for compound **3c**Appendix 7-3C. ¹H-NMR (Pyridine-d₅) spectrum for compound **3e**

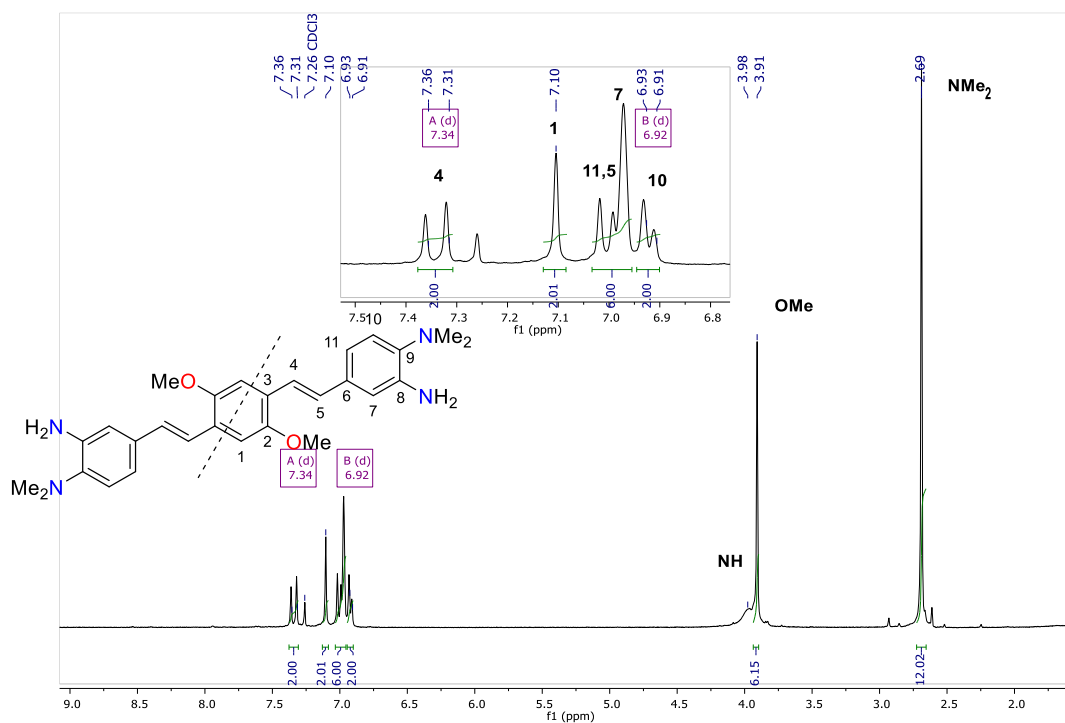
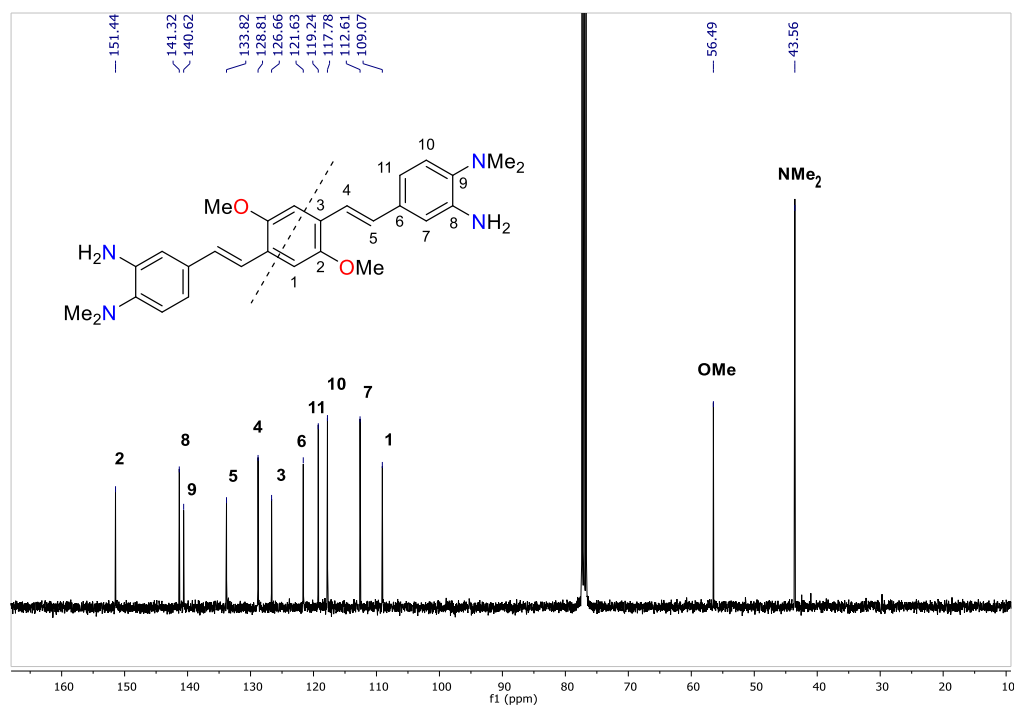
Appendix 7-3D. $^1\text{H-NMR}$ (Pyridine- d_5) spectrum for compound **3f**Appendix 7-3E. ^{13}C CP/MAS-NMR (100 MHz, KBr) spectrum for compound **3g**

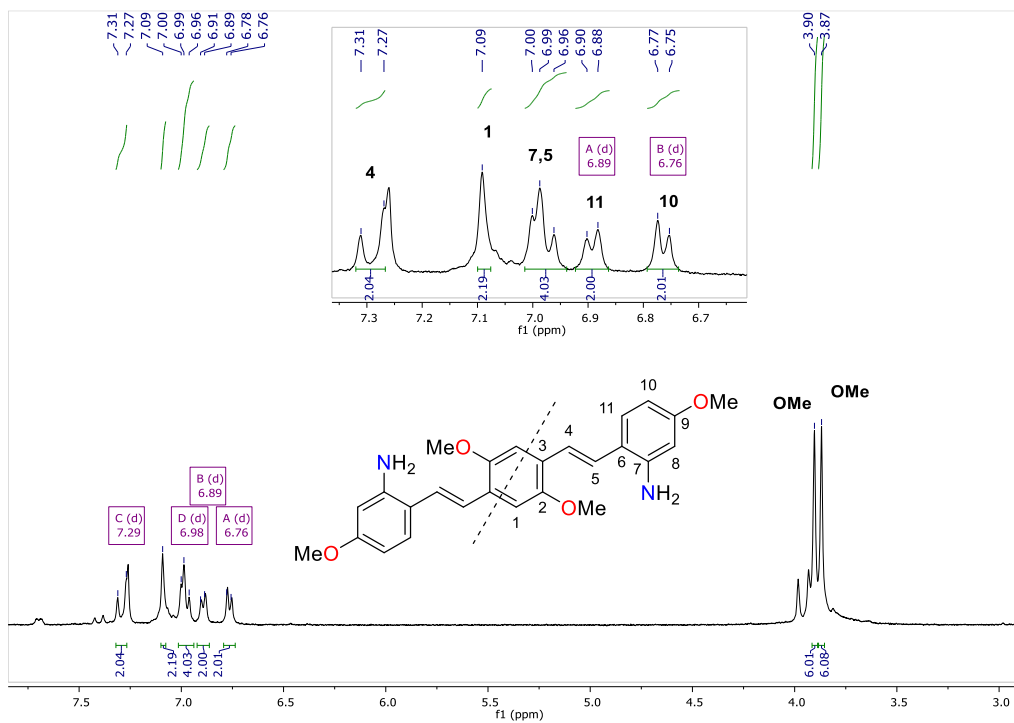
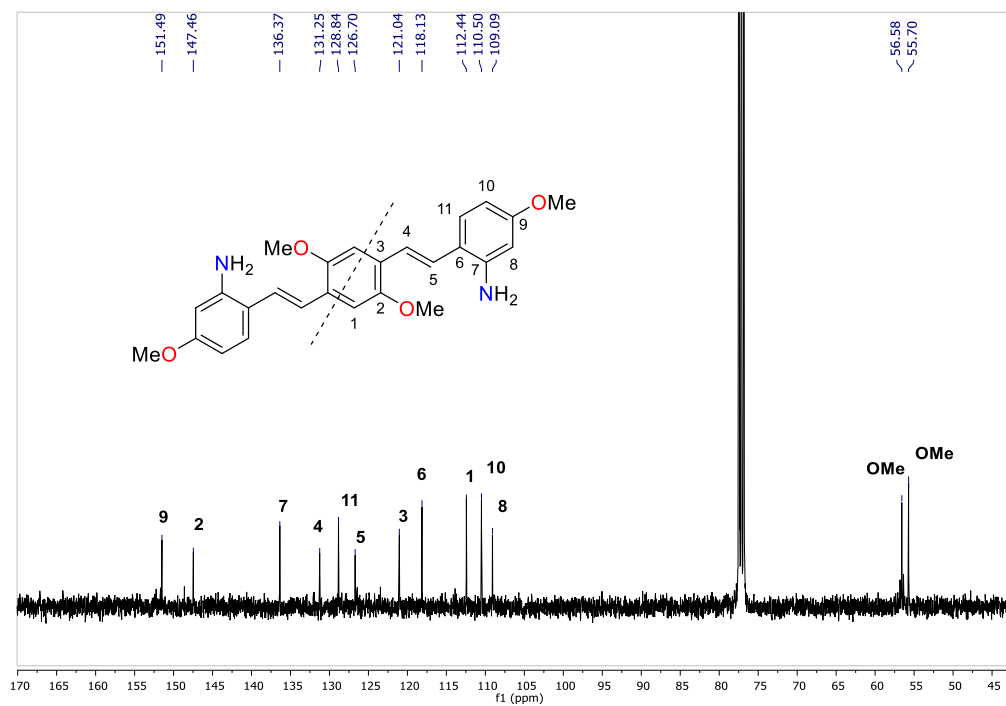
Appendix 7-3F. ¹H-NMR (Pyridine-d₅) spectrum for compound 3hAppendix 7-3G. ¹H-NMR (CDCl₃) spectrum for compound 3i

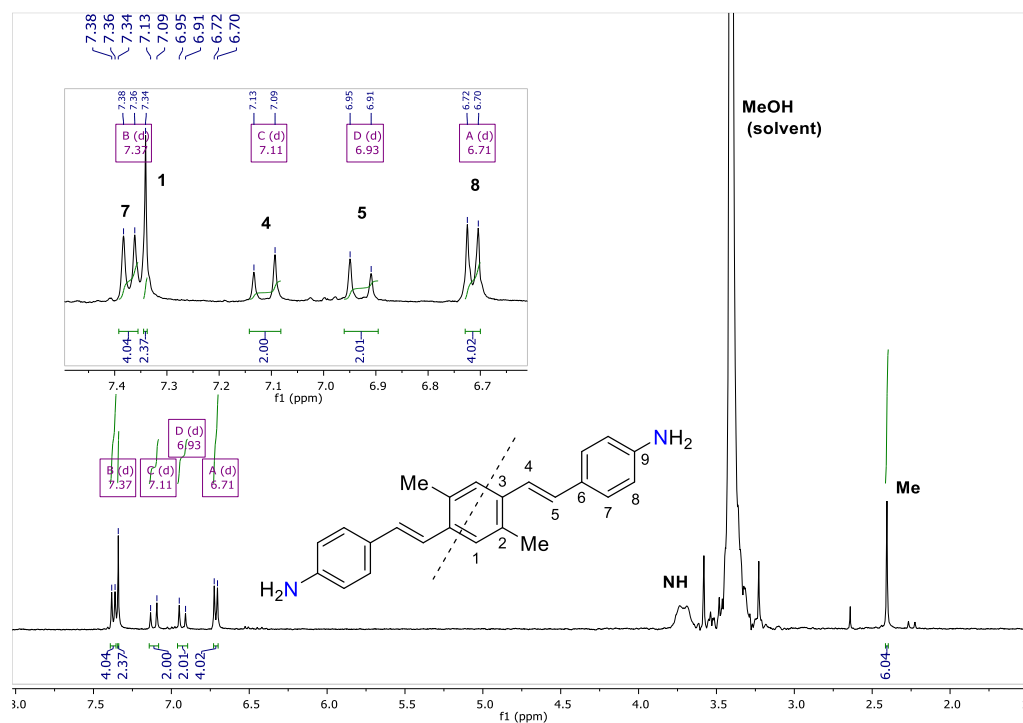
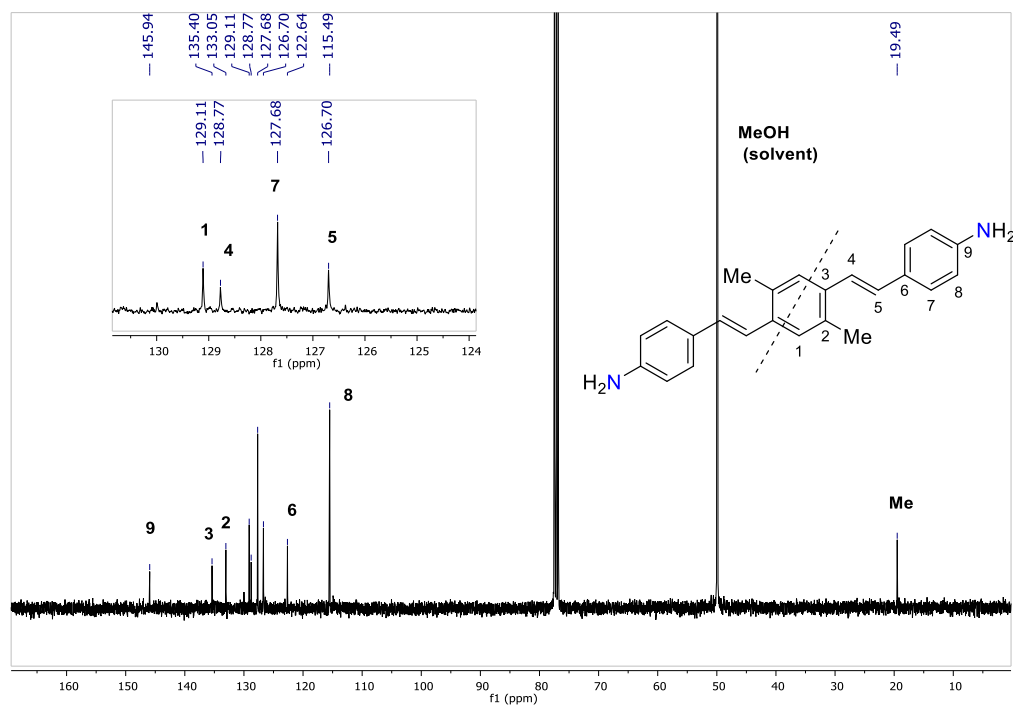
Appendix 7-3H. $^{13}\text{C-NMR}$ (CDCl_3) spectrum for compound **3i**Appendix 7-3I. $^1\text{H-NMR}$ (Pyridine- d_5) spectrum for compound **3j**

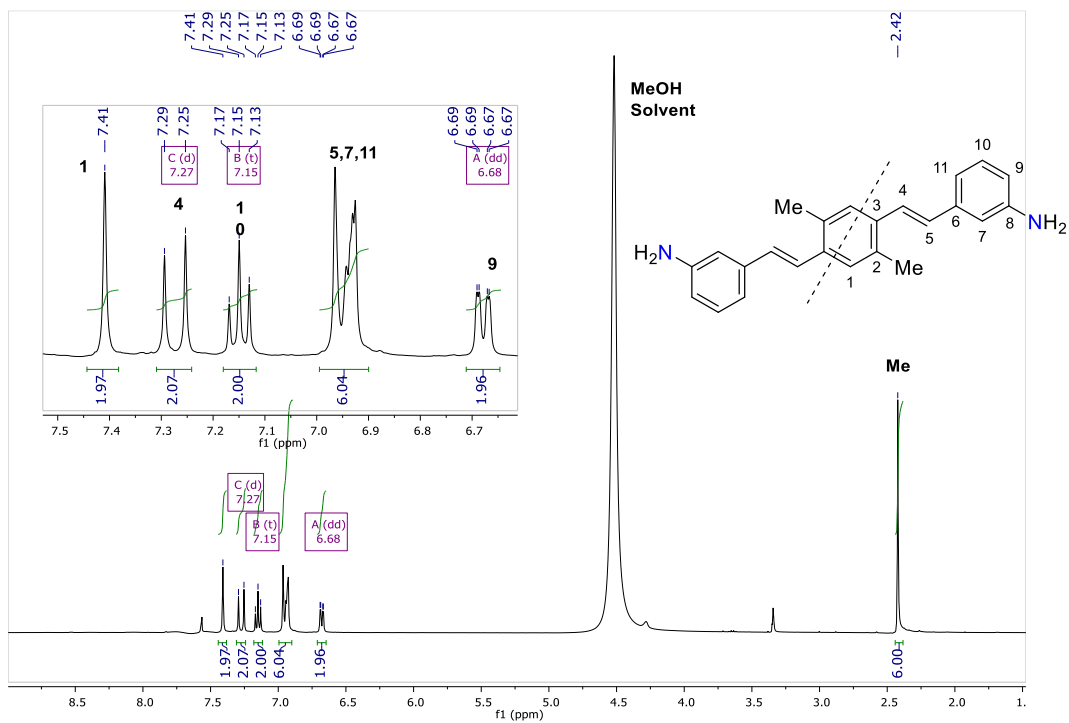
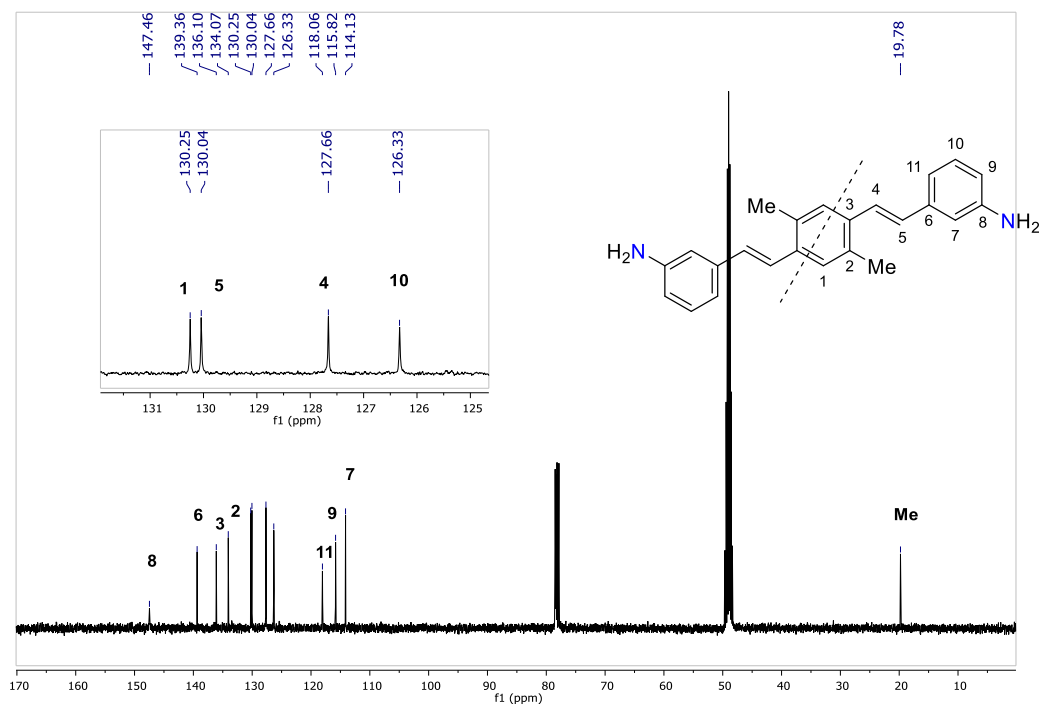
Appendix 7-3J. $^1\text{H-NMR}$ ($\text{CDCl}_3/\text{DMSO-d}_6$) spectrum for compound **4b**Appendix 7-3K. $^{13}\text{C-NMR}$ ($\text{CDCl}_3/\text{DMSO-d}_6$) spectrum for compound **4b**

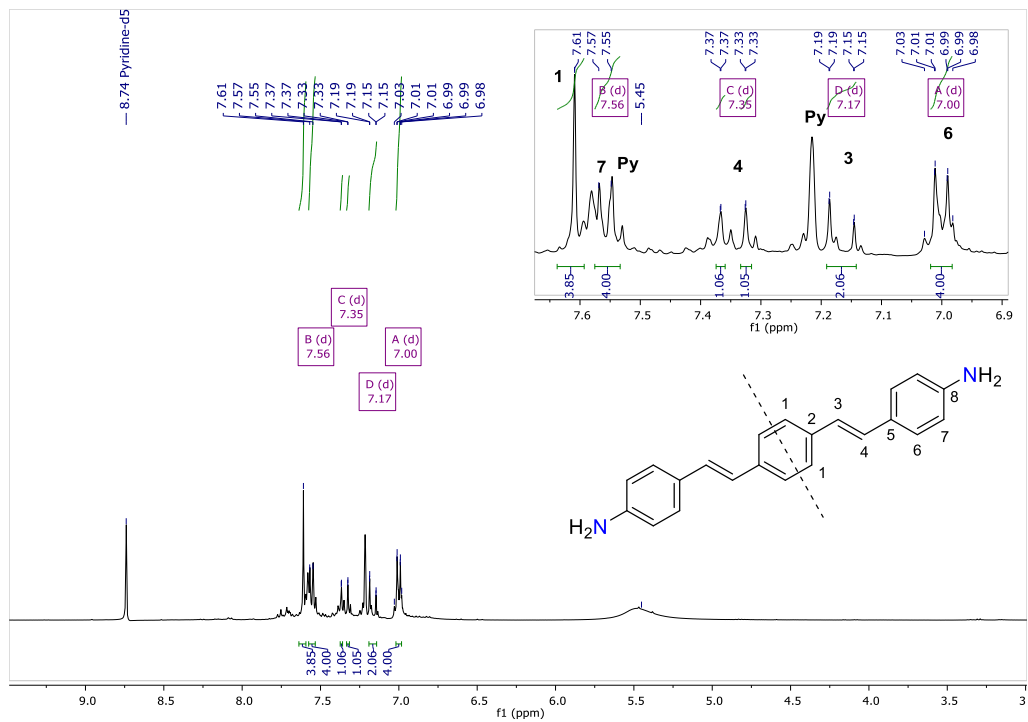
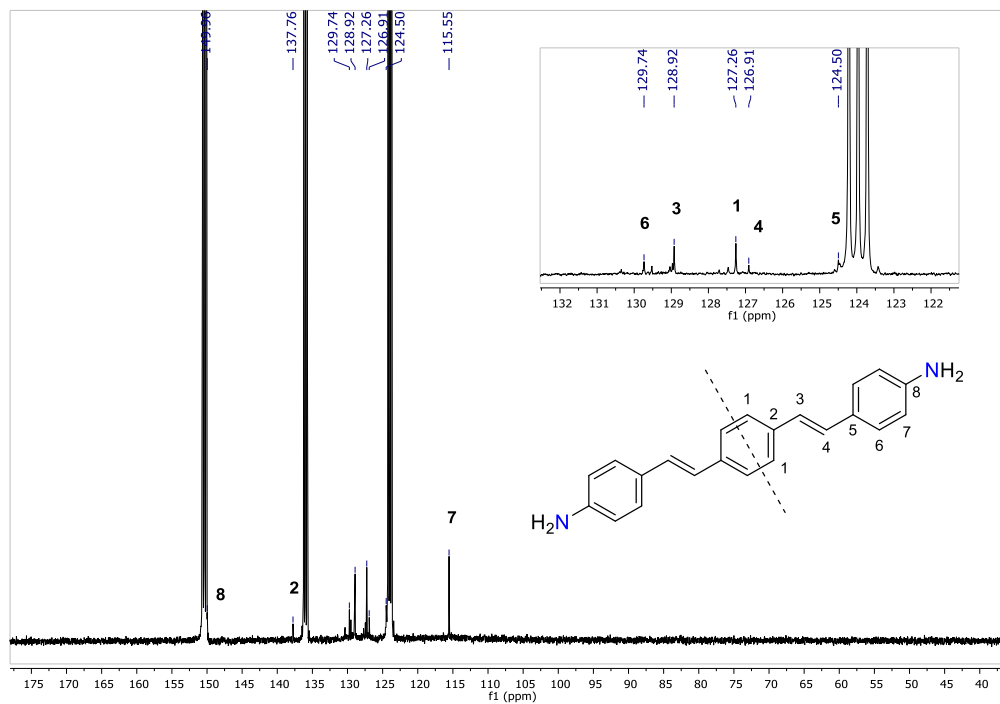
Appendix 7-3L. $^1\text{H-NMR}$ (DMSO- d_6) spectrum for compound **4c**Appendix 7-3M. $^{13}\text{C-NMR}$ (DMSO- d_6) spectrum for compound **4c**

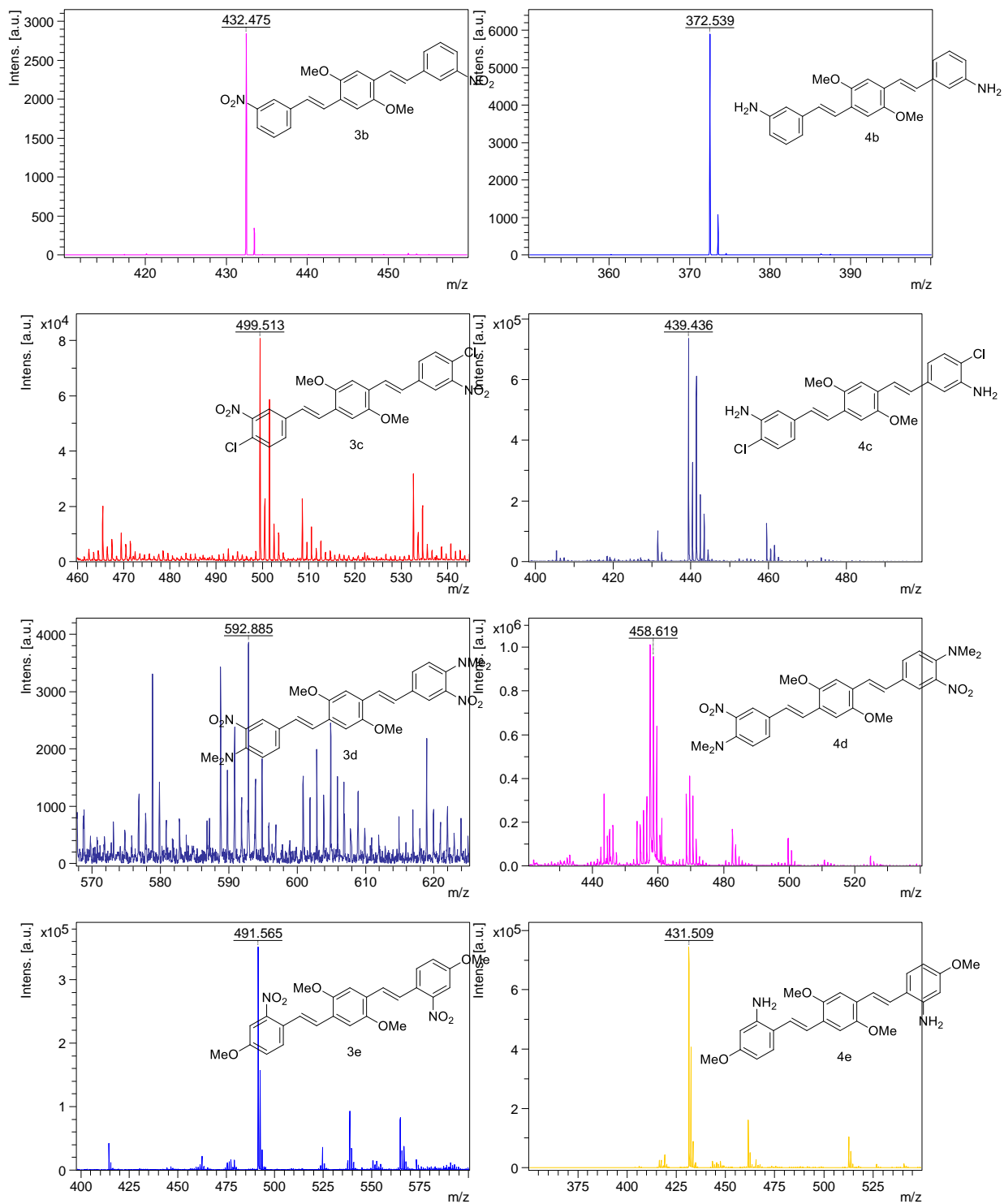
Appendix 7-3N. $^1\text{H-NMR}$ (CDCl_3) spectrum for compound **4d**Appendix 7-3O. $^{13}\text{C-NMR}$ (CDCl_3) spectrum for compound **4d**

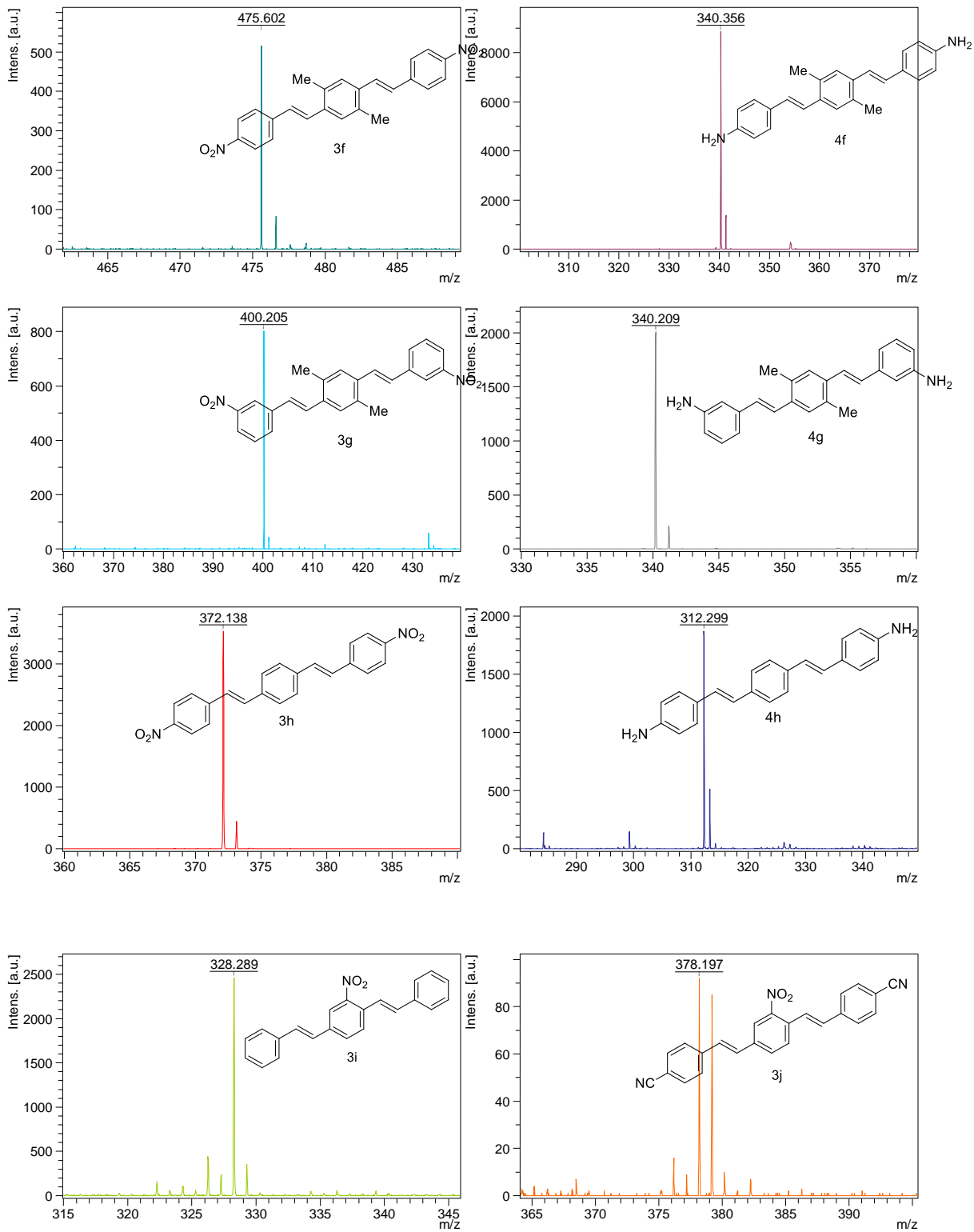
Appendix 7-3P. $^1\text{H-NMR}$ (CDCl_3) spectrum for compound **4e**Appendix 7-3Q. $^{13}\text{C-NMR}$ (CDCl_3) spectrum for compound **4e**

Appendix 7-3R. $^1\text{H-NMR}$ (CDCl_3) spectrum for compound **4f**Appendix 7-3S. $^{13}\text{C-NMR}$ (CDCl_3) spectrum for compound **4f**

Appendix 7-3T. $^1\text{H-NMR}$ (CDCl_3) spectrum for compound **4g**Appendix 7-3U. $^{13}\text{C-NMR}$ (CDCl_3) spectrum for compound **4g**

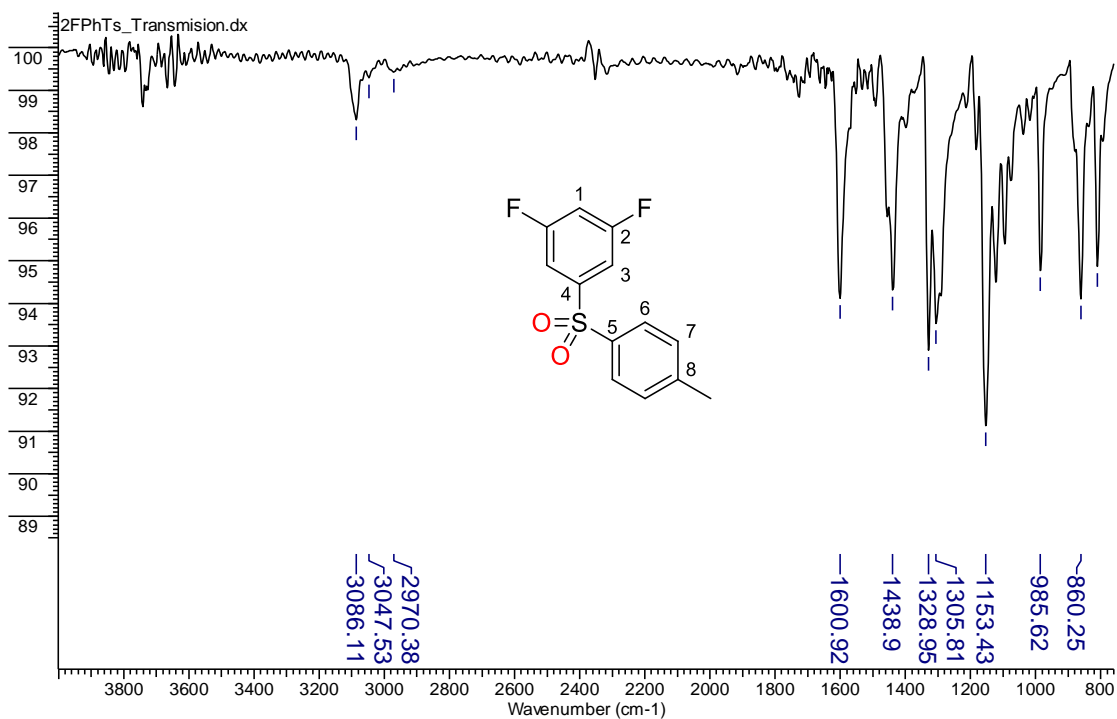
Appendix 7-3V. $^1\text{H-NMR}$ (Pyridine- d_5) spectrum for compound **4h**Appendix 7-3W. $^{13}\text{C-NMR}$ (Pyridine- d_5) spectrum for compound **4h**

Appendix 7-3X. MALDI-ToF spectra of NO₂ OPVs **3b-3j** and NH₂ OPVs **4b-4h**

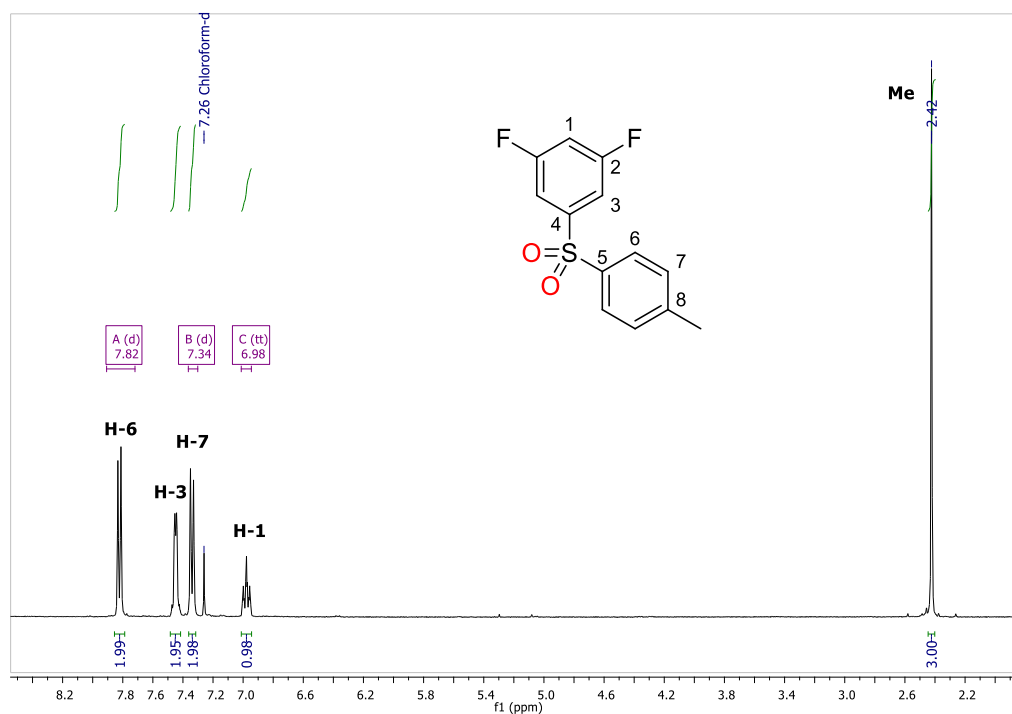


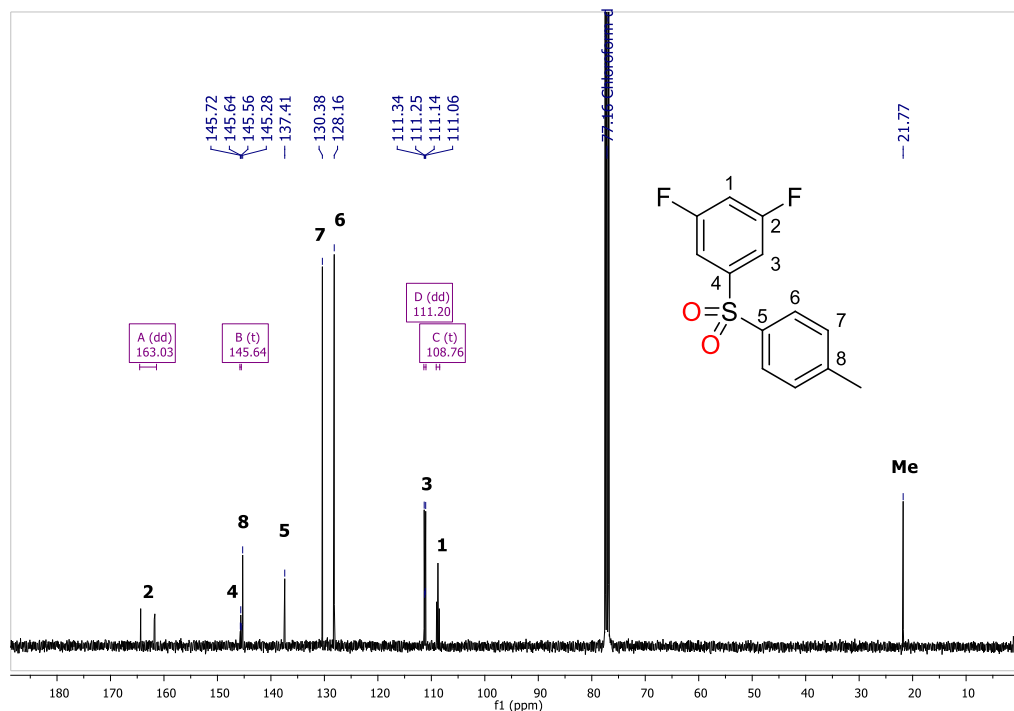
7.4 Experimental data for polymerization precursors

Appendix 7-4A. IR spectrum for compound 5



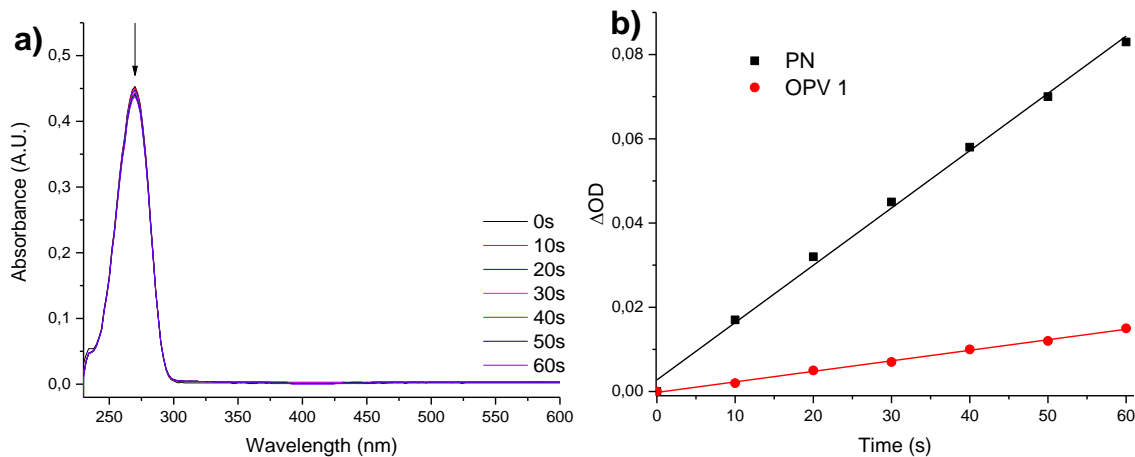
Appendix 7-4B. ¹H-NMR (CDCl₃) spectrum for compound 5



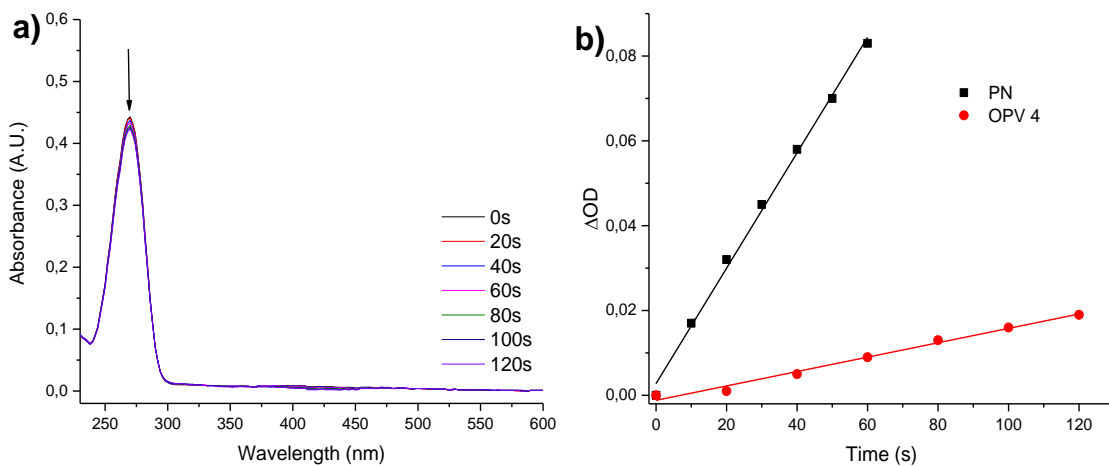
Appendix 7-4C. ^{13}C -NMR (CDCl_3) spectrum for compound **5**


7.5 Plots for Φ_{Δ} estimation

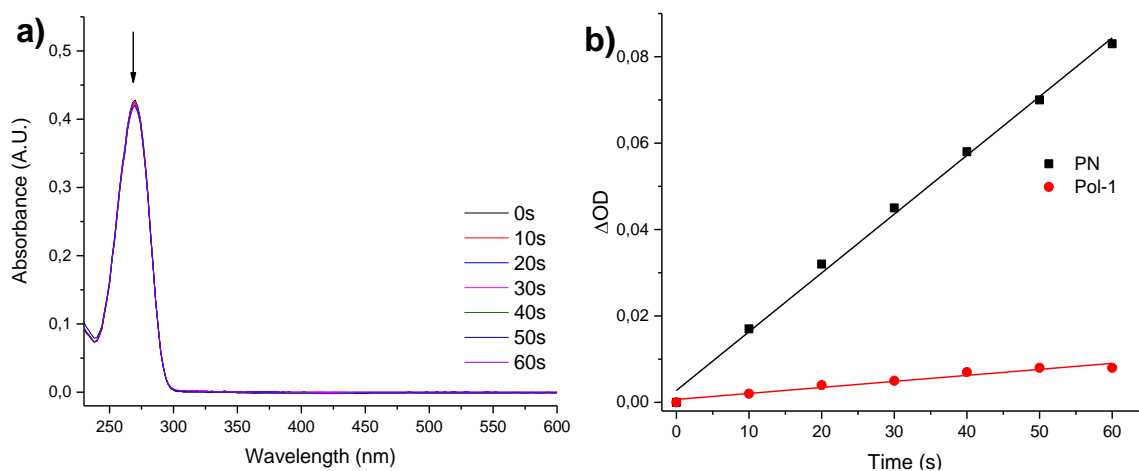
Appendix 7-5A. (a) Absorption spectra of furfuraldehyde upon irradiation in the presence of **OPV 1** (recorded at 10 s interval). (b) Plot of change in absorbance of furfuraldehyde at 270 nm vs irradiation time ($\lambda_{\text{irr}} = 350\text{-}450$ nm) in the presence of **OPV 1** against phenalenone (PN) as the standard in MeCN.



Appendix 7-5B. (a) Absorption spectra of furfuraldehyde upon irradiation in the presence of **OPV 4** (recorded at 20 s interval). (b) Plot of change in absorbance of furfuraldehyde at 270 nm vs irradiation time ($\lambda_{\text{irr}} = 350\text{-}450$ nm) in the presence of **OPV 4** against phenalenone (PN) as the standard in MeCN.

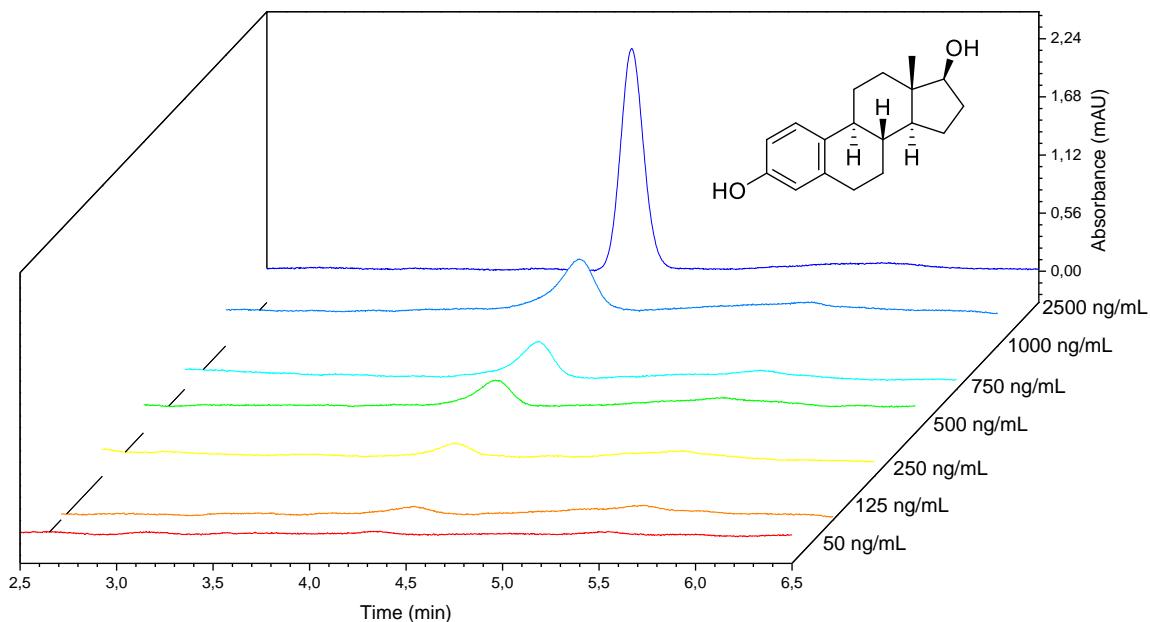


Appendix 7-5C. (a) Absorption spectra of furfuraldehyde upon irradiation in the presence of **Pol-1** (recorded at 10 s interval). (b) Plot of change in absorbance of furfuraldehyde at 270 nm vs irradiation time ($\lambda_{\text{irr}} = 350\text{-}450$ nm) in the presence of **Pol-1** against phenalenone (PN) as the standard in MeCN.

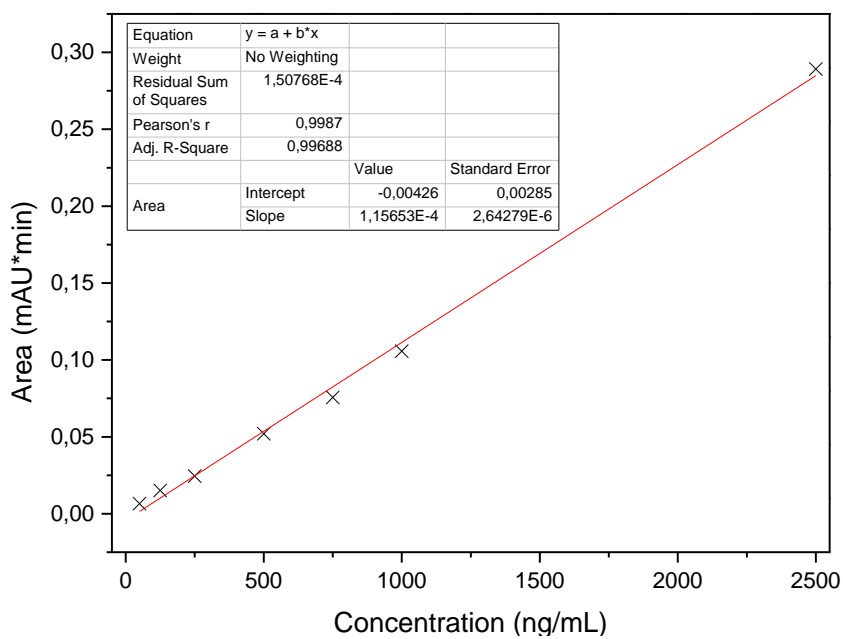


7.6 HPLC calibration curve for 17 β -estradiol

Appendix 7-6A. Comparative HPLC traces of 17 β -estradiol standards in the 50 to 2500 ng/mL concentration range.



Appendix 7-6B. Calibration curve used in the determination of 17 β -estradiol by HPLC.

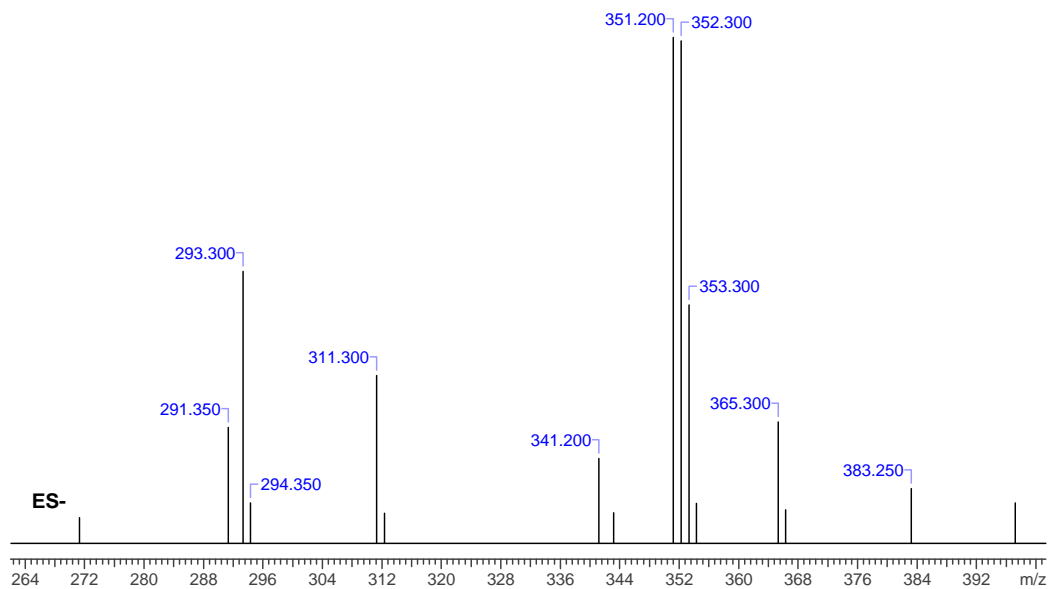


7.7 Mass spectra set for 17 β -estradiol UPLC traces in poultry litter extracts

Appendix 7-7A. 17 β -estradiol Q-TOF mass spectrum from standard.

Retention Time: 5.896

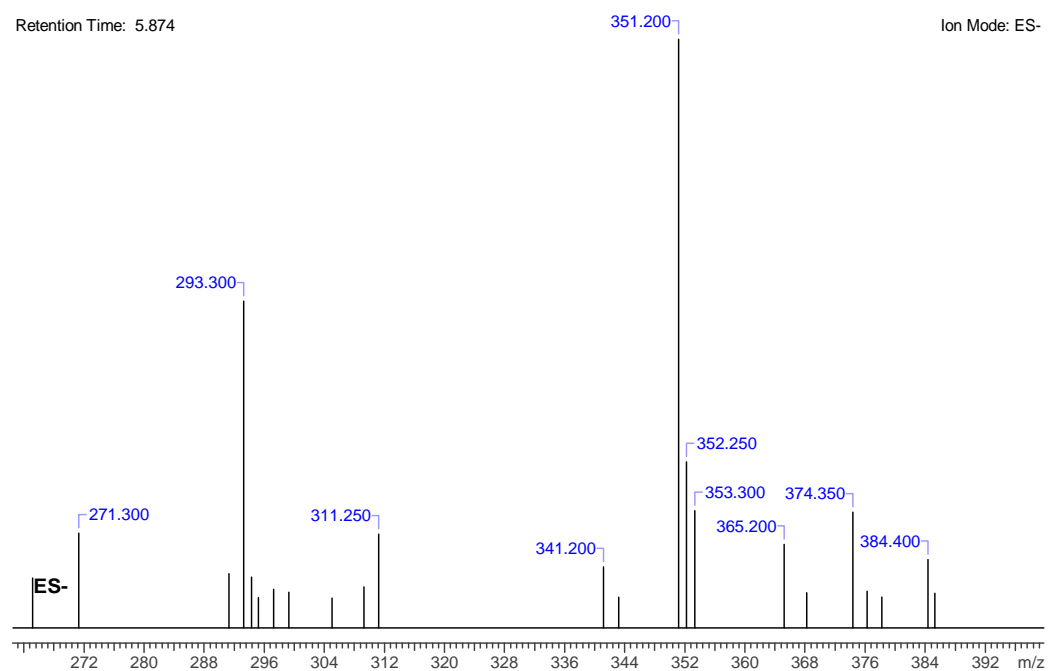
Ion Mode: ES-

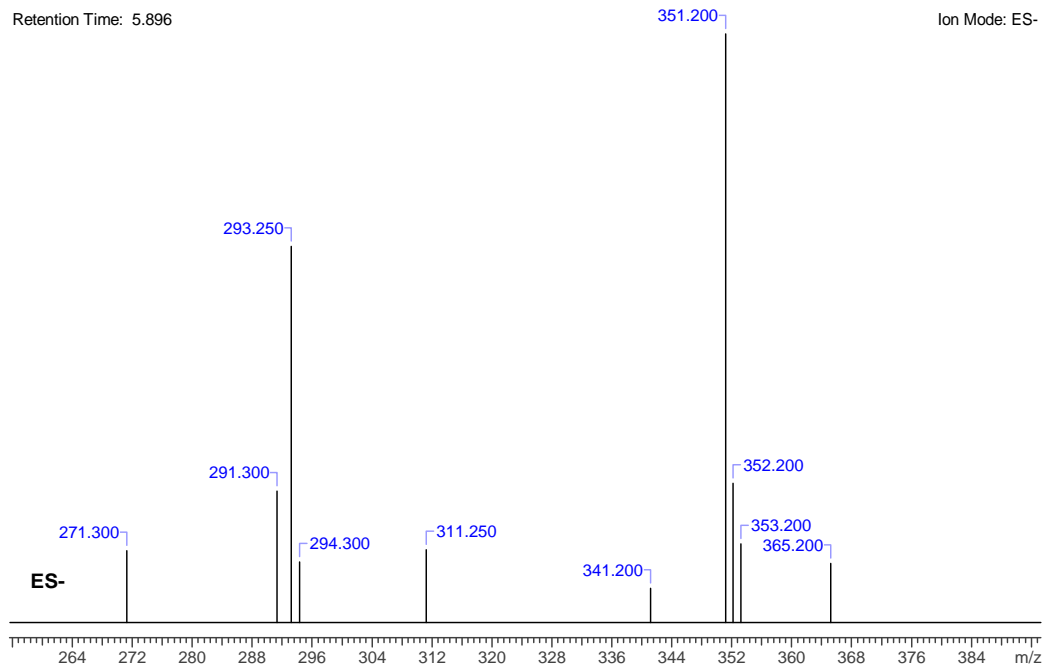


Appendix 7-7B. 17 β -estradiol Q-TOF mass spectrum from methanol extract.

Retention Time: 5.874

Ion Mode: ES-



Appendix 7-7C. 17 β -estradiol Q-TOF mass spectrum from water extract.

7.8 Publications and conferences

- M. Acelas, A. F. Sierra, C. A. Sierra. Exploring the Nitro Group Reduction in Low-Solubility Oligo-Phenylenevinylene Systems: Rapid Synthesis of Amino Derivatives. *Synthetic Communications*, **2020**, 50 (9), 1335 – 1352.
<https://doi.org/10.1080/00397911.2020.1731828>
- 50th General Assembly and 47th IUPAC World Chemistry Congress. Oligo-phenylenevinylenes as photocatalyst for the degradation of indigo carmine in textile wastewater treatment. Paris, France. July 7-12, **2019**.
- M. Acelas, C. A. Sierra. The Oligomer Approach: An Effective Strategy to Assess Phenylene Vinylene Systems as Organic Heterogeneous Photocatalysts in the Degradation of Aqueous Indigo Carmine Dye. *Journal of Photochemistry and Photobiology A: Chemistry*, **2021**, 405, 112980.
<https://doi.org/10.1016/j.jphotochem.2020.112980>

-
- M. Acelas, C. A. Sierra. Estimation of singlet oxygen quantum yield in oligo (phenylene vinylene)s using furfuraldehyde as a chemical acceptor. In preparation
 - M. Acelas, N. J. Castellanos, C. A. Sierra. Stability and Performance Enhancement of an Oligo (phenylene vinylene) Photocatalyst via Surface Grafting onto TiO₂ for Visible-Light Indigo Carmine Degradation. *ChemistrySelect*, **2022**, 7(9), e202103460. <https://doi.org/10.1002/slct.202103460>
 - 34° Congreso Latinoamericano de Química CLAQ 2020. Oligo (phenylene vinylene)-grafted TiO₂ photocatalyst for visible-light driven control of 17β-estradiol in water. Cartagena, Colombia. October 11-15, **2021**.
 - M. Acelas, L.D. Pérez, C. A. Sierra. Boosting the photocatalytic performance of the oligo (phenylene vinylene) moiety by copolymerization for the heterogeneous degradation of indigo carmine dye. In preparation.

References

- (1) Oelgemöller, M.; Jung, C.; Mattay, J. Green Photochemistry: Production of Fine Chemicals with Sunlight. *Pure Appl. Chem.* **2007**, *79*, 1939–1947. <https://doi.org/10.1351/pac200779111939>.
- (2) Romero, N. A.; Nicewicz, D. A. Organic Photoredox Catalysis. *Chem. Rev.* **2016**, *116*, 10075–10166. <https://doi.org/10.1021/acs.chemrev.6b00057>.
- (3) Amos, S. G. E.; Garreau, M.; Buzzetti, L.; Waser, J. Photocatalysis with Organic Dyes: Facile Access to Reactive Intermediates for Synthesis. *Beilstein J. Org. Chem.* **2020**, *16*, 1163–1187. <https://doi.org/10.3762/bjoc.16.103>.
- (4) Blayney, A. J.; Perepichka, I. F.; Wudl, F.; Perepichka, D. F. Advances and Challenges in the Synthesis of Poly(p-Phenylene Vinylene)-Based Polymers. *Isr. J. Chem.* **2014**, *54*, 674–688. <https://doi.org/10.1002/ijch.201400067>.
- (5) Muktha, B.; Madras, G.; Guru Row, T. N.; Scherf, U.; Patil, S. Conjugated Polymers for Photocatalysis. *J. Phys. Chem. B* **2007**, *111*, 7994–7998. <https://doi.org/10.1021/jp071096n>.
- (6) Li, X.; Yan, H.; Durrant, J. Studies on the Photo-Stability of Poly p-(Phenylene Vinylene). *Spectrosc. Spectral Anal. (Beijing, China)* **2004**, *25*, 743–746.
- (7) Liras, M.; Barawi, M.; De La Peña O’Shea, V. A. Hybrid Materials Based on Conjugated Polymers and Inorganic Semiconductors as Photocatalysts: From Environmental to Energy Applications. *Chem. Soc. Rev.* **2019**, *48*, 5454–5487. <https://doi.org/10.1039/c9cs00377k>.
- (8) Young, C. A.; Hammack, A.; Lee, H. J.; Jia, H.; Yu, T.; Marquez, M. D.; Jamison, A. C.; Gnade, B. E.; Lee, T. R. Poly(1,4-Phenylene Vinylene) Derivatives with Ether Substituents to Improve Polymer Solubility for Use in Organic Light-Emitting Diode Devices. *ACS Omega* **2019**, *4*, 22332–22344. <https://doi.org/10.1021/acsomega.9b02396>.
- (9) Diederich, F.; Martin, R. E. Linear Monodisperse p -Conjugated Oligomers : *Angew. Chem. Int. Ed.* **1999**, *38*, 1350–1377. [https://doi.org/10.1002/\(SICI\)1521-](https://doi.org/10.1002/(SICI)1521-)

- 3773(19990517)38:10<1350::AID-ANIE1350>3.0.CO;2-6.
- (10) Mikroyannidis, J. A.; Tsagkournos, D. V.; Balraju, P.; Sharma, G. D. Synthesis and Photovoltaic Properties of an Alternating Phenylenevinylene Copolymer with Substituted-Triphenylamine Units along the Backbone for Bulk Heterojunction and Dye-Sensitized Solar Cells. *J. Power Sources* **2011**, *196*, 2364–2372. <https://doi.org/10.1016/j.jpowsour.2010.09.118>.
- (11) Müller, C. D.; Falcou, A.; Reckefuss, N.; Rojahn, M.; Wiederhorn, V.; Rudati, P.; Frohne, H.; Nuyken, O.; Becker, H.; Meerholz, K. Multi-Colour Organic Light-Emitting Displays by Solution Processing. *Nature* **2003**, *421*, 829–833. <https://doi.org/10.1038/nature01390>.
- (12) Morgado, J.; Cacialli, F.; Friend, R. H.; Chuah, B. S.; Moratti, S. C.; Holmes, A. B. Luminescence Properties of PPV-Based Copolymers with Crown Ether Substituents. *Synth. Met.* **2000**, *111*, 449–452. [https://doi.org/10.1016/S0379-6779\(99\)00397-5](https://doi.org/10.1016/S0379-6779(99)00397-5).
- (13) Ng, P. K.; Gong, X.; Chan, S. H.; Lam, L. S.; Chan, W. K. The Role of Ruthenium and Rhenium Diimine Complexes in Conjugated Polymers That Exhibit Interesting Opto-Electronic Properties. *Chem. - A Eur. J.* **2001**, *7*, 4358–4367. [https://doi.org/10.1002/1521-3765\(20011015\)7:20<4358::AID-CHEM4358>3.0.CO;2-M](https://doi.org/10.1002/1521-3765(20011015)7:20<4358::AID-CHEM4358>3.0.CO;2-M).
- (14) Hsieh, B. R.; Yu, Y.; Vanlaeken, A. C.; Lee, H. General Methodology toward Soluble Poly(p-Phenylenevinylene) Derivatives. *Macromolecules* **1997**, *30*, 8094–8095. <https://doi.org/10.1021/ma9713771>.
- (15) Yu, C. Y.; Lai, Y. C. Soluble Phenylenevinylene Polymers Containing Tetraphenylethene Units by Ring-Opening Metathesis Polymerization. *Macromol. Chem. Phys.* **2018**, *219*, 1–5. <https://doi.org/10.1002/macp.201800135>.
- (16) Sierra, C. A.; Lahti, P. M. A Photoluminescent , Segmented Oligo-Polyphenylenevinylene Copolymer with Hydrogen-Bonding Pendant Chains. *Chem. Mater.* **2004**, *16*, 55–61. <https://doi.org/10.1021/cm034708z>.
- (17) Carvajal, T. R.; Kuebler, S. M.; Sierra, C. A. Synthesis of Novel Phenylenevinylene Linkers with Electron-Donating Substituents by the Heck Reaction. *Synth. Met.* **2015**, *209*, 183–187. <https://doi.org/10.1016/j.synthmet.2015.07.024>.
- (18) Díaz, C.; Alzate, D.; Rodríguez, R.; Ochoa, C.; Sierra, C. A. High Yield and Stereospecific Synthesis of Segmented Poly (p-Phenylene Vinylene) by the Heck Reaction. *Synth. Met.* **2013**, *172*, 32–36.

- <https://doi.org/10.1016/j.synthmet.2013.03.023>.
- (19) Castellanos-García, L. J.; Agudelo, B. C.; Rosales, H. F.; Cely, M.; Ochoa-Puentes, C.; Blanco-Tirado, C.; Sierra, C. A.; Combariza, M. Y. Oligo P-Phenylenevinylene Derivatives as Electron Transfer Matrices for UV-MALDI. *J. Am. Soc. Mass Spectrom.* **2017**, *28*, 2548–2560. <https://doi.org/10.1007/s13361-017-1783-z>.
- (20) Mikroyannidis, J. A. Synthesis by the Gilch Method of Blue-Light-Emitting Poly (p-Phenylenevinylene) Derivatives Bearing Highly Phenylated Pendants. *Chem. Mater.* **2003**, *15*, 1865–1871. <https://doi.org/10.1021/cm0209113>.
- (21) Son, S.; Dodabalapur, A.; Lovinger, A. J.; Galvin, M. E. Luminescence Enhancement by the Introduction of Disorder into Poly(p-Phenylene Vinylene). *Science.* **1995**, *269*, 376–378. <https://doi.org/10.1126/science.269.5222.376>.
- (22) Lowet, F.; Vanderzande, D.; Gelan, J.; Mullens, J. A New Synthetic Route to a Soluble High Molecular Weight Precursor for Poly(p-Phenylenevinylene) Derivatives. *Macromolecules* **1995**, *28*, 1330–1331. <https://doi.org/10.1021/ma00108a079>.
- (23) Nomura, K. Well-Defined End-Functionalized Conjugated Polymers/Oligomers Exhibiting Unique Emission Properties through the End Groups: The Exclusive Synthesis by Combined Olefin Metathesis with Wittig-Type Coupling. *Macromol. Mater. Eng.* **2019**, *304*, 1900307. <https://doi.org/10.1002/mame.201900307>.
- (24) Kim, K.; Ahn, T. Synthesis and Light-Emitting Properties of a Carbazole-Containing Hyperbranched Conjugated Poly(Phenylene Vinylene). *Mol. Cryst. Liq. Cryst.* **2020**, *705*, 112–119. <https://doi.org/10.1080/15421406.2020.1743427>.
- (25) Liu, Z.; Yuan, Y.; Wen, X.; Zhang, J.; Lei, G.; Zhang, P. Synthesis, Characterization, Photoluminescent, and Electroluminescent Properties of Poly(Biphenylenevinylene-Alt-Methoxyoctyloxyphenylenevinylene). *Polym. Bull.* **2013**, *70*, 1221–1235. <https://doi.org/10.1007/s00289-012-0843-6>.
- (26) Pfeiffer, S.; Hörhold, H. H. Synthesis of Soluble MEH-PPV and MEH-PPB by Horner Condensation Polymerization. *Synth. Met.* **1999**, *101*, 109–110. [https://doi.org/10.1016/S0379-6779\(98\)01279-X](https://doi.org/10.1016/S0379-6779(98)01279-X).
- (27) Lehmann, M.; Maier, P. Shape-Persistent, Sterically Crowded Star Mesogens: From Exceptional Columnar Dimer Stacks to Supermesogens. *Angew. Chemie - Int. Ed.* **2015**, *54*, 9710–9714. <https://doi.org/10.1002/anie.201501988>.

- (28) Rotas, G.; Stranius, K.; Tkachenko, N.; Tagmatarchis, N. Ultralong 20 Milliseconds Charge Separation Lifetime for Photoilluminated Oligophenylenevinylene–Azafullerene Systems. *Adv. Funct. Mater.* **2018**, *28*, 1702278. <https://doi.org/10.1002/adfm.201702278>.
- (29) Sierra, A. F.; Rodríguez, R.; Sierra, C. A. Synthesis of a Stereoselective Nitro Phenylenevinylene Derivative by the Heck Reaction Using Phosphites. *Rev. Colomb. Quim.* **2010**, *39*, 163–171.
- (30) Liang, F.; Pu, Y. J.; Kurata, T.; Kido, J.; Nishide, H. Synthesis and Electroluminescent Property of Poly(p-Phenylenevinylene)s Bearing Triarylamine Pendants. *Polymer (Guildf)*. **2005**, *46*, 3767–3775. <https://doi.org/10.1016/j.polymer.2005.03.036>.
- (31) Zhang, W.; Zhu, L.; Qin, J.; Yang, C. Novel Water-Soluble Red-Emitting Poly(p - Phenylenevinylene) Derivative: Synthesis, Characterization, and Fluorescent Acetylcholinesterase Assays. *J. Phys. Chem. B* **2011**, *115*, 12059–12064. <https://doi.org/10.1021/jp206930v>.
- (32) Ramírez-Pradilla, J. S.; Blanco-Tirado, C.; Combariza, M. Y. Electron-Transfer Ionization of Nanoparticles, Polymers, Porphyrins, and Fullerenes Using Synthetically Tunable α -Cyanophenylenevinylenes as UV MALDI-MS Matrices. *ACS Appl. Mater. Interfaces* **2019**, *11*, 10975–10987. <https://doi.org/10.1021/acsami.8b22246>.
- (33) Pasco, S. T.; Lahti, P. M.; Karasz, F. E. Synthesis of Substituted Poly(p - Phenylenevinylene) Copolymers by the Heck Method for Luminescence Studies . *Macromolecules* **1999**, *32*, 6933–6937. <https://doi.org/10.1021/ma990825x>.
- (34) Flores-Rojas, G. G.; Lijanová, I. V.; Morales-Saavedra, O. G.; Sanchez-Montes, K.; Martínez-García, M. Synthesis and NLO Behavior of Oligo(Phenylenevinylene)-Porphyrin Dendrimers. *Dye. Pigm.* **2013**, *96*, 125–129. <https://doi.org/10.1016/j.dyepig.2012.07.011>.
- (35) Flores-Noria, R.; Vázquez, R.; Arias, E.; Moggio, I.; Rodríguez, M.; Ziolo, R. F.; Rodríguez, O.; Evans, D. R.; Liebig, C. Synthesis and Optoelectronic Properties of Phenylenevinylenequinoline Macromolecules. *New J. Chem.* **2014**, *38*, 974–984. <https://doi.org/10.1039/c3nj01193c>.
- (36) Nojima, M.; Ohta, Y.; Yokozawa, T. Investigation of Catalyst-Transfer Condensation Polymerization for Synthesis of Poly(p-Phenylenevinylene). *J. Polym. Sci. Part A Polym. Chem.* **2014**, *52*, 2643–2653. <https://doi.org/10.1002/pola.27281>.

- (37) Babudri, F.; Cardone, A.; Chiavarone, L.; Ciccarella, G.; Farinola, G. M.; Naso, F.; Scamarcio, G. Synthesis and Characterization of Poly(2,3,5,6-Tetrafluoro-1,4-Phenylenevinylene). *Chem. Commun.* **2001**, 1940–1941. <https://doi.org/10.1039/b105029j>.
- (38) Sharma, A.; Sharma, N.; Kumar, R.; Shard, A.; Sinha, A. K. Direct Olefination of Benzaldehydes into Hydroxy Functionalized Oligo (p-Phenylenevinylene)s via Pd-Catalyzed Heterodomino Knoevenagel- Decarboxylation-Heck Sequence and Its Application for Fluoride Sensing π -Conjugated Units. *Chem. Commun.* **2010**, *46*, 3283–3285. <https://doi.org/10.1039/c001980a>.
- (39) Allolio, C.; Strassner, T. Palladium Complexes with Chelating Bis-NHC Ligands in the Mizoroki-Heck Reaction-Mechanism and Electronic Effects, a DFT Study. *J. Org. Chem.* **2014**, *79*, 12096–12105. <https://doi.org/10.1021/jo501897s>.
- (40) Cárdenas, J. C.; Fadini, L.; Sierra, C. A. Triphenylphosphite and Ionic Liquids: Positive Effects in the Heck Cross-Coupling Reaction. *Tetrahedron Lett.* **2010**, *51*, 6867–6870. <https://doi.org/10.1016/j.tetlet.2010.10.104>.
- (41) Cárdenas, J. C.; Ochoa-Puentes, C.; Gutiérrez-Puebla, E.; Sierra, C. A. Synthesis, Crystal Structure Determination and Photoluminescence Properties of a Pure anti *trans-trans* Phenylenevinylene Derivative. *Synth. Met.* **2016**, *215*, 194–199. <https://doi.org/10.1016/j.synthmet.2016.02.021>.
- (42) Estrada, S. E.; Ochoa-Puentes, C.; Sierra, C. A. Phenylenevinylene Oligomers by Mizoroki-Heck Cross Coupling Reaction. Structural and Optoelectronic Characterization. *J. Mol. Struct.* **2017**, *1133*, 448–457. <https://doi.org/10.1016/j.molstruc.2016.12.032>.
- (43) Baptista, M. S.; Cadet, J.; Di Mascio, P.; Ghogare, A. A.; Greer, A.; Hamblin, M. R.; Lorente, C.; Nunez, S. C.; Ribeiro, M. S.; Thomas, A. H.; Vignoni, M.; Yoshimura, T. M. Type I and Type II Photosensitized Oxidation Reactions: Guidelines and Mechanistic Pathways. *Photochem. Photobiol.* **2017**, *93*, 912–919. <https://doi.org/10.1111/php.12716>.
- (44) Neville, S. P.; Kirkby, O. M.; Kaltsoyannis, N.; Worth, G. A.; Fielding, H. H. Identification of a New Electron-Transfer Relaxation Pathway in Photoexcited Pyrrole Dimers. *Nat. Commun.* **2016**, *7*, 11357. <https://doi.org/10.1038/ncomms11357>.
- (45) El-Khouly, M. E.; Ito, O.; Smith, P. M.; D'Souza, F. Intermolecular and

- Supramolecular Photoinduced Electron Transfer Processes of Fullerene-Porphyrin/Phthalocyanine Systems. *J. Photochem. Photobiol. C Photochem. Rev.* **2004**, *5*, 79–104. <https://doi.org/10.1016/j.jphotochemrev.2004.01.003>.
- (46) Marin, M. L.; Santos-Juanes, L.; Arques, A.; Amat, A. M.; Miranda, M. A. Organic Photocatalysts for the Oxidation of Pollutants and Model Compounds. *Chem. Rev.* **2012**, *112*, 1710–1750. <https://doi.org/10.1021/cr2000543>.
- (47) Yan, M.; Rothberg, L. J.; Papadimitrakopoulos, F.; Galvin, M. E.; Miller, T. M. Defect Quenching of Conjugated Polymer Luminescence. *Phys. Rev. Lett.* **1994**, *73*, 744–747. <https://doi.org/10.1103/PhysRevLett.73.744>.
- (48) Papadimitrakopoulos, F.; Yan, M.; Rothberg, L. J.; Katz, H. E.; Chandross, E. A.; Galvin, M. E. Thermal and Photochemical Origin of Carbonyl Group Defects in Poly-(p-Phenylenevinylene). *Mol. Cryst. Liq. Cryst.* **1994**, *256*, 663–669.
- (49) Scurlock, R. D.; Wang, B.; Ogilby, P. R.; Sheats, J. R.; Clough, R. L. Singlet Oxygen as a Reactive Intermediate in the Photodegradation of an Electroluminescent Polymer. *J. Am. Chem. Soc.* **1995**, *117*, 10194–10202. <https://doi.org/10.1021/ja00146a004>.
- (50) Cumpston, B. H.; Jensen, K. F. Photo-Oxidation of Polymers Used in Electroluminescent Devices. *Synth. Met.* **1995**, *73*, 195–199. [https://doi.org/10.1016/0379-6779\(95\)80015-8](https://doi.org/10.1016/0379-6779(95)80015-8).
- (51) Dam, N.; Scurlock, R. D.; Wang, B.; Ma, L.; Sundahl, M.; Ogilby, P. R. Singlet Oxygen as a Reactive Intermediate in the Photodegradation of Phenylenevinylene Oligomers. *Chem. Mater.* **1999**, *11*, 1302–1305. <https://doi.org/10.1021/cm9807687>.
- (52) Chambon, S.; Rivaton, A.; Gardette, J. L.; Firon, M.; Lutsen, L. Aging of a Donor Conjugated Polymer: Photochemical Studies of the Degradation of Poly[2-Methoxy-5-(30,70-Dimethyloctyloxy)-1,4-Phenylenevinylene]. *J. Polym. Sci. Part A Polym. Chem.* **2007**, *45*, 317–331. <https://doi.org/10.1002/pola.21815>.
- (53) Chambon, S.; Rivaton, A.; Gardette, J. L.; Firon, M. Reactive Intermediates in the Initiation Step of the Photo-Oxidation of MDMO-PPV. *J. Polym. Sci. Part A Polym. Chem.* **2009**, *47*, 6044–6052. <https://doi.org/10.1002/pola.23628>.
- (54) Chambon, S.; Rivaton, A.; Gardette, J. L.; Firon, M. Photo- and Thermo-Oxidation of Poly(p-Phenylene-Vinylene) and Phenylene-Vinylene Oligomer. *Polym. Degrad. Stab.* **2011**, *96*, 1149–1158. <https://doi.org/10.1016/j.polymdegradstab.2011.02.002>.
- (55) Chambon, S.; Rivaton, A.; Gardette, J. L.; Firon, M. Photo- and Thermal Degradation

- of MDMO-PPV:PCBM Blends. *Sol. Energy Mater. Sol. Cells* **2007**, *91*, 394–398. <https://doi.org/10.1016/j.solmat.2006.10.015>.
- (56) Ferreira, G. R.; Nowacki, B.; Magalhães, A.; DeAzevedo, E. R.; De Sá, E. L.; Akcelrud, L. C.; Bianchi, R. F. Controlling Photo-Oxidation Processes of a Polyfluorene Derivative: The Effect of Additives and Mechanism. *Mater. Chem. Phys.* **2014**, *146*, 212–217. <https://doi.org/10.1016/j.matchemphys.2014.02.037>.
- (57) Chambon, S.; Manceau, M.; Firon, M.; Cros, S.; Rivaton, A.; Gardette, J. L. Photo-Oxidation in an $^{18}\text{O}_2$ Atmosphere: A Powerful Tool to Elucidate the Mechanism of UV-Visible Light Oxidation of Polymers - Application to the Photodegradation of MDMO-PPV. *Polymer (Guildf)*. **2008**, *49*, 3288–3294. <https://doi.org/10.1016/j.polymer.2008.04.001>.
- (58) Chambon, S.; Rivaton, A.; Gardette, J. L.; Firon, M. Durability of MDMO-PPV and MDMO-PPV: PCBM Blends under Illumination in the Absence of Oxygen. *Sol. Energy Mater. Sol. Cells* **2008**, *92*, 785–792. <https://doi.org/10.1016/j.solmat.2007.12.003>.
- (59) Du, J.; Xie, N.; Wang, X.; Sun, L.; Zhao, Y.; Wu, F. Optical Limiting Effects of Cyano Substituted Distyrylbenzene Derivatives. *Dye. Pigment.* **2016**, *134*, 368–374. <https://doi.org/10.1016/j.dyepig.2016.07.035>.
- (60) Cumpston, B. H.; Jensen, K. F. Photooxidative Stability of Substituted Poly(Phenylene Vinylene) (PPV) and Poly(Phenylene Acetylene) (PPA). *J. Appl. Polym. Sci.* **1998**, *69*, 2451–2458. [https://doi.org/10.1002/\(sici\)1097-4628\(19980919\)69:12<2451::aid-app16>3.0.co;2-%23](https://doi.org/10.1002/(sici)1097-4628(19980919)69:12<2451::aid-app16>3.0.co;2-%23).
- (61) Santos, F. S. dos; Bertuzzi, D. L.; Pedroso, A. V.; Voinarovicz, M. A.; Klíder, K. C. C. W. do. S.; Péres, L. O.; Garcia, J. R. Evaluation of the Photocurrent Value for Poly(2,5-Dicyano- p -Phenylene-Vinylene)-Co-(p-Phenylene-Vinylene) (DCN-PPV/PPV). *J. Solid State Electrochem.* **2016**, *20*, 2551–2557. <https://doi.org/10.1007/s10008-016-3217-4>.
- (62) Koch, A. T. H.; Harrison, N. T.; Haylett, N.; Daik, R.; Feast, W. J.; Friend, R. H. Enhanced Photostability of Poly(1,3-Phenylene Diphenylvinylene)-Derivatives by Diphenyl-Substitution. *Synth. Met.* **1999**, *100*, 113–122. [https://doi.org/10.1016/S0379-6779\(98\)00166-0](https://doi.org/10.1016/S0379-6779(98)00166-0).
- (63) Li, R.; Mo, Y.; Shi, R.; Li, P.; Li, C.; Wang, Z.; Wang, X.; Li, S. Synthesis and

- Properties of Poly(p-Phenylene Vinylene) Derivatives with Hyperbranched Structure and Containing a Nitro Substituent. *Monatshefte fur Chemie* **2014**, *145*, 85–90. <https://doi.org/10.1007/s00706-013-1051-2>.
- (64) Song, S.; Park, S. H.; Jung, J.; Kim, I.; Lee, K.; Jin, Y.; Suh, H. Increasing of Stability Depended on the Position of Alkoxy Group in PPV. *Synth. Met.* **2011**, *161*, 1186–1193. <https://doi.org/10.1016/j.synthmet.2011.03.032>.
- (65) Rimmelé, M.; Ableidinger, K.; Marsh, A. V.; Cheetham, N. J.; Taublaender, M. J.; Buchner, A.; Prinz, J.; Fröhlich, J.; Unterlass, M. M.; Heeney, M.; Glöcklhofer, F. Thioalkyl- and Sulfone-Substituted Poly(p-Phenylene Vinylene)S. *Polym. Chem.* **2019**, *10*, 738–750. <https://doi.org/10.1039/c8py01717d>.
- (66) Lux, A.; Holmes, A. B.; Cervini, R.; Davies, J. E.; Moratti, S. C.; Grüner, J.; Cacialli, F.; Friend, R. H. New CF₃-Substituted PPV-Type Oligomers and Polymers for Use as Hole Blocking Layers in LEDs. *Synth. Met.* **1997**, *84*, 293–294. [https://doi.org/10.1016/s0379-6779\(97\)80757-6](https://doi.org/10.1016/s0379-6779(97)80757-6).
- (67) Kim, Y.; Swager, T. M. Ultra-Photostable n-Type PPVs. *Chem. Commun.* **2005**, 372–374. <https://doi.org/10.1039/b412948b>.
- (68) Tsuji, H.; Nakamura, E. Carbon-Bridged Oligo(Phenylene Vinylene)s: A de Novo Designed, Flat, Rigid, and Stable π -Conjugated System. *Acc. Chem. Res.* **2019**, *52*, 2939–2949. <https://doi.org/10.1021/acs.accounts.9b00369>.
- (69) Morales-Vidal, M.; Boj, P. G.; Villalvilla, J. M.; Quintana, J. A.; Yan, Q.; Lin, N. T.; Zhu, X.; Ruangsapapichat, N.; Casado, J.; Tsuji, H.; Nakamura, E.; Díaz-García, M. A. Carbon-Bridged Oligo(p-Phenylenevinylene)s for Photostable and Broadly Tunable, Solution-Processable Thin Film Organic Lasers. *Nat. Commun.* **2015**, *6*, 1–8. <https://doi.org/10.1038/ncomms9458>.
- (70) Song, S.; Jin, Y.; Kim, S. H.; Moon, J.; Kim, K.; Kim, J. Y.; Park, S. H.; Lee, K.; Suh, H. Stabilized Polymers with Novel Indenoindene Backbone against Photodegradation for LEDs and Solar Cells. *Macromolecules* **2008**, *41*, 7296–7305. <https://doi.org/10.1021/ma801420e>.
- (71) Wakabayashi, J.; Gon, M.; Tanaka, K.; Chujo, Y. Near-Infrared Absorptive and Emissive Poly(p-Phenylene Vinylene) Derivative Containing Azobenzene-Boron Complexes. *Macromolecules* **2020**, *53*, 4524–4532. <https://doi.org/10.1021/acs.macromol.0c00745>.
- (72) Neugebauer, H.; Brabec, C.; Hummelen, J. C.; Sariciftci, N. S. Stability and

- Photodegradation Mechanisms of Conjugated Polymer/Fullerene Plastic Solar Cells. *Sol. Energy Mater. Sol. Cells* **2000**, *61*, 35–42. [https://doi.org/10.1016/S0927-0248\(99\)00094-X](https://doi.org/10.1016/S0927-0248(99)00094-X).
- (73) Nothaft, M.; Höhla, S.; Jelezko, F.; Pflaum, J.; Wrachtrup, J. The Role of Oxygen-Induced Processes on the Emission Characteristics of Single Molecule Emitters. *Phys. Status Solidi Basic Res.* **2012**, *249*, 661–665. <https://doi.org/10.1002/pssb.201100794>.
- (74) Ozimova, A. E.; Bruevich, V. V.; Dittrich, T.; Paraschuk, D. Y. Enhanced Photostability and Red-NIR Photosensitivity of Conjugated Polymer Charge-Transfer Complexes. *Macromol. Symp.* **2010**, *296*, 138–143. <https://doi.org/10.1002/masy.201051021>.
- (75) Gonçalves, V. C.; Carvalho, A. J.; Balogh, D. T. Polymeric Coatings for Photostability Enhancement of Poly(p-Phenylene Vinylene) Derivative Films. *Polym. Int.* **2010**, *59*, 637–641. <https://doi.org/10.1002/pi.2741>.
- (76) Gonçalves, V. C.; Olivati, C. A.; Carvalho, A. J. F.; Balogh, D. T. Effect of a Polymeric Protective Coating on Optical and Electrical Properties of Poly(p-Phenylene Vinylene) Derivatives. *J. Nanomater.* **2013**, *160464*. <https://doi.org/10.1155/2013/160464>.
- (77) Le Rendu, P.; Nguyen, T. P.; Carrois, L. Cellulose Acetate and PVDC Used as Protective Layers for Organic Diodes. *Synth. Met.* **2003**, *138*, 285–288. [https://doi.org/10.1016/S0379-6779\(02\)01294-8](https://doi.org/10.1016/S0379-6779(02)01294-8).
- (78) Gedelian, C. A.; Ou, Y.; Li, H.; Lu, T. M. Use of Ultra-Thin Aluminum Oxide Layer to Reduce Photoluminescence Decay in Poly(p-Phenylene Vinylene) Films. *Thin Solid Films* **2010**, *518*, 4367–4369. <https://doi.org/10.1016/j.tsf.2010.01.031>.
- (79) Lee, H. C.; Lee, T. W.; Lim, Y. T.; Park, O. O. Improved Environmental Stability in Poly(p-Phenylene Vinylene)/Layered Silicate Nanocomposite. *Appl. Clay Sci.* **2002**, *21*, 287–293. [https://doi.org/10.1016/S0169-1317\(02\)00090-X](https://doi.org/10.1016/S0169-1317(02)00090-X).
- (80) Jing, C.; Chen, L.; Shi, Y.; Jin, X. Synthesis and Characterization of Exfoliated MEH-PPV/Clay Nanocomposites by in Situ Polymerization. *Eur. Polym. J.* **2005**, *41*, 2388–2394. <https://doi.org/10.1016/j.eurpolymj.2005.05.007>.
- (81) Saramas, D.; Martin, D. C.; Magaraphan, R. Optical Films Based on Poly(p-Phenylene Vinylene) (PPV) and Its Nanocomposites. *Rev. Adv. Mater. Sci.* **2003**, *5*,

- 199–204.
- (82) Yang, S. H.; Nguyen, T. P.; Le Rendu, P.; Hsu, C. S. Optical and Electrical Investigations of Poly(p-Phenylene Vinylene)/ Silicon Oxide and Poly(p-Phenylene Vinylene)/Titanium Oxide Nanocomposites. *Thin Solid Films* **2005**, *471*, 230–235. <https://doi.org/10.1016/j.tsf.2004.05.130>.
- (83) Yang, S. H.; Le Rendu, P.; Nguyen, T. P.; Hsu, C. S. Fabrication of MEH-PPV/SiO₂ and MEH-PPV/TiO₂ Nanocomposites with Enhanced Luminescent Stabilities. *Rev. Adv. Mater. Sci.* **2007**, *15*, 144–149.
- (84) Švrček, V.; Fujiwara, H.; Kondo, M. Improved Transport and Photostability of Poly(Methoxy-Ethylexyloxy- Phenylenevinilene) Polymer Thin Films by Boron Doped Freestanding Silicon Nanocrystals. *Appl. Phys. Lett.* **2008**, *92*, 143301. <https://doi.org/10.1063/1.2905269>.
- (85) Zhang, J.; Wang, B. J.; Ju, X.; Liu, T.; Hu, T. D. New Observations on the Optical Properties of PPV/TiO₂ Nanocomposites. *Polymer*. **2001**, *42*, 3697–3702. [https://doi.org/10.1016/S0032-3861\(00\)00703-5](https://doi.org/10.1016/S0032-3861(00)00703-5).
- (86) Vu, T. T. D.; Mighri, F.; Do, T. O.; Aiji, A. Synthesis of Capped TiO₂ Nanocrystals of Controlled Shape and Their Use with MEH-PPV to Develop Nanocomposite Films for Photovoltaic Applications. *J. Nanosci. Nanotechnol.* **2012**, *12*, 2815–2824. <https://doi.org/10.1166/jnn.2012.5792>.
- (87) Yang, B. D.; Yoon, K. H.; Chung, K. W. Effect of TiO₂ and SiO₂ Nanoparticles on the Stability of Poly(p-Phenylene Vinylene) Precursor. *Synth. Met.* **2004**, *143*, 25–29. <https://doi.org/10.1016/j.synthmet.2003.10.006>.
- (88) Van der Zanden, B.; Goossens, A. Oxygen Doping of TiO₂/Poly(Phenylene-Vinylene) Bilayer Solar Cells. *J. Appl. Phys.* **2003**, *94*, 6959–6965. <https://doi.org/10.1063/1.1621054>.
- (89) Nielsen, C. B.; Arnbjerg, J.; Johnsen, M.; Jørgensen, M.; Ogilby, P. R. Molecular Tuning of Phenylene-Vinylene Derivatives for Two-Photon Photosensitized Singlet Oxygen Production. *J. Org. Chem.* **2009**, *74*, 9094–9104. <https://doi.org/10.1021/jo9020216>.
- (90) Poulsen, T. D.; Frederiksen, P. K.; Jørgensen, M.; Mikkelsen, K. V.; Ogilby, P. R. Two-Photon Singlet Oxygen Sensitizers: Quantifying, Modeling, and Optimizing the Two-Photon Absorption Cross Section. *J. Phys. Chem. A* **2001**, *105*, 11488–11495. <https://doi.org/10.1021/jp011974w>.

- (91) Frederiksen, P. K.; Jørgensen, M.; Ogilby, P. R. Two-Photon Photosensitized Production of Singlet Oxygen. *J. Am. Chem. Soc.* **2001**, *123*, 1215–1221. <https://doi.org/10.1021/ja003468a>.
- (92) Frederiksen, P. K.; Mcllroy, S. P.; Nielsen, C. B.; Nikolajsen, L.; Skovsen, E.; Jørgensen, M.; Mikkelsen, K. V.; Ogilby, P. R. Two-Photon Photosensitized Production of Singlet Oxygen in Water. *J. Org. Chem.* **2005**, *127*, 255–269. <https://doi.org/10.1021/jo0482099>.
- (93) Nielsen, C. B.; Johnsen, M.; Arnbjerg, J.; Pittelkow, M.; Mcllroy, S. P.; Ogilby, P. R.; Jørgensen, M. Synthesis and Characterization of Water-Soluble Phenylene-Vinylene-Based Singlet Oxygen Sensitizers for Two-Photon Excitation. *J. Org. Chem.* **2005**, *70* (18), 7065–7079. <https://doi.org/10.1021/jo050507y>.
- (94) Dubinina, G. G.; Price, R. S.; Abboud, K. A.; Wicks, G.; Wnuk, P.; Stepanenko, Y.; Drobizhev, M.; Rebane, A.; Schanze, K. S. Phenylene Vinylene Platinum(II) Acetylides with Prodigious Two-Photon Absorption. *J. Am. Chem. Soc.* **2012**, *134*, 19346–19349. <https://doi.org/10.1021/ja309393c>.
- (95) Dubinina, G. G.; Price, R. S.; Wicks, G.; Wnuk, P.; Stepanenko, Y.; Drobizhev, M.; Rebane, A.; Schanze, K. S. Modified p -Phenylene Vinylene Platinum (II) Acetylides with Enhanced Two-Photon Absorption in Solid Host . *Org. Photonic Mater. Devices XV* **2013**, 8622, 86220I. <https://doi.org/10.1117/12.2004180>.
- (96) Wu, W. High-Performance Conjugated Polymer Photosensitizers. *Chem* **2018**, *4*, 1762–1764. <https://doi.org/10.1016/j.chempr.2018.07.017>.
- (97) Wu, W.; Mao, D.; Xu, S.; Kenry; Hu, F.; Li, X.; Kong, D.; Liu, B. Polymerization-Enhanced Photosensitization. *Chem* **2018**, *4*, 1937–1951. <https://doi.org/10.1016/j.chempr.2018.06.003>.
- (98) Wang, B.; Yuan, H.; Liu, Z.; Nie, C.; Liu, L.; Lv, F.; Wang, Y.; Wang, S. Cationic Oligo(p-Phenylene Vinylene) Materials for Combating Drug Resistance of Cancer Cells by Light Manipulation. *Adv. Mater.* **2014**, *26*, 5986–5990. <https://doi.org/10.1002/adma.201402183>.
- (99) Chen, Y.; Zhou, L.; Wang, J.; Liu, X.; Lu, H.; Liu, L.; Lv, F.; Wang, S. Photoactive Oligo(p-Phenylenevinylene) Functionalized with Phospholipid Units for Control and Visualization of Delivery into Living Cells. *ACS Appl. Mater. Interfaces* **2018**, *10*, 27555–27561. <https://doi.org/10.1021/acsami.8b07847>.

- (100) Liu, Y.; Tian, L.; Li, Y.; Chen, Y.; Chen, Y.; Liu, L.; Wang, S. Photoactive Oligo(p-Phenylene Vinylene) Material for Functional Regulation of Induced Pluripotent Stem Cells. *ACS Appl. Mater. Interfaces* **2020**, *12*, 3438–3444. <https://doi.org/10.1021/acsami.9b19331>.
- (101) Li, S.; Yuan, H.; Chen, H.; Wang, X.; Zhang, P.; Lv, F.; Liu, L.; Wang, S. Cationic Poly(p-Phenylene Vinylene) Materials as a Multifunctional Platform for Light-Enhanced SiRNA Delivery. *Chem. - An Asian J.* **2016**, *11*, 2686–2689. <https://doi.org/10.1002/asia.201600447>.
- (102) Zhu, C.; Yang, Q.; Liu, L.; Lv, F.; Li, S.; Yang, G.; Wang, S. Multifunctional Cationic Poly(p-Phenylene Vinylene) Polyelectrolytes for Selective Recognition, Imaging, and Killing of Bacteria over Mammalian Cells. *Adv. Mater.* **2011**, *23*, 4805–4810. <https://doi.org/10.1002/adma.201102850>.
- (103) Yuan, H.; Chong, H.; Wang, B.; Zhu, C.; Liu, L.; Yang, Q.; Lv, F.; Wang, S. Chemical Molecule-Induced Light-Activated System for Anticancer and Antifungal Activities. *J. Am. Chem. Soc.* **2012**, *134*, 13184–13187. <https://doi.org/10.1021/ja304986t>.
- (104) Guo, J.; Xing, C.; Yuan, H.; Chai, R.; Zhan, Y. Oligo (p-Phenylene Vinylene)/Polyisocyanopeptide Biomimetic Composite Hydrogel-Based Three-Dimensional Cell Culture System for Anticancer and Antibacterial Therapeutics. *ACS Appl. Bio Mater.* **2019**, *2*, 2520–2527. <https://doi.org/10.1021/acsabm.9b00217>.
- (105) Liu, S.; Yuan, H.; Bai, H.; Zhang, P.; Lv, F.; Liu, L.; Dai, Z.; Bao, J.; Wang, S. Electrochemiluminescence for Electric-Driven Antibacterial Therapeutics. *J. Am. Chem. Soc.* **2018**, *140*, 2284–2291. <https://doi.org/10.1021/jacs.7b12140>.
- (106) Jiang, L.; Bai, H.; Liu, L.; Lv, F.; Ren, X.; Wang, S. Luminescent, Oxygen-Supplying, Hemoglobin-Linked Conjugated Polymer Nanoparticles for Photodynamic Therapy. *Angew. Chemie - Int. Ed.* **2019**, *58*, 10660–10665. <https://doi.org/10.1002/anie.201905884>.
- (107) Guiglion, P.; Butchosa, C.; Zwiijnenburg, M. A. Polymer Photocatalysts for Water Splitting: Insights from Computational Modeling. *Macromol. Chem. Phys.* **2016**, *217*, 344–353. <https://doi.org/10.1002/macp.201500432>.
- (108) Mansha, M.; Khan, I.; Ullah, N.; Qurashi, A. Synthesis, Characterization and Visible-Light-Driven Photoelectrochemical Hydrogen Evolution Reaction of Carbazole-Containing Conjugated Polymers. *Int. J. Hydrogen Energy* **2017**, *42*, 10952–10961. <https://doi.org/10.1016/j.ijhydene.2017.02.053>.

- (109) Lanzarini, E.; Antognazza, M. R.; Biso, M.; Ansaldo, A.; Laudato, L.; Bruno, P.; Metrangolo, P.; Resnati, G.; Ricci, D.; Lanzani, G. Polymer-Based Photocatalytic Hydrogen Generation. *J. Phys. Chem. C* **2012**, *116*, 10944–10949. <https://doi.org/10.1021/jp212107f>.
- (110) Bi, S.; Yang, C.; Zhang, W.; Xu, J.; Liu, L.; Wu, D.; Wang, X.; Han, Y.; Liang, Q.; Zhang, F. Two-Dimensional Semiconducting Covalent Organic Frameworks via Condensation at Arylmethyl Carbon Atoms. *Nat. Commun.* **2019**, *10*, 2467. <https://doi.org/10.1038/s41467-019-10504-6>.
- (111) Jin, E.; Lan, Z.; Jiang, Q.; Geng, K.; Li, G.; Wang, X.; Jiang, D. 2D Sp² Carbon-Conjugated Covalent Organic Frameworks for Photocatalytic Hydrogen Production from Water. *Chem* **2019**, *5*, 1632–1647. <https://doi.org/10.1016/j.chempr.2019.04.015>.
- (112) Wang, Z. J.; Li, R.; Landfester, K.; Zhang, K. A. I. Porous Conjugated Polymer via Metal-Free Synthesis for Visible Light-Promoted Oxidative Hydroxylation of Arylboronic Acids. *Polymer* **2017**, *126*, 291–295. <https://doi.org/10.1016/j.polymer.2017.04.052>.
- (113) Oppelt, K. T.; Gasiorowski, J.; Egbe, D. A. M.; Kollender, J. P.; Himmelsbach, M.; Hassel, A. W.; Sariciftci, N. S.; Knör, G. Rhodium-Coordinated Poly(Arylene-Ethynylene)-alt -Poly(Arylene-Vinylene) Copolymer Acting as Photocatalyst for Visible-Light-Powered NAD⁺/NADH Reduction. *J. Am. Chem. Soc.* **2014**, *136*, 12721–12729. <https://doi.org/10.1021/ja506060u>.
- (114) Soo, H. Sen; Agiral, A.; Bachmeier, A.; Frei, H. Visible Light-Induced Hole Injection into Rectifying Molecular Wires Anchored on Co₃O₄ and SiO₂ Nanoparticles. *J. Am. Chem. Soc.* **2012**, *134*, 17104–17116. <https://doi.org/10.1021/ja306162g>.
- (115) Katsoukis, G.; Frei, H. Heterobinuclear Light Absorber Coupled to Molecular Wire for Charge Transport across Ultrathin Silica Membrane for Artificial Photosynthesis. *ACS Appl. Mater. Interfaces* **2018**, *10*, 31422–31432. <https://doi.org/10.1021/acsami.8b11684>.
- (116) Edri, E.; Frei, H. Charge Transport through Organic Molecular Wires Embedded in Ultrathin Insulating Inorganic Layer. *J. Phys. Chem. C* **2015**, *119*, 28326–28334. <https://doi.org/10.1021/acs.jpcc.5b09994>.
- (117) Katsoukis, G.; Jo, W. J.; Frei, H. Structure and Orientation of Molecular Wires

- Embedded in Ultrathin Silica Membrane for Artificial Photosynthesis Elucidated by Polarized FT-IRRAS. *J. Phys. Chem. C* **2019**, *123*, 18905–18913. <https://doi.org/10.1021/acs.jpcc.9b02523>.
- (118) Erdur, S.; Yilmaz, G.; Goen Colak, D.; Cianga, I.; Yagci, Y. Poly(Phenylenevinylene)s as Sensitizers for Visible Light Induced Cationic Polymerization. *Macromolecules* **2014**, *47*, 7296–7302. <https://doi.org/10.1021/ma5019457>.
- (119) Chang, D. W.; Dai, L. Photo-Induced Formation and Self-Assembling of Gold Nanoparticles in Aqueous Solution of Amphiphilic Dendrimers with Oligo(*p*-Phenylene Vinylene) Core Branches and Oligo(Ethylene Oxide) Terminal Chains. *Nanotechnology* **2007**, *18*, 365605. <https://doi.org/10.1088/0957-4484/18/36/365605>.
- (120) Ghosh, S.; Kouamé, N. A.; Ramos, L.; Remita, S.; Dazzi, A.; Deniset-Besseau, A.; Beaunier, P.; Goubard, F.; Aubert, P. H.; Remita, H. Conducting Polymer Nanostructures for Photocatalysis under Visible Light. *Nat. Mater.* **2015**, *14*, 505–511. <https://doi.org/10.1038/nmat4220>.
- (121) Sirimanne, P. M.; Premalal, E. V. A. Optical Properties of Poly-[2-Methoxy-5-(2-Ethyl-Hexyloxy)-Phenylene Vinylene and its Application in Photovoltaic Cells. *Sri Lankan J. Phys.* **2007**, *8*, 29–37. <http://doi.org/10.4038/sljpv.v8i0.211>.
- (122) Spitsina, N.; Romanova, I.; Lobach, A.; Yakuschenko, I.; Kapunov, M.; Tolstov, I.; Triebel, M.; Frankevich, E. Poly(2-Methoxy-5-(2'-Ethyl-Hexyloxy)-1,4-Phenylenevinylene)(MEH-PPV)/Nitrogen Containing Derivatives of Fullerene Composites: Optical Characterization and Application in Flexible Polymer Solar Cells. *J. Low Temp. Phys.* **2006**, *142*, 201–206. <https://doi.org/10.1007/s10909-006-9010-5>.
- (123) Lei, T.; Dou, J.-H.; Cao, X.-Y.; Wang, J.-Y.; Pei, J. Electron-Deficient Poly(*p*-Phenylene Vinylene) Provides Electron Mobility over $1 \text{ Cm}^2 \text{ V}^{-1} \text{ s}^{-1}$ under Ambient Conditions. *J. Am. Chem. Soc.* **2013**, *135*, 12168–12171. <https://doi.org/10.1021/ja403624a>.
- (124) Lee, H.; Vak, D.; Baeg, K.-J.; Nah, Y.-C.; Kim, D.-Y.; Noh, Y.-Y. Synthesis of Poly(*p*-Phenylene-Vinylene) Derivatives Containing an Oxadiazole Pendant Group and Their Applications to Organic Electronic Devices. *J. Nanosci. Nanotechnol.* **2013**, *13*, 3321–3330. <https://doi.org/10.1166/jnn.2013.7291>.

- (125) Yong, W.-W.; Lu, H.; Li, H.; Wang, S.; Zhang, M.-T. Photocatalytic Hydrogen Production with Conjugated Polymers as Photosensitizers. *ACS Appl. Mater. Interfaces* **2018**, *10*, 10828–10834. <https://doi.org/10.1021/acsami.7b18917>.
- (126) Thomas, S. W.; Joly, G. D.; Swager, T. M. Chemical Sensors Based on Amplifying Fluorescent Conjugated Polymers. *Chem. Rev.* **2007**, *107*, 1339–1386. <https://doi.org/10.1021/cr0501339>.
- (127) Noguchi, T.; Roy, B.; Yoshihara, D.; Sakamoto, J.; Yamamoto, T.; Shinkai, S. A Chiral Recognition System Orchestrated by Self-Assembly: Molecular Chirality, Self-Assembly Morphology, and Fluorescence Response. *Angew. Chemie - Int. Ed.* **2017**, *56*, 12518–12522. <https://doi.org/10.1002/anie.201706142>.
- (128) McGehee, M. D.; Heeger, A. J. Semiconducting (Conjugated) Polymers as Materials for Solid-State Lasers. *Adv. Mater.* **2000**, *12*, 1655–1668. [https://doi.org/10.1002/1521-4095\(200011\)12:22<1655::AID-ADMA1655>3.0.CO;2-2](https://doi.org/10.1002/1521-4095(200011)12:22<1655::AID-ADMA1655>3.0.CO;2-2).
- (129) Laughlin, B. J.; Smith, R. C. Gilch and Horner-Wittig Routes to Poly(p-Phenylenevinylene) Derivatives Incorporating Monoalkyl Defect-Free 9,9-Dialkyl-1,4-Fluorenylene Units. *Macromolecules* **2010**, *43*, 3744–3749. <https://doi.org/10.1021/ma902346w>.
- (130) Sato, S.; Tajima, K.; Hashimoto, K. Synthesis and Characterization of Regioregular Cyano-Substituted Poly(p-Phenylenevinylene). *Macromolecules* **2009**, *42*, 1785–1788. [https://doi.org/10.1016/0022-3999\(83\)90056-9](https://doi.org/10.1016/0022-3999(83)90056-9).
- (131) Campbell, T. W.; McDonald, R. N. Synthesis of Hydrocarbon Derivatives by the Wittig Synthesis .1. Distyrylbenzenes. *J. Org. Chem.* **1959**, *24*, 1246–1251. <https://doi.org/10.1021/jo01091a022>.
- (132) Cárdenas, J. C.; Ochoa-Puentes, C.; Gutiérrez-Puebla, E.; Sierra, C. A. Synthesis, Crystal Structure Determination and Photoluminescence Properties of a Pure Anti *trans-trans* Phenylenevinylene Derivative. *Synth. Met.* **2016**, *215*, 194–199. <https://doi.org/10.1016/j.synthmet.2016.02.021>.
- (133) Díaz, C.; Alzate, D.; Rodríguez, R.; Ochoa, C.; Sierra, C. A. High Yield and Stereospecific Synthesis of Segmented Poly (p-Phenylene Vinylene) by the Heck Reaction. *Synth. Met.* **2013**, *172*, 32–36. <https://doi.org/10.1016/j.synthmet.2013.03.023>.

- (134) Estrada-Flórez, S. E.; Moncada, F. S.; Lanterna, A. E.; Sierra, C. A.; Scaiano, J. C. Spectroscopic and Time-Dependent DFT Study of the Photophysical Properties of Substituted 1,4-Distyrylbenzenes. *J. Phys. Chem. A* **2019**, *123*, 6496–6505. <https://doi.org/10.1021/acs.jpca.9b04492>.
- (135) Du, Z. T.; Liu, R.; Wang, J. R.; Li, A. P. Synthesis of a Diamino Substituted Terphenyldivinyl Chromophore. *Molecules* **2009**, *14*, 2111–2117. <https://doi.org/10.3390/molecules14062111>.
- (136) Denny, W. A.; Atwell, G. J.; Baguley, B. C.; Cain, B. F. Potential Antitumor Agents. 29. Quantitative Structure-Activity Relationships for the Antileukemic Bisquaternary Ammonium Heterocycles. *J. Med. Chem.* **1979**, *22*, 134–150. <https://doi.org/10.1021/jm00188a005>.
- (137) Caruso, U.; Casalboni, M.; Fort, A.; Fusco, M.; Panunzi, B.; Quatela, A.; Roviello, A.; Sarcinelli, F. New Side-Chain Polyurethanes with Highly Conjugated Push-Pull Chromophores for Second Order NLO Applications. *Opt. Mater.* **2005**, *27*, 1800–1810. <https://doi.org/10.1016/j.optmat.2004.11.009>.
- (138) Roviello, A.; Borbone, F.; Carella, A.; Diana, R.; Roviello, G.; Panunzi, B.; Ambrosio, A.; Maddalena, P. High Quantum Yield Photoluminescence of New Polyamides Containing Oligo-PPV Amino Derivatives and Related Oligomers. *J. Polym. Sci. Part A Polym. Chem.* **2009**, *47*, 2677–2689. <https://doi.org/10.1002/pola.23353>.
- (139) Zhou, B. Y.; He, Q.; Yang, Y.; Zhong, H.; He, C.; Sang, G.; Liu, W.; Yang, C. Binaphthyl-Containing Green- and Red-Emitting Molecules for Solution-Processable Organic Light-Emitting Diodes. *Adv. Funct. Mater.* **2008**, *18*, 3299–3306. <https://doi.org/10.1002/adfm.200800375>.
- (140) Brouwer, A. M. Standards for Photoluminescence Quantum Yield Measurements in Solution (IUPAC Technical Report). *Pure Appl. Chem* **2011**, *83*, 2213–2228. <https://doi.org/10.1351/PAC-REP-10-09-31>.
- (141) Denmark, S. E.; Butler, C. R. Vinylation of Aryl Bromides Using an Inexpensive Vinylpolysiloxane. *Org. Lett.* **2006**, *8*, 63–66. <https://doi.org/10.1021/ol052517r>
- (142) Zheng, G. C.; Cai, Z. Bin; Pan, Y. L.; Bai, L.; Zhou, Y. T.; Li, S. L.; Tian, Y. P. Synthesis and Two-Photon Absorption Properties of Novel 2-Substituted-4,5-Diphenyl-1H-Imidazoles. *Tetrahedron* **2016**, *72*, 2988–2996. <https://doi.org/10.1016/j.tet.2016.04.015>.
- (143) Gabr, Y. Studies on the Copolymerization of 4-Aminostyrene with 4-Nitro- and 2,4-

- Dinitrostyrene. *Acta Chim. Slov.* **2007**, *54*, 818–824.
- (144) Channe Gowda, D.; Mahesh, B.; Gowda, S. Zinc-Catalyzed Ammonium Formate Reductions: Rapid and Selective Reduction of Aliphatic and Aromatic Nitro Compounds. *Indian J. Chem. - Sect. B Org. Med. Chem.* **2001**, *40*, 75–77. <https://doi.org/10.1002/chin.200123046>.
- (145) Howard, J. L.; Cao, Q.; Browne, D. L. Mechanochemistry as an Emerging Tool for Molecular Synthesis: What Can It Offer? *Chem. Sci.* **2018**, *9*, 3080–3094. <https://doi.org/10.1039/c7sc05371a>.
- (146) Shahabi, D.; Tavakol, H. One-Pot Synthesis of Quinoline Derivatives Using Choline Chloride / Tin (II) Chloride Deep Eutectic Solvent as a Green Catalyst. *J. Mol. Liq.* **2016**, *220*, 324–328. <https://doi.org/10.1016/j.molliq.2016.04.094>.
- (147) Saikachi, H.; Muto, H. Reaction of Aromatic p-Substituted Biphosphanes with Bisaldehydes. *Chem. Pharm. Bull.* **1971**, *19*, 959–969. <https://doi.org/10.1248/cpb.19.959>.
- (148) Murata, T.; Gondo, Y.; Itabashi, K. The Reduction of Aromatic Nitro Compounds with Hydrogen Sulfide. *J. Syn. Org. Chem. JPN* **1977**, *35*, 61–63. <https://doi.org/10.5059/yukigoseikyokaishi.35.61>
- (149) Cope, O. J.; Brown, R. K. The Reduction of Nitrobenzene by Sodium Sulphide in Aqueous Ethanol. *Can. J. Chem.* **1961**, *39*, 1695–1710. <https://doi.org/10.1139/v61-217>.
- (150) Boys, M. L.; Downs, V. L. Preparation of Primary Thioamides from Nitriles Using Sodium Hydrogen Sulfide and Diethylamine Hydrochloride. *Synth. Commun.* **2006**, *36*, 295–298. <https://doi.org/10.1080/00397910500377099>.
- (151) Shiraishi, Y.; Takeshita, S.; Isobe, T. Two Photoenergy Conversion Modes of YVO₄:Eu³⁺ Nanoparticles: Photoluminescence and Photocatalytic Activity. *J. Phys. Chem. C* **2015**, *119*, 13502–13508. <https://doi.org/10.1021/acs.jpcc.5b03425>.
- (152) Cao, X.; Meng, L.; Li, Z.; Mao, Y.; Lan, H.; Chen, L.; Fan, Y.; Yi, T. Large Red-Shifted Fluorescent Emission via Intermolecular π - π Stacking in 4-Ethynyl-1,8-Naphthalimide-Based Supramolecular Assemblies. *Langmuir* **2014**, *30*, 11753–11760. <https://doi.org/10.1021/la503299j>.
- (153) Zhao, J.; Sun, L.; Canepa, S.; Sun, H.; Yesibolati, M. N.; Sherburne, M.; Xu, R.; Sritharan, T.; Loo, J. S. C. C.; Ager, J. W.; Barber, J.; Mølhave, K.; Xu, Z. J.

- Phosphate Tuned Copper Electrodeposition and Promoted Formic Acid Selectivity for Carbon Dioxide Reduction. *J. Mater. Chem. A* **2017**, *5*, 11905–11916. <https://doi.org/10.1039/c7ta01871a>.
- (154) Othman, I.; Mohamed, R. M.; Ibrahim, F. M. Study of Photocatalytic Oxidation of Indigo Carmine Dye on Mn-Supported TiO₂. *J. Photochem. Photobiol. A Chem.* **2007**, *189*, 80–85. <https://doi.org/10.1016/j.jphotochem.2007.01.010>.
- (155) Li, H. X.; Xu, B.; Tang, L.; Zhang, J. H.; Mao, Z. G. Reductive Decolorization of Indigo Carmine Dye with *Bacillus* Sp. MZS10. *Int. Biodeterior. Biodegrad.* **2015**, *103*, 30–37. <https://doi.org/10.1016/j.ibiod.2015.04.007>.
- (156) Vautier, M.; Guillard, C.; Herrmann, J. M. Photocatalytic Degradation of Dyes in Water: Case Study of Indigo and of Indigo Carmine. *J. Catal.* **2001**, *201*, 46–59. <https://doi.org/10.1006/jcat.2001.3232>.
- (157) Barka, N.; Assabbane, A.; Nounah, A.; Ichou, Y. A. Photocatalytic Degradation of Indigo Carmine in Aqueous Solution by TiO₂-Coated Non-Woven Fibres. *J. Hazard. Mater.* **2008**, *152*, 1054–1059. <https://doi.org/10.1016/j.jhazmat.2007.07.080>.
- (158) Mittal, A.; Mittal, J.; Kurup, L. Batch and Bulk Removal of Hazardous Dye, Indigo Carmine from Wastewater through Adsorption. *J. Hazard. Mater.* **2006**, *137*, 591–602. <https://doi.org/10.1016/j.jhazmat.2006.02.047>.
- (159) Mittal, A.; Mittal, J.; Kurup, L. Utilization of Hen Feathers for the Adsorption of Indigo Carmine from Simulated Effluents. *J. Environ. Prot. Sci* **2007**, *1*, 92–100.
- (160) Prado, A. G. S.; Torres, J. D.; Faria, E. A.; Dias, S. C. L. Comparative Adsorption Studies of Indigo Carmine Dye on Chitin and Chitosan. *J. Colloid Interface Sci.* **2004**, *277*, 43–47. <https://doi.org/10.1016/j.jcis.2004.04.056>.
- (161) Wang, J.; Lu, L.; Feng, F. Improving the Indigo Carmine Decolorization Ability of a *Bacillus Amyloliquefaciens* Laccase by Site-Directed Mutagenesis. *Catalysts* **2017**, *7*, 275. <https://doi.org/10.3390/catal7090275>.
- (162) Palma-Goyes, R. E.; Silva-Agrede, J.; González, I.; Torres-Palma, R. A. Comparative Degradation of Indigo Carmine by Electrochemical Oxidation and Advanced Oxidation Processes. *Electrochim. Acta* **2014**, *140*, 427–433. <https://doi.org/10.1016/j.electacta.2014.06.096>.
- (163) Flox, C.; Ammar, S.; Arias, C.; Brillas, E.; Vargas-Zavala, A. V.; Abdelhedi, R. Electro-Fenton and Photoelectro-Fenton Degradation of Indigo Carmine in Acidic Aqueous Medium. *Appl. Catal. B Environ.* **2006**, *67*, 93–104.

- <https://doi.org/10.1016/j.apcatb.2006.04.020>.
- (164) Hammami, S.; Oturana, M. A.; Oturana, N.; Bellakhal, N.; Dachraoui, M. Comparative Mineralization of Textile Dye Indigo by Photo-Fenton Process and Anodic Oxidation Using Boron-Doped Diamond Anode. *Desalin. Water Treat.* **2012**, *45*, 297–304. <https://doi.org/10.1080/19443994.2012.692059>.
- (165) Subramani, A. K.; Byrappa, K.; Ananda, S.; Lokanatha Rai, K. M.; Ranganathaiah, C.; Yoshimura, M. Photocatalytic Degradation of Indigo Carmine Dye Using TiO₂ Impregnated Activated Carbon. *Bull. Mater. Sci.* **2007**, *30*, 37–41. <https://doi.org/10.1007/s12034-007-0007-8>.
- (166) Sood, S.; Kumar, S.; Umar, A.; Kaur, A.; Mehta, S. K.; Kansal, S. K. TiO₂ Quantum Dots for the Photocatalytic Degradation of Indigo Carmine Dye. *J. Alloys Compd.* **2015**, *650*, 193–198. <https://doi.org/10.1016/j.jallcom.2015.07.164>.
- (167) Huo, P.; Kumar, P.; Liu, B. The Mechanism of Adsorption, Diffusion, and Photocatalytic Reaction of Organic Molecules on TiO₂ Revealed by Means of On-Site Scanning Tunneling Microscopy Observations. *Catalysts* **2018**, *8*, 616. <https://doi.org/10.3390/catal8120616>.
- (168) Bora, L. V.; Mewada, R. K. Visible/Solar Light Active Photocatalysts for Organic Effluent Treatment: Fundamentals, Mechanisms and Parametric Review. *Renew. Sustain. Energy Rev.* **2017**, *76*, 1393–1421. <https://doi.org/10.1016/j.rser.2017.01.130>.
- (169) Lima, C. S.; Batista, K. A.; García Rodríguez, A.; Souza, J. R.; Fernandes, K. F. Photodecomposition and Color Removal of a Real Sample of Textile Wastewater Using Heterogeneous Photocatalysis with Polypyrrole. *Sol. Energy* **2015**, *114*, 105–113. <https://doi.org/10.1016/j.solener.2015.01.038>.
- (170) Nowakowska, M.; Szczubiałka, K. Photoactive Polymeric and Hybrid Systems for Photocatalytic Degradation of Water Pollutants. *Polym. Degrad. Stab.* **2017**, *145*, 120–141. <https://doi.org/10.1016/j.polymdegradstab.2017.05.021>.
- (171) Wang, Z. J.; Li, R.; Landfester, K.; Zhang, K. A. I. Porous Conjugated Polymer via Metal-Free Synthesis for Visible Light-Promoted Oxidative Hydroxylation of Arylboronic Acids. *Polymer*. **2017**, *126*, 291–295. <https://doi.org/10.1016/j.polymer.2017.04.052>.
- (172) Cárdenas, J. C.; Ochoa-Puentes, C.; Sierra, C. A. Phenylenevinylene Systems: The

- Oligomer Approach. In *Conducting Polymers*; 2016; p Ch. 10. <https://doi.org/10.5772/63394>
- (173) Nath, K.; Chandra, M.; Pradhan, D.; Biradha, K. Supramolecular Organic Photocatalyst Containing a Cubanelike Water Cluster and Donor – Acceptor Stacks: Hydrogen Evolution and Dye Degradation under Visible Light. *ACS Appl. Mater. Interfaces* **2018**, *10*, 29417–29424. <https://doi.org/10.1021/acsami.8b07437>.
- (174) Takeda, N.; Torimoto, T.; Sampath, S.; Kuwabata, S.; Yoneyama, H. Effect of Inert Supports for Titanium Dioxide Loading on Enhancement of Photodecomposition Rate of Gaseous Propionaldehyde. *J. Phys. Chem.* **1995**, *99*, 9986–9991. <https://doi.org/10.1021/j100024a047>.
- (175) Bresolí-Obach, R.; Torra, J.; Zanocco, R. P.; Zanocco, A. L.; Nonell, S. Singlet Oxygen Quantum Yield Determination Using Chemical Acceptors. In *Reactive Oxygen Species Methods and Protocols*; Espada, J., Ed.; Humana: New York, 2020; Vol. 2202, pp 165–188. <https://doi.org/10.1007/978-1-0716-0896-8>.
- (176) Beghetto, C.; Renken, C.; Eriksson, O.; Jori, G.; Bernardi, P.; Ricchelli, F. Implications of the Generation of Reactive Oxygen Species by Photoactivated Calcein for Mitochondrial Studies. *Eur. J. Biochem.* **2000**, *267*, 5585–5592. <https://doi.org/10.1046/j.1432-1327.2000.01625.x>.
- (177) Young, R. H.; Martin, R. L.; Chinh, N.; Mallon, C.; Kayser, R. H. Substituent Effects in Dye-Sensitized Photooxidation Reactions of Furans. *Can. J. Chem.* **1972**, *50*, 932–938. <https://doi.org/10.1139/v72-144>.
- (178) Xu, H.; Cooper, W. J.; Jung, J.; Song, W. Photosensitized Degradation of Amoxicillin in Natural Organic Matter Isolate Solutions. *Water Res.* **2011**, *45*, 632–638. <https://doi.org/10.1016/j.watres.2010.08.024>.
- (179) Batista, A. P. S.; Teixeira, A. C. S. C.; Cooper, W. J.; Cottrell, B. A. Correlating the Chemical and Spectroscopic Characteristics of Natural Organic Matter with the Photodegradation of Sulfamerazine. *Water Res.* **2016**, *93*, 20–29. <https://doi.org/10.1016/j.watres.2015.11.036>.
- (180) Prieto-Montero, R.; Sola-Llano, R.; Montero, R.; Longarte, A.; Arbeloa, T.; López-Arbeloa, I.; Martínez-Martínez, V.; Lacombe, S. Methylthio BODIPY as a Standard Triplet Photosensitizer for Singlet Oxygen Production: A Photophysical Study. *Phys. Chem. Chem. Phys.* **2019**, *21*, 20403–20414. <https://doi.org/10.1039/c9cp03454d>.
- (181) Adarsh, N.; Avirah, R. R.; Ramaiah, D. Tuning Photosensitized Singlet Oxygen

- Generation Efficiency of Novel Aza-BODIPY Dyes. *Org. Lett.* **2011**, *12*, 5720–5723. <https://doi.org/10.1021/ol200572p>.
- (182) Ormond, A. B.; Freeman, H. S. Effects of Substituents on the Photophysical Properties of Symmetrical Porphyrins. *Dye. Pigm.* **2013**, *96*, 440–448. <https://doi.org/10.1016/j.dyepig.2012.09.011>.
- (183) Delanaye, L.; Bahri, M. A.; Tfibel, F.; Fontaine-Aupart, M. P.; Mouithys-Mickalad, A.; Heine, B.; Piette, J.; Hoebeke, M. Physical and Chemical Properties of Pyropheophorbide-a Methyl Ester in Ethanol, Phosphate Buffer and Aqueous Dispersion of Small Unilamellar Dimyristoyl-L- α -Phosphatidylcholine Vesicles. *Photochem. Photobiol. Sci.* **2006**, *5*, 317–325. <https://doi.org/10.1039/b513219c>.
- (184) Innocenzi, P.; Kozuka, H.; Yoko, T. Fluorescence Properties of the Ru(Bpy)₃²⁺ Complex Incorporated in Sol-Gel-Derived Silica Coating Films. *J. Phys. Chem. B* **1997**, *101*, 2285–2291. <https://doi.org/10.1021/jp970004z>.
- (185) Urgoitia, G.; Sanmartin, R.; Herrero, M. T.; Domínguez, E. Aerobic Cleavage of Alkenes and Alkynes into Carbonyl and Carboxyl Compounds. *ACS Catal.* **2017**, *7*, 3050–3060. <https://doi.org/10.1021/acscatal.6b03654>.
- (186) Kuang, L.; Zhao, Y.; Zhang, W.; Ge, S. Roles of Reactive Oxygen Species and Holes in the Photodegradation of Cationic and Anionic Dyes by TiO₂ under UV Irradiation. *J. Environ. Eng.* **2015**, *142*, 04015065. [https://doi.org/10.1061/\(asce\)ee.1943-7870.0001032](https://doi.org/10.1061/(asce)ee.1943-7870.0001032).
- (187) Dong, G.; Yang, L.; Wang, F.; Zang, L.; Wang, C. Removal of Nitric Oxide through Visible Light Photocatalysis by G-C₃N₄ Modified with Perylene Imides. *ACS Catal.* **2016**, *6*, 6511–6519. <https://doi.org/10.1021/acscatal.6b01657>.
- (188) Schneider, J.; Bahnemann, D. W. Undesired Role of Sacrificial Reagents in Photocatalysis. *J. Phys. Chem. Lett.* **2013**, *4*, 3479–3483. <https://doi.org/10.1021/jz4018199>.
- (189) Seraghni, N.; Ghoul, I.; Lemmize, I.; Reguig, A.; Debbache, N.; Sehili, T. Use of Oxalic Acid as Inducer in Photocatalytic Oxidation of Cresol Red in Aqueous Solution under Natural and Artificial Light. *Environ. Technol.* **2018**, *39*, 2908–2915. <https://doi.org/10.1080/09593330.2017.1369580>.
- (190) Ollis, D. F. Kinetics of Photocatalyzed Reactions: Five Lessons Learned. *Front. Chem.* **2018**, *6*, 378. <https://doi.org/10.3389/fchem.2018.00378>.

- (191) Ma, L.; Wang, X.; Wang, B.; Chen, J.; Wang, J.; Huang, K.; Zhang, B.; Cao, Y.; Han, Z.; Qian, S.; Yao, S. Photooxidative Degradation Mechanism of Model Compounds of Poly(p-Phenylenevinylenes) [PPVs]. *Chem. Phys.* **2002**, *285*, 85–94. [https://doi.org/10.1016/S0301-0104\(02\)00691-2](https://doi.org/10.1016/S0301-0104(02)00691-2).
- (192) Niu, J.; Dai, Y.; Yin, L.; Shang, J.; Crittenden, J. C. Photocatalytic Reduction of Triclosan on Au-Cu₂O Nanowire Arrays as Plasmonic Photocatalysts under Visible Light Irradiation. *Phys. Chem. Chem. Phys.* **2015**, *17*, 17421–17428. <https://doi.org/10.1039/c5cp02244d>.
- (193) Navio, J. A.; Fuentes Mota, J.; Pradera Adrian, M. A.; García Gómez, M. Oxidation of 2-Furoic Acid via Singlet Oxygen Generated Photochemically. *J. Photochem. Photobiol. A Chem.* **1990**, *52*, 91–95. [https://doi.org/10.1016/1010-6030\(90\)87094-R](https://doi.org/10.1016/1010-6030(90)87094-R).
- (194) Fabregat, V.; Burguete, M. I.; Galindo, F.; Luis, S. V. Singlet Oxygen Generation by Photoactive Polymeric Microparticles with Enhanced Aqueous Compatibility. *Environ. Sci. Pollut. Res.* **2014**, *21*, 11884–11892. <https://doi.org/10.1007/s11356-013-2311-8>.
- (195) Gollnick, K.; Miinchen, D.-; Germany, W. Singlet oxygen photooxygenation of furans: Isolation and reactions of (4+2)-cycloaddition products (unsaturated sec.-ozonides). *Tetrahedron* **1985**, *41*, 2057–2068. [https://doi.org/10.1016/S0040-4020\(01\)96576-7](https://doi.org/10.1016/S0040-4020(01)96576-7).
- (196) Lower, S. K.; El-Sayed, M. A. The Triplet State and Molecular Electronic Processes in Organic Molecules. *Chem. Rev.* **1966**, *66*, 199–241. <https://doi.org/10.1021/cr60240a004>.
- (197) Witkoš, K.; Lech, K.; Jarosz, M. Identification of Degradation Products of Indigoids by Tandem Mass Spectrometry. *J. Mass Spectrom.* **2015**, *50*, 1245–1251. <https://doi.org/10.1002/jms.3641>.
- (198) Chacón-Patiño, M. L.; Blanco-Tirado, C.; Hinestroza, J. P.; Combariza, M. Y. Biocomposite of Nanostructured MnO₂ and Figue Fibers for Efficient Dye Degradation. *Green Chem.* **2013**, *15*, 2920–2928. <https://doi.org/10.1039/b000000x>.
- (199) Koppenol, W. H.; Stanbury, D. M.; Bounds, P. L. Electrode Potentials of Partially Reduced Oxygen Species, from Dioxygen to Water. *Free Radic. Biol. Med.* **2010**, *49*, 317–322. <https://doi.org/10.1016/j.freeradbiomed.2010.04.011>.
- (200) Mukthar Ali, M.; Arya Nair, J. S.; Sandhya, K. Y. Role of Reactive Oxygen Species in the Visible Light Photocatalytic Mineralization of Rhodamine B Dye by P25–

- Carbon Dot Photocatalyst. *Dye. Pigment.* **2019**, *163*, 274–284. <https://doi.org/10.1016/j.dyepig.2018.11.057>.
- (201) El-Mansy, M. A. M. Quantum Chemical Studies on Structural, Vibrational, Nonlinear Optical Properties and Chemical Reactivity of Indigo Carmine Dye. *Spectrochim. Acta - Part A Mol. Biomol. Spectrosc.* **2017**, *183*, 284–290. <https://doi.org/10.1016/j.saa.2017.04.047>.
- (202) Lacombe, S.; Pigot, T. Materials for Selective Photo-Oxygenation vs. Photocatalysis: Preparation, Properties and Applications in Environmental and Health Fields. *Catal. Sci. Technol.* **2016**, *6*, 1571–1592. <https://doi.org/10.1039/c5cy01929j>.
- (203) Li, W.; Zhang, W.; Dong, X.; Yan, L.; Qi, R.; Wang, W.; Xie, Z.; Jing, X. Porous Heterogeneous Organic Photocatalyst Prepared by HIPE Polymerization for Oxidation of Sulfides under Visible Light. *J. Mater. Chem.* **2012**, *22*, 17445–17448. <https://doi.org/10.1039/c2jm32778c>.
- (204) Dervaux, J.; Cormier, P. A.; Struzzi, C.; Scardamaglia, M.; Bittencourt, C.; Petaccia, L.; Cornil, D.; Lasser, L.; Cornil, J.; Lazzaroni, R.; Snyders, R. Probing the Interaction between 2,2'-Bithiophene-5-Carboxylic Acid and TiO₂ by Photoelectron Spectroscopy: A Joint Experimental and Theoretical Study. *J. Chem. Phys.* **2017**, *147*, 244704. <https://doi.org/10.1063/1.5008800>.
- (205) Liu, B.; Terano, M. Investigation of the Physico-Chemical State and Aggregation Mechanism of Surface Cr Species on a Phillips CrOx/SiO₂ Catalyst by XPS and EPMA. *J. Mol. Catal. A Chem.* **2001**, *172*, 227–240. [https://doi.org/10.1016/S1381-1169\(01\)00121-2](https://doi.org/10.1016/S1381-1169(01)00121-2).
- (206) Hu, F.; Lei, X. Synthesis of Diaryl Sulfones at Room Temperature: Cu-Catalyzed Cross-Coupling of Arylsulfonyl Chlorides with Arylboronic Acids. *ChemCatChem* **2015**, *7*, 1539–1542. <https://doi.org/10.1002/cctc.201500174>.
- (207) Castellanos, N. J.; Martínez, F.; Lynen, F.; Biswas, S.; Van Der Voort, P.; Arzoumanian, H. Dioxygen Activation in Photooxidation of Diphenylmethane by a Dioxomolybdenum(VI) Complex Anchored Covalently onto Mesoporous Titania. *Transit. Met. Chem.* **2013**, *38*, 119–127. <https://doi.org/10.1007/s11243-012-9668-2>.
- (208) Jia, X.; Ma, J.; Xia, F.; Xu, Y.; Gao, J.; Xu, J. Carboxylic Acid-Modified Metal Oxide Catalyst for Selectivity-Tunable Aerobic Ammoxidation. *Nat. Commun.* **2018**, *9*, 933.

- <https://doi.org/10.1038/s41467-018-03358-x>.
- (209) Frank, O.; Zikalova, M.; Laskova, B.; Kürti, J.; Koltai, J.; Kavan, L. Raman Spectra of Titanium Dioxide (Anatase, Rutile) with Identified Oxygen Isotopes (16, 17, 18). *Phys. Chem. Chem. Phys.* **2012**, *14*, 14567–14572. <https://doi.org/10.1039/c2cp42763j>.
- (210) Belekbir, S.; El Azzouzi, M.; El Hamidi, A.; Rodríguez-Lorenzo, L.; Santaballa, J. A.; Canle, M. Improved Photocatalyzed Degradation of Phenol, as a Model Pollutant, over Metal-Impregnated Nanosized TiO₂. *Nanomaterials* **2020**, *10*, 996. <https://doi.org/10.3390/nano10050996>.
- (211) Pighini, C.; Aymes, D.; Millot, N.; Saviot, L. Low-Frequency Raman Characterization of Size-Controlled Anatase TiO₂ Nanopowders Prepared by Continuous Hydrothermal Syntheses. *J. Nanoparticle Res.* **2007**, *9*, 309–315. <https://doi.org/10.1007/s11051-005-9061-6>.
- (212) Abdulrazzak, F. H.; Hussein, F. H. Effects of Nanoparticle Size on Catalytic and Photocatalytic Activity of Carbon Nanotubes-Titanium Dioxide Composites. *J. Environ. Anal. Chem.* **2015**, *02*, 1000e110. <https://doi.org/10.4172/2380-2391.1000e110>.
- (213) Ho, W. K. H.; Bao, Z. Y.; Gan, X.; Wong, K. Y.; Dai, J.; Lei, D. Probing Conformation Change and Binding Mode of Metal Ion-Carboxyl Coordination Complex through Resonant Surface-Enhanced Raman Spectroscopy and Density Functional Theory. *J. Phys. Chem. Lett.* **2019**, *10*, 4692–4698. <https://doi.org/10.1021/acs.jpcllett.9b01435>.
- (214) Geisler, T.; Dohmen, L.; Lenting, C.; Fritzsche, M. B. K. Real-Time in Situ Observations of Reaction and Transport Phenomena during Silicate Glass Corrosion by Fluid-Cell Raman Spectroscopy. *Nat. Mater.* **2019**, *18*, 342–348. <https://doi.org/10.1038/s41563-019-0293-8>.
- (215) Nawaz, R.; Kait, C. F.; Chia, H. Y.; Isa, M. H.; Huei, L. W. Glycerol-Mediated Facile Synthesis of Colored Titania Nanoparticles for Visible Light Photodegradation of Phenolic Compounds. *Nanomaterials* **2019**, *9*, 1586. <https://doi.org/10.3390/nano9111586>.
- (216) Luo, Y. B.; Wang, X. L.; Xu, D. Y.; Wang, Y. Z. Preparation and Characterization of Poly(Lactic Acid)-Grafted TiO₂ Nanoparticles with Improved Dispersions. *Appl. Surf. Sci.* **2009**, *255*, 6795–6801. <https://doi.org/10.1016/j.apsusc.2009.02.074>.

- (217) Smith, M.; Scudiero, L.; Espinal, J.; McEwen, J. S.; Garcia-Perez, M. Improving the Deconvolution and Interpretation of XPS Spectra from Chars by Ab Initio Calculations. *Carbon N. Y.* **2016**, *110*, 155–171. <https://doi.org/10.1016/j.carbon.2016.09.012>.
- (218) Ruiz-Cañas, M. C.; Quintero, H. I.; Corredor, L. M.; Manrique, E.; Romero Bohórquez, A. R. New Nanohybrid Based on Hydrolyzed Polyacrylamide and Silica Nanoparticles: Morphological, Structural and Thermal Properties. *Polymers (Basel)*. **2020**, *12*, 1152. <https://doi.org/10.3390/POLYM12051152>.
- (219) Kaur, A.; Chahal, P.; Hogan, T. Selective Fabrication of SiC/Si Diodes by Excimer Laser under Ambient Conditions. *IEEE Electron Device Lett.* **2016**, *37*, 142–145. <https://doi.org/10.1109/LED.2015.2508479>.
- (220) Vashisth, A.; Khatri, S.; Hahn, S. H.; Zhang, W.; Van Duin, A. C. T.; Naraghi, M. Mechanical Size Effects of Amorphous Polymer-Derived Ceramics at the Nanoscale: Experiments and ReaxFF Simulations. *Nanoscale* **2019**, *11*, 7447–7456. <https://doi.org/10.1039/c9nr00958b>.
- (221) Sosa, N.; Chanlek, N.; Wittayakun, J. Facile Ultrasound-Assisted Grafting of Silica Gel by Aminopropyltriethoxysilane for Aldol Condensation of Furfural and Acetone. *Ultrason. Sonochem.* **2020**, *62*, 104857. <https://doi.org/10.1016/j.ultsonch.2019.104857>.
- (222) Wei, Y.; Rakhatkyzy, M.; Salih, K. A. M.; Wang, K.; Hamza, M. F.; Guibal, E. Controlled Bi-Functionalization of Silica Microbeads through Grafting of Amidoxime/Methacrylic Acid for Sr(II) Enhanced Sorption. *Chem. Eng. J.* **2020**, *402*, 125220. <https://doi.org/10.1016/j.cej.2020.125220>.
- (223) Post, P.; Wurlitzer, L.; Maus-Friedrichs, W.; Weber, A. P. Characterization and Applications of Nanoparticles Modified In-Flight with Silica or Silica-Organic Coatings. *Nanomaterials* **2018**, *8*, 530. <https://doi.org/10.3390/nano8070530>.
- (224) Primo, A.; Corma, A.; García, H. Titania Supported Gold Nanoparticles as Photocatalyst. *Phys. Chem. Chem. Phys.* **2011**, *13*, 886–910. <https://doi.org/10.1039/c0cp00917b>.
- (225) IUPAC Recommendations for the Characterization of Porous Solids (Technical Report). *Pure Appl. Chem.* **1994**, *66*, 1739–1758. <https://doi.org/10.1351/pac199466081739>.

- (226) Thommes, M.; Kaneko, K.; Neimark, A. V.; Olivier, J. P.; Rodriguez-Reinoso, F.; Rouquerol, J.; Sing, K. S. W. Physisorption of Gases, with Special Reference to the Evaluation of Surface Area and Pore Size Distribution (IUPAC Technical Report). *Pure Appl. Chem.* **2015**, *87*, 1051–1069. <https://doi.org/10.1515/pac-2014-1117>.
- (227) Makuła, P.; Pacia, M.; Macyk, W. How To Correctly Determine the Band Gap Energy of Modified Semiconductor Photocatalysts Based on UV-Vis Spectra. *J. Phys. Chem. Lett.* **2018**, *9*, 6814–6817. <https://doi.org/10.1021/acs.jpcllett.8b02892>.
- (228) Pedone, A.; Bloino, J.; Barone, V. Role of Host-Guest Interactions in Tuning the Optical Properties of Coumarin Derivatives Incorporated in MCM-41: A TD-DFT Investigation. *J. Phys. Chem. C* **2012**, *116*, 17807–17818. <https://doi.org/10.1021/jp305294u>.
- (229) van Hal, P. A.; Wienk, M. M.; Kroon, J. M.; Verhees, W. J. H.; Slooff, L. H.; van Gennip, W. J. H.; Jonkheijm, P.; Janssen, R. A. J. Photoinduced Electron Transfer and Photovoltaic Response of a MDMO-PPV:TiO₂ Bulk-Heterojunction. *Adv. Mater.* **2003**, *15*, 118–121. <https://doi.org/10.1002/adma.200390022>.
- (230) Bledowski, M.; Wang, L.; Ramakrishnan, A.; Khavryuchenko, O. V.; Khavryuchenko, V. D.; Ricci, P. C.; Strunk, J.; Cremer, T.; Kolbeck, C.; Beranek, R. Visible-Light Photocurrent Response of TiO₂-Polyheptazine Hybrids: Evidence for Interfacial Charge-Transfer Absorption. *Phys. Chem. Chem. Phys.* **2011**, *13*, 21511–21519. <https://doi.org/10.1039/c1cp22861g>.
- (231) DiStefano, T. H.; Eastman, D. E. The Band Edge of Amorphous SiO₂ by Photoinjection and Photoconductivity Measurements. *Solid State Commun.* **1971**, *9*, 2259–2261. [https://doi.org/10.1016/0038-1098\(71\)90643-0](https://doi.org/10.1016/0038-1098(71)90643-0).
- (232) Astašauskas, V.; Bellissimo, A.; Kuksa, P.; Tomastik, C.; Kalbe, H.; Werner, W. S. M. Optical and Electronic Properties of Amorphous Silicon Dioxide by Single and Double Electron Spectroscopy. *J. Electron Spectros. Relat. Phenomena* **2020**, *241*, 146829. <https://doi.org/10.1016/j.elspec.2019.02.008>.
- (233) Fatimah, I.; Prakoso, N. I.; Sahroni, I.; Musawwa, M. M.; Sim, Y. L.; Kooli, F.; Muraza, O. Physicochemical Characteristics and Photocatalytic Performance of TiO₂/SiO₂ Catalyst Synthesized Using Biogenic Silica from Bamboo Leaves. *Heliyon* **2019**, *5*, e02766. <https://doi.org/10.1016/j.heliyon.2019.e02766>.
- (234) Kaiti, S.; Himmelberg, P.; Williams, J.; Abdellatif, M.; Fossum, E. Linear Poly(Arylene Ether)s with Pendant Phenylsulfonyl Groups: Nucleophilic Aromatic Substitution

- Activated from the Meta Position. *Macromolecules* **2006**, *39*, 7909–7914. <https://doi.org/10.1021/ma061248x>.
- (235) Zhao, Z.; Zhang, H.; Lam, J. W. Y.; Tang, B. Z. Aggregation-Induced Emission: New Vistas at the Aggregate Level. *Angew. Chemie - Int. Ed.* **2020**, *59*, 9888–9907. <https://doi.org/10.1002/anie.201916729>.
- (236) Parrott, E. P. J.; Tan, N. Y.; Hu, R.; Zeitler, J. A.; Tang, B. Z.; Pickwell-Macpherson, E. Direct Evidence to Support the Restriction of Intramolecular Rotation Hypothesis for the Mechanism of Aggregation-Induced Emission: Temperature Resolved Terahertz Spectra of Tetraphenylethene. *Mater. Horizons* **2014**, *1*, 251–258. <https://doi.org/10.1039/c3mh00078h>.
- (237) Li, S.; Zhao, W.; Zhang, J.; Liu, X.; Zheng, Z.; He, C.; Xu, B.; Wei, Z.; Hou, J. Influence of Covalent and Noncovalent Backbone Rigidification Strategies on the Aggregation Structures of a Wide-Band-Gap Polymer for Photovoltaic Cells. *Chem. Mater.* **2020**, *32*, 1993–2003. <https://doi.org/10.1021/acs.chemmater.9b04971>.
- (238) Pinnock, S. S.; Malele, C. N.; Che, J.; Jones, W. E. The Role of Intermolecular Interactions in Solid State Fluorescent Conjugated Polymer Chemosensors. *J. Fluoresc.* **2012**, *22*, 583–589. <https://doi.org/10.1007/s10895-011-0993-1>.
- (239) Demyanenko, A. V.; Bogomolov, A. S.; Dozmorov, N. V.; Svyatova, A. I.; Pyryaeva, A. P.; Goldort, V. G.; Kochubei, S. A.; Baklanov, A. V. Singlet Oxygen 1O_2 in Photocatalysis on TiO_2 . Where Does It Come From? *J. Phys. Chem. C* **2019**, *123*, 2175–2181. <https://doi.org/10.1021/acs.jpcc.8b09381>.
- (240) Berr, M. J.; Wagner, P.; Fischbach, S.; Vaneski, A.; Schneider, J.; Suscha, A. S.; Rogach, A. L.; Jäckel, F.; Feldmann, J. Hole Scavenger Redox Potentials Determine Quantum Efficiency and Stability of Pt-Decorated CdS Nanorods for Photocatalytic Hydrogen Generation. *Appl. Phys. Lett.* **2012**, *100*, 223903. <https://doi.org/10.1063/1.4723575>.
- (241) Johnson, J. W.; Wroblowa, H.; Bockris, J. O. M. The Mechanism of the Electrochemical Oxidation of Oxalic Acid. *Electrochim. Acta* **1964**, *9*, 639–651. [https://doi.org/10.1016/0013-4686\(64\)80036-0](https://doi.org/10.1016/0013-4686(64)80036-0).
- (242) Arimi, A.; Günemann, C.; Curti, M.; Bahnemann, D. W. Regarding the Nature of Charge Carriers Formed by Uv or Visible Light Excitation of Carbon-Modified Titanium Dioxide. *Catalysts* **2019**, *9*, 697. <https://doi.org/10.3390/catal9080697>.

- (243) Leandri, V.; Gardner, J. M.; Jonsson, M. Coumarin as a Quantitative Probe for Hydroxyl Radical Formation in Heterogeneous Photocatalysis. *J. Phys. Chem. C* **2019**, *123*, 6667–6674. <https://doi.org/10.1021/acs.jpcc.9b00337>.
- (244) Krieger, W.; Lamsfuß, J.; Zhang, W.; Kockmann, N. Local Mass Transfer Phenomena and Chemical Selectivity of Gas-Liquid Reactions in Capillaries. *Chem. Eng. Technol.* **2017**, *40*, 2134–2143. <https://doi.org/10.1002/ceat.201700420>.
- (245) Plácido, J.; Chanagá, X.; Ortiz-Monsalve, S.; Yepes, M.; Mora, A. Degradation and Detoxification of Synthetic Dyes and Textile Industry Effluents by Newly Isolated *Leptosphaerulina* Sp. from Colombia. *Bioresour. Bioprocess.* **2016**, *3*, 6. <https://doi.org/10.1186/s40643-016-0084-x>.
- (246) Fenavi. *Caracterización Económica Del Sector Avícola En El Departamento de Santander*, 2016. <https://fenavi.org/publicaciones-programa-economico/caracterizacion-economica-del-sector-avicola-en-santander/>
- (247) Aznar, R.; Albero, B.; Pérez, R. A.; Sánchez-Brunete, C.; Miguel, E.; Tadeo, J. L. Analysis of Emerging Organic Contaminants in Poultry Manure by Gas Chromatography–Tandem Mass Spectrometry. *J. Sep. Sci.* **2018**, *41*, 940–947. <https://doi.org/10.1002/jssc.201700883>.
- (248) Hakk, H.; Millner, P.; Larsen, G. Decrease in Water-Soluble 17 β -Estradiol and Testosterone in Composted Poultry Manure with Time. *J. Environ. Qual.* **2005**, *34*, 943–950. <https://doi.org/10.2134/jeq2004.0164>.
- (249) Adeel, M.; Song, X.; Wang, Y.; Francis, D.; Yang, Y. Environmental Impact of Estrogens on Human, Animal and Plant Life: A Critical Review. *Environ. Int.* **2017**, *99*, 107–119. <https://doi.org/10.1016/j.envint.2016.12.010>.
- (250) Herman, J. S.; Mills, A. L. Biological and Hydrogeological Interactions Affect the Persistence of 17beta-Estradiol in an Agricultural Watershed. *Geobiology* **2003**, *1*, 141–151. <https://doi.org/10.1046/j.1472-4669.2003.00011.x>.
- (251) Murcia, J. J.; Cely, Á. C.; Rojas, H. A.; Hidalgo, M. C.; Navío, J. A. Fluorinated and Platinized Titania as Effective Materials in the Photocatalytic Treatment of Dyestuffs and Stainedwastewater Coming from Handicrafts Factories. *Catalysts* **2019**, *9*, 179. <https://doi.org/10.3390/catal9020179>.
- (252) Lima, C. S.; Batista, K. A.; García Rodríguez, A.; Souza, J. R.; Fernandes, K. F. Photodecomposition and Color Removal of a Real Sample of Textile Wastewater Using Heterogeneous Photocatalysis with Polypyrrole. *Sol. Energy* **2015**, *114*, 105–

113. <https://doi.org/10.1016/j.solener.2015.01.038>.
- (253) Sun, J.; Qiao, L.; Sun, S.; Wang, G. Photocatalytic Degradation of Orange G on Nitrogen-Doped TiO₂ Catalysts under Visible Light and Sunlight Irradiation. *J. Hazard. Mater.* **2008**, *155*, 312–319. <https://doi.org/10.1016/j.jhazmat.2007.11.062>.
- (254) Upreti, A. R.; Li, Y.; Khadgi, N.; Naraginti, S.; Zhang, C. Efficient Visible Light Photocatalytic Degradation of 17 α -Ethinyl Estradiol by a Multifunctional Ag-AgCl/ZnFe₂O₄ Magnetic Nanocomposite. *RSC Adv.* **2016**, *6*, 32761–32769. <https://doi.org/10.1039/c6ra00707d>.
- (255) Yilmaz, B.; Kadioglu, Y. Determination of 17 β -Estradiol in Pharmaceutical Preparation by UV Spectrophotometry and High Performance Liquid Chromatography Methods. *Arab. J. Chem.* **2017**, *10*, S1422–S1428. <https://doi.org/10.1016/j.arabjc.2013.04.018>.
- (256) Alqahtani, S. S.; Bin Humaid, D. M.; Alshail, S. H.; Alshammari, D. T.; Al-Showiman, H.; Alzoman, N. Z.; Maher, H. M. Development and Validation of a High Performance Liquid Chromatography/Diode Array Detection Method for Estrogen Determination: Application to Residual Analysis in Meat Products. *Open Chem.* **2020**, *18*, 995–1010. <https://doi.org/10.1515/chem-2020-0118>.
- (257) Salierno, J. D.; Pollack, S. J.; Van Veld, P. A.; Ottinger, M. A.; Yonkos, L. T.; Kane, A. S. Steroid Hormones and Anthropogenic Contaminants in Poultry Litter Leachate. *Water. Air. Soil Pollut.* **2012**, *223*, 2181–2187. <https://doi.org/10.1007/s11270-011-1014-3>.
- (258) Kumar, A.; Kumar, A.; Sharma, G.; Naushad, M.; Veses, R. C.; Ghfar, A. A.; Stadler, F. J.; Khan, M. R. Solar-Driven Photodegradation of 17- β -Estradiol and Ciprofloxacin from Waste Water and CO₂ Conversion Using Sustainable Coal-Char/Polymeric-g-C₃N₄/RGO Metal-Free Nano-Hybrids. *New J. Chem.* **2017**, *41*, 10208–10224. <https://doi.org/10.1039/c7nj01580a>.
- (259) Mazellier, P.; Méité, L.; De Laat, J. Photodegradation of the Steroid Hormones 17 β -Estradiol (E2) and 17 α -Ethinylestradiol (EE2) in Dilute Aqueous Solution. *Chemosphere* **2008**, *73*, 1216–1223. <https://doi.org/10.1016/j.chemosphere.2008.07.046>.
- (260) Ohko, Y.; Iuchi, K. I.; Niwa, C.; Tatsuma, T.; Nakashima, T.; Iguchi, T.; Kubota, Y.; Fujishima, A. 17 β -Estradiol Degradation by TiO₂ Photocatalysis as a Means of

- Reducing Estrogenic Activity. *Environ. Sci. Technol.* **2002**, *36*, 4175–4181. <https://doi.org/10.1021/es011500a>.
- (261) Shore, L. S.; Shemesh, M. Naturally Produced Steroid Hormones and Their Release into the Environment. *Pure Appl. Chem.* **2003**, *75*, 1859–1871. <https://doi.org/10.1351/pac200375111859>.
- (262) Takroui, K.; Chen, T.; Papadopoulos, E.; Sahoo, R.; Kabha, E.; Chen, H.; Cantel, S.; Wagner, G.; Halperin, J. A.; Aktas, B. H.; Chorev, M. Structure-Activity Relationship Study of 4EGI-1, Small Molecule EIF4E/EIF4G Protein-Protein Interaction Inhibitors. *Eur. J. Med. Chem.* **2014**, *77*, 361–377. <https://doi.org/10.1016/j.ejmech.2014.03.034>.
- (263) Cao, J.; Feng, J. X.; Wu, Y. X.; Pei, X. Q.; Yan, J. J.; Liu, Y.; Qin, W. J.; Zhang, X. Bin. An Ion-Responsive Fluorescent Compound Based on NO-Photoisomerisation Styryl Derivative Linked to Monoaza-15-Crown-5. *Supramol. Chem.* **2011**, *23*, 407–410. <https://doi.org/10.1080/10610278.2010.532215>.
- (264) Klaus, F.; Baudisch, O. Über Die Einwirkung Der Salpetrigen Säure Auf P-Dimethylamino-benzoesäure-methylester Und P-Dimethylamino Benzaldehyd. (Reaktionen Tertiärer Amine Und Beitrag Zur Sterischen Hinderung). *Ber. Dtsch. Chem. Ges.* **1918**, *51*, 1036–1048. <https://doi.org/10.1002/cber.191805101127>.
- (265) Muraki, T.; Togo, H.; Yokoyama, M. Reactivity and Synthetic Utility of 1-(Arenesulfonyloxy) Benziodoxolones. *J. Org. Chem.* **1999**, *64*, 2883–2889. <https://doi.org/10.1021/jo9825207>.
- (266) Berliner, E.; Monack, C. The Nucleophilic Displacement in the Benzene Series. *Am. Chem. Soc.* **1951**, *74*, 1574–1579. <https://doi.org/10.1021/ja01126a069>.
- (267) Yang, Z.; Geise, H. J.; Mehbod, M.; Debrue, G.; Visser, J. W.; Sonneveld, E. J.; Van't dack, L.; Gijbels, R. Conductivity and Electron Density of Undoped Model Compounds of Poly(Phenylene Vinylene). *Synth. Met.* **1990**, *39*, 137–151.
- (268) Mates, T. E.; Ober, C. K.; Norwood, R. Conductivity and Third-Order Nonlinear Optical Measurements of Polymers with Distyrylbenzene and Diphenylbutadiene Segments. *Chem. Mater.* **1993**, *5*, 217–221. <https://doi.org/10.1021/cm00026a012>.